Design and Control of a Self-Sensing Piezoelectric Reticle Assist Device

by

Darya Amin-Shahidi

Submitted to the Department of Mechanical Engineering
in partial fulfillment of the requirements for the degree of

Doctor of Philosophy

at the

MASSACHUSETTS INSTITUTE OF TECHNOLOGY

June 2013

Author .....
Department of Mechanical Engineering
May 20, 2013

Certified by .....
David L. Trumper
Professor of Mechanical Engineering
Thesis Supervisor

Accepted by .....
David E. Hardt
Chairman, Department Committee on Graduate Theses

Design and Control of a Self-Sensing Piezoelectric Reticle Assist Device

by

Darya Amin-Shahidi

Submitted to the Department of Mechanical Engineering
on May 20, 2013, in partial fulfillment of the
requirements for the degree of
Doctor of Philosophy

Abstract

This thesis presents the design and control techniques of a device for managing the inertial loads on photoreticle of lithography scanners. Reticle slip, resulting from large inertial loads, is a factor limiting the throughput and accuracy of the lithography scanners. Our reticle-assist device completely eliminates reticle slip by carrying 96% of the inertial loads. The primary contributions of this thesis include the design and implementation of a practical high-force density reticle assist device, the development of a novel charge-controlled power amplifier with DC hysteresis compensation, and the development of a sensorless control method.

A lithography scanner exposes a wafer by sweeping a slit of light passing through a reticle. The scanner controls the motion of the reticle and the wafer. The reticle-stage moves the photoreticle. To avoid deforming the reticle, it is held using a vacuum clamp. Each line scan consists of acceleration at the ends of the line and a constant-speed motion in the middle of the line, where exposure occurs. If the reticle's inertial force approaches or exceeds the clamp's limit, nanometer-level pre-sliding slip or sliding slip will occur. The assist device carries the inertial load by exerting a feed-forward force on the reticle's edge. The device retracts back during the sensitive exposure interval to avoid disturbing the reticle. The reticle is at the heart of the scanner, where disturbances directly affect the printing accuracy.

Our reticle assist device consists of an approach mechanism and a piezoelectric stack actuator. The approach mechanism positions the actuator 1-μm from the reticle edge. The actuator, with 15-μm range, extends to push on the reticle. We have developed control techniques to enable high-precision high-bandwidth force compensation without using any sensors. We have also developed a novel charge-controlled amplifier with a more robust feedback circuit and a method for hysteresis compensation at DC. These technologies were key to achieving high-bandwidth high-precision sensorless force control. When tested with a trapezoidal force profile with 6400 N/s rate and 60 N peak force, the device canceled 96% of the inertial force.

Thesis Supervisor: David L. Trumper
Title: Professor of Mechanical Engineering

Acknowledgments

I would like to thank my thesis advisor Professor David L. Trumper for his unconditional support and invaluable feedback throughout the years of my studies. His teachings and tips provided me with the opportunity to successfully complete each and every one of my projects. He gave me the freedom to explore and consequently learn a great amount. He has trusted me with numerous opportunities which were important to my professional development. Throughout the years, he created a friendly and productive environment for us in the laboratory. It has been an honor and privilege to work with him.

I would also like to thank my thesis committee for giving me their time and support and providing me with invaluable feedback. Professor Alex H. Slocum's energy and knowledge was an inspiration to me. Not only has he assisted me with my thesis, but he has also been a wonderful mentor both academically and professionally. I would like to thank Professor Markus Zahn who taught me important concepts in electromagnetism. He has been very kind in putting aside his time for my thesis and closely monitoring my progress. I would also like to thank Professor Martin L. Culpepper who helped me early on in identifying important research problems and directing my efforts.

I would like to thank ASML for their collaboration and financial support. I would like to thank Stephen Roux who was my manager during my internship at ASML. His support and input was instrumental to the realization of this project. I would also like to thank Mark Schuster and Christopher Ward for their constant involvement and feedback. I would like to thank Santiago Del Puerto and Enrico Zordan whose initial work on the reticle slip problem was a great resource to this project.

I would like to thank National Instruments for the hardware donation and their technical support. I especially thank Lesley Yu, NI field engineer for her time and technical support.

My dear labmates created a very friendly atmosphere in our labratory and offered me their help. I had many stimulating discussions with Mohammad Imani Nejad. He

shared his knowledge in manufacturing with me and patiently answered many of my questions. I enjoyed working with Ian MacKenzie on the control of the reluctance actuators. Lei Zhou, Zehn Sun, Minkyun Noh, and Jun young Yoon helped me with using the macro-scale AFM for teaching mechatronics. Roberto Melendez introduced me to the nice people at MIT Sailing Pavilion and taught me sailing.

I would also like to thank Laura Zaganjori for her efficient and helpful administrative support. I would also like to thank the mechanical department office staff, especially Leslie Regan. I would like to thank my friends with whom I have spent many hours either socializing or playing sports. They have made my life a lot more interesting and enjoyable.

I am indebted to my parents for their boundless support throughout my life and up until today, without them I would not have been where I am at this moment. Sophiya Shahla, my wife, has made tremendous sacrifice for my study. She has been a great friend and has helped me in every step of the way. I thank her for being extremely supportive and understanding.

This work was sponsored by ASML and performed at the Massachusetts Institute of Technology.

To My Grandparents

Contents

List of Figures

List of Tables

Chapter 1

Introduction

The semiconductor industry manufactures the chips which are the basic building blocks of electronic devices, and is among the fastest advancing industries. The industry's main technological drivers have been manufacturing denser circuits at faster rates. In this way, more powerful devices can be built for cheaper prices. Gordon Moore predicted in 1965 that the number of transistors in a device will double every two years. His prediction has remained accurate until this day. This has been partly due to the fact that the Moore's law has been used as a roadmap for the industry's advancement [59]. While shrinking the devices at an exponential rate, the industry has worked to increase the manufacturing throughput. The two conflicting goals of improved manufacturing precision and throughput have led to many challenges. The higher inertial loads of the faster moving next-generation scanners can cause the reticles to slip. Reticle slip can be a major error source of the next generation scanners. The main focus of this thesis is addressing the reticle slip problem. In collaboration with ASML, we have developed a solid-state reticle assist device, which uses a piezoelectric stack actuator to exert a normal force on the reticle's edge to cancel the inertial loads and prevent reticle slip. Using this design, we have successfully demonstrated the potential to eliminate reticle slip even under high acceleration. By preventing reticle slip, this technology can help enable higher throughput without sacrificing precision. In the following sections, we present the background of the reticle-slip problem. Next, we review the relevant prior art work. Finally, we outline

a summary of this thesis and list its main contributions.

1.1 Background

Optical lithography is the semiconductor industry's most common manufacturing process, where a master pattern printed on a transparent substrate, called the reticle, is transferred onto a silicon wafer. The scanners are currently the most common lithography manufacturing equipment. A scanner moves both the reticle and the wafer relative to each other and exposes the wafer using a slit of light passing through the reticle[14]. To achieve faster scan speeds and higher throughput, scanners must operate at higher accelerations. The reticle can slip as a result of the large inertial loads of the next generation scanners. To avoid deforming the reticle, it is held in place using a vacuum chuck. The vacuum chuck's maximum clamping force is set by the vacuum surface area, which is limited by the standard size of the reticles. The inertial loads of the next-generation scanners can exceed the clamping force limit. Reticle slip can be a major error source and addressing it is key to enabling higher throughput. At the same time, scanners are complex and highly optimized machines. Reticle, which holds the master pattern being printed, is at the heart of these equipments. Modifications close to this sensitive part of the scanner must be made with care as they can directly affect the scanner's performance. Interactions with the reticle must be well regulated to avoid disturbing the its pattern by more than 1nm. The main focus of this thesis has been creating a solution to fully eliminate the reticle slip problem without hindering the performance of the rest of the system. The manufacturers of the scanners have considered different solutions to this problem, which are discussed in Section 1.2. The main focus of this thesis is to create a technology, which can eliminate the bottleneck on throughput set by the reticle slip problem without worsening, if not improving, the performance of the scanner in the other areas. This works has been carried in collaboration with ASML, the world's leading provider of the lithography scanners.

1.2 Prior Art

ASML, Nikon, and Canon are the main current manufacturers of lithography scanners. They have all searched for methods to solve the reticle slip problem. In the following subsections, we review the solutions generated by the industry which are available in the patent literature. The prior art references can be categorized into two groups according to their general approach toward solving the problem: modifying the clamp mechanism and externally compensating the inertial forces.

1.2.1 Modified Clamping Mechanisms

The reticle slip problem can occur when the reticle's inertial load exceeds the reticle's clamping force limit. As a result, improving the clamping mechanism is one potential way to solve the problem.

Shibazaki, of Nikon, has designed a mechanical clamping mechanism, which can increase the normal force available for clamping the reticle [74][73][74]. A sketch of the clamping mechanism in the open and closed position is shown in Figure 1-1. The reticle (R) is clamped between the rigid support (203/211) and the clamp end (322). A flexible clamp end (322) is used to uniformly distribute the clamping force across the reticle and avoid generating parasitic forces in the other directions. To operate the clamp, the actuation end (363) is moved by a cam and follower mechanism. The locking element (364a) is used to lock the mechanism once it is clamped. This design relies on a rigid support (203/211) underneath the reticle. However a rigid support under the reticle will over-constrain it and can deform the reticle. Also, exerting a clamping force through the reticle can distort the reticle, which will distort the printed layers.

Baggen et al., of ASML, propose using actuators to exert opposing clamping forces on the reticle only during the acceleration intervals and not through the constant speed scan intervals [12]. In this way, the reticle deformation resulting from the additional clamping forces is not present during the scan interval and thus will not distort the printed layers. As shown in Figure 1-2, a reticle (20) is clamped to a

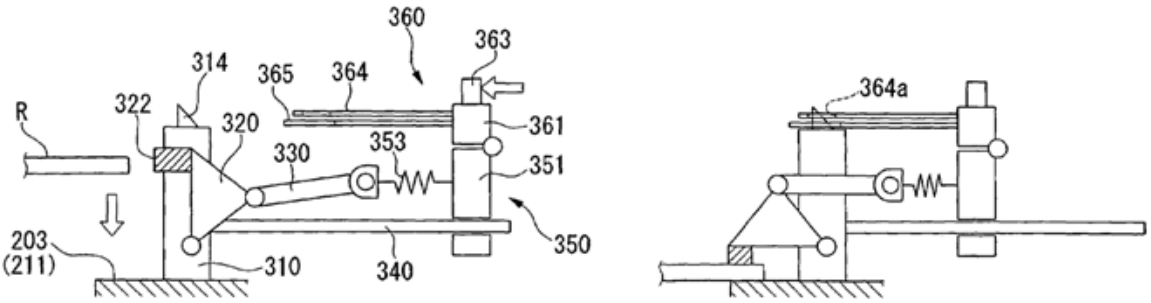

Figure 1-1: Schematic diagram of Nikon's mechanical clamping mechanism invented by Shibazaki shown in open (left) and closed (right) positions. Figure is taken from US Patent 8,253,929 [74].

stage (10) using the vacuum surfaces (15). Clamping forces (30) are exerted onto the reticle. Baggen et al. state that the clamping forces can be generated using a variety of actuators: voice coil motor, piezoelectric, electromagnetic, and pneumatic bellows. For the clamping forces to be effective their stiffness in the scan direction (Y) must be higher than the original vacuum clamp stiffness. Although the diagram shows the clamping forces oriented in the XY plane, Baggen et al. also describe an arrangement where the clamping forces are oriented in the out-of-plane direction. The actively applied clamping forces must be synchronized to avoid creating reticle slip due to a one-sided clamping load. The clamping forces are overconstraining the reticle and can result in small reticle displacements. As well, the impact forces of the repeating clamping action can displace or even damage the reticle unless the reticle is approached under control.

Zordan, of ASML, suggests that a clamping structure which is more compliant to the shape of the reticle can have a higher slip force limit, even without increasing the clamping forces [87]. According to Zordan, with higher compliance, high-stress corners are not formed and the shearing friction stress is distributed more uniformly. As a result, the slip condition occurs at higher loads. Perspective and cross-sectional views of one embodiment of this invention are shown in Figure 1-3. A reticle (30) is held by the vacuum cups (22). The vacuum cups are attached to the stage using membranes (20). As shown in the perspective view, the vacuum clamp on each side of the reticle (30) is formed by a series of smaller vacuum clamps. Breaking the vacuum

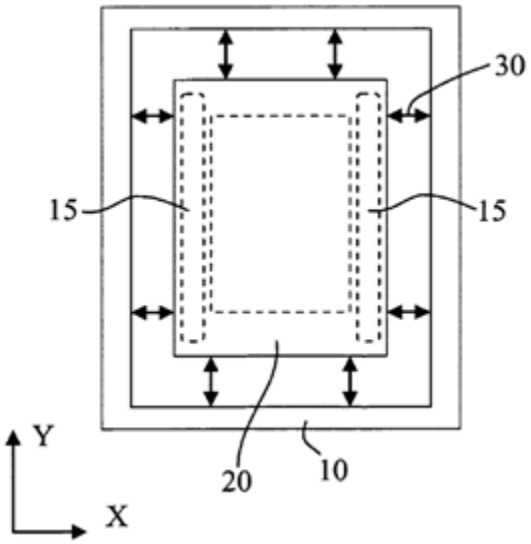

Figure 1-2: Schematic diagram of ASML's active clamping mechanism invented by Baggen et al. Figure is taken from US Patent 7,459,701 [12].

clamps into a series of smaller clamps increases the clamp compliance, where each clamp can easily deform to the shape of the reticle. Also, due to the smaller width of the membranes (20), the corner stresses resulting from elastic deformation of the membranes in the Y direction are minimized.

1.2.2 Reticle Assist Devices

The reticle slips if the inertial load carried by the clamp exceeds its force limit. One way to avoid slip is to use a device to exert an external force on the reticle which can fully or partially cancel the inertial load. In this way, less force is carried by the clamp, and slip can be avoided. In this thesis, we call such a device a reticle assist device.

Iwamoto, of Canon, invented a reticle assist device which generates the compensating forces using the inertia of two masses and a lever [35]. As shown in Figure 1-4, the reticle (101) is clamped to the stage (113). The mass (104) is attached to the end of the lever (103) and moves around the pivot (105). As the stage accelerates, the inertial load of the mass (104) is carried by the reticle (101). Because a pivot is used, the resulting external load on the reticle is opposite to the reticle's inertial load.

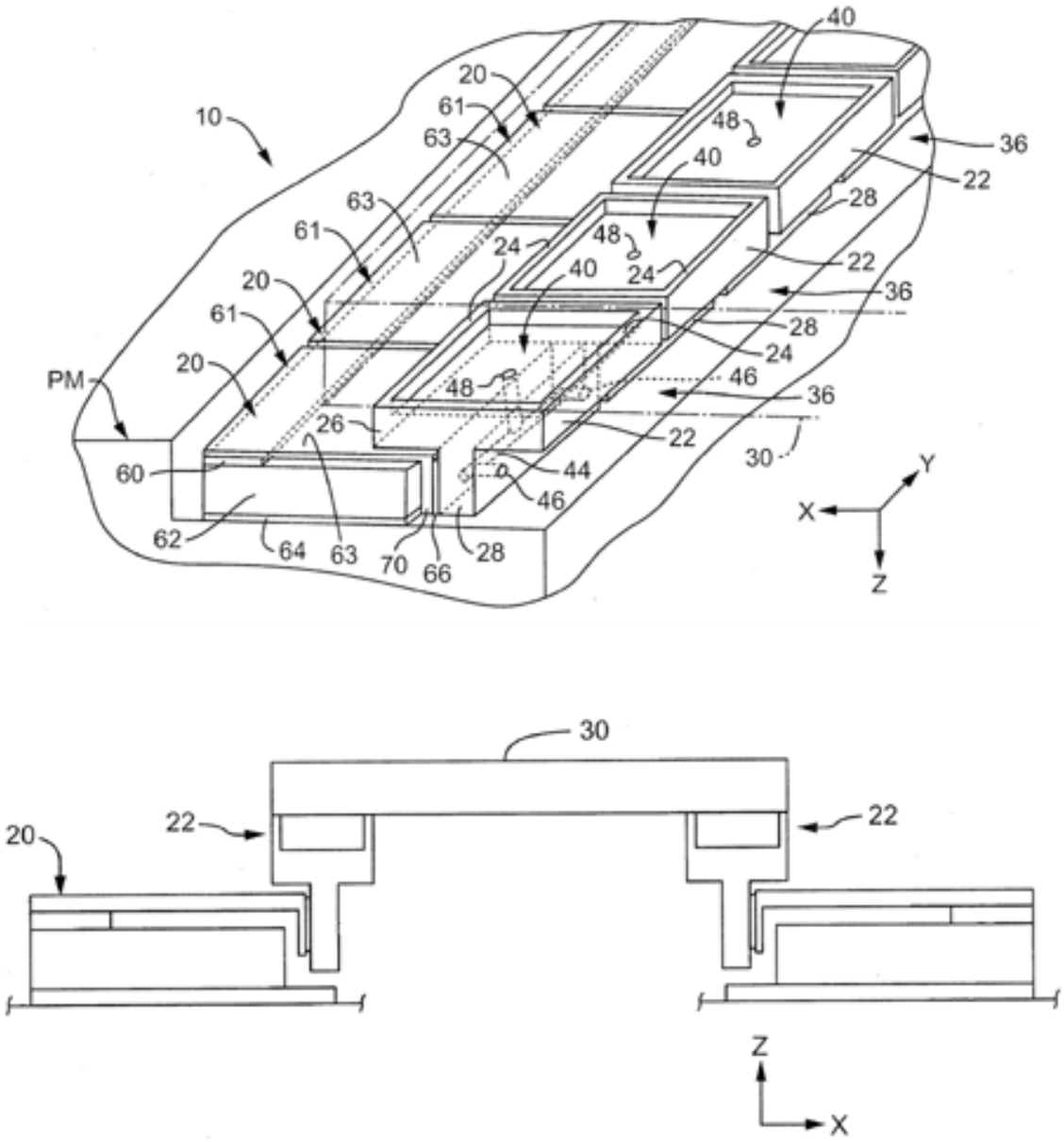

Figure 1-3: ASML's compliant clamp design invented by Enrico Zordan. Figure is taken from US Patent Application 13/168,109 [87].

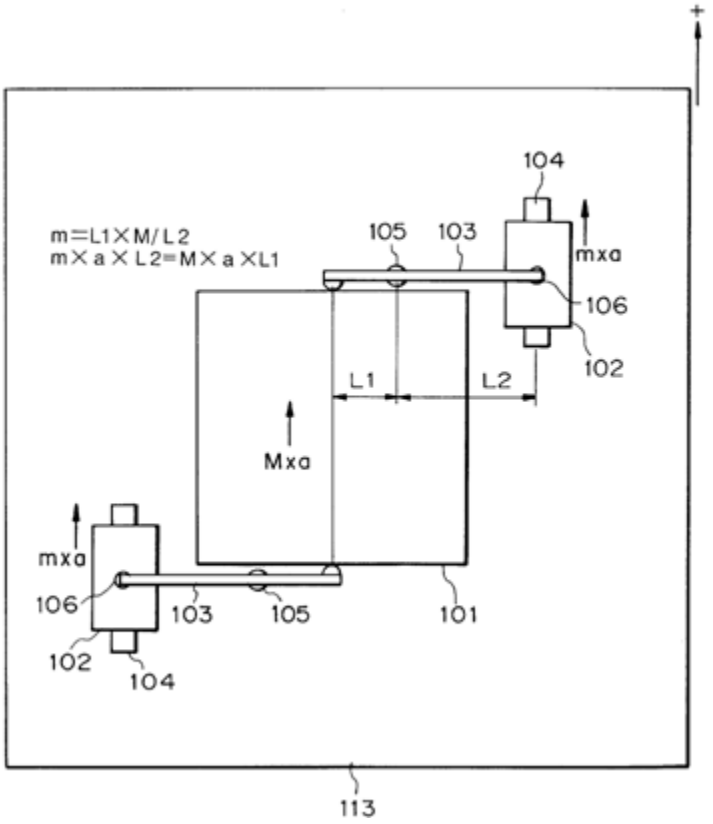

Figure 1-4: Schematic drawing of Canon's reticle assist device idea by Iwamoto. Figure is taken from US Patent 6,469,773 [35].

The length ratio of L1 to L2 and the mass m can be selected such that the resulting external load fully cancels the reticle's inertial load. Two of the pivot devices, one on each side, are used to cancel the inertial loads in both directions. The design has two major shortcomings. First, the added inertia and lever can add unwanted dynamics to the stage. Second, the masses are able to move freely by the inertial loads, and contact between the reticle and the device is not controlled. Unwanted contact during the exposure interval can distort the patterns being printed. Additionally, large impact forces between the reticle and the assist device can move or damage the reticle.

Jacobs et al., of ASML, propose using actuators with a lever mechanism to exert a force on the reticle [36]. As shown in Figure 1-5, linear motors (LM) push on a reticle (MA) through a lever pivoting around a pivot (PAX). One device is used on each side to enable cancelation of the inertial loads in both directions. Using the actuators to

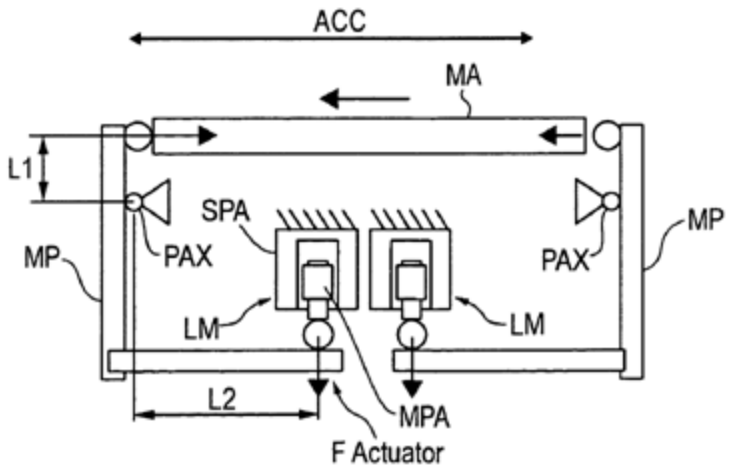

Figure 1-5: Schematic drawing of ASML's active pivoted reticle assist device idea by Jacobs et al. Figure is taken from US Patent 7,667,822 [36].

control the levers' positions, this device can make controlled contact with the reticle. Jacobs et al. state that the linear motor can be replaced with a piezoelectric actuator. As another alternative, the patent lists using a deformable pressurized chamber for creating a pushing force.

Baggen et al., in the patent, which was discussed in Section 1.2.1, suggests that the clamping actuators, which are oriented in the scan direction, can be used to exert a next force on the reticle to cancel the inertial load [12]. As shown in Figure 1-2, the actuators (60-63) can create a net force on the reticle (52), which is clamped to the stage (50).

Del Puerto and Zordan have designed a linear reticle assist device, which uses linear motors to exert pushing forces on the reticle [69]. As shown in Figure 1-7, the reticle (470) is clamped to the stage (420) through the vacuum surfaces (480A-B). Linear motors (430A-D) can push on reticle (470) through the rods (492A-B). The stage (420) is driven using linear motors. The same current driving the stage can be used to drive the assist device's linear motors. The force constant of the linear motors (430A-D) can be set such that the pushing force fully cancels the inertial force.

A key difficulty for devices making repeating contact with the reticle is controlling them to avoid large impact forces. Zordan, of ASML, has invented a mechanism to limit the contact forces. As shown in Fig 1-8, the pushing tip (48) is fixed to the

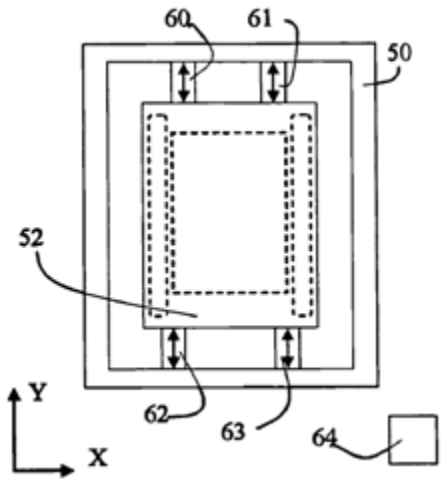

Figure 1-6: Schematic drawing of ASML's reticle assist device idea by Baggen et al. Figure is taken from US Patent 7,459,701 [12].

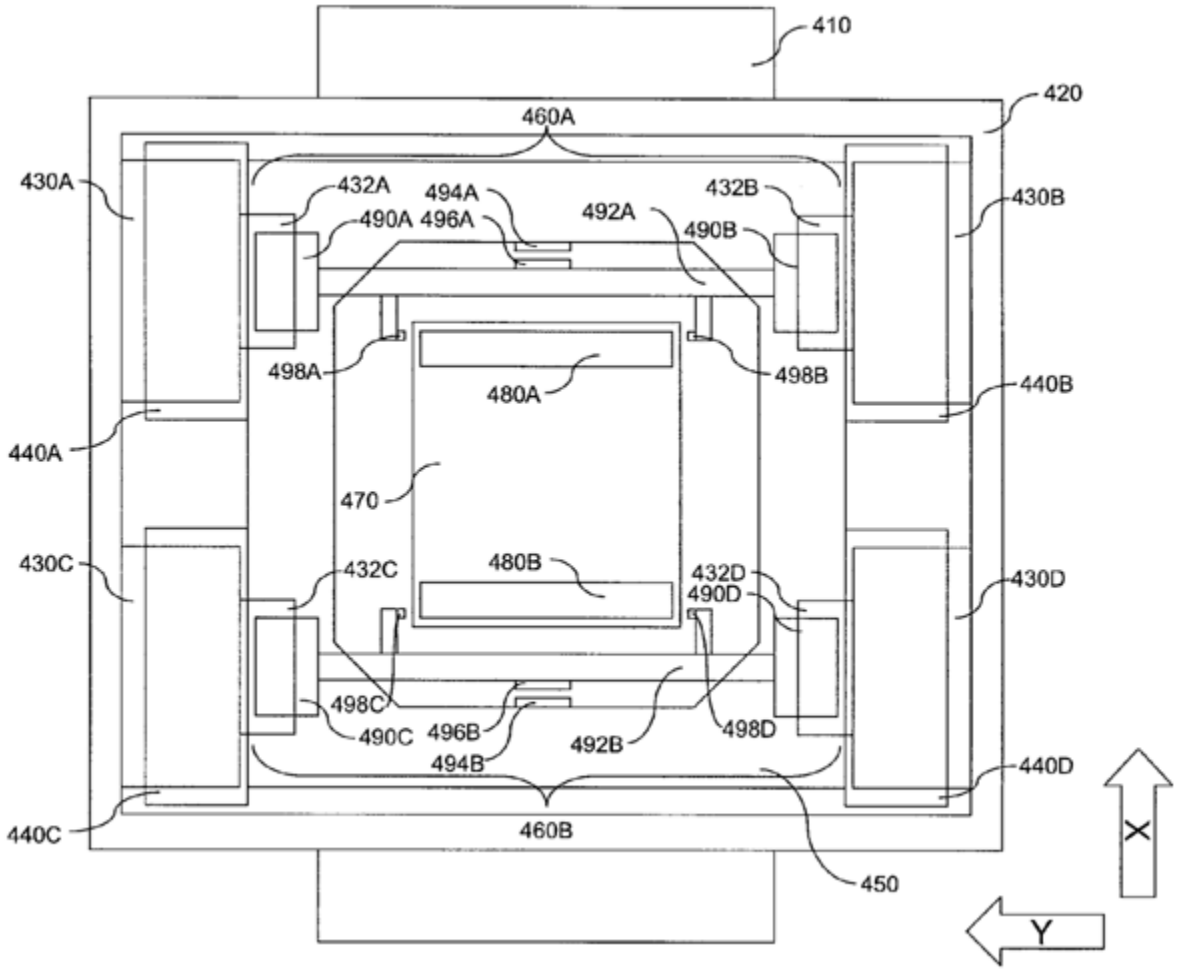

Figure 1-7: ASML's reticle assist device design by Del Puerto and Zordan. Figure is taken from US Patent Application 12/627,771 [69]

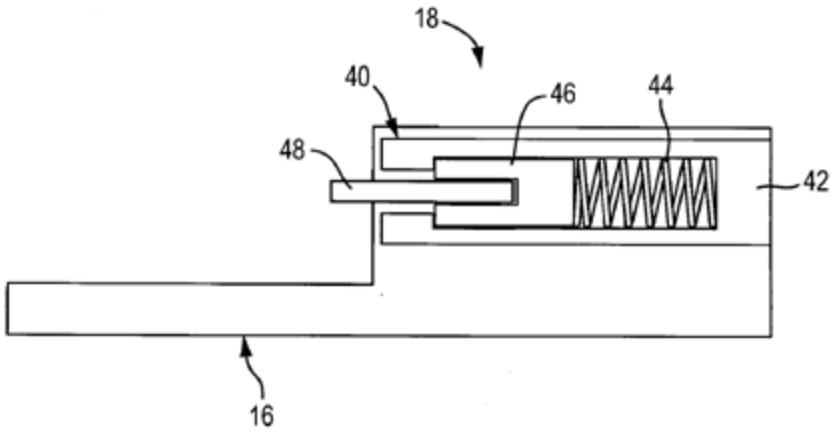

Figure 1-8: ASML's force-limiting pushing tip mechanism by Zordan. Figure is taken from US Patent Application 13/022,247 [86].

preloaded part (46), which is preloaded by the spring (44) to the actuator's moving body (40). If the pushing force exceeds the preload force of the spring, the preloaded part (46) will detach from the actuator body and the excess force is carried by the spring (44). If a flexible spring is used, the static force cannot rise significantly above the spring preload force. To limit the dynamic force, the inertia of the moving elements (48, 46, and 44) must be limited. The effectiveness of this design in limiting the impact forces depends on the contact speed and the inertia of the moving elements. By automatically limiting the contact forces, this design can potentially simplify the control and operation of reticle assist devices.

In the summer of 2010, following a summer internship at ASML, I filed a patent application on a solid-state reticle assist device and its operation [4]. As shown in Figure 1-9, the reticle (470) is clamped to the stage (450). The magnetostrictive solid-state element (466) can be energized by the coil (462) to extend and exert a pushing force on the reticle (470). The magnetostrictive element has a short-range of motion, so it is positioned close to the reticle using the position element (464) and is fixed using the clamp (465). To set the gap 467, the element is extend by the desired gap. Next, the element is preloaded against the reticle. Finally the element is clamped. In this way the gap is set to the desired value when the element's extension is reversed. From this position, the magnetostrictive element can extend to make contact and push on the reticle. The current driving the stage motors can be used

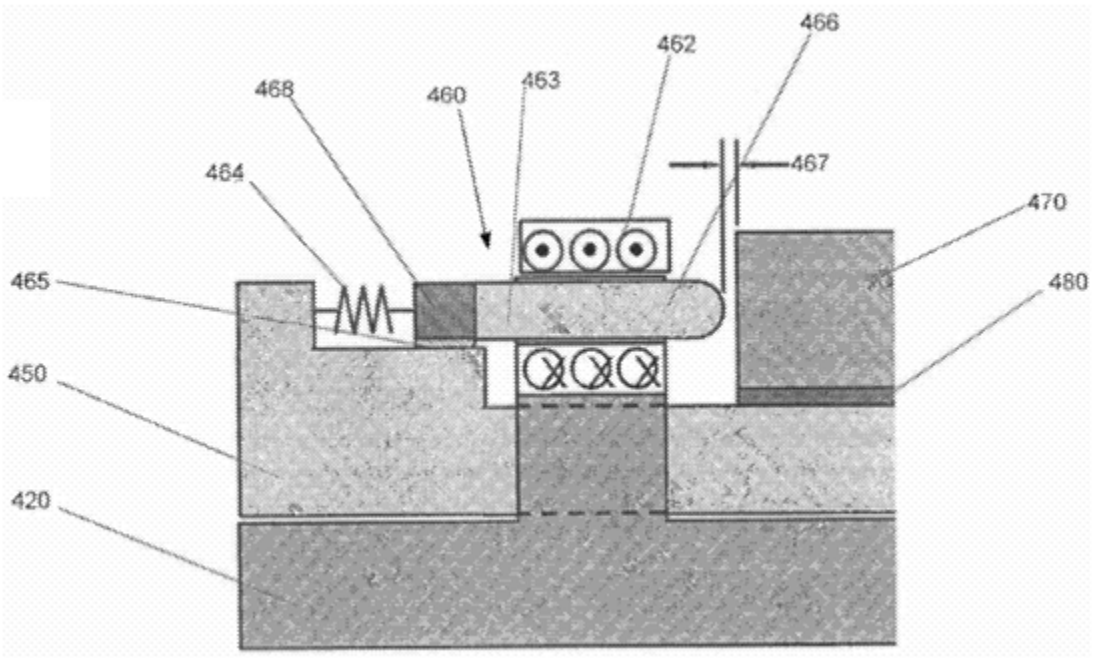

Figure 1-9: ASML's solid-state reticle assist device idea by Amin-Shahidi. Figure is taken from US Patent Application 13/281,718 [4].

to energize the assist device's coil (462) as well. The patent application states that other solid-state actuator elements, such as a piezoelectric element, can replace the magnetostrictive element.

1.3 Thesis Overview

The main focus of this thesis is to design and test a reticle assist device which advances the state of the art and enables higher manufacturing throughput without sacrificing accuracy. After considering the different possible reticle-assist technologies, we found solid-state devices to be the most suitable for this application. A piezoelectric element can have a very high force density. With very low mass and no moving parts, such a device can have excellent dynamics and good reliability. We have developed techniques which enable a bare piezoelectric element, without any force or strain sensors, to cancel the inertial forces by better than 95%. In this way we can create a practical and effective solution for addressing the reticle slip problem. In the following subsections, we provide a brief overview of this thesis. We cover the

reticle assist device, its enabling technologies, control, and experimental results.

1.3.1 Solid-State Reticle Assist Device

A photo of the completed assist device and its CAD drawing are shown in Fig 1-10. This design uses a piezoelectric stack actuator to generate the pushing forces. In the current prototype, the piezo stack has a range of 15 μm and a natural resonance frequency of approximately 25 kHz with the pusher-tip payload. The piezo actuator is fixed to a coarse positioning stage, which is used to position the piezo actuator when a new reticle is loaded. The coarse positioning stage uses a monolithic flexure to guide its motion. The stage is driven by a pneumatic bellow. The stage has a vacuum clamp, which is used to clamp and hold the position of the coarse stage. When positioned near the reticle, the piezo actuator can extend to exert a pushing force on the reticle. The pushing force is limited by the capacity of the coarse positioning stage's vacuum clamp and can be as high as 100 N with the present design. We use a spherical pushing tip to ensure that the piezo's load is centered on its axis and does not create a bending moment on the piezo stack. When scanning the wafer, the coarse stage is clamped and the reticle assist device has no moving parts except for the piezo ceramic actuator extending by less than 5 μm. While the piezo actuator weighs less than 15 g, it can produce forces as large as 100 cN on the reticle. The detailed design of the reticle assist device is described in Chapter 3.

1.3.2 Hybrid Charge Amplifier

We have designed and built a high performance charge amplifier which improves on the state of the art in terms of its control robustness and linearity. Piezoelectric elements exhibit strong hysteresis when used under voltage control. Charge control can be used to improve their linearity. We have designed and built a high performance charge amplifier using an APEX MP38 [9] linear power device. Pictures of the amplifier box and the printed circuit board are shown in Figure 1-11. The power amplifier has better than 100kHz small-signal bandwidth. A switch enables the user

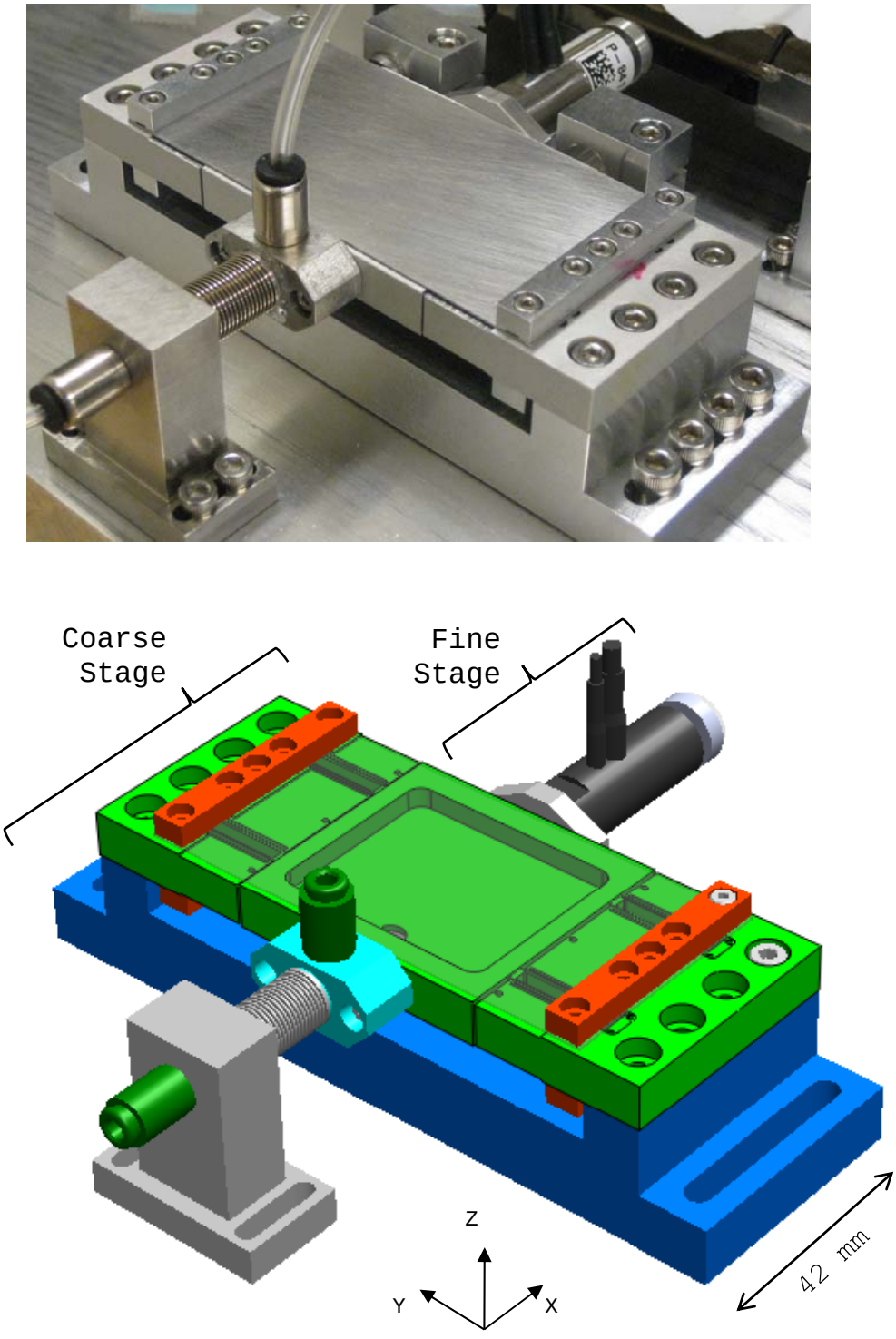

Figure 1-10: Photo (top) and CAD drawing (bottom) of the piezoelectric reticle assist device.

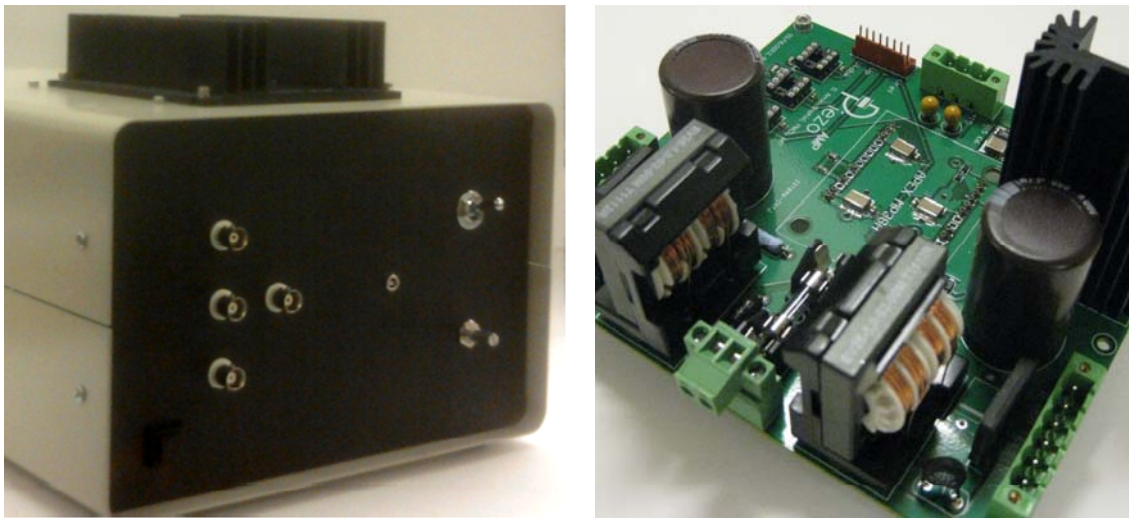

Figure 1-11: Photos of the charge amplifier box (left) and circuit board (right).

to select between voltage or charge-control mode. The amplifier uses a novel feedback controller which is less sensitive to added series load impedance. Conventional charge amplifiers control charge in the high-frequency range and voltage in the low-frequency range. The piezo's hysteresis appears as a positioning error when a low frequency reference signal is present. We have invented a compensation scheme which enables controlling charge at all frequencies. The compensation scheme is executed in software and acts at the charge amplifier's reference terminal. The algorithm can sample at a relatively low frequency and therefore can be added to the system by using a low-cost micro-controller. Because the algorithm acts at the charge amplifier's reference terminal, it can be integrated with existing charge amplifiers as well. The piezoelectric actuator's motion versus reference curves using different control methods are shown in Figure 1-12. Charge control is more linear compared to voltage control, and compensated charge control is significantly more linear than standard charge control. Using compensated charge control, we can eliminate the need for a strain sensor and associated closed-loop control of the piezoelectric actuator. We present the charge amplifier design in detail in Chapter 4.

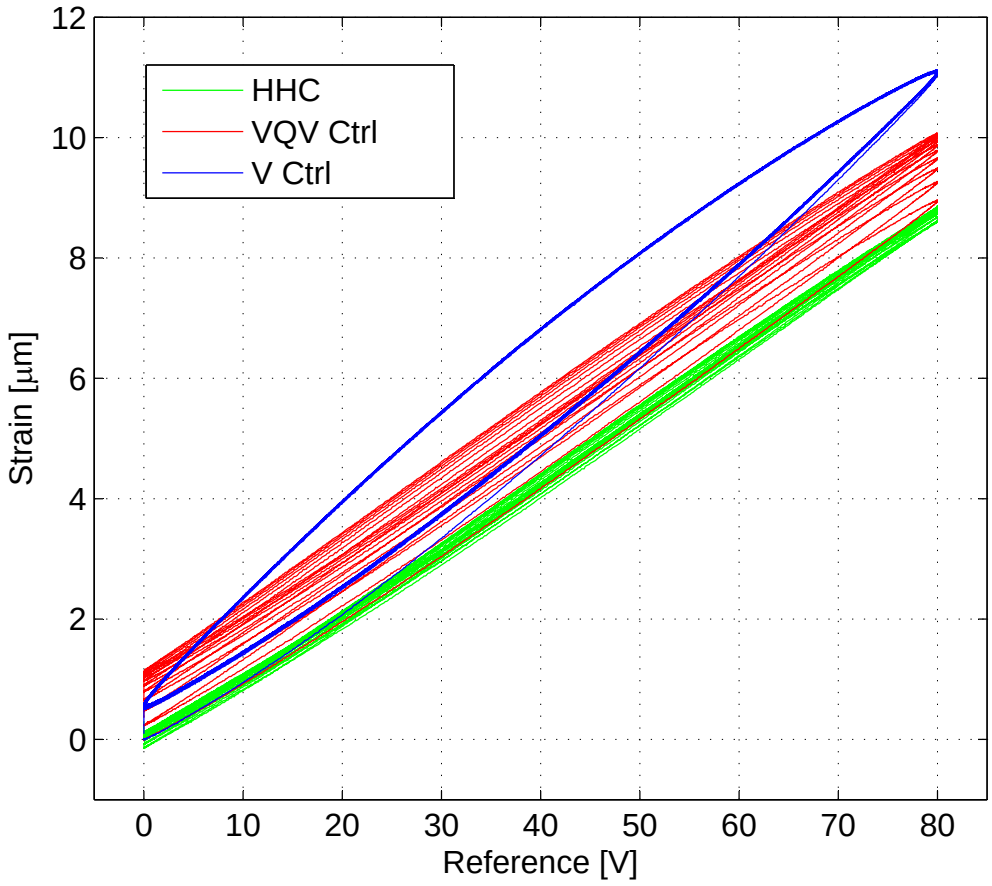

Figure 1-12: Piezoelectric actuator's displacement versus reference command using different control methods: voltage control (V-Ctrl), charge control (Q-Ctrl), and inverse-hysteresis feedback compensation (Q-Ctrl & HHC).

1.3.3 Self-Sensing Contact Detection

A key challenge when using the reticle assist device is registering the device's position relative to the reticle's edge. Relative position to the reticle's edge is required for avoiding tip-reticle impacts, and in many cases, for precise force control. We have applied an innovative self-sensing method for detecting reticle-tip contact with high-sensitivity and without the need for any sensors. In a fashion similar to self-sensing atomic force microscopy, the self-sensing module excites the piezo actuator at its natural frequency and monitors the piezo's voltage and current signals and their phase difference. As shown in Figure 1-13, the phase difference changes sharply when the tip contacts the reticle. This is used to detect reticle-tip contact. We have previously used a similar self-sensing method with a high-accuracy atomic force microscope (HAFM), which has been designed to be used as a metrology probe for the sub-atomic measuring machine (SAMM). The SAMM stage is a magnetically-suspended positioning stage, which has been designed in the doctorate dissertation of Holmes [33]. Figure 1-14 shows the HAFM integrated with the SAMM. The image of the triangular grating, which is shown in Figure 1-14, has been captured using the HAFM as the probe and SAMM as the XY scanner. We have also used the self-sensing technique with a macro-scale magnetic AFM profiler (MAP). We have designed the MAP to be used for teaching Mechatronics (2.737), a graduate-level course offered by the Mechanical Engineering Department at at MIT. Figure 1-15 shows MAP imaging an MIT key chain. The self-sensing method and its application to the reticle-assist device, HAFM, and MAP are presented in Chapter 5.

1.3.4 Reticle Assist Device Control and Experimental Results

We describe our control method, which has demonstrated better than 95% inertial force cancellation without using any position or force sensors. The algorithm includes a force versus contact-compression calibration map, which is used to control the force in open-loop. The algorithm uses charge control with nonlinear feedback

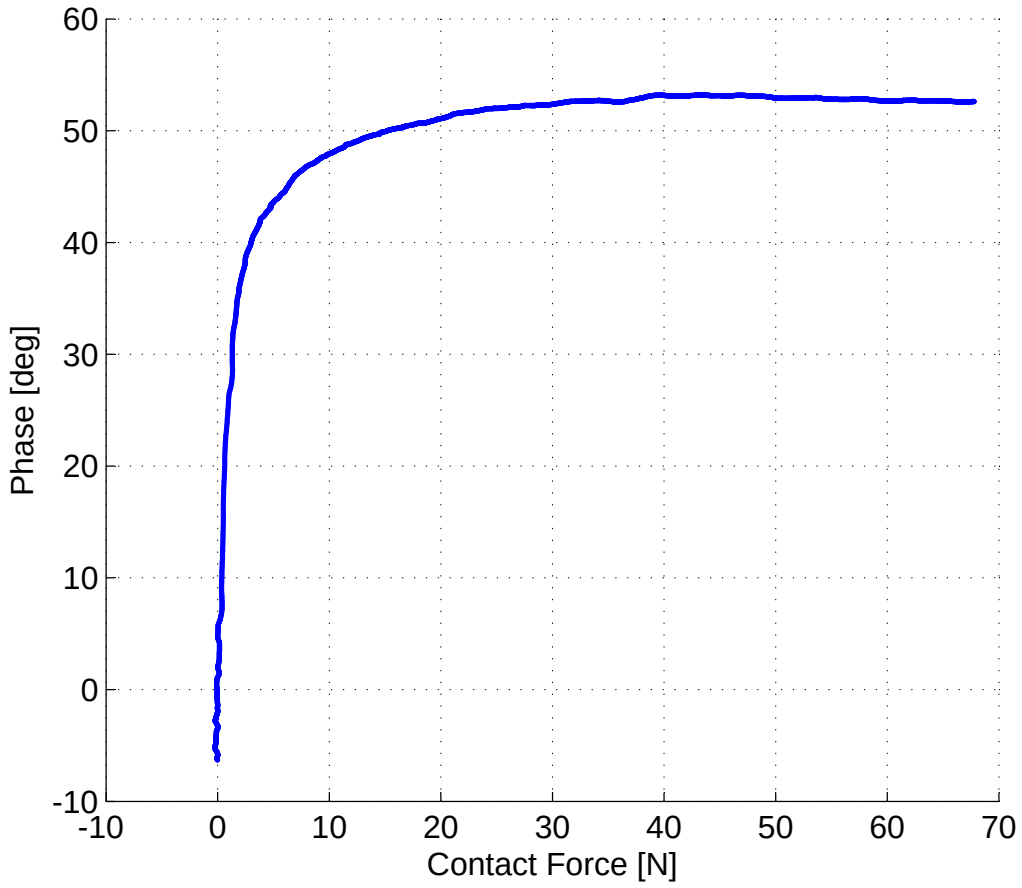

Figure 1-13: Piezoelectric actuator's voltage to current signals phase difference when excited at its natural frequency shown versus the tip-reticle contact force. The sharp change in the phase difference is used to detect tip-reticle contact.

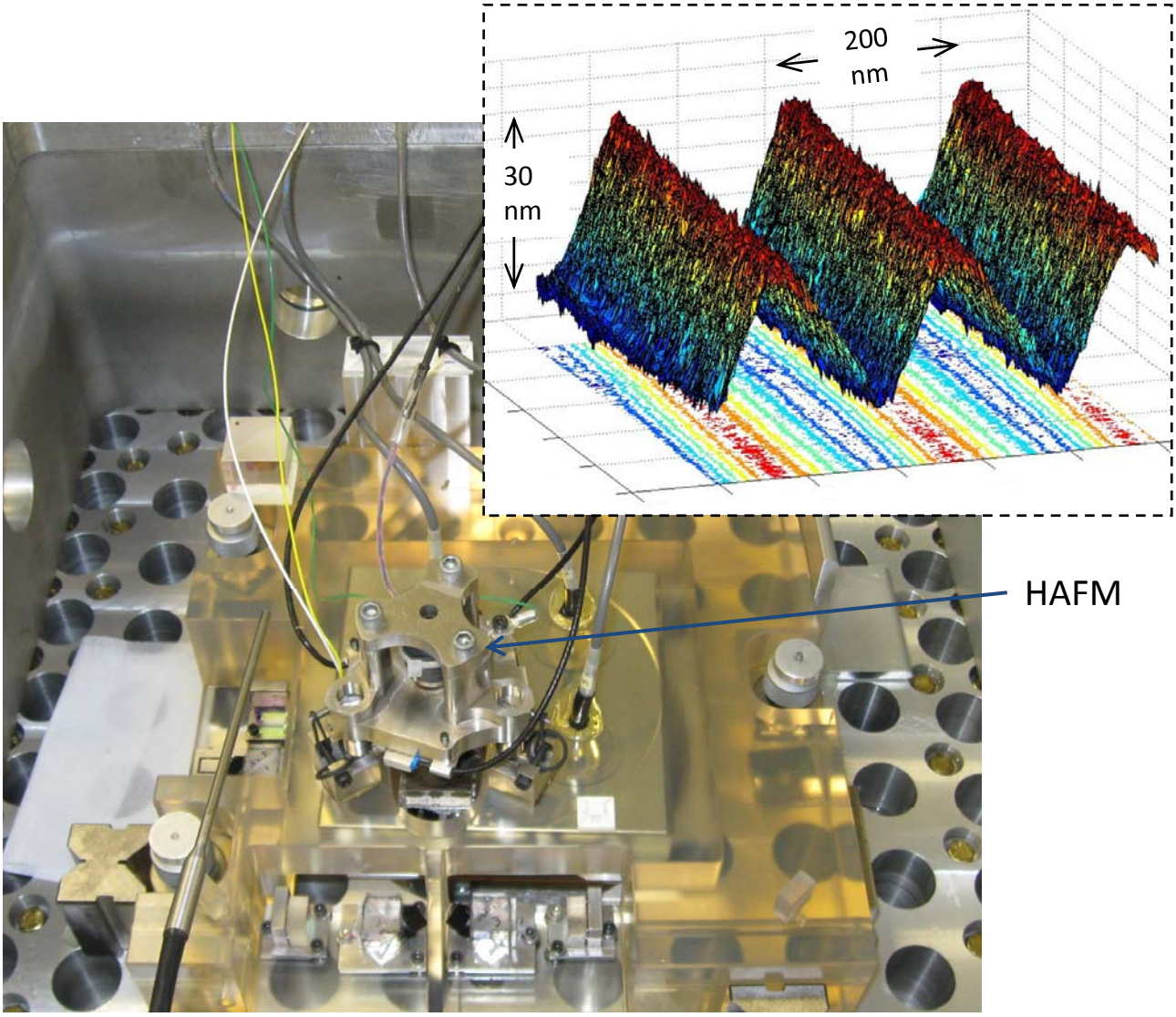

Figure 1-14: The high-accuracy atomic force microscope (HAFM) is installed on the sub-atomic measuring machine (SAMM). HAFM and the SAMM are used to capture the inset image of the triangular grating.

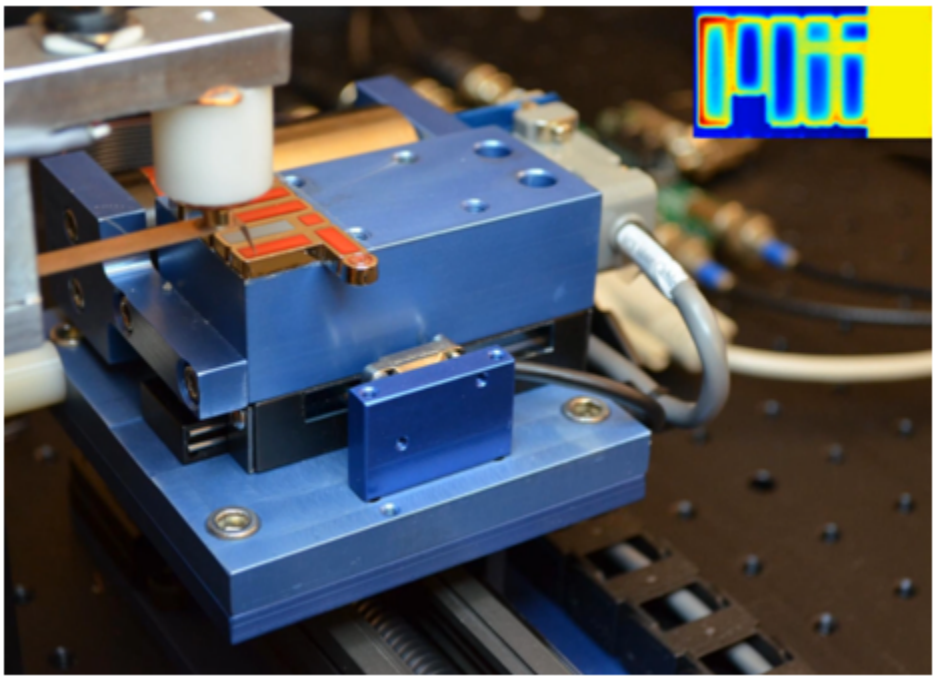

Figure 1-15: Macro-scale atomic force microscope profiler (MAP) is shown capturing an image of an MIT key chain.

compensation to linearly control the piezo's extension without the need for strain feedback. This is augmented with self-sensing contact detection in every cycle to register the assist device's position relative to the reticle. The algorithm includes a state machine which automatically commands the subsystems to create an arbitrary inertial load profile. Figure 1-16 shows a time trace of the inertial load profile and the piezoelectric actuator's charge reference commanded for canceling that load. The plot also shows an estimate of the reticle edge location obtained using the self-sensing contact detection method. When loading a new reticle, the edge location is set by the coarse approach mechanism. The expected edge location is updated using the self-sensing method before every pushing cycle. The edge location is determined as the required amplifier reference voltage for the piezoelectric actuator to arrive at the reticle edge. The change in this measurement is due to the charge amplifier's slow transient resulting from the uncompensated piezo hysteresis and the the noise in the edge detection algorithm. It is not an actual displacement of the reticle edge. As it can be seen, the device approaches the reticle to find its edge, pushes on the reticle

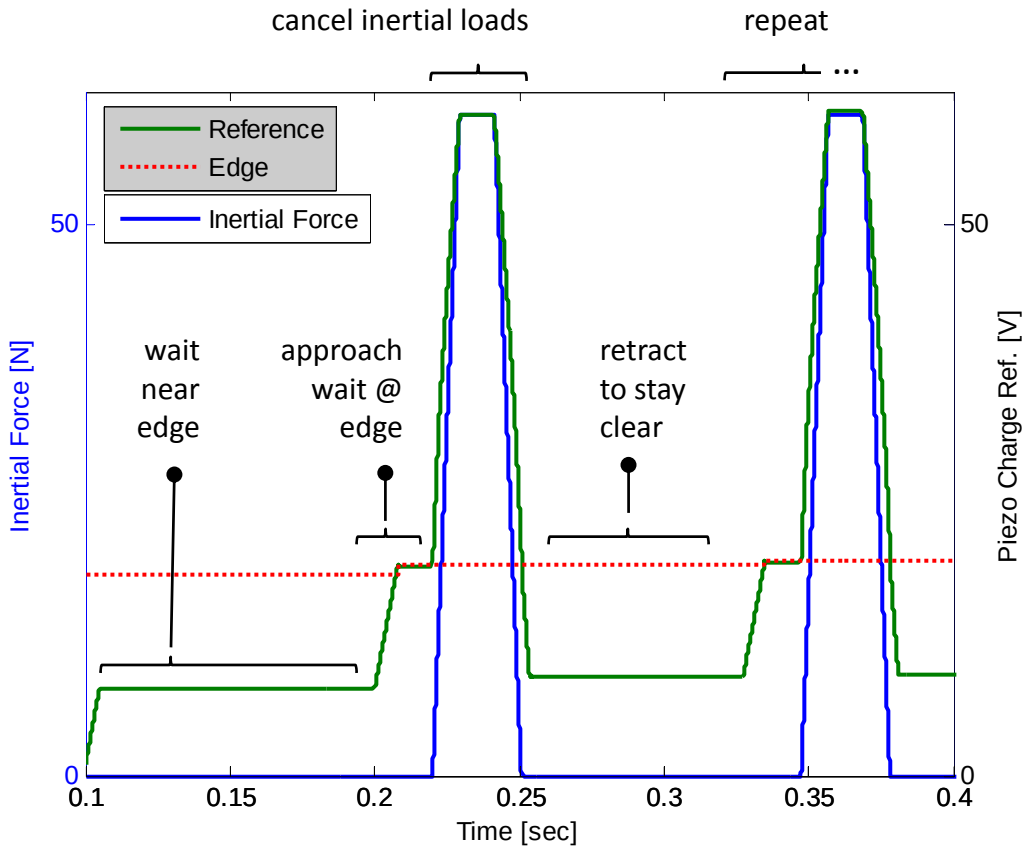

Figure 1-16: Time trace of the inertial load profile and the piezo charge reference required for canceling the load generated by the control system.

to cancel the inertial load during the acceleration interval, and retracts back to avoid disturbing the reticle during the exposure interval. The assist device's resulting force compensation (F) is plotted versus the inertial force (F_R) in Figure 1-17. The reticle assist device's control system is presented in Chapter 6, Section 6.1.

We have tested the effectiveness of the reticle assist device in compensating the reticle inertial loads. The experimental setup is shown in Figure 1-18. The setup consists of a reticle mounted on a stationary vacuum clamp. Coils are attached to the top and bottom surfaces of the reticle. These coils are used with magnet arrays to generate forces acting on the reticle's center of gravity. This allows us to simulate the reticle inertial loads using a stationary setup. The experimental setup has capacitive displacement sensors which monitor the location of the reticle and the assist device's clamp relative to the base plate. The setup also has the vacuum and pressurized air

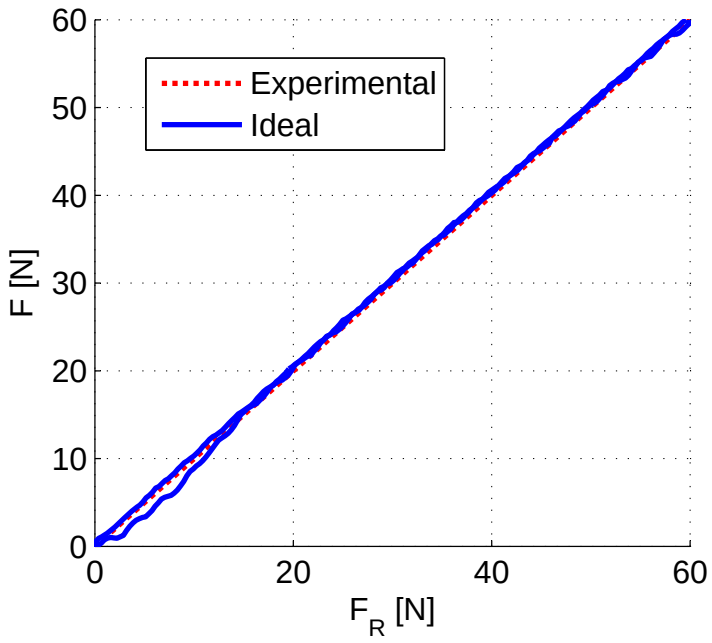

Figure 1-17: Assist device's resulting compensation force versus the inertial load plotted for 10 consecutive cycles.

lines used with the clamps and the pneumatic bellow. We used the coils to generate a 60-N simulated inertial load profile and monitored the reticle's displacement with and without using the reticle assist device. As can be seen in Fig. 1-19, the reticle assist device is very effective at preventing reticle-slip. Without an assist device, the reticle moves as the clamps deform elastically by about 1 μm. However, some amount of this deformation is not reversed, and the reticle slips by more than 100 nm after 10 acceleration cycles. However, with this reticle assist device, the clamps elastically deform by only 20 nm and the reticle does not slip even after 10 cycles. The experimental procedures and results are presented in Chapter 6, Section 6.2.

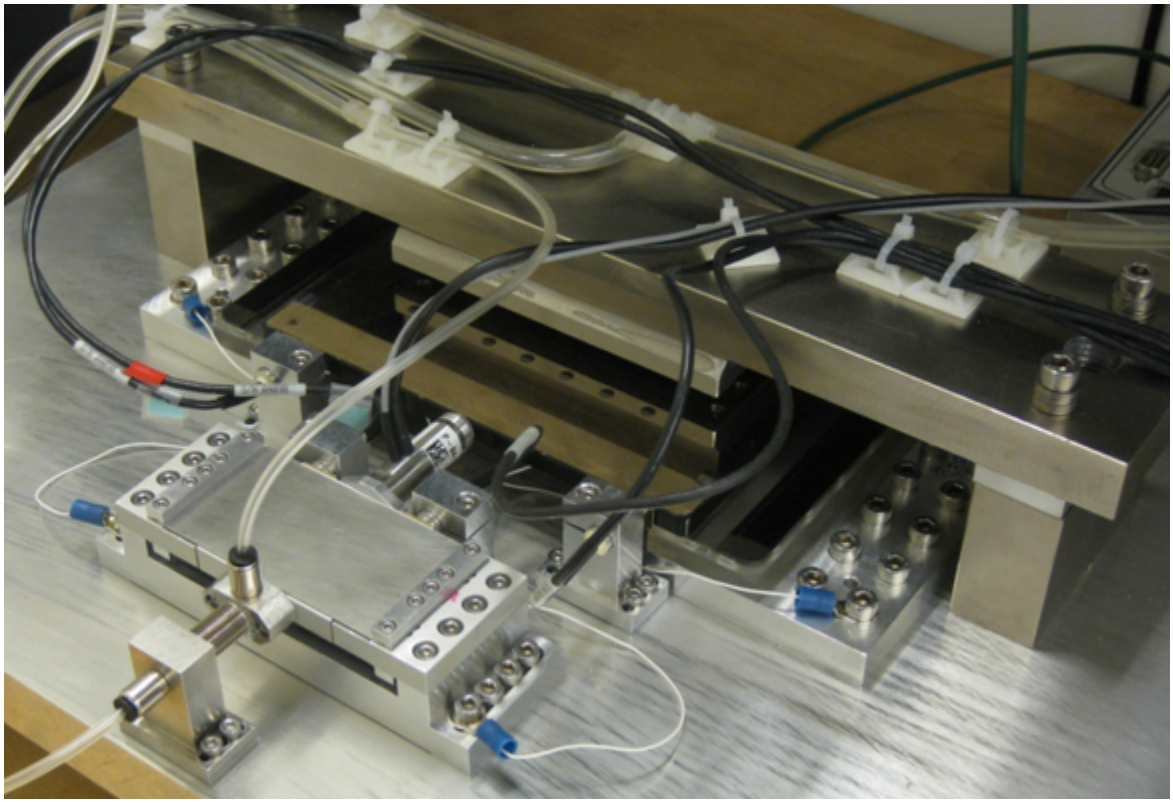

Figure 1-18: Picture of the experimental setup used for testing and development of the reticle assist device (RAD).

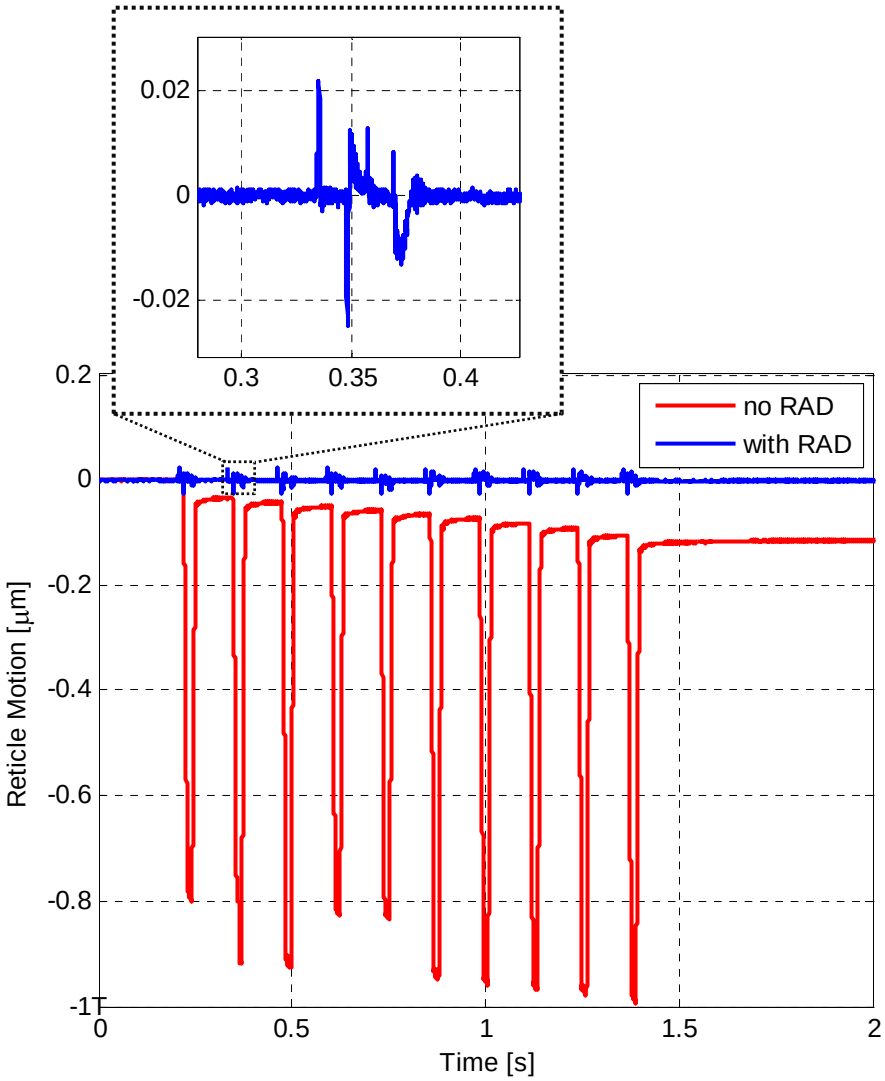

Figure 1-19: The reticle motion relative to the stage as a result of a 60-N simulated inertial load profile with and without using our reticle assist device (RAD).

Chapter 2

Reticle Slip Problem and Conceptual Solutions

In this chapter, we describe the reticle slip problem, present promising conceptual designs, and conclude by selecting the most suitable concept for designing the reticle assist device.

2.1 Reticle Slip Problem

A simplified diagram of a lithography scanner is shown in Figure 2-1. The scanner exposes the wafer by sweeping an exposure slit across the reticle. To map the reticle to a whole die on the wafer, the scanner moves the wafer and the reticle relative to each other with nanometer-level coordination of motion. The reticle stage holds the reticle using a vacuum clamp and moves it in the X-direction. The reticle stage's linear motion path consists of acceleration at the ends of each scan and constant-speed motion in the middle of the scan. Figure 2-1 shows the reticle stage accelerating (a_R) in the X-direction, which results in an inertial force (F_I) being in the negative x-direction. A large inertial force can cause reticle slip and displace the reticle to the location shown using the dotted box. As the inertial force approaches the clamp's force limit, significant pre-sliding slip starts to occur. Sliding slip can occur if the inertial force exceeds the clamp's limit. For more perspective on lithography machines, Butler [14]

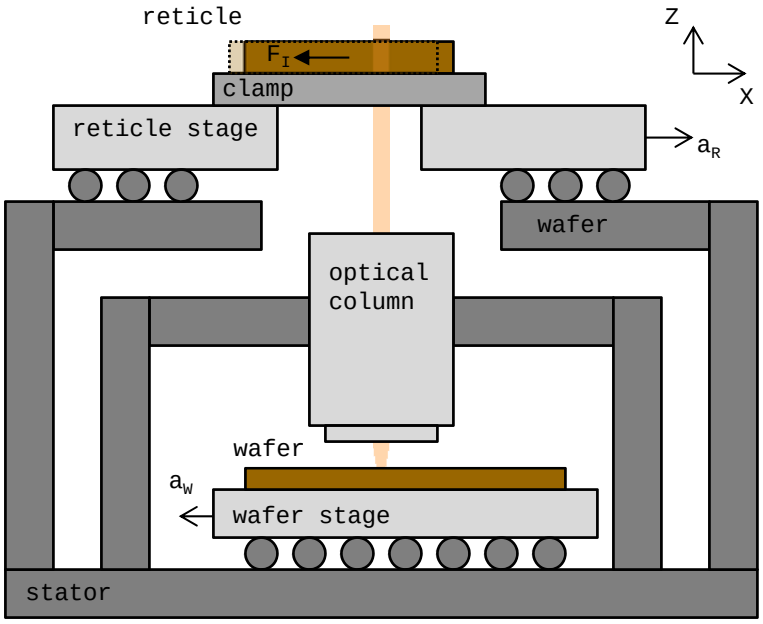

Figure 2-1: Simplified diagram of a lithography scanner.

provides a detailed description of the operation and position control of lithography scanners.

To avoid deforming the reticle, a vacuum clamp is used for holding it. The reticle size and shape is set by the industry standard. Therefore, the available vacuum clamp area is limited. Given the restriction on the allowable materials, the coefficient of friction at the clamp's interface cannot be increased. As a result, a limit is set on the clamp's maximum force carrying capacity. The reticle inertial force for the next generation scanners can approach or even exceed this limit. Consequently, reticle slip can be a major error source for the next generation scanners.

2.2 Application Requirements

One method to address the slip problem is to use a reticle assist device, which fully or partially carries the reticle's inertial force by exerting a force on the reticle's edge. The reticle assist device will be placed on the reticle stage and will be interacting with the reticle. Being so close to the heart of the lithography process, the assist device must satisfy several application requirements in order to avoid disturbing the

lithography process and degrading the scanner's performance. The main requirements and guidelines for designing the reticle assist device are as the following:

1. Low added mass from the assist device is required to ensure good reticle stage dynamics. A total mass budget of 0.3 kg, 0.15 kg per side, is provided to us as an approximate guideline.

2. Lifetime of at least 7 years with continuous operation is expected. During the assist device's life time, 1 million reticle exchanges and 500 million pushing cycles can occur.

3. High reliability is required. The scanners are designed with high reliability for operation with minimum down time.

4. Output force must counteract the reticle's inertial force during the acceleration interval, such that the remaining net force on the reticle is less than 30% of the inertial force. The device must be cable of exerting forces up to 50 N.

5. No disturbance on the reticle should cause more than 1-nm reticle motion or pattern deformation during the exposure interval. A compressive force of approximately 2 N can cause as much as 1 nm deformation within the reticle's patterned area.

6. Fast transient time of 1 ms between when the acceleration cycle is complete and when the assist device creates no disturbance on the reticle is required.

7. Pusher vibration modes must be above 1 kHz to avoid negatively impacting the stage dynamics and motion control.

8. Reticle size variation of ± 0.4 mm and any additional reticle positioning tolerance should be tolerated by the assist device. As a result, the assist device is required to have a coarse adjustment range of 1 mm.

9. No damage to reticle is allowed. The contact stresses induced within the reticle must be limited to avoid damage.

10. No large impact forces can be tolerated. Large impact forces can damage the reticle or cause slip. The reticle-tip contact must be controlled to avoid impact.

11. Cables or lines connecting to the assist device can disturb the stage and must be minimized.

12. Illumination light cone cannot be blocked by the assist device.

13. Contaminating the scanner's enclosure by particle generation or leakage is not allowed.

2.3 Conceptual Designs

We considered several different actuation technologies for designing a reticle assist device (RAD). In the following subsections, we describe the most promising conceptual designs.

2.3.1 Piezoelectric Concept

A simplified diagram of the piezoelectric RAD concept is shown in Figure 2-2. The device uses a piezoelectric actuator to push on the reticle. The piezoelectric actuator has a limited range (order of 10 μm), and thus requires a coarse actuation mechanism to adjust the piezo's position according to the variations in the reticle size and position. The coarse approach mechanism consists of a pneumatic bellow and a vacuum clamp. The coarse adjustment is performed by preloading the piezo against the reticle, extending the piezo by the desired gap size, and activating the vacuum clamp. The bellow and the vacuum clamp can be operated using on-off pneumatic-valves. It is possible to design a pneumatic circuit logic such that the bellow and the device's clamp are actuated from the reticle clamp's vacuum supply, but with fixed delays. In this way, no additional vacuum lines need to be brought onto the reticle stage. The piezoelectric device is solid-state, meaning that it has no moving parts. It has very fast dynamics and its motion can be controlled with high precision. The piezoelectric assist device also has the advantage of being light. For example, a commercially

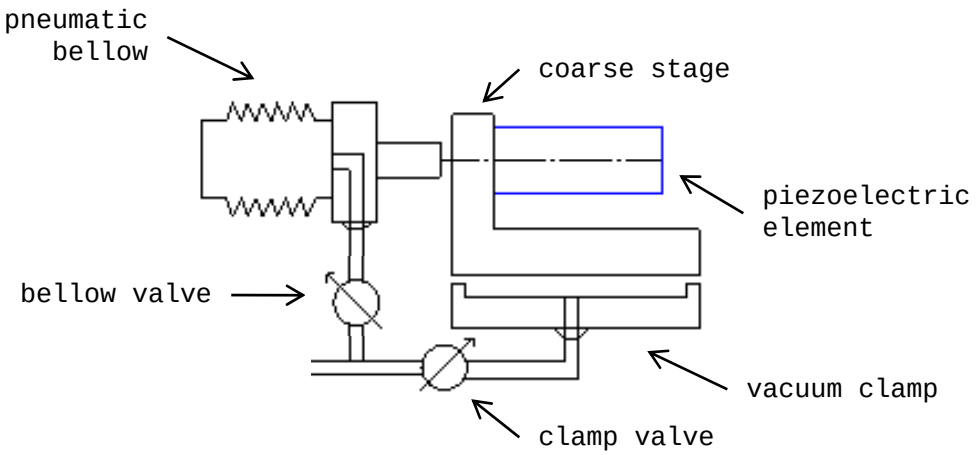

Figure 2-2: Conceptual design of a piezoelectric reticle assist device.

available piezo stack actuator weighing less than 20 g has a range of 15 μm and can exert a pushing force as high as 100 N [66].

2.3.2 Magnetostrictive Concept

The magnetostrictive assist device concept is similar to the piezoelectric concept, which was described in Section 2.3.1, except that the piezoelectric element is replaced by a magnetostrictive element and its associated driving coils. A simplified diagram of the magnetostrictive RAD concept is shown in Figure 2-3. The device uses a magnetostrictive actuator to push on the reticle. The actuator consists of a magnetostrictive element with a coil wrapped around it. Energizing the coil creates a magnetic field through the element, which extends its length. Given the actuator's limited range, it is used with a coarse adjustment mechanism. Compared to the piezoelectric assist device, the magnetostrictive assist device has two main disadvantages: it is heavier and less efficient. First the copper coils and magnetic circuit add to the actuator's mass. Also, the coil resistive power loss dissipates energy even when holding a constant extension. The heat from the coils can result in thermal expansion of the magnetostrictive actuator and other stage components. However, the magnetostrictive actuator has two advantages. It requires a current source, and thus can potentially be directly driven in series with the reticle stage's motor coil currents. Also, the magnetostrictive element does not have a stack construction and

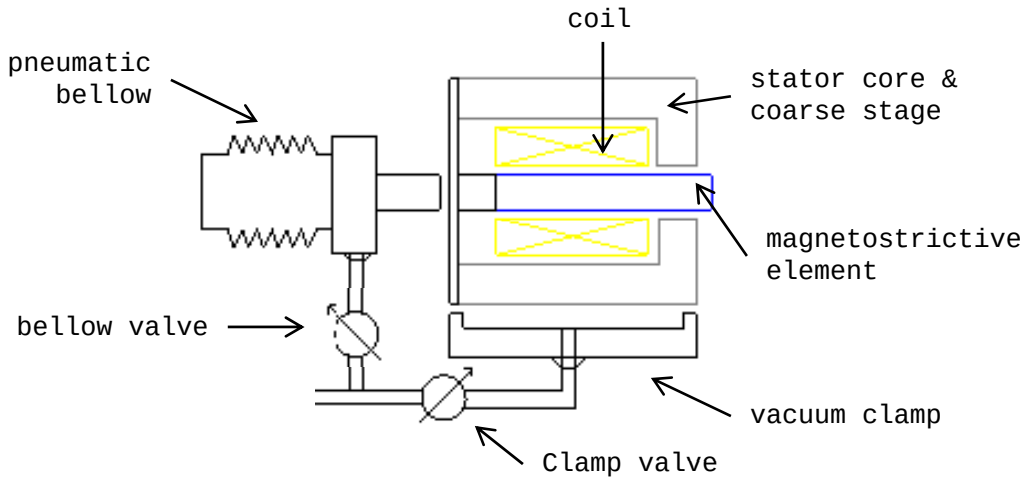

Figure 2-3: Conceptual design of a magnetostrictive reticle assist device.

is mechanically stronger, whereas piezoelectric elements can suffer brittle fracture. For a pushing force of 75 N, an actuation range of 10 μm, and 1.6 W maximum dissipation, the expected mass of the assist device's magnetostrictive element, coils, and magnetic cores is estimated to be 270 g. This mass estimate does not include the coarse adjustment mechanism.

2.3.3 Electromagnetic Concept

Another option is a moving iron actuator similar to the flux-steering actuator designed by [50]. A simplified diagram of this assist device concept is shown in Figure 2-4. The electromagnetic actuator uses a permanent magnet to create a bias magnetic field in the air gaps on the two sides of the armature. The coils are used to steer the flux towards one side of the armature and create a net force in that direction. The permanent magnet makes the actuator more efficient because with a bias a larger net force can be generated for a given change in the coil current. The main disadvantage of the electromagnetic actuator is that it is open-loop unstable and requires closed-loop control with displacement sensor feedback. The key advantage of the concept is that it can be designed to have a range of 1 mm, and thus can be used without a coarse approach mechanism. For a pushing force of 75 N, an actuation range of 1 mm, and 1.2 W maximum power dissipation, the expected mass of the assist device's

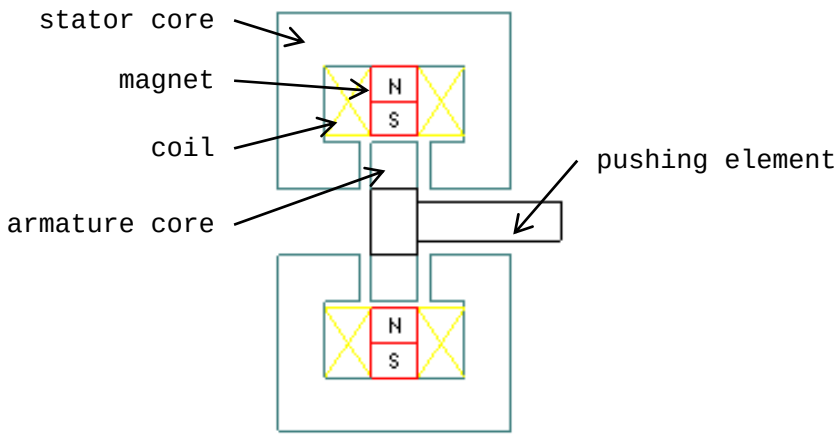

Figure 2-4: Conceptual design of an electromagnetic reticle assist device, inspired by actuator design of Lu [50].

coils and magnetic core is estimated to be 220 g. The mass estimate does not include the supporting structure.

2.3.4 Piezo Stepping Motor Concept

A simplified diagram of a piezo stepper assist device concept is shown in Figure 2-5. Piezo steppers, such as the Physik Instrumente's PiezoWalk® linear motors, are commercially available. The mover is moved forward by the shear piezos and is clamped using the normal piezos. A set of two legs can work together to step the mover forward or backward. We can use the stepping actuation for coarse adjustment and use the shear piezos, with the normal piezos in the clamped state, for fine actuation and exerting the pushing forces on the reticle. Disadvantages of the piezo steppers are their high cost and the possibility of wear as a result of the repeated clamping action and the shear loading of the normal piezos. The Physik Instrumente N-111.20 PiezoWalk® has a range of 10 mm, a maximum force of 50 N, and weight of 245 g. The piezoelectric motor is expected to dissipate little energy.

2.3.5 Pneumatic/Hydraulic Bellow Concept

We have also considered using pneumatic or hydraulic bellows for creating the pushing forces. The bellows are very light. However, it is very difficult to control their motion

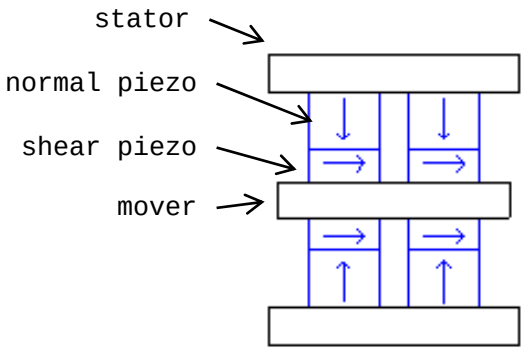

Figure 2-5: Piezo stepping motor concept.

and output force with sufficient speed and precision. To make the bellows compact enough, they would also require a relatively high actuating pressure. For example, with a surface area of $A = 1\ cm^2$, a pressure difference of $P = 50 \times 10^4\ Pa \simeq 5\ Atm$ is required to create a pushing force of $F = P \times A = 50\ N$ This introduces a significant chance of leakage and failure over the life time of the scanner.

2.4 Concept Selection

We have selected the piezoelectric concept for designing the reticle assist device. The piezoelectric assist device uses solid-state actuation and has no moving parts, except for micrometer-level elastic extension of the piezo. The main advantages of the piezoelectric assist device are as the following:

- Low Mass: the piezo actuator mass can be less than 20 g. The total mass including the coarse approach stage can be less than 100 g.
- Long Life Time: the piezo device has no moving parts and no fundamental wear mechanism.
- High Reliability: The piezo device is simple and does not have many failure modes. In its failed state, the device is a solid piece which does not affect the scanner's operation.
- Excellent Dynamics: the assist device can be designed to have no low-frequency vibration modes; first mode can be in excess of 1 kHz.

- Open-Loop Stable: the piezo is open-loop stable and can be operated without a sensor and a closed-loop controller.
- High Control Bandwidth: the piezo's motion and force can be controlled at a high bandwidth.
- High Control Resolution: the piezo's motion can be controlled with high resolution.

Given these advantages, a piezoelectric assist device can provide a practical solution to the reticle slip problem. In the following chapter, we present the detailed design of an assist device based on the piezoelectric conceptual design.

Chapter 3

High-Force-Density Reticle Assist Device

In this chapter, we first present the mechanical design of a piezoelectric reticle assist device (RAD), which has been designed based on the piezoelectric RAD concept introduced in Chapter 2. This configuration has been experimentally implemented and tested. In Section 3.3, we present ideas for more efficient packaging of the assist device. In Section 3.4, we present a concept for a magnetostrictive fine actuator design, which can be used as an alternative to the piezoelectric fine actuator.

Figure 3-1 shows a CAD model of the device. It consists of a coarse stage, for reaching the reticle's edge, and a fine stage, for exerting pushing forces on the reticle. The mechanical design of the fine and coarse stages are described in Sections 3.1 and 3.2, respectively.

3.1 Fine Stage

A CAD model of the fine stage is shown in Figure 3-2. The fine stage consists of a piezoelectric actuator, a spherical push-tip, and an adapter piece for mounting the actuator to the coarse stage.

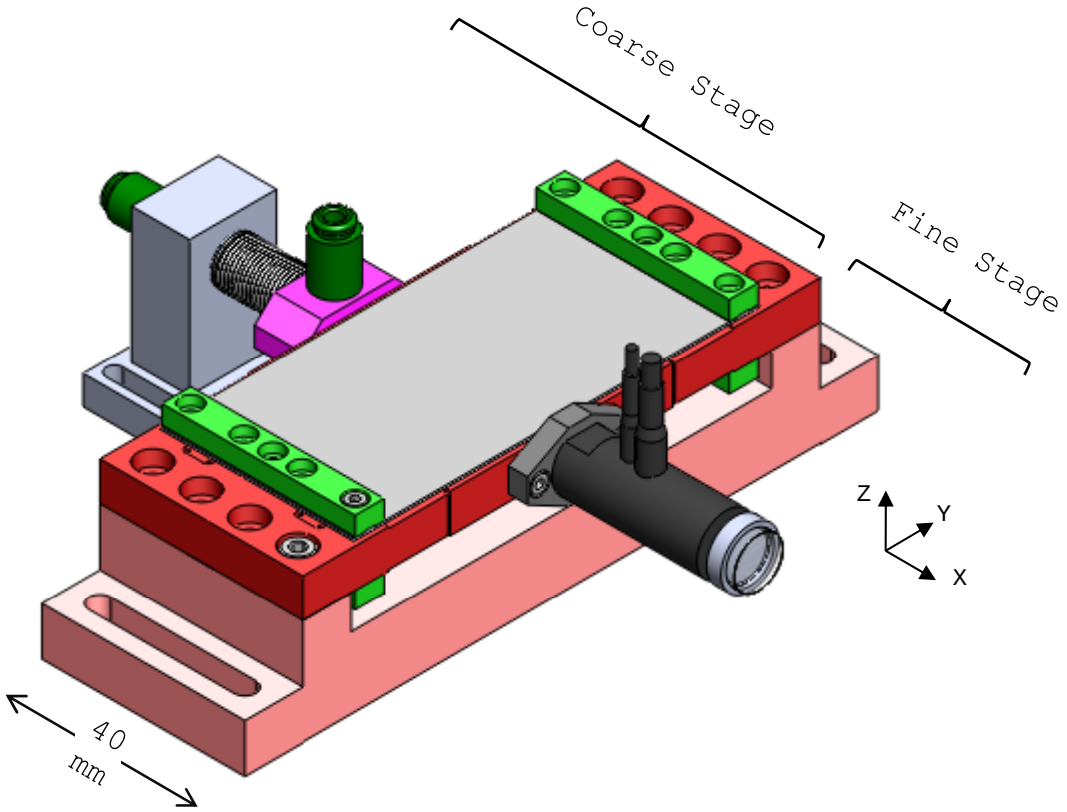

Figure 3-1: CAD design of the reticle assist device. The device consists of two sub-assemblies: a coarse approach mechanism and a fine actuation mechanism.

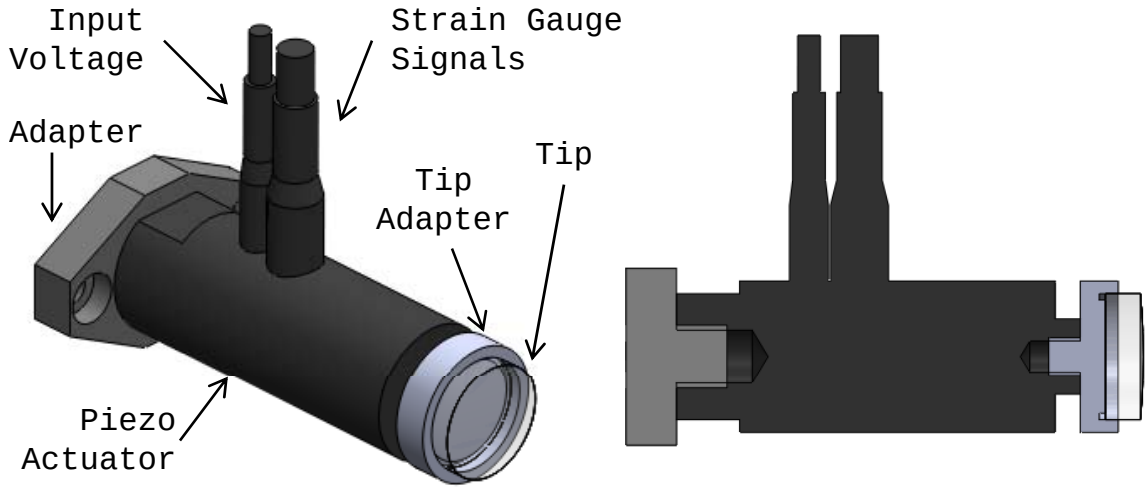

Figure 3-2: CAD model of the actuator used for exerting the pushing force on the reticle.

3.1.1 Piezoelectric Actuator

The fine stage uses a Physik Instrumente P-841.10 piezoelectric stack actuator [66]. The actuator has a specified 0-100 V input voltage range and a position range of 15 μm. It has a stiffness of 57 N/μm and can carry up to 1000 N in compression and 50 N in tension. The actuator parts are enclosed by a stainless steel can. The piezo stack actuator is fixed to the bottom of the can. A part attached to the other end of the piezo stack extends out of the enclosure and has a threaded hole on the outside. Inside its enclosure, the piezo stack actuator is preloaded in compression to avoid damage, which can be caused by tensile loads. Typically, Belleville washers are used to preload the moving end of the actuator against the inside of the enclosure.

3.1.2 Pushing Tip Design

We use a spherical pushing tip to ensure that the tip-reticle contact and the resulting pushing force are centered on the piezo actuator's axis. Eccentric forces can create a bending moment on the piezo actuator. With a large eccentricity, the bending moments can create tensile loads, which can damage the brittle piezo stack. Angular misalignment between the piezo and the reticle edge can result in eccentric loading. Using a small tip diameter reduces the eccentricity for a given angular misalignment.

We use a plano-convex spherical lens, model 63-479 from Edmund Optics [19], as our spherical tip. The lens has a spherical radius of curvature of 50 mm. It is made of N-BK7 uncoated glass. Using a lens provided us with a cost effective off-the-shelf component of controlled radius. We could not find a lens with an approximately the same size but a larger radius of curvature. We center the lens and the piezo stack by centering them to the lens adapter part. The lens is fitted to the adapter using a interference fit. The adapter is centered to the piezo stack using the threaded bolt. The adapter is manufactured such that the fit surface and the threaded extrusion are concentric. The lens is preloaded and is fixed to the adapter using Araldite® LY 5052 epoxy [34]. For the final product, the spherical tip and its adapter can be custom machined as one part. In that case, the tip can also have a larger radius of

curvature.

Another concern is the stress induced in the reticle via contact. According to Slocum [76], the maximum allowable contact pressure (q^{max}) for brittle material can be calculated as

$$q^{max} = \frac{2\sigma_{maxflex}}{1-2\nu}, \tag{3.1}$$

where $\sigma_{maxflex}$ and ν are the maximum allowable flexural stress and the Poisson's ratio for the reticle material, respectively. The contact pressure can be estimated based on the Hertz contact model using the following equation:

$$q = \frac{a\ E_e}{\pi\ R_e} \tag{3.2}$$

where parameters R_e, E_e are the equivalent radius of curvature and equivalent elastic modulus of contact given as

$$E_e = \frac{1}{\frac{1-\nu_1^2}{E_1} + \frac{1-\nu_2^2}{E_2}} \tag{3.3}$$

$$R_e = \frac{1}{\frac{1}{R_{1-major}} + \frac{1}{R_{1-minor}} + \frac{1}{R_{2-major}} + \frac{1}{R_{2-minor}}} \tag{3.4}$$

$$\tag{3.5}$$

where E and R are the modulus of elasticity and the radius of curvature of the contact surfaces 1 and 2, and a is the radius of the resulting contact area and can be calculated as

$$a = (\frac{3FR_e}{2E_e})^{1/3} \tag{3.6}$$

where F is the contact force.

For our system, using the parameters in table 3.1, the contact pressure is calculated as 195 MPa. According to equation 3.1, a flexural strength of 67 MPa is required for allowing a contact pressure of 200 MPa.

Table 3.1: Table of contact parameters

Parameter	Description	Value
E_1	Elastic Modulus of reticle	74 GPa
ν_1	Poisson's ratio of reticle	0.17
E_2	Elastic Modulus of tip	81 GPa
ν_2	Poisson's ratio of tip	0.21
F	contact force	60N

Reticles are typically made from fused silica. Searching in the literature, we have found a wide range of flexural strength values for fused silica, which depend on the size of the loading area and the surface defects of the material. Determining the flexural strength of the reticle material was considered to be beyond the scope of this thesis. Here, we have presented methods for estimating the stress levels. The tip radius can be increased to reduce the stress to levels below the allowable flexural strength of the reticle. For example, using a spherical tip radius of 200 mm, we can reduce the maximum contact stress to 77.4 MPa and the required flexural strength to 25.4 MPa. We have loaded the contact for several thousands of cycles, and so far, our test reticle has not experienced any visible failures.

3.2 Coarse Stage

Due to reticel and handler tolerances, the reticle edge position can vary by as much as ± 500 μm. The pusher fine stage has a limited range of 15 μm. The coarse stage is thus used to position the fine stage close to the reticle, so the the piezoelectric actuator can reach and push on the reticle. A CAD model of the coarse stage is shown in Figure 3-3. The coarse stage consists of a flexural bearing for guiding the motion, a pneumatic bellow for actuating the stage, and a vacuum clamp for clamping and holding the stage's position. The design of the coarse stage parts is described in the following subsections.

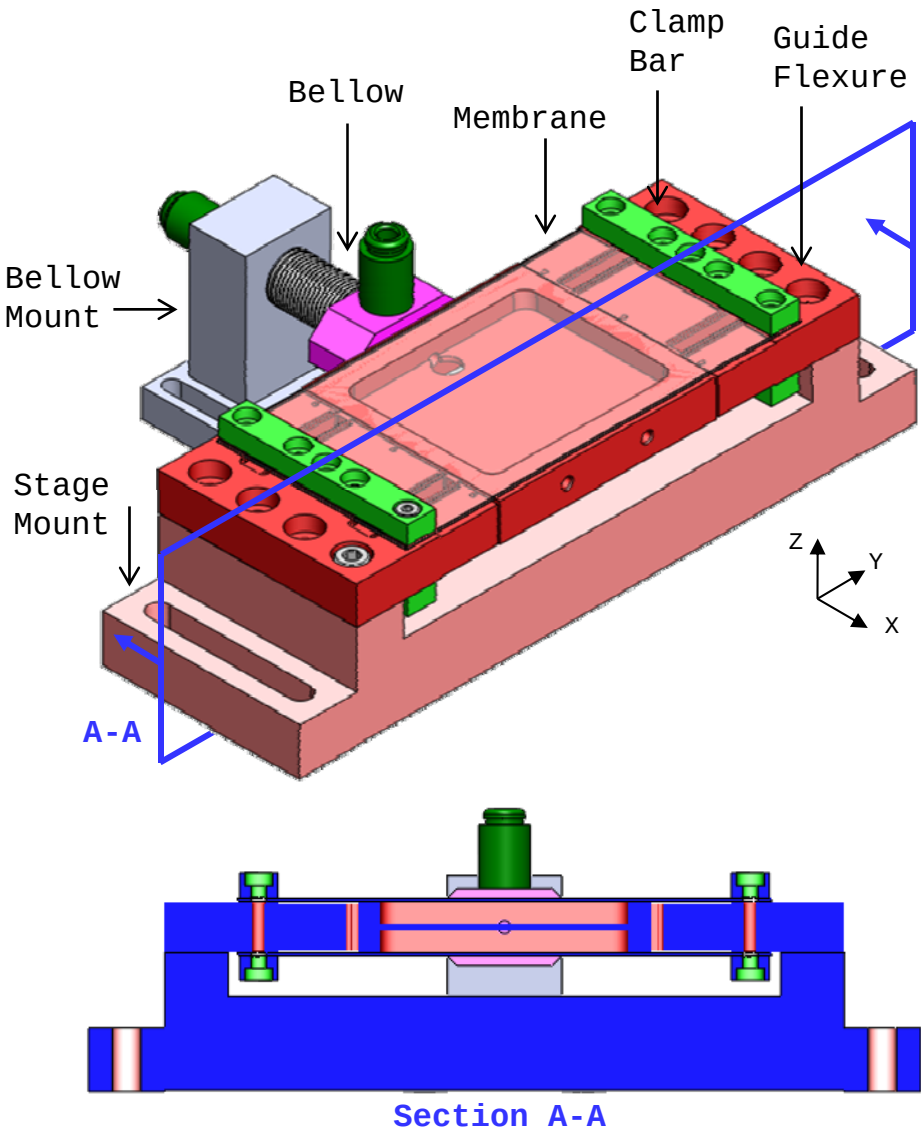

Figure 3-3: CAD design of the coarse approach mechanism (top) and a cross-sectional view (bottom); the top membrane is made transparent to better show the coarse stage's design.

3.2.1 Guide Flexure

The coarse stage uses a flexural bearing for guiding its motion. The flexure constrains the motion of the stage to the X-direction. The guide flexure design is shown in Figure 3-4. The flexural consists of four flexural legs. We use back-to-back flexural legs to allow a larger range of motion for a given size. With the back-to-back design, the flexures are not stressed along their length as their deformations in the Y-direction cancel out. The flexure blades are designed to have a thickness of 0.2 mm. The blades are joined at their ends using a 1-mm thick link. This thicker link is used to reduce the torsional compliance of the flexure legs and avoid low-frequency vibration modes. The flexure guide is made out of Aluminum Alloy 2024-T4 to achieve low mass and high strength. The flexure blades are machined using an electric discharge machining (EDM) process. The EDM manufacturing steps are shown in Figure 3-4. The order of the cuts is selected to ensure that the surfaces are fixed at the time they are being cut. In this way, the required manufacturing tolerances can be achieved.

The guide flexure's stiffness can be calculated as the following:

$$k_f = 4 \times 2 \times \frac{6EI}{L^3} = 5 \text{ N/mm} \tag{3.7}$$

where E = 73 MPa, t = 0.2 mm, L = 15 mm, w = 0.74 mm, and I = $\frac{1}{12}wt^3$ are the modulus of elasticity, thickness, length, width, and the bending moment of inertia of the flexure blades respectively. The maximum bending normal stress in the blades can be calculated as the following:

$$\sigma_{max} = \frac{3tE}{2L^2} \times \delta_{max} = 48 \text{ MPa} \tag{3.8}$$

where δ_{max} =0.5 mm is the maximum deformation about the guide flexure's center position. We use round corners to limit the stress-concentraion in the corners. Using COSMOS FEA software we predict a maximum von Mises stress of 80MPa at the end of the flexure blades. The flexure stage operates once each time a new reticle is loaded, and thus, as a conservative estimate, we expect the flexure to go through less

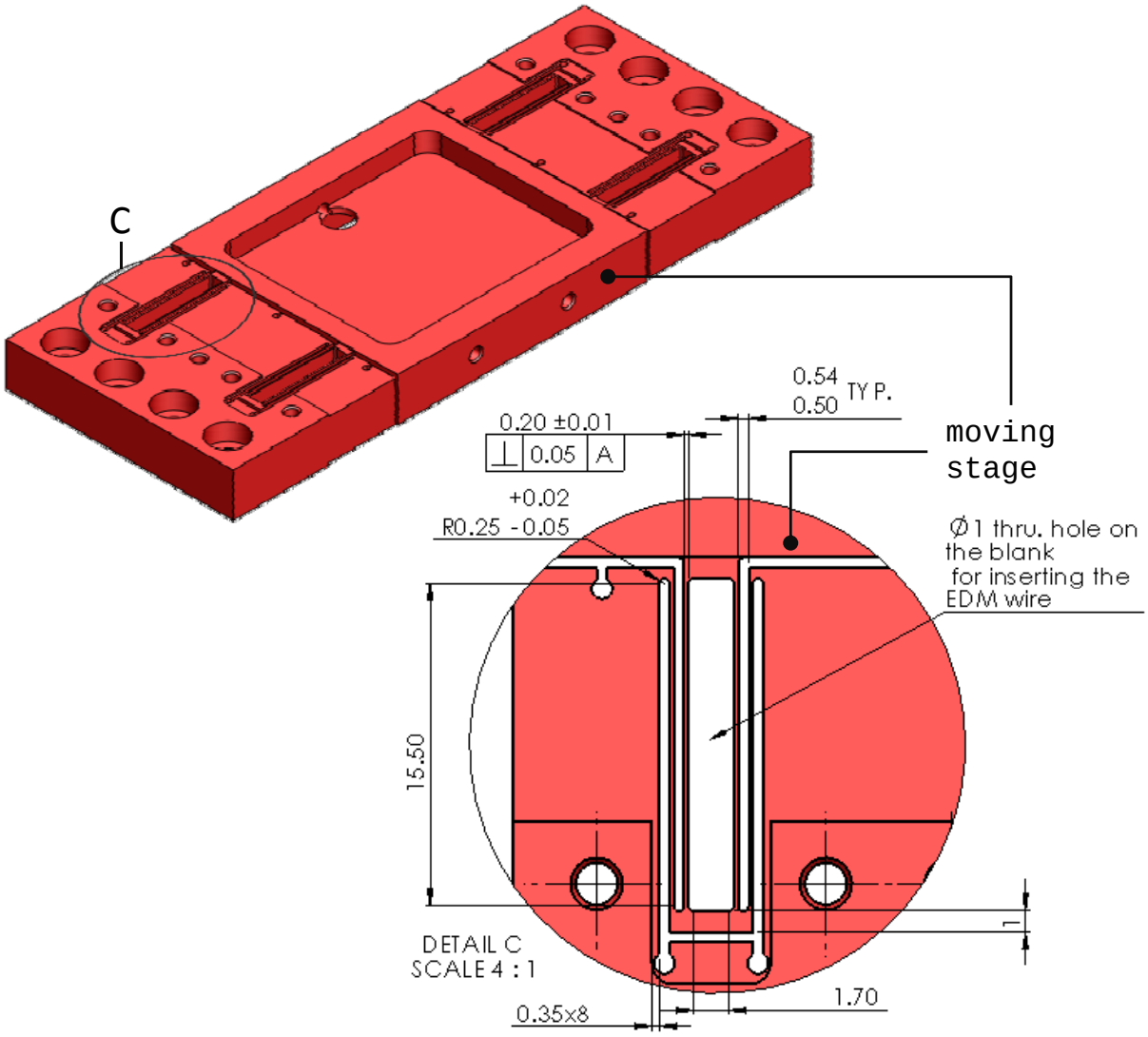

Figure 3-4: CAD model and partial drawing of the coarse stage's guide flexure showing its design.

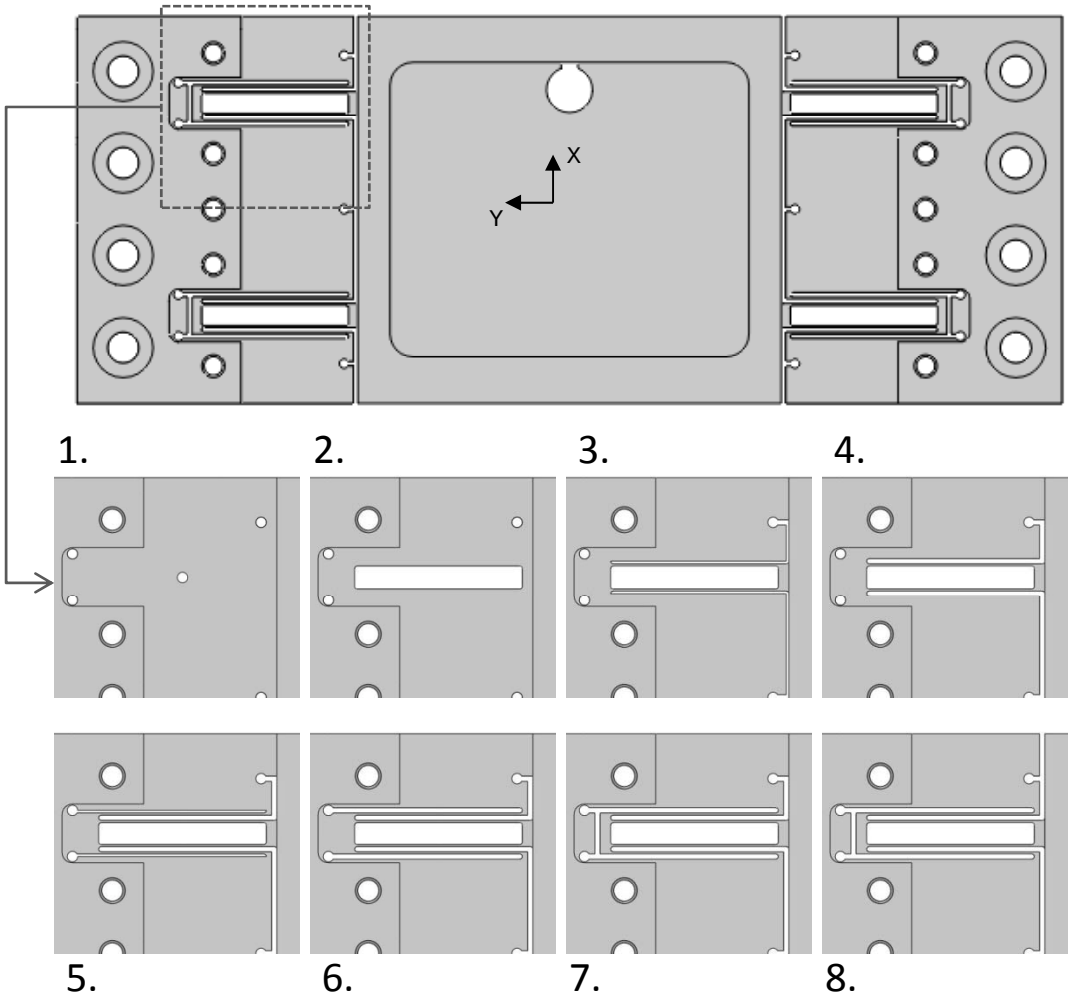

Figure 3-5: Top-view of the coarse flexural stage (top) showing the flexure design. The steps for the EDM manufacturing process are shown for one flexure leg.

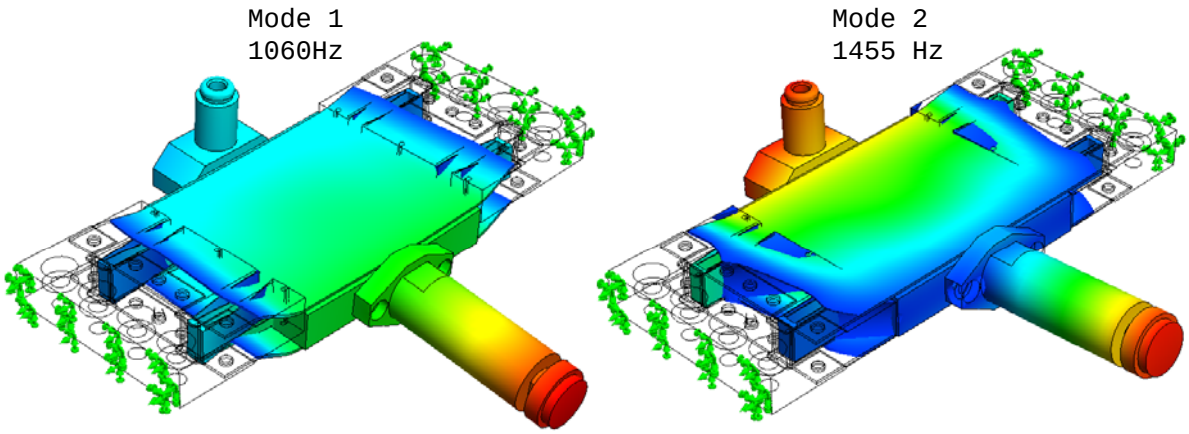

Figure 3-6: First two vibration modes of the reticle-assist device computed with the vacuum clamp activated.

than a million cycles. The fatigue analysis data provided in [72] shows that notched 2024-T4 Aluminum alloy with 100MPa load did not fail in over 1 million cycles.

It is desired to design the flexures to be soft in the X-direction so that the coarse stage can be actuated by ± 0.5 mm using the bellow at a reasonably low pressure. Using thin flexure blades provides lower stiffness in the X-direction. It also provides a larger range of motion for a given stress level. However, reducing the flexure's thickness reduces the system's stiffness in other degrees of freedom as well and can result in low-frequency vibration modes. Using COSMOS, we calculated the device's vibration modes, when in the clamped state. The first two vibration modes are shown in Figure 3-6. The first mode is mainly translational in the Z-direction, and the second mode is mainly torsional around the Y-direction. The first two modes cause a displacement in the Z-direction at the tip, and thus do not affect the reticle assist device's control. However, these vibration modes can affect the control of the scanner stage and must be above 1 kHz, which is satisfied.

3.2.2 Preload Actuator

We use the coarse stage to prelaod the piezoelectric actuator against the reticle's edge. Therefore, we need a preloading force with only on-off control to actuate the coarse

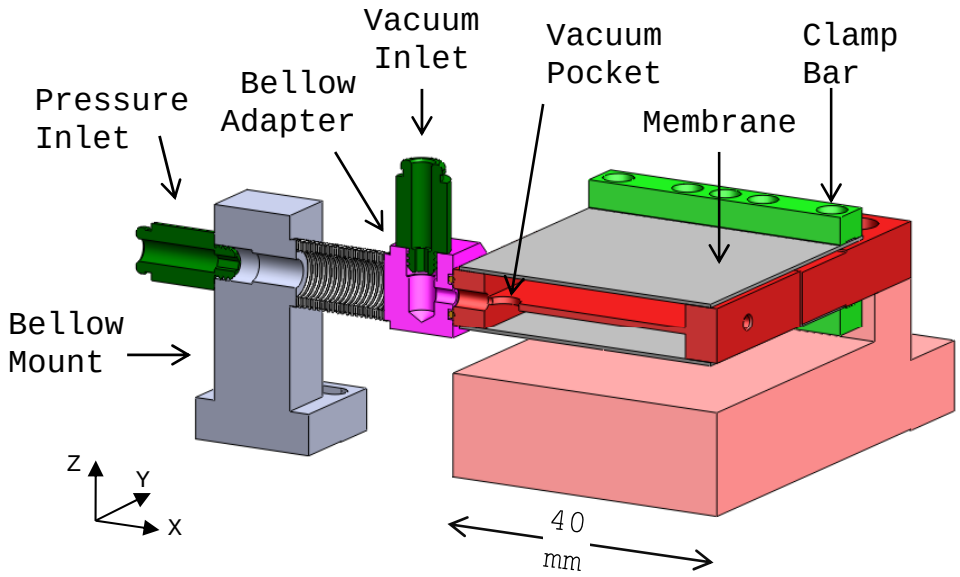

Figure 3-7: CAD cross-sectional view of the coarse approach mechanism showing the bellow and the vacuum clamp design.

stage. We use a Servometer[1] FC-6 pneumatic bellow. As shown in Figure 3-7, the bellow adapter part connects the bellow to the guide flexure. The bellow is connected to its mount on its other side. We pressurize the bellow through a port on its mount.

The bellow has an effective area of $A_b = 47$ mm^2 and a stiffness of $k_b = 1.9$ N/mm. The bellow's actuation range (Δx_b) for a given change in pressure (ΔP) can be calculated as the following:

$$\Delta x_b = \frac{\Delta P \times A_b}{k_f + k_b} \tag{3.9}$$

where k_b and k_f are the stiffness of the bellow and the guide flexure in the X-direction respectively. Using an actuation pressure of 1 Atm a range of 6.8 mm can be reached, which would be the coarse actuation range if the bellow is used with a vacuum line. For our experimental setup, we use a 100 psi pressure line with a pressure regulator to control the bellow's pressure and expansion. We require 1.5 Atm of differential pressure for an actuation range of 1-mm. The bellow can create forces in only one direction. We can use a positioning offset to preload the bellow's stiffness and shift the actuator's output force range to achieve a bi-directional actuation force.

[1] www.servometer.com

The bellow is connected to its mating parts by soldering according to the procedure provided by [67]. Brazing is not recommended as the raised temperatures from the flame can damage the bellow. Stainless steel 304L or 316L is recommenced as the hub material. The hubs are tinned using a flux for stainless steel, such as Kester #815. A Superior #30 flux is recommended for the bellows. To connect the bellow to the hubs, first the bellow and the hubs are fluxed and tinned separately. Next, the two are joined together. At each stage, the parts are cleaned by placing them in Kester #5760 neutralizer for 5 minutes and in boiling water for another 5 minutes.

3.2.3 Clamp

Once the piezo actuator is preloaded against the reticle, we use a clamping mechanism to hold its position. Once activated, the clamping mechanism must be rigid in the direction of actuation. A high-stiffness mechanical loop is required for achieving large enough pushing forces within the limited fine actuation range. The clamp must also be precise, such that the clamp's activation does not displace the piezo. We use a vacuum clamp, whose design is shown in Figure 3-7.

Vacuum pockets are machined into the two sides of the coarse stage's guide flexure. Two membranes cover the vacuum pockets and are used to clamp the guide flexure's moving part to its stator. The membranes are fixed to the guide flexure's stator using clamping bars. The vacuum line is connected through the bellow adapter. The connection between the bellow adapter and the guide flexure is sealed using an O-ring. Once vacuum is applied, the membranes are loaded against the guide flexure, which rigidly constrains the guide flexure in the X-direction.

The vacuum clamp uses the surface area on both sides of the guide flexure and can thus generate larger clamping force. A symmetric design also improves the clamping mechanism's precision by creating a uniform constraint. A symmetric clamp is also more rigid because the forces are balanced on the top and bottom planes, and thus the structure is not loaded by bending moments. The total vacuum pocket area, including both sides, is 1875 mm^2. Based on experimental results, the clamp can carry more than 80 N of pushing force without sliding.

The guide flexure is made from Aluminum Alloy 2024-T4. To increase the hardness of the vacuum clamp surface and avoid wear, the outer surface of the guide flexure is hard anodized with a thickness of 5 μm. Blue tempered 1095 Spring Steel with a hardness of more than 50 RHC is used for the membranes. To achieve a uniform and close contact, the guide flexure is designed to have its stator and moving parts on the same plane. To achieve the required flatness on the guide flexure and the membrane surfaces, the parts are precision machined using milling and are then lapped by hand.

3.3 Designs for Integration

The reticle assist device prototype has been designed for experimental verification of the design and development of the control algorithms. We have designed the setup for easy assembly and operation. Currently, we have a series design where the bellow, the clamp, and the piezo actuator are connected in series. We call this a '3L' design, since the three lengths add into the overall length. This simplifies the assembly and the operation of the device. However, for integration with the scanners, the design can be packaged more efficiently into a '1L' design. Figure 3-8 shows two ways of nesting the components within the guide flexure. The nested design is expected to have a lower volume and better vibrational dynamics.

In both designs, the piezo actuator and the bellow are nested inside the guide flexure. To save volume and cost, the piezo actuator can be custom manufactured using a piezo-stack. The design on the left uses a pneumatic bellow as the coarse approach actuator. The design on the right uses a a pressure pocket formed by the guide flexure, the membranes, and the stator to actuate the coarse approach stage.

3.4 Magnetostrictive Actuator

Magnetostrictive elements are another type of commonly used solid-state actuator. Application of a magnetic field results in extension of the magnetostrictive element. The elements are energized using current carrying coils. A magnetostrictive actuator

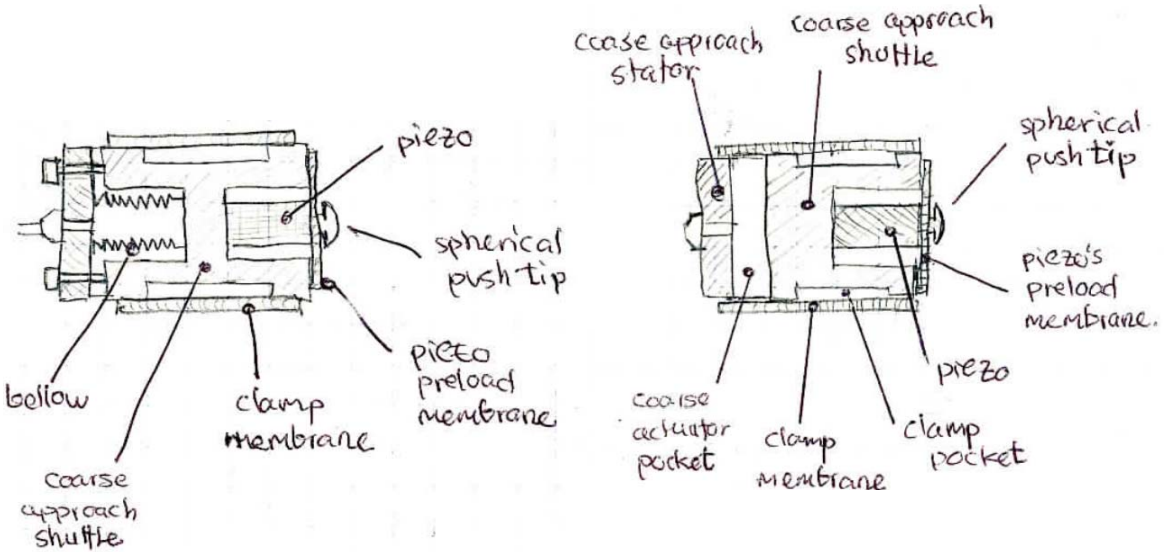

Figure 3-8: Ideas for more efficient packaging of the reticle assist device into a '1L' design.

is suitable for use as a reticle assist device because it uses a current source, and thus can be driven using the scanner motor currents. However, thermal length changes can be a significant source of error for magnetostrictive actuators. The heat from the resistive energy loss in the coils can raise the temperature of the elements and cause thermal expansion. The motion range of magnetostrictive elements is limited to less than 0.2% of their active length. Over such a small range of motion, thermal length variations can become significant. We have designed a thermally balanced magnetostrictive actuator, which eliminates the thermal variations. It also increases the actuation range by stacking two elements in series. The design of the actuator is described in the following subsections.

The thermally-balanced magnetostrictive design is provided as an alternative to the piezoelectric stack actuator. Compared to the piezoelectric actuator, the magnetostrictive actuator will have a larger mass and higher power dissipation, and hence, is not selected for detailed prototyping.

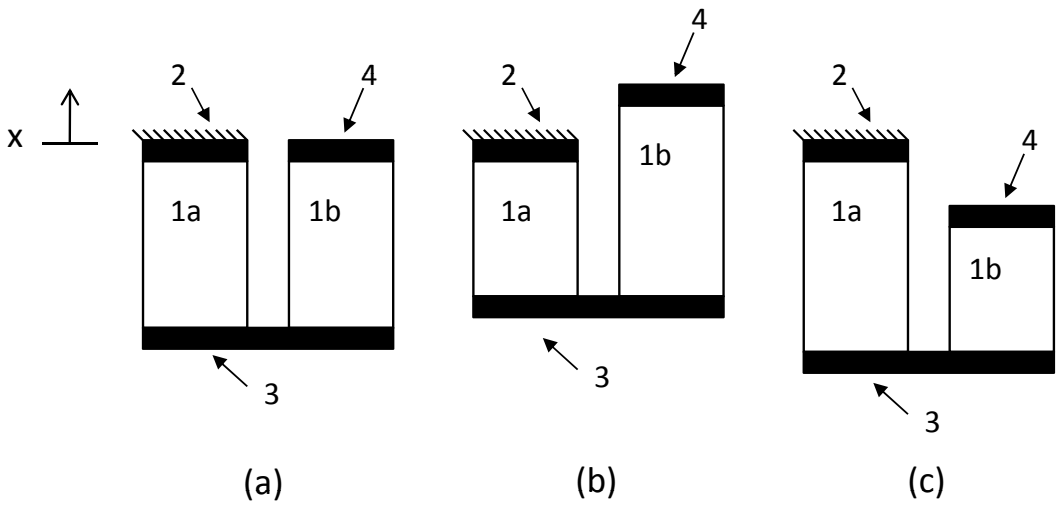

Figure 3-9: Thermally-balanced actuation method: the actuator is shown in its neutral position (a), positive extension (b), and negative extension (c).

3.4.1 Thermally-Balanced Configuration

To eliminate thermal length variation, two actuators are used back to back and are driven differentially, as shown in Figure 3-9. Element (1a) moves the middle frame (3) relative to the fixed reference frame (2). Element (1b) rides on the middle frame (3) and moves the actuation end (4) relative to the middle frame (3). The actuator is in it neutral position when both elements (1a) and (1b) are driven to their mid-range of motion. Driving the elements (1a) and (1b) differentially around this neutral position results in the motion of the actuation end (4). Contracting element (1a) and extending element (1b) moves the actuation end (4) in the positive x-direction relative to the fixed reference frame (2). Extending element (1a) and contracting element (1b) moves the actuation end (4) in the negative x-direction relative to the fixed frame (2). However, any thermally induced length change of elements (1a) and (1b) will be equal and will cancel out. As a result, the actuation end (4) will not move due to thermal length variations.

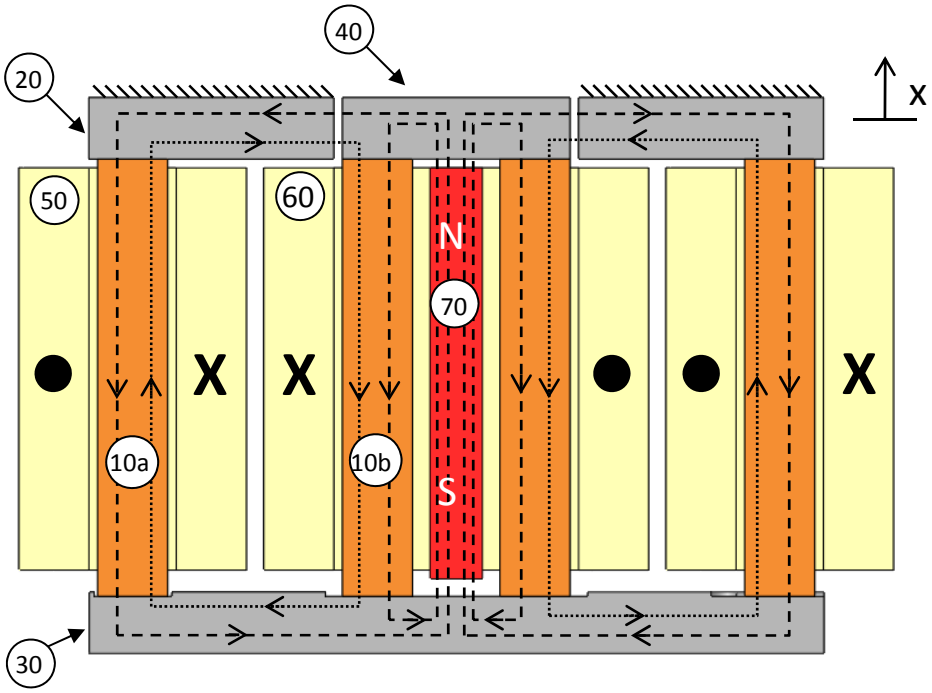

Figure 3-10: An example embodiment of the thermally balanced solid-state actuator's magnetic design using magnetostrictive elements.

3.4.2 Magnetic Design

The magnetostrictive elements can only increase in length, a bias magnetic field is required to enable bi-directional changes in length. To create a thermally balanced design, two elements should be used as in Figure 3-9. A differential magnetic field added to one element and subtracted from the other element around a magnetically biased operating point results in the motion of the actuation end (4) relative to the reference frame (2). Figure 3-10 shows one possible embodiment of the magnetic circuit design.

In the design shown in Figure 3-11, the magnetostrictive elements (10a) and (10b) are used on the outside and the inside respectively. The magnetic cores (20), (30), and (40) are magnetically permeable and close the magnetic path. Core (20) is fixed to a reference frame. Core (30) is moved by element (10a) and connects the two elements (10a) and (10b). Core (40) is moved relative to core (30) by the element (10b). A permanent magnet (70) is used to create a bias magnetic field through the elements

(10a) and (10b) in the same direction. The flux lines generated by the permanent magnet are shown as dashed lines. The coil (50) wraps around the element (10a). Coil (60) wraps in the opposite direction around element (10b). A current through the coils (50) and (60) creates a differential magnetic field within the elements of the same magnitude but opposite directions and thus one element 10a lengthens while the other element 10b shortens, and vice versa. The flux lines generated by the coils are shown as dotted lines. The use of two coils (50) and (60) creates a magnetic quadrupole, whose stray field will decay much faster. It also balances the differential field, such that the two elements (10a) and (10b) are driven by the same differential field amplitude. In this design, the bias magnetic field is provided by a permanent magnet. In this way, the actuator is at its desired magnetic bias using zero current and without any loss.

3.4.3 Mechanical Design

Detailed mechanical design is shown in Figure 3-11. The main frame (21) is the reference frame. The back core (20) is fixed to the main frame (21). The magnetostrictive element (10a) is located between the back core (20) and the middle core (30). The magnetostrictive element (10b) is positioned between the middle core (30) and the actuation-end core (40). The permanent magnet (70) is placed at the center and provides the magnetic bias. The outside coil (50) wraps around the outer magnetostrictive element (10a). The inside coil (60) wraps around the inner magnetostrictive element (10b). The two flexure plates (81) and (82) are used on the two ends to constrain the actuator's motion, but more importantly, put the magnetostrictive elements under a bias mechanical compressive stress. The bias mechanical compressive stress improves the element's magnetostriction coefficient (strain/field) and prevents compressive to tensile stress reversals. The coupling (41) is used to connect the actuating end to the load. To allow misalignments between the coupling (41) and the load, the coupling (41) is stiff only in the axial direction and flexible in all other degrees of freedom. For pushing applications, the coupling must have a high (or infinite) radius of curvature, to avoid large stress concentration at the point

Table 3.2: Magnetostrictive actuator design parameters

Parameter	**Description**	**Value**
A	Area of a single magnetostrictive element	25 mm^2
L	Length of a single magnetostrictive element	25 mm
d	Average magnetostrictive constant	$2 \times 10^{-}8$ m/A
E	Elastic Modulus of magnetostrictive elements	30 GPa
n	Coil turns per unit length	10^4 turns/m

of contact.

Using the design parameter values provided in table 3.2, the actuator can close a gap of 2 μm and exert a pushing force of 70N when a excitation current of 1.2 A is applied. The peak power dissipation is estimated to be 1.9W.

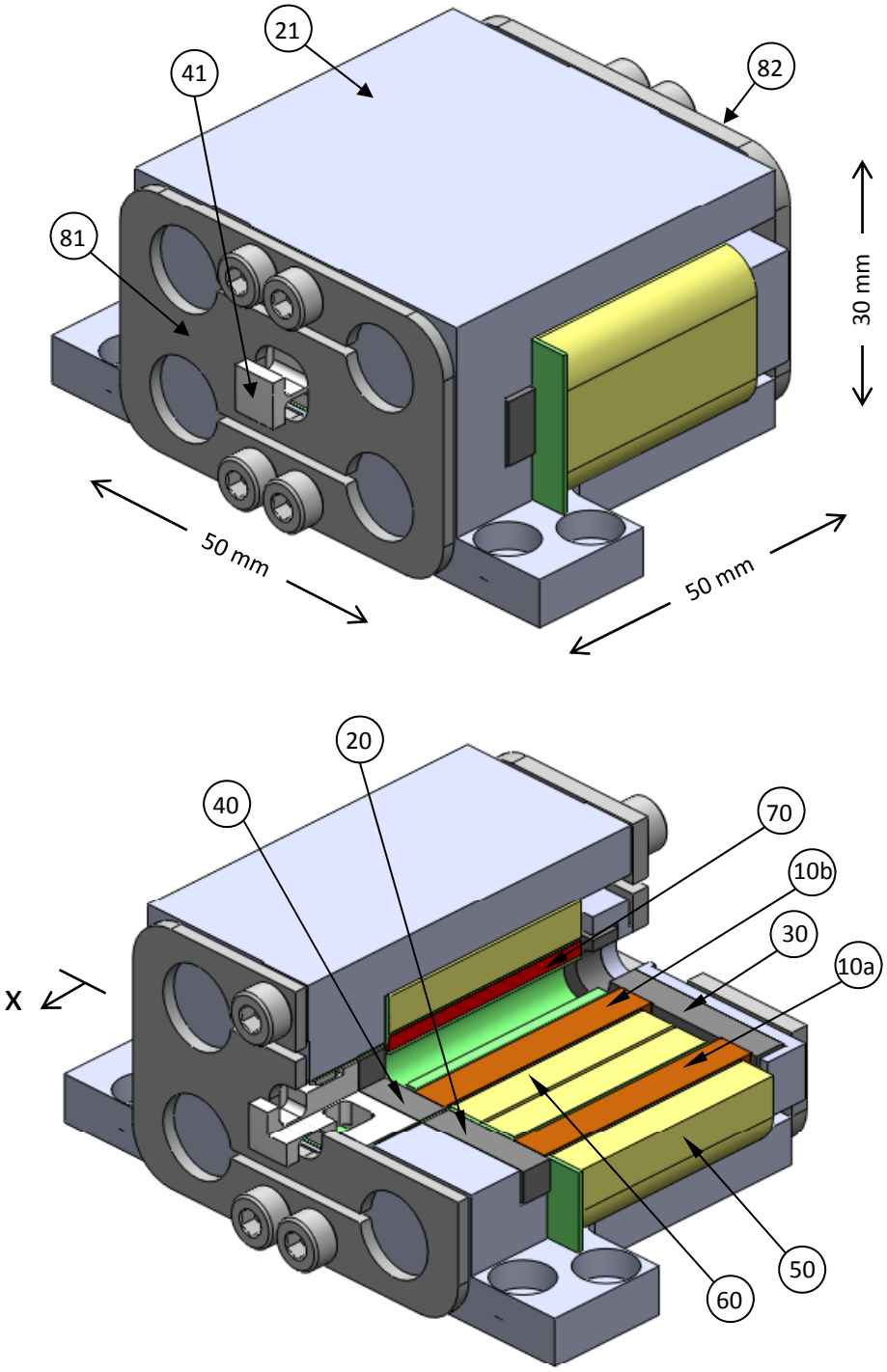

Figure 3-11: CAD Model of the thermally-balanced magnetostrictive actuator design (top) and its cross-sectioned view (bottom).

Chapter 4

Hybrid Charge Controller

Piezoelectric actuators have excellent motion resolution and high bandwidth. As a result they are widely used in precision motion applications, such as scanning probe microscopy and laser mirror alignment. The most common way of driving piezoelectric actuators is using a voltage amplifier to apply a voltage to the actuator in an open-loop fashion. This relies on the actuator voltage-displacement behavior; however, piezoelectric elements exhibit strong hysteresis. One way to eliminate the error caused by hysteresis is controlling the actuator in closed-loop using displacement- or strain-sensor feedback. Using a closed-loop controller has several disadvantages for high-frequency applications. It can reduce the system's control bandwidth, when compared to the open-loop operation, which is limited by only the actuator's mechanical dynamics. Using a displacement sensor also can add noise to the system, and can thus worsen the resolution. Finally, using closed-loop control requires the addition of a sensor as well as implementing a controller. An effective alternative for reducing the hysteresis is charge control [15] [62]. Commercial piezo ceramics have a high relative permittivity ($\varepsilon_r > 1000$), and thus the displacement charge is almost equal to the polarization charge ($D \simeq P$) [62]. Therefore, controlling charge is almost equivalent to controlling polarization, which results from alignment of the dipoles within the piezoelectric ceramic. Polarization and mechanical strain result from the same ionic movement and are directly related [62][52]. Therefore, charge control can significantly improve an actuator's linearity.

In this chapter, we first review prior art piezo charge amplifiers. We also present the design of our novel charge amplifier which advances the state of the art. We provide experimental results obtained using the amplifier. Finally, we describe a magnetic analogue of piezo charge control, where controlling magnetic flux can improve a magnetic actuator's linearity. We present methods for magnetic flux control supported by experimental results.

4.1 Prior Art Charge Amplifiers

In 1981, Comstock patented a charge amplifier design for improving the linearity of piezoelectric driven deformable mirror [15]. As shown in Figure 4-1, Comstock's design uses a sense capacitor (32) in series with the piezoelectric actuator (10) to sense accumulated charge via voltage. The sensed voltage is fed back to the power amplifier (30) for closed-loop charge control. This configuration is however sensitive to the finite resistance of the capacitors at low frequencies causing the charge to drift after a period of time. To eliminate the drift problem, Comstock's design included switches (34, 35, and 41) controlled by a timer (37) to reset and initialize the piezoelectric actuator (10) and the charge amplifier. Main et al. use an amplifier with a similar design [52]:

In 1982, Newcomb and Flinn used a current controller to control the charge on a piezoelectric actuator by controlling the time integral of the current [62]. However, due to offset errors, the integral of the current can drift with time resulting in a charge control error. As a result, this control method is only effective for a limited period of time unless an initialization method is introduced or another feedback is used for quasi-static tracking.

In 1988, Kaizuka and Siu suggested inserting a capacitor in series with the piezoelectric actuator not for sensing charge but for reducing the sensitivity of the induced charge to the hysteresis of the piezoelectric actuator when driven using a voltage source [40]. This can most easily explained at the limit where the inserted capacitor is significantly smaller than the piezoelectric actuator's capacitance. At this limit, the total series capacitance is approximately equal to the small capacitance of the

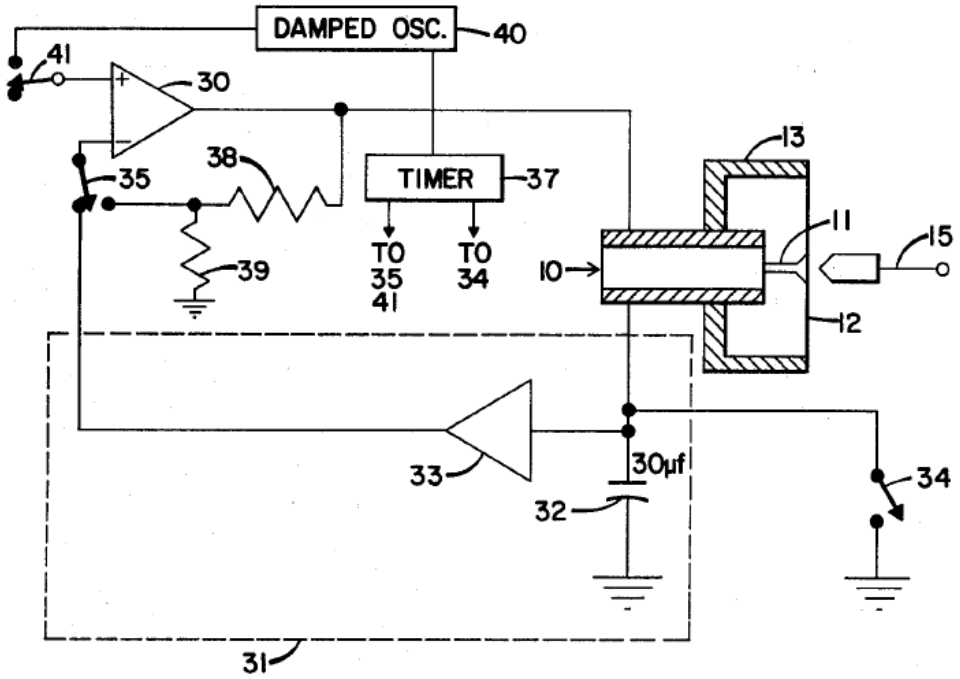

Figure 4-1: Comstock's charge amplifier design. This figure is copied from US Patent 4,263,527 [15].

inserted capacitor and is thus relatively insensitive to the piezoelectric element's capacitance. As a result, the induced charge is approximately given by the applied voltage multiplied by the inserted capacitance (Q = Cv) and is less sensitive to the changing capacitance of the piezoelectric actuator. A short mathematical proof of this is also provided in [56]. This method is effective when the inserted capacitor has a low capacitance when compared to the piezoelectric element's. Smaller capacitance results in a larger impedance meaning that most of the voltage is dropped across the inserted capacitance. Although this is a very simple method to improve the linearity of the piezoelectric actuators, it requires significantly higher total drive voltage, as only a portion of the voltage output goes to driving the piezoelectric element.

In 2001, Tonoli et al. added a resistor in parallel to the sensing capacitor to prevent drift [82]. A simplified schematic of their charge amplifier design is shown in Figure 4-2. The added resistor (R1) is used to compensate the drift, which can be caused by the leakage resistance of the piezo actuator (Rp). The resistive feedback formed by R1 and Rp is dominant at low frequencies while the capacitive feedback formed by C1 and

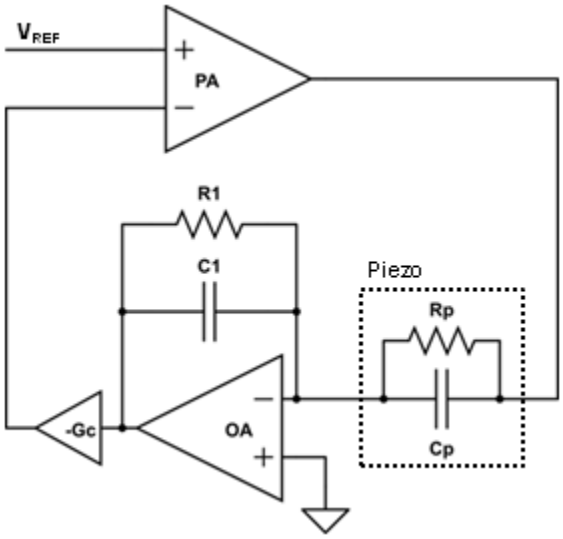

Figure 4-2: Charge amplifier design by Tonoli et al. The diagram has been reproduced from [82].

Cp is active at high frequencies. As a result, charge is sensed and controlled at high frequencies, and voltage is controlled at low frequencies. The values of R1, Rp, and C1 are selected such that the resistive and capacitive feedbacks have matching gains and break-frequencies. In this configuration, the load currents are sourced by the operational amplifier (OA). This can be a problem in higher frequency applications where the piezoelectric actuator's capacitive currents can be too large.

In 2003, Fleming and Moheimani designed a charge controller similar to the design in [15] but added an auxiliary control loop to eliminate drift by using voltage feedback in DC [23]. In this way, charge could be controlled at higher frequency and voltage at lower frequencies. This solution required designing two separate controllers for charge and voltage.

Another simpler implementation was provided by Yi and Veillette in 2005, where the architecture of the passive feedback circuit resulted in voltage control in DC and charge control at higher frequencies [84]. As shown in Figure 4-3, Yi and Veillette used an inverting amplifier configuration. The feedback voltage is dominated by the resistors R1 and R2 at low frequencies and by the capacitor C1 and the piezoelectric element at higher frequencies. In their design, the piezo is referenced to the pseudo-ground at the op-amp's inverting input and is not floating. However, the load current

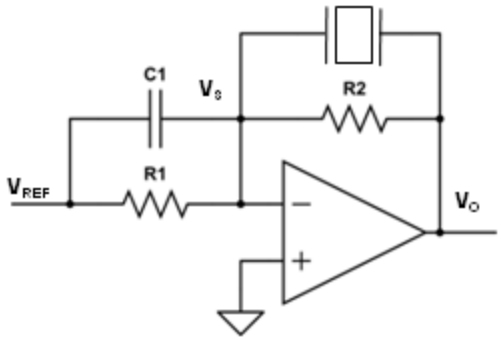

Figure 4-3: Yi and Veillette's charge amplifier design. The diagram has been reproduced from [84].

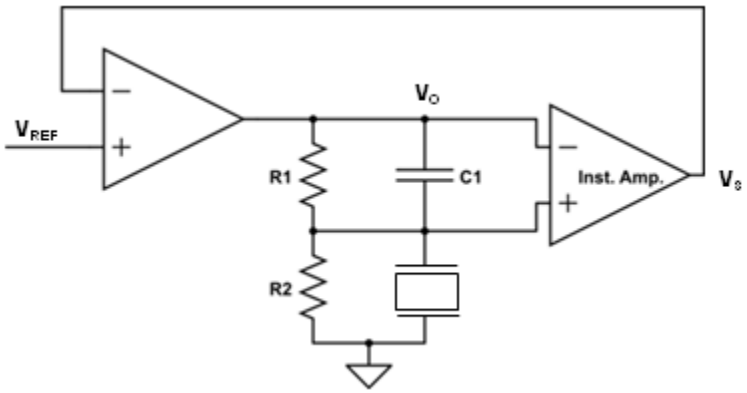

Figure 4-4: Fleming and Moheimani's charge amplifier design. The diagram has been reproduced from [24].

must be supplied at the reference signal terminal (V_{REF}). The reference signal driver may have a finite impedance which thus affects the feedback gain. Additionally, the piezoelectric current at higher frequencies can be too large for the driver of the reference signal.

In 2006, Fleming and Moheimani [24] suggested an improved configuration where the passive feedback circuit results in voltage control at low frequency and charge control at higher frequencies. A simple schematic of this design is shown in Figure 4-4. In this configuration, the load currents are sunk through ground. In the configuration presented by [24], the piezoelectric load is referenced to ground and not floating. However, this configuration requires a high-voltage and high common-mode-rejection instrumentation amplifier to measure the voltage on C_1 [22].

A modified version of this configuration, where no additional active components

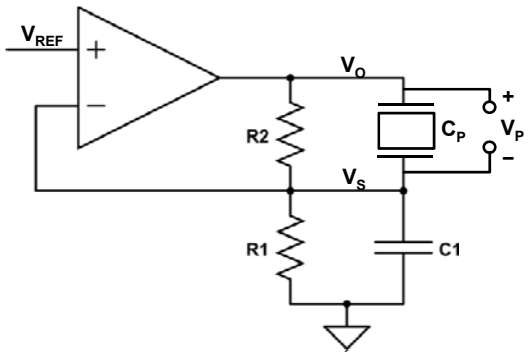

Figure 4-5: PiezoDrive's charge amplifier design. The diagram has been reproduced from [1].

are required is provided in a technical report on PiezoDrive's website[1] [1], and reproduced in Figure 4-5. The modified configuration is identical to the design in [15] but with an added resistive (R1 and R2) feedback path for preventing low-frequency drift.

4.2 Analysis of Conventional V-Q Charge Amplifier

A common commercial charge amplifier design is shown in Figure 4-5. In this section we analyze such a charge amplifier configuration. A block diagram of the charge amplifier is shown in Figure 4-6. The power amplifier is represented by the transfer function $G_{PA}(s)$. The signals V_{Ref}, V_O, V_S represent the amplifier reference voltage, output voltage and sensed feedback voltage, respectively. A simple way to understand this design is to look at the low and high frequency limits. At low frequencies (quasi-static), the feedback is dominated by the resistors because they have a much lower impendence than the capacitors in this frequency range. At high frequencies, the capacitors have a lower impedance than the resistors and dominate the feedback. The voltage on the capacitive feedback circuit is proportional to charge, and therefore, can be viewed as sensing charge. The resistive network voltage feedback is included to avoid low frequency drift which can result from static charge measurement. For this

[1]PiezoDrive has been founded in 2009 by Dr. Andrew Fleming (http://www.piezodrive.com)

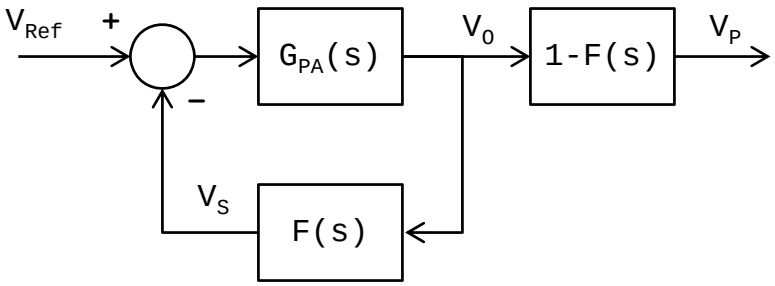

Figure 4-6: Block diagram of the charge amplifier design shown in Figure 4-5.

mixed voltage-charge (V-Q) feedback circuit to work uniformly over all frequencies, the resistors and capacitors must be sized appropriately, as presented below.

The feedback voltage V_S is related to the output voltage V_O through the transfer function F(s). For the design shown in Figure 4-5, the transfer function F(s) can be calculated as

$$F(s) = \frac{V_S}{V_O} = \frac{R_1(R_2C_ps + 1)}{R_2(R_1C_1s + 1) + R_1(R_2C_ps + 1)}. \tag{4.1}$$

The feedback transfer function F(s) can be approximated at the high and low frequency limits as

$$F(s) \simeq \begin{cases} \frac{R_1}{R_1+R_2} & s \ll \omega_{VQ} \quad \text{Voltage Control} \\ \frac{C_p}{C_1+C_p} & s \gg \omega_{VQ} \quad \text{Charge Control} \end{cases}, \tag{4.2}$$

where ω_{VQ} is the frequency around which the transition from voltage to charge control occurs. For a smooth transition from voltage to charge control, a constant feedback gain across all frequencies is desired. This can be achieved by selecting the components such that the following condition is satisfied:

$$R_1C_1 = R_2C_p = \tau_{VQ} = \frac{1}{\omega_{VQ}} \tag{4.3}$$

Using the above expression, the transfer functions F(s) can be simplified as

$$F(s) = \frac{V_S}{V_O} = \frac{R_1(\tau_{VQ}s + 1)}{R_2(\tau_{VQ}s + 1) + R_1(\tau_{VQ}s + 1)} = \frac{R_1}{R_1 + R_2}. \tag{4.4}$$

The charge across the piezoelectric actuator is equal to the charge across the sense capacitor (C_1) and is given as $Q_P = C_1 \times V_S$. Assuming stable operation of the loop, V_S is controlled to be equal to V_{Ref}. Thus, the closed-loop charge control gain is given as

$$\frac{Q_P}{V_{Ref}} = C_1. \tag{4.5}$$

However, the equivalent closed-loop voltage gain is a more relevant parameter, when designing the amplifier. Any piezo stack actuator is specified for a certain operating voltage range. It is important that the closed-loop voltage gain is designed such that the voltage range of the reference signal (V_{Ref}) is mapped to the full voltage range of the actuator. The voltage across the piezo actuator (V_P) can be calculated as below:

$$V_P = V_O - V_S = V_S(\frac{1}{F(s)} - 1) = V_S(\frac{R_2 + R_1}{R1} - 1) = V_S\frac{R_2}{R_1} \tag{4.6}$$

Assuming large loop gain and stable operation of the amplifier, the signal V_R must be approximately equal to V_S. Therefore, the amplifier's closed-loop voltage gain can be given as

$$\frac{V_P}{V_{Ref}} = \frac{R_2}{R_1}. \tag{4.7}$$

For this research, we use a piezo actuator with a voltage range of 100 V. To map our controller's 0-10V output range to the piezo's 0-100V range, we select a closed loop gain of 10 as

$$\frac{V_P}{V_{Ref}} = \frac{R_2}{R_1} = 10 \Rightarrow R_2 = 10R_1. \tag{4.8}$$

We select the value of C_1 according to (4.3) to match the resistive and capacitive

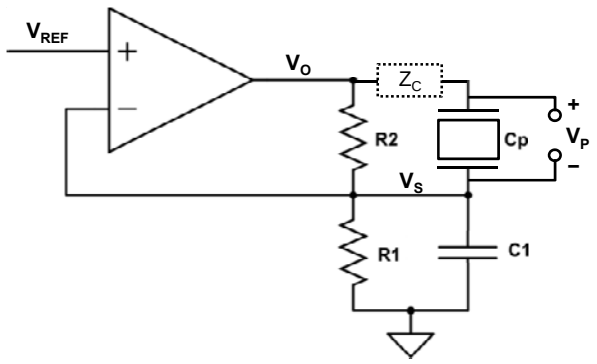

Figure 4-7: Charge amplifier design with the resistor R_c modeling the resistance of the cable connecting the piezo actuator the amplifier

feedbacks:

$$R_1 C_1 = R_2 C_p \Rightarrow C_1 = \frac{R_2}{R_1} \times C_p = 10 C_p \tag{4.9}$$

Our actuator has a capacitance of $C_p = 1.5\ \mu F$. We choose $R_2 = 100\ k\Omega$ to achieve a voltage- to charge-control frequency of 10 kHz. For a closed-loop voltage gain of 10, the component values for our charge amplifier, designed around the configuration shown in Figure 4-5, can thus be calculated using (4.3) and (4.7) as

$$\begin{aligned} R_1 &= 10\ k\Omega \\ R_2 &= 100\ k\Omega \\ C_1 &= 15\ \mu F \\ C_p &= 1.5\ \mu F \end{aligned} \quad . \tag{4.10}$$

Typically, piezo actuators have a voltage range of 100 V or more. On the other hand, the reference signal drivers have a voltage range of 10 V or less. As a result, a closed loop gain of larger than 1 is typically required. This means that the feedback transfer function F(s) has a gain of less than unity. This helps with the stability of the circuit, as most linear power amplifiers are stable when used with a scalar feedback gain of less than unity.

The control system's stability can be analyzed using loop-shaping and the Nyquist criterion based on the resulting feedback transfer function F(s) and the power de-

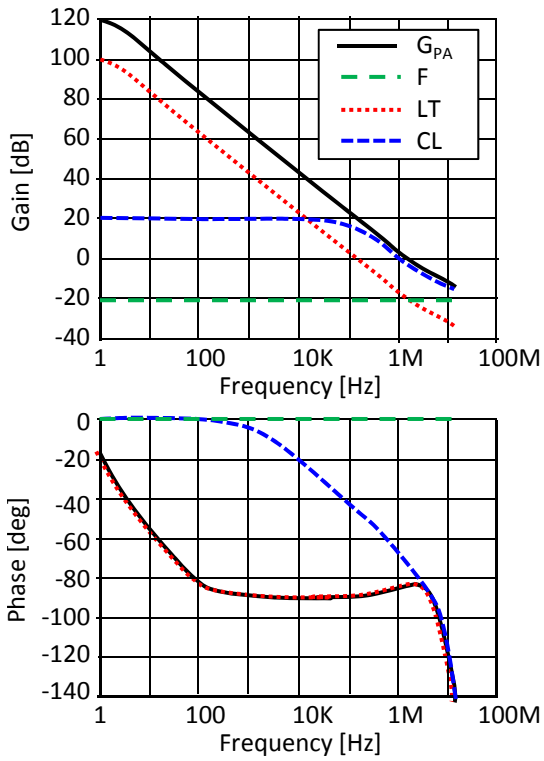

Figure 4-8: Frequency responses of the amplifier open-loop $G_{PA}(s)$, feedback F(s), loop transmission LT(s), and the closed loop CL(s) transfer functions showing the amplifier loop-shaping design

vice's frequency response $G_{PA}(s)$. The frequency responses in Figure 4-8 show the loop shaping design of the charge control loop. We use an APEX MP38A power device [9] with an external compensation capacitor of 470 pF. The power device's frequency response is reproduced from its datasheet [9]. Using (4.2), the feedback gain can be calculated as $F(s)=\frac{1}{11}$. The loop transmission ratio can be calculated as $LT(s)=G_{PA}(s) \times F(s)$. The loop transmission has a unity gain cross-over frequency of 100 kHz with 90° of phase margin. Given the positive phase margin of 90°, the closed loop response is expected to be stable and damped. The closed loop transfer function can be calculated as

$$CL(s) = \frac{V_P(s)}{V_{Ref}(s)} = \frac{G_{PA}(s)}{G_{PA}(s)F(s)+1}[1 - F(s)].$$

The expected feedback transfer function F(s), as given by 4.1, is based on an ideal circuit, shown in Figure 4-5, with no series impedances. In practice, the cables and connections have impedance, which can affect the feedback circuit. Figure 4-7 shows the charge amplifier circuit with the impedance Z_C modeling the impedance of the connection to the piezo actuator. The series impedance can include a resistance and an inductance and can be modeled as $Z_C=R_C+L_Cs$. Using MATLAB, we recalculate the feedback transfer function to reflect the effect of the series impedance. MATLAB's *margin* function is used to numerically calculate the charge control loop's phase margin and unity gain cross-over frequency for different series impedance values. Figure 4-9 shows the phase margin and the unity gain cross-over frequency versus the load impedance for the conventional V-Q amplifier design presented in this section. As can be seen, the series load impedance can reduce the controller's phase margin and even destabilize the amplifier.

The sensitivity of the charge controller to the cabling impedance makes the design and implementation of charge amplifiers difficult. It also prevents purposeful addition of a series resistance for passive damping and passive current limiting. In the next section, we present a new charge amplifier design, which significantly reduces the charge amplifier's sensitivity to presence of a series load resistance. We refer to the

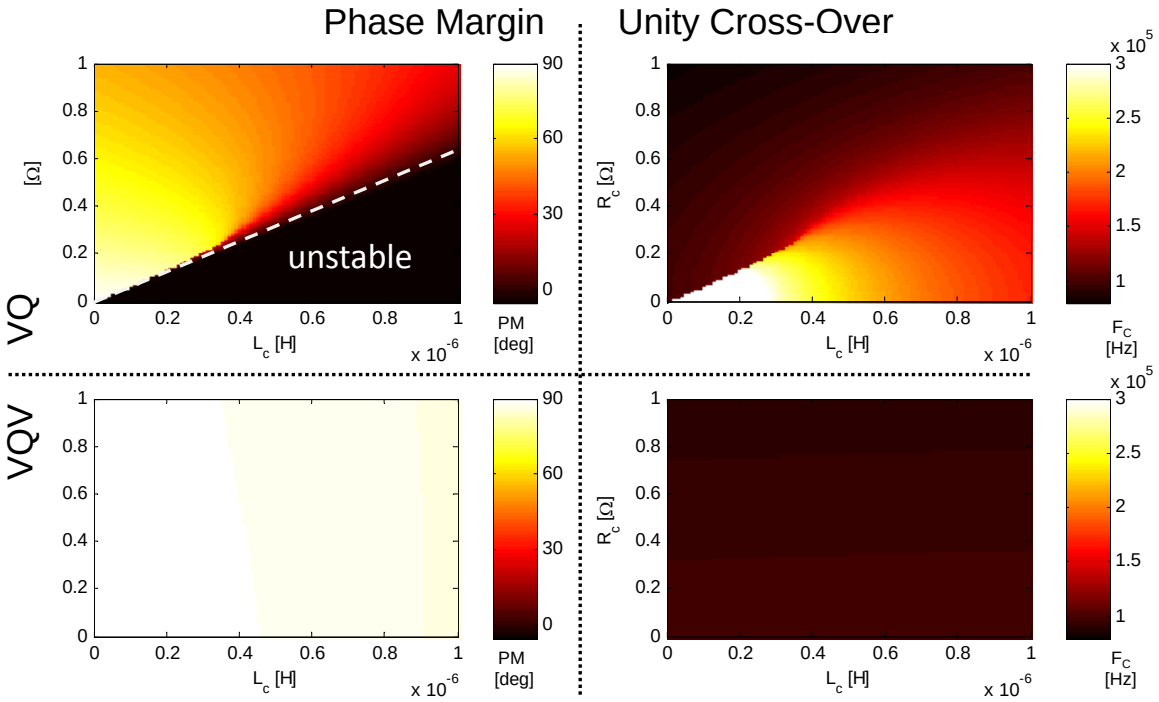

Figure 4-9: Feedback phase lag at the cross over for different cable resistance (R_c) values displayed for the V-Q and V-Q-V charge amplifiers.

this new design as the V-Q-V Charge amplifier.

4.3 Novel V-Q-V Charge Amplifier

In the previous section, we discussed the sensitivity of the conventional charge amplifier designs to the presence of a series load resistance. In this section, we present a new charge amplifier design which mitigates this problem.

With the conventional V-Q charge amplifier design, the capacitive leg of the feedback circuit is active at the cross over. The phase lag is a result of the series resistance (R_c) creating a pole with the capacitors (C_1 and C_p). This effect can be significantly attenuated if the feedback circuit is designed to be resistive at the cross-over, as in the proposed design shown in Figure 4-10. This charge amplifier controls charge in the mid-band and voltage in the low- and high-frequency bands. Because the amplifier is controlling voltage at the cross-over frequency, and has an active resistive feedback circuit at that frequency, it is not as sensitive to the addition of any series resistance.

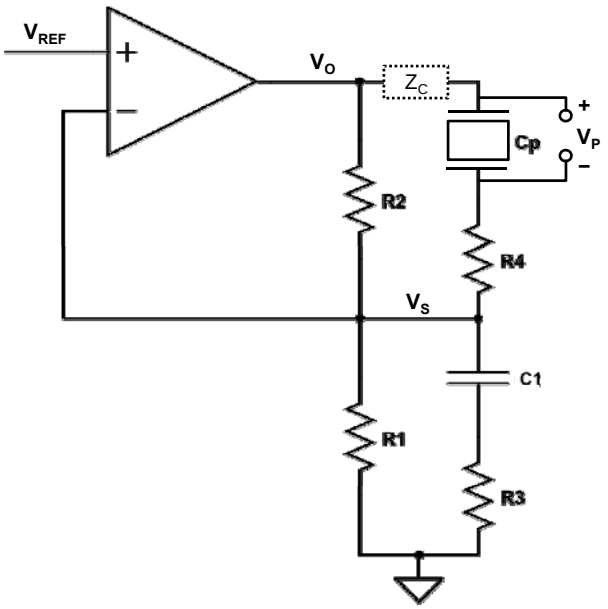

Figure 4-10: Schematic design of the new V-Q-V charge amplifier design.

The charge to voltage control transition frequency can be selected to be above the desired mechanical control frequency and below the amplifier's cross-over frequency. In this way, charge is controlled within the desired control bandwidth and voltage control is active at the cross-over frequency. This improves the charge amplifier's robustness without sacrificing its performance within the desired control bandwidth.

To better understand the circuit, first consider the low frequency ($\omega \ll \frac{1}{R_1 C_1}$), where the capacitors have a higher impedance than their corresponding parallel resistors. In this case, the capacitive leg of the feedback circuit can be ignored and the feedback voltage V_s is driven by R_2 and R_1. This is the low-frequency voltage-control range. Next, consider the middle frequency range ($\frac{1}{R_1 C_1} \ll \omega \ll \frac{1}{R_3 C_1}$), where the capacitors C_1 and C_p have a lower impedance than their corresponding parallel resistors R_1 and R_2 but higher impedance than their series resistors R_3 and R_4. In this range, the feedback is mainly influenced by the capacitors. This is the charge-control range. Finally, consider the high frequency range ($\frac{1}{R_3 C_1} \ll \omega$) where the series resistors R_3 and R_4 have a higher impedance than their corresponding capacitors C_1 and C_p. In this range, the capacitors can be neglected and the feedback voltage is dominated by resistors R_3 and R_4.

$$F(s) \simeq \begin{cases} \frac{R_1}{R_1+R_2} & \omega \ll \frac{1}{R_1 C_1} & \text{Voltage Control} \\ \frac{C_p}{C_1+C_p} & \frac{1}{R_1 C_1} \ll \omega \ll \frac{1}{R_3 C_1} & \text{Charge Control} \\ \frac{R_3}{R_3+R_4} & \omega \gg \frac{1}{R_3 C_1} & \text{Voltage Control} \end{cases} \tag{4.11}$$

For the charge amplifier to work without unwanted time transients, the feedback gain given by (4.11) must be constant over the whole frequency range. Equation 4.3 derived for matching the V-Q amplifier's feedback also matches the feedback gain for low- and mid-frequency bands. To match the gain over the high-frequency band to the low- and mid-frequency bands, the following condition must be satisfied:

$$R_3 C_1 = R_4 C_p. \tag{4.12}$$

The frequency where the charge-control to voltage-control transition occurs can be calculated as

$$\omega_{QV} = \frac{1}{R_3 C_1} = \frac{1}{R_4 C_p}. \tag{4.13}$$

Given a desired charge-control bandwidth, the values of the resistors R_3 and R_4 can be calculated using (4.12) and (4.13). The process for selection of the rest of the circuit component values for the V-Q-V charge amplifier is the same as for the V-Q charge amplifier.

For our design, we have selected $\omega_{QV} = 10$ kHz, which is 10 times below the designed amplifier's cross-over frequency and only slightly lower than our piezo actuator's mechnical resonance frequency of approximately 20kHz. In any case, driving the piezo above 10 kHz is not practical since near the resonance frequency, the mechanical dynamics degrade the open-loop accuracy. Overexciting the piezo near resonance can also damage the actuator. The required R_3 and R_4 resistor values can be calculated

as

$$\begin{aligned} R_3 &= \frac{1}{\omega_{Q-V} C_1} = 1\Omega \\ R_4 &= R_3 \frac{C_1}{C_p} = 10\Omega \end{aligned} \quad . \tag{4.14}$$

Given the above component selection, the resulting feedback phase lag at the 100 kHz desired cross-over frequency is plotted versus the series resistance in Figure 4-9. As can be seen, the new design is significantly less sensitive to the the added series resistance. This increases the amplifier's phase margin and improves its robustness to the addition of series cable resistance.

4.4 Charge Amplifier Hardware

4.4.1 Mechanical Design

To test our charge control method we have built a custom charge amplifier, which is shown in Figure 4-11. The amplifier's front panel has connectors for connecting the piezoelectric actuator, giving a reference voltage, and sensing current, voltage, and charge. A switch on the front panel allows the user to switch between charge- and voltage-control modes. A potentiometer is also provided for fine tuning the resistive leg of the feedback circuit. The amplifier is powered from the wall outlet. The bottom part of the enclosure is used for the AC-DC power supply components. The printed circuit board (PCB) and the heat sink are connected to the top side of the enclosure.

A side cross-sectional view of the enclosure box is shown in Figure 4-12. We use an APEX[1] MP38A power device [9]. As shown in Figure 4-12, the power device comes on its own printed circuit board (PCB). The power device has its components on one side of that PCB and a plated heat sink on the opposing side. The power device's plated side is fixed to the main heat sink using two screws. The main heat sink is fixed to the top surface of the power amplifier. The enclosure has an opening cutout for the device pins to pass through and connect to the charge amplifier's PCB. The

[1]Apex Microtechnology: www.apexanalog.com

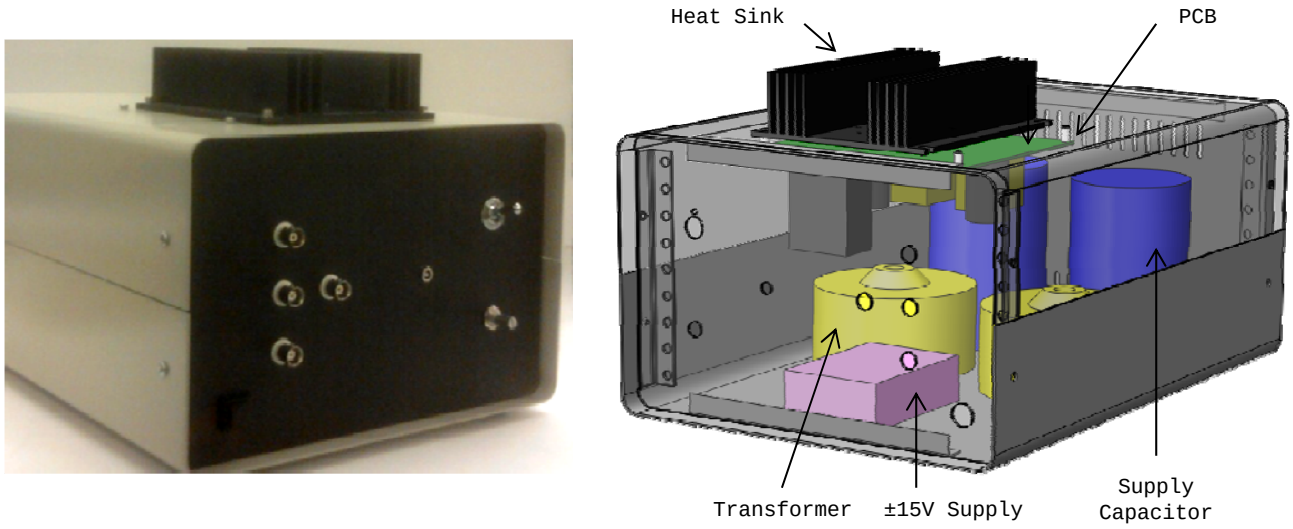

Figure 4-11: The assembled custom charge amplifier (left) and CAD design (right).

amplifier's PCB has a socket matching the pin pattern of the power device. The PCB is mounted onto the bottom side of the enclosure's top. Spacers are used to position the PCB at the right distance from the power device.[8]

4.4.2 Circuit Design

In this section, we describe the detailed circuit design of the charge amplifier. The circuit diagram of the power device and its feedback circuit is shown in Figure 4-13. The design of the measurement buffers is shown in Figure 4-14. The schematic of the 110-V DC supply is shown in Figure 4-15. Net labels, which mark the signals in the schematic diagrams, are used to identify the signals and show the connection between the schematic diagrams. The net labels are consistent with the signal convention used within the rest of this chapter. for example, the amplifier reference, output, feedback, and piezo voltages are labeled as V_{ref}, V_o, V_s, and V_p, respectively.

As shown in Figure 4-13, the feedback circuit is formed by the resistors R_1, R_2, R_3, R_4 and capacitor C_1 according to the V-Q-V design, which was described in Section 4.3. The R_{adj} potentiometer in the resistive leg of the feedback circuit can be used to fine tune the resistive feedback circuit and match it to the capacitive feedback circuit. The circuit is designed to be flexible. To use as a V-Q amplifier, the resistors

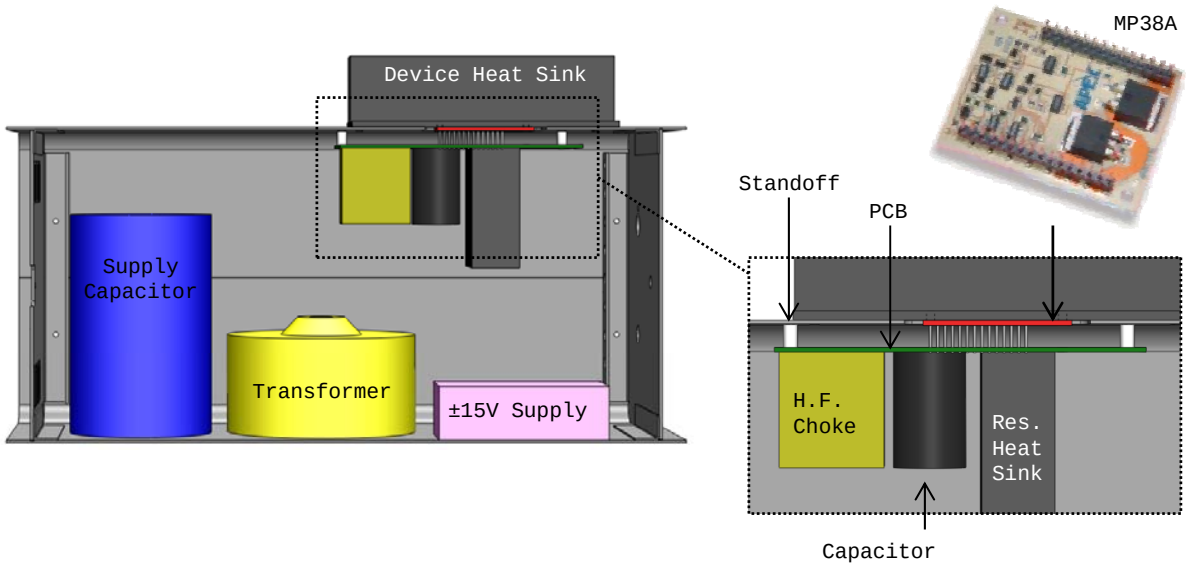

Figure 4-12: Side cross-sectional view of the charge amplifier.

R_4 and R_3 can be short-circuited by placing 0 Ω resistors. The jumpers QF and VF represent a two-position toggle switch, which enables the user to select between voltage-control and charge control. Note that the position of the switch must not be changed when the device is powered on. Switching the feedback configuration, while the amplifier is powered on, can damage the power device.

Mechanical shocks on the piezo motion system can raise the piezo's voltage beyond the power supplies' range and potentially damage the amplifier's output circuitry. To protect the power device's output, we have added two external fly-back diodes D_3 and D_4. Although the amplifier has internal fly back diodes, they should not be counted on for repeated high-energy pulses. The two back to back diodes D_1 and D_2 protect the power device's differential inputs from large differential voltages as an input differential voltage beyond ±20 V can damage the power device. The resistor R_7 is placed in series with the output and is used by the power device's internal circuitry for current sensing and limiting. The value of $R_7 = 0.1$ Ω limits the output current to 7 A. [9][7]

The amplifier box has BNC output connectors for sensing the piezo's current and voltage. In charge control mode, the feedback voltage can also be used as an estimate of the piezo charge. The circuit diagram of the buffers measuring piezo

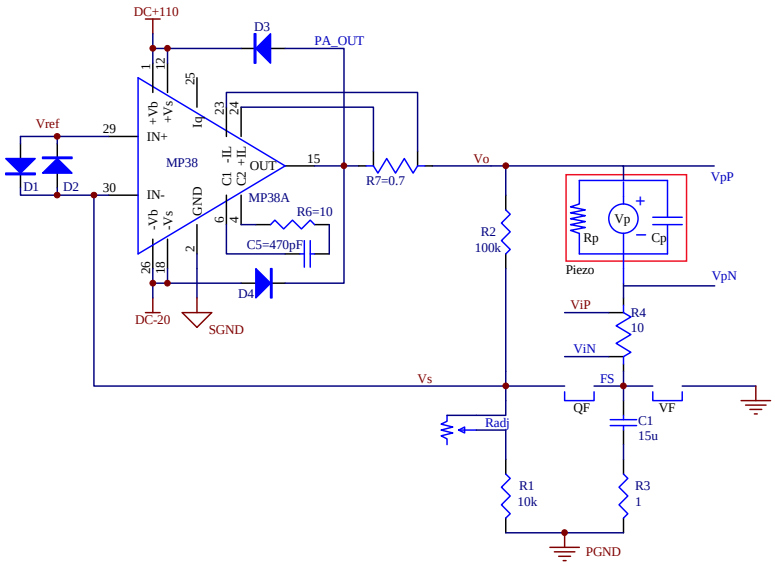

Figure 4-13: Circuit design of the charge amplifier showing the power device and its feedback circuit.

voltage ($V_p/10$), current (V_i), and charge (V_{sB}) are shown in Figure 4-14. Differential analog adder-subtractor buffers are implemented using single op-amps and are used for sensing the piezo's voltage and current. Current is sensed by measuring the voltage across the resistor R_4 as $V_i \simeq \frac{1}{2}(V_{iP} - V_{iN})$. Piezo voltage is measured by finding the difference between the voltages on the two sides of the piezo as $V_p = \frac{1}{10}(V_pP - V_pN)$. Charge is estimated as the feedback voltage (V_s) under the charge-control mode and is buffered using a voltage follower (V_{sB}). The differential buffers for current and voltage sensing are designed to work with the $\pm$15V supplies. However, they have a finite input impedance. This can be a problem when measuring high-impedance voltage sources, such as the piezo's negative voltage (V_{pN}). We have mitigated this problem by choosing large resistor values for the differential buffer to increase its input impedance relative to the measurement source impedance.To fully solve the problem, we can use a voltage follower to buffer V_{pN} before measuring it using the differential buffer.

The amplifier's common ground plane is divided into a power ground (PGND) and a signal ground (SGND). The piezo current returns through power ground (PGND). The signal ground (SGND) is used by the buffers as a common reference and serves

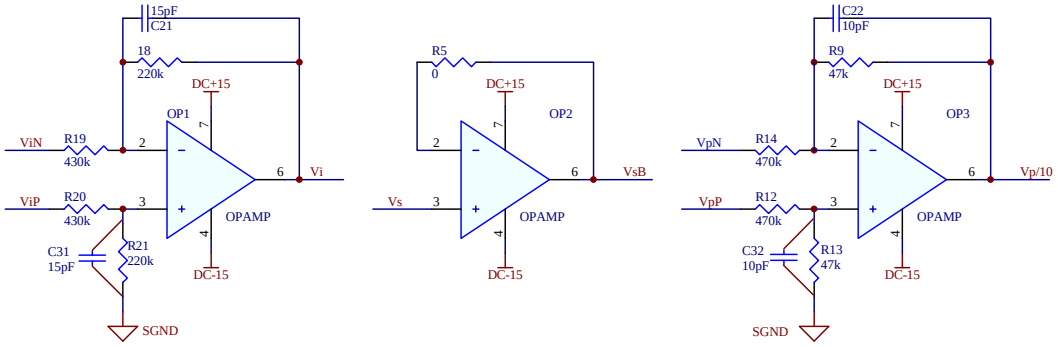

Figure 4-14: Schematic design of the charge amplifier showing the buffers measuring the piezo current (left), the feedback voltage (middle), and the piezo voltage (right).

as a return path for the low-current measurement signals. The two grounds are joined at only a single point. In this way, the relatively large piezo currents cannot return through the signal ground and thus do not disturb the measurements.

We have built linear AC-DC power supplies into the amplifier box, so that the amplifier can be directly powered from the wall. The amplifier uses +120V, -20V, and ±15V DC supplies. We built our own linear AC-DC supply to generate the +110V and -20V DC supplies from the wall outlet 120V RMS AC voltage. We use an off the shelf Acopian DB15-20 linear AC-DC supply for generating ±15V DC supplies. A schematic of the +120-V DC power supply is shown in Figure 4-15 as an example. The 120-V RMS wall outlet voltage (L120) is connected to the circuit through a current-limiting fuse (F1). We use a bi-directional TransZorbs to prevent line voltage transients from reaching the output side [7]. We also use a unidirectional Tranzorb on the DC output to prevent supply output over voltage. We use a toroidal transformers to scale the 120V RMS line voltage to 80V RMS, which corresponds to 113V peak-to-peak voltage. We use a full bridge rectifier to change the sinusoidal signal into a single-sided positive signal, which charges the supply capacitors up to 113V minus the diodes' voltage drop. We have placed a negative temperature coefficient (NTC) resistor in the current path to limit the inrush currents at the power up of the amplifier. The NTC resistor has a high initial resistance, which prevents inrush currents. As current flows, the resistor heats up, and the resistance drops. An inductive high-frequency choke is added in the current path to filter high-

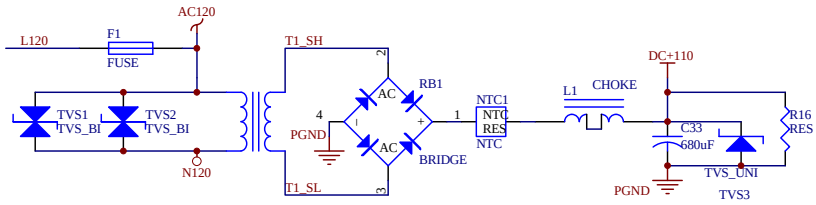

Figure 4-15: Circuit design of the charge amplifier showing its 110-V AC-DC power supply.

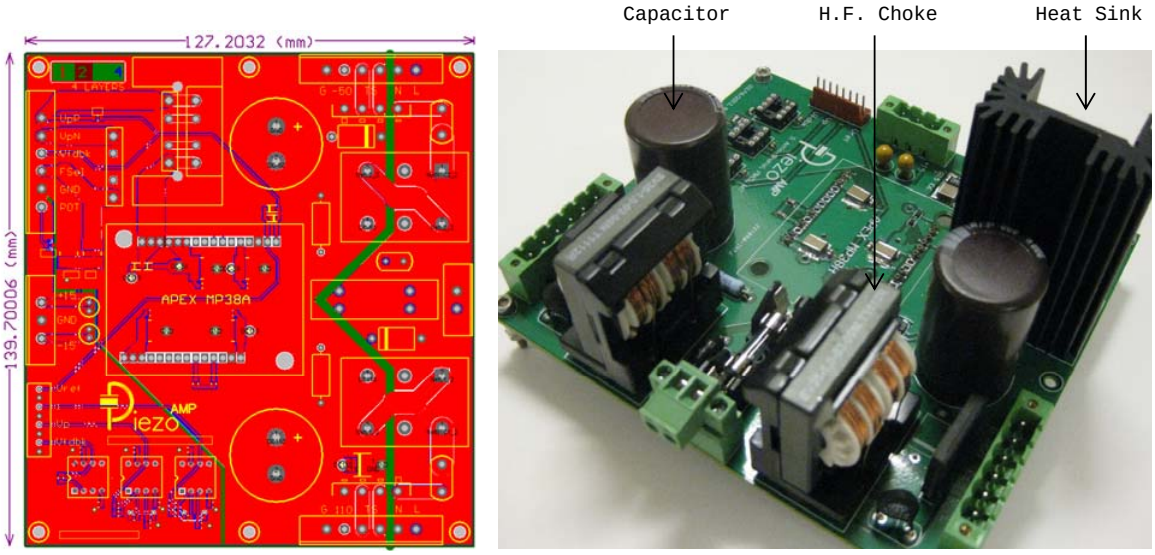

Figure 4-16: The amplifier's printed circuit board design (left) and manufactured circuit board (right).

frequency supply noise. In this way, we generate a linear DC supply of 110V with very low high-frequency noise. The 120-Hz ripple and other low frequency supply variations can be rejected by the power device.

The charge amplifier's assembled printed circuit board is shown in Figure 4-16.

4.5 Hybrid Hysteresis Compensation

Practical charge amplifiers control charge in AC and voltage in DC. Assuming a linear capacitive model for the piezo actuator, voltage-control in DC is an approximation of charge control . This is an inaccurate approximation because of the very fact that motivates the design of charge amplifiers: the piezo's voltage-charge hysteresis. Due to the existence of voltage-charge hysteresis, the DC and AC feedback will never be

perfectly matched. This mismatch results in slow transients in time, from a correctly controlled charge value in AC to an incorrectly controlled charge in DC. The transients occurs with the same time constant as the charge amplifier's voltage-to-charge-control transition time constant τ_{VQ} given by (4.3). This limitation is not a big problem for AC motion control applications, such as AFM scanners, which follow a periodic scan at a certain frequency. However, even in those cases the user must wait for the transients to die out if the scan signal has a DC component. This is one practical limitation on using a very long time constant τ_{VQ}. The problem is much worse for applications where DC position control is also of interest. Conventional V-Q charge amplifiers do not compensate hysteresis in DC and thus open-loop position control shows inaccuracies.

One common way, which can be found in the literature, for achieving a higher accuracy in DC is using an inverse hysteresis compensator, where an inverse hysteresis model of the piezo is implemented and is used to soft-linearize the piezo [39][27][16][58][48]. A path-deterministic hysteresis model is used in [39] which does not model the non-local memory of hysteresis. Ge and Jouaneh [27] use an inverse Preisach hysteresis model to compensate for hysteresis. Croft et al. use an inverted Preisach hysteresis model to compensate for hysteresis. They use separate inverse models to compensate for the vibration modes and creep. Mokaberi and Requicha [58] use an inverse Prandtl-Ishlinskii model to compensate for hysteresis and creep. The Prantl-Ishlinskii model can include both creep and hysteresis and has a unique analytical inverse. Lee et al. [48] use an inverse Maxwell resistive capacitor hysteresis (MRC) model, which is a special case of the Prisach model [48]. The effectiveness of the inverse hysteresis models depends on the accuracy of the hysteresis model. Obtaining an accurate hysteresis model over a wide frequency band and accurately calculating the inverse in real-time is difficult. Any inaccuracy in the inverse hysteresis model can appear as motion control error.

We have developed an alternative hysteresis compensation method, which combines the advantages of both charge-control and inverse hysteresis compensation. Charge control is a simple and effective way of eliminating hysteresis at all frequen-

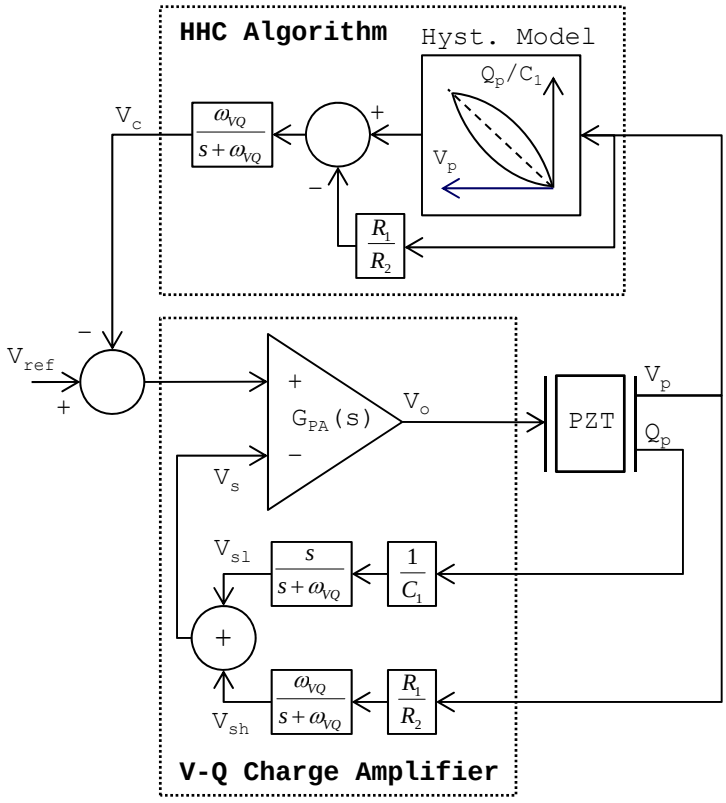

Figure 4-17: Block diagram showing the charge amplifier, piezoelectric device, and the hybrid hysteresis compensation algorithm.

cies except for quasi-static frequencies. We propose using an inverse hysteresis model of the piezo to compensate for the amplifier's hysteresis over quasi-static frequencies only. In this way, the charge amplifier's effectiveness at high frequencies is not affected by any inaccuracy of the hysteresis model. At the same time, an accurate hysteresis model can be developed over the limited quasi-static frequency range. Since the compensation is active at low frequencies, it does not require a fast sampling rate and is easier to calculate in real-time. We have developed a configuration where this partial inverse hysteresis compensation technique can be applied to any existing charge amplifier.

The block diagram in Figure 4-17 shows a V-Q amplifier driving the piezoelectric device while utilizing the hysteresis compensation algorithm. The naming convention for this diagram are consistent with the schematic diagram oft he V-Q amplifier shown in Figure 4-7. The charge amplifier actively changes the voltage (V_p) applied

to the piezo such that the feedback voltage (V_s) follows the reference voltage (V_{ref}). The feedback voltage (V_s) is an estimate of the piezo charge (Q_p) calculated by a complementary filter pair based on the piezo charge (Q_p) at high frequencies and the piezo voltage (V_p) at quasi-static frequencies. Assuming stable operation of the amplifier, the feedback voltage (V_s) can be related to the piezo voltage (V_p) as

$$\frac{V_s(s)}{V_p(s)} = \frac{R_1}{R_2}\frac{R_2C_ps+1}{R_1C_1s+1}.$$

The resulting transfer function can be divided into low-pass and high-pass transfer functions as

$$\frac{V_s(s)}{V_p(s)} = \frac{R_1}{R_2}\frac{1/R_1C_1}{s+1/R_1C_1} + \frac{C_p}{C_1}\frac{s}{s+1/R_1C_1}.$$

The equation above can be rewritten to relate the feedback voltage (V_s) to the piezo voltage (V_p) and charge (Q_p) as

$$\begin{aligned} V_s(s) &= \frac{R_1}{R_2}\frac{\omega_{vq}}{s+\omega_{vq}}V_p(s) + \frac{C_p}{C_1}\frac{s}{s+\omega_{vq}}V_p(s) \\ &= \underbrace{\frac{R_1}{C_pR_2}\frac{\omega_{vq}}{s+\omega_{vq}}C_pV_p(s)}_{V_{sl}} + \underbrace{\frac{1}{C_1}\frac{s}{s+\omega_{vq}}Q_p(s)}_{V_{sh}}, \end{aligned} \tag{4.15}$$

where ω_{V-Q} is the voltage-to-charge control transition frequency and is given as $\omega_{V-Q} = 1/R_1C_1$. As can be seen, the feedback voltage (V_s) is calculated using a actual charge measurement (Q_p) at high frequencies and an estimate of charge, which is given by piezo voltage multiplied by an estimate of the piezo the capacitance (C_pV_p). As a result, conventional charge amplifiers cannot eliminate hysteresis over low frequencies. This results in errors and slow time transients which are problematic, specially when quasi-static motion control is required. We solve this problem by modifying the feedback voltage to include a closer estimate of the charge over quasi-static frequencies. The compensation algorithm achieves this without requiring any modification to the charge amplifier hardware. As shown in Figure 4-17, we use an inverse hysteresis model to estimate charge based on the piezo voltage (V_p). We

use the charge estimate ($\hat{Q}_p$) to replace the low-frequency portion of the feedback voltage (V_{fl}). We implement this by injecting the difference of the two ($V_{fl} - \hat{Q}_p$)) at the charge reference (V_{ref}) terminal. To match the frequency content, we filter this difference using a low-pass-filter equivalent to the low-pass-filter of the amplifier's complimentary filter pair. In this way, the amplifier controls charge based on an almost hysteresis-free estimate of charge at low frequencies as well and thus can eliminate hysteresis at low frequencies.

The application of the low-pass filter to the hysteresis model's output makes it much easier to calculate the compensator's output in real-time. The low-pass filter's bandwidth is typically between 0.1-1 Hz; therefore, the compensator's sampling rate does not need to be any faster than 100 Hz, which is very easy to obtain in practice. Any high-frequency numerical computation noise will be filtered by the low-pass filter. Finally, any inaccuracy of the inverse hysteresis model does not affect the charge amplifier's satisfactory performance at eliminating hysteresis at higher frequencies. The general idea is to compensate the charge amplifier's feedback over only the frequencies where inaccuracies exist. The implementation, which is shown in Figure 4-17, is an effective and simple way of integrating this algorithm with any existing charge amplifier without requiring any modification to the hardware. With a small modification in software, hysteresis can be eliminated at both high and quasi-static frequencies. The experimental results in Section 4.6 show the effectiveness of this method at eliminating hysteresis over quasi-static frequencies.

We use a Maxwell slip model for predicting the hysteresis between the piezo's voltage and charge. Such a hysteresis model was first developed by James C. Maxwell in 1800's [30]. As shown in Figure 4-18, Maxwell's slip model consists of n blocks carrying a load (F) in parallel with different force limits (F_i) and through connections with different stiffness (k_i). The model captures how the friction load is carried by surface asperities whose stiffness and load limits are different. The Maxwell's slip hysteresis model can be fitted to the experimental data more closely if more elements are used. Lazan [47] formulates the model with the number of elements approaching infinity [30]. The Maxwell slip model can be used to model hysteresis in other domains

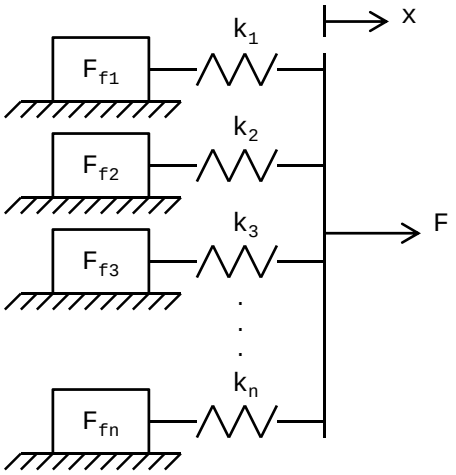

Figure 4-18: Schematic diagram of the Maxwell slip model with n elements with stiffness k_i and force limit F_i, where i is an integer from 1 to n. The model simulates the presiding friction hysteresis between force (F) and the displacement (x).

besides mechanical friction. References [30], [48], and [28] have applied the Maxwell's slip model to piezoelectric actuators.

We use a Maxwell slip model with four elements to model the hysteresis between the voltage and charge of our piezo actuator. Figure 4-19 shows the model fitted to the experimental data. The hysteresis model's parameters are provided in table 4.1. To experimentally fit the hysteresis model, charge must be measured versus voltage. Although no direct measurement of charge is available, the feedback voltage is dominated by charge at frequencies above the amplifier's V-Q transition frequency (ω_{VQ}). To obtain the experimental hysteresis data, we excite the piezoelectric actuator using a sinusoidal excitation between 0V to 100V at 50Hz, which is 50 times higher than the charge amplifier's ω_{VQ} frequency of 1 Hz. Using a significantly higher frequency can introduce errors resulting from the Q-V transition frequency, limited measurement bandwidth, and dynamic vibration modes.

We implement the hybrid hysteresis compensation (HHC) algorithm in real-time on a dSpace controller at a 20-kHz sampling rate. The experimental results in Section 4.6 show the effectiveness of this method at eliminating hysteresis at low frequencies.

Index (i)	Stiffness (k_i) [V/C]	Force Limit (F_i) [V]
1	0.114	2
2	0.054	2
3	0.092	2.4
4	0.675	∞

Table 4.1: Stiffness and force limit values for modeling the hysteresis between the voltage and charge of our piezoelectric actuator.

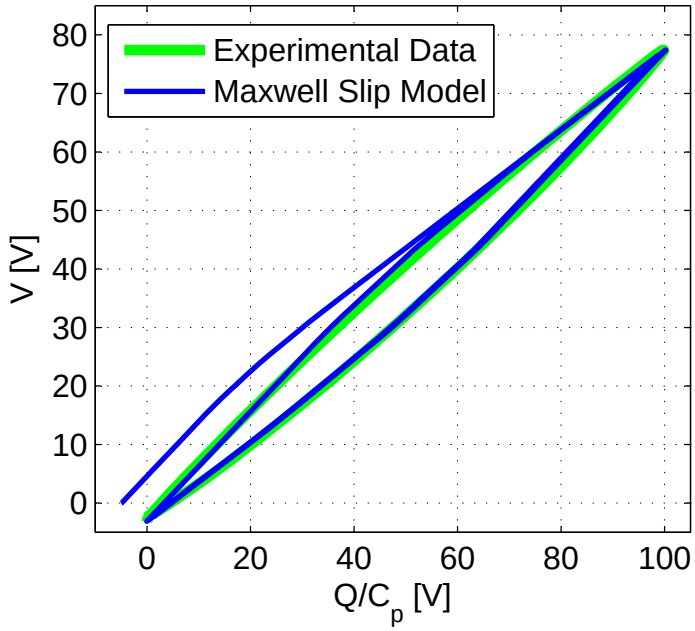

Figure 4-19: Experimental voltage-charge hysteresis of our piezo actuator and the fitted Maxwell's slip model.

4.6 Experimental Results

In this section, we present experimental data demonstrating the performance of the V-Q-V charge amplifier and the hybrid hysteresis compensation algorithm. We test the charge amplifier with a 10-Hz sinusoidal reference signal changing from 0 V to 80 V for 10 cycles. The reference signal contains a 40-V quasi-static offset and a $\pm 40V$ 10-Hz sinusoidal signal. In this way the charge amplifier is tested over both quasi-static and high frequencies. We use the same reference signal to drive the amplifier in voltage (V) control mode, voltage-charge-voltage (V-Q-V) control mode, and V-Q-V control mode with hybrid hysteresis compensation (HHC). The time plot of the experimental data for this test is shown in Figure 4-20. The experimental data is viewed as an XY plot of the strain versus reference voltage in Figure 4-21. As can be seen in Figure 4-21, the resulting hysteresis with voltage control is approximately 20%. Voltage-Charge-Voltage (VQV) control reduces the per cycle hysteresis to approximately 5%, but a slow transient exists which results in an offset drift of more than 15% of the full-scale strain range. Applying the HHC algorithm, the per-cycle hysteresis is reduced to 2% and the time-transient drift is reduced to 2%. The improvement is a result of eliminating hysteresis in quasi-static frequencies, and matching the feedback gains for high-frequencies and quasi-static frequencies. The results could be improved further by using a more accurate hysteresis model.

4.7 Magnetic Analogue

Magnetic actuators have non-linearities resulting from the hysteresis between magnetic field and magnetic flux density within their magnetically permeable core. In analogy to charge control of piezoelectric devices, magnetic flux control of magnetic actuators can improve their linearities and eliminate the effect of hysteresis. In this section, we present a method for controlling magnetic-flux and demonstrate that magnetic flux control can significantly improve an electromagnetic actuator's linearity.

One common way of linearizing the quadratic current-to-force relation of magnetic

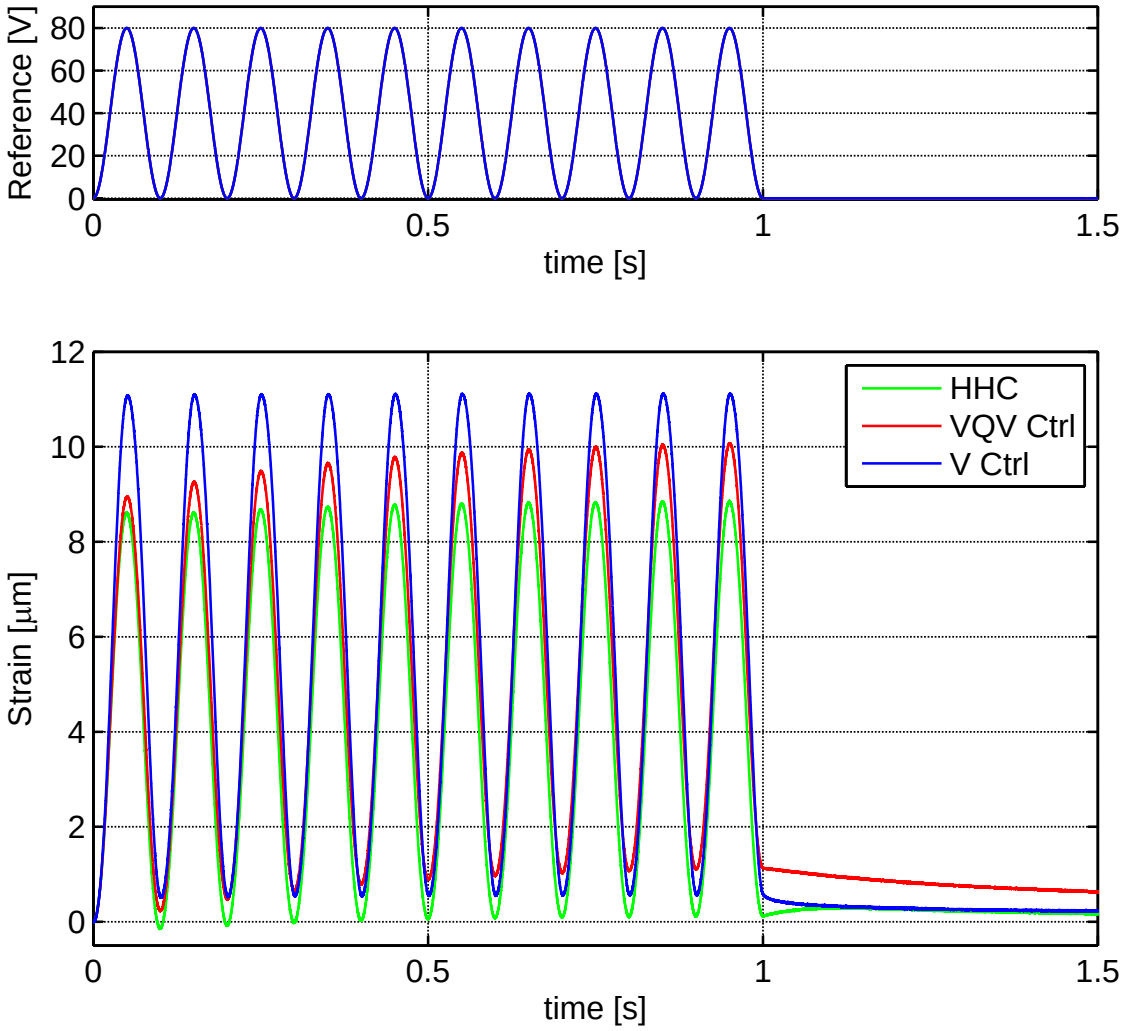

Figure 4-20: Time plot of piezo's strain in response to 10-Hz 0 to 80 V sinusoidal reference signal using the power amplifier in voltage control mode (V Ctrl), voltage-charge-voltage control mode (VQV Ctrl), and VQV control mode with hybrid hysteresis compensation (HHC).

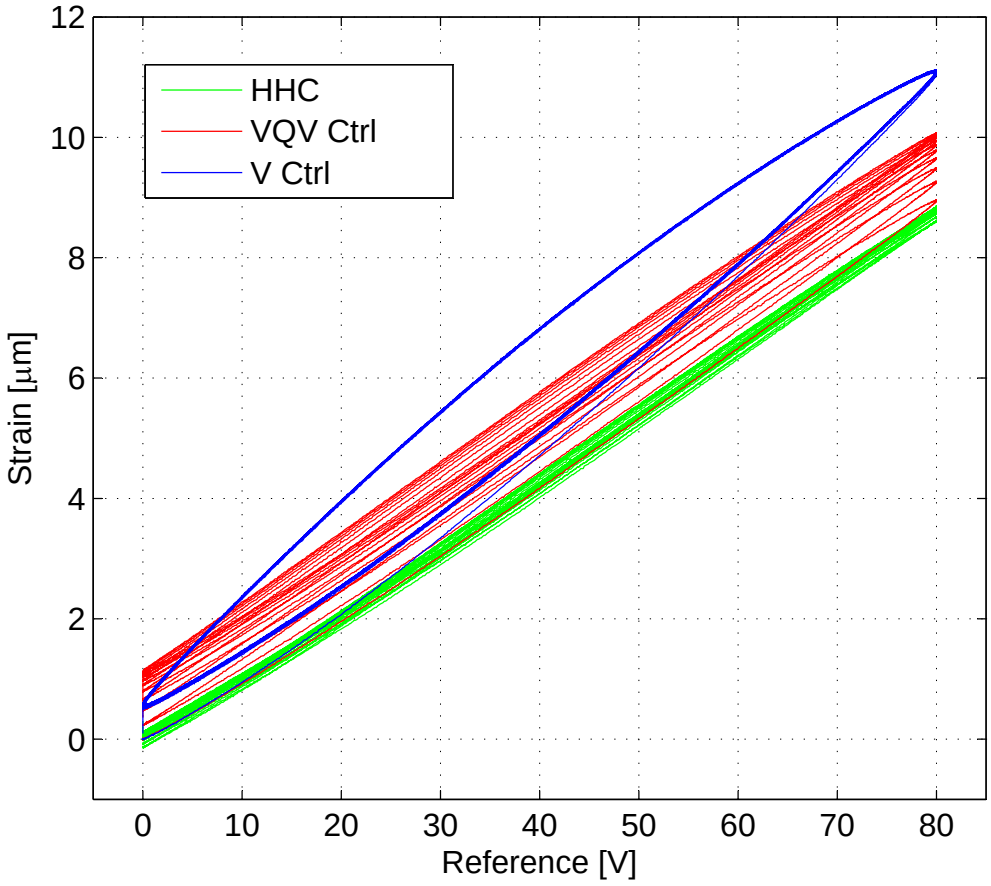

Figure 4-21: XY plot of the piezo's strain versus a 10-Hz 0 to 80 V sinusoidal reference signal using the power amplifier in voltage (V Ctrl) control mode, voltage-charge-voltage (VQV Ctrl) control mode, and VQV control mode with hybrid hysteresis compensation (HHC).

bearings is bias current linearization [54]. This method requires symmetric operation around a bias current. Bias current linearization also does not compensate for the hysteresis in the actuator core. Direct control of flux addresses this problem. Groom has patented a magnetic actuator, which uses permanent magnet bias linearization and flux feedback [31]. The invention uses Hall effect sensors to measure flux. In this work, we implement magnetic flux control without the use of Hall-effect sensors. We estimate the magnetic flux using a sense coil. By eliminating the sensor, the minimum air gap is no longer limited by the thickness of the Hall effect sensor. Also unlike a Hall sensor, a sense coil is not sensitive to the changes in temperature.

Normal-flux electromagnetic actuators (such as reluctance actuators) can achieve a high force-density. However, they have non-linear input-output constitutive equations and have additional non-linearities resulting from hysteresis. As a result, such actuators are difficult to use for precision applications. The motivation behind the work presented in this section is to develop control techniques for precisely controlling the output force of such actuators over a range of changing gaps. We achieve this by using an internal magnetic-flux control loop. We use lookup tables, based on experimental calibration data, to determine the magnetic flux reference resulting in the desired output force. We have designed and implemented a setup for experimental testing of our control methods, as shown in Figure 4-22. We have experimentally demonstrated successful magnetic flux control, force control, and position control. The work presented in this section is in collaboration with Ross I. MacKenzie, who is a PhD candidate in our lab, and has also been supported by ASML.

4.7.1 Experimental Setup

The assembled experimental setup for this work is shown in Figure 4-22. A solid model of the experimental setup is shown in Figure 4-23. In this solid model a Lorentz actuator replaces one of the reluctance actuators. We use the setup for researching the linearization of the normal-flux reluctance actuators through magnetic-flux control, and utilizing them for precision motion control. The setup consists of a linear airbearing driven by two actuators. The reluctance actuators can only generate a

pulling force; therefore, we use one on each side to enable generating forces in both directions. For testing and comparison purposes, it is possible to replace one of the actuators with a linear voice coil actuator, as shown in the CAD model of Figure 4-23. We use a linear BH20 Sony encoder head [79] with a 7-mm BE10 linear scale [78] and a BD96-B1100HC interpolator [77] to measure the linear motion of the airbearing with 0.25nm resolution. A more detailed view of the encoder assembly is shown in the CAD model of Figure 4-24. Each actuator is connected to its mounting bracket through three load cells. In this way, the actuator forces are transferred to the stationary frame through the load cells and can be measured by them. We use Kistler 9212 load cells[42], which primarily measure compressive forces. The load cells have two threaded holes at their ends. We use a bolt, which passes through the centroid of the triangle made by the load cells, to preload the load cells in compression. We use Belleville washers to increase the compliance of the preload mechanism, which facilitates precise adjustment of the preload force. We set the preload by tightening the bolt and monitoring the load cell signals. We use a Kistler 5010 charge amplifier[43] to measure the load cells' charge output. We connect the output of the load cells on each side in parallel and thus can use a single charge amplifier for each side to measure their added output charge. In this way the resulting equivalent load cell constant is the average of the three load cells' force to charge constants. We use linear voltage power amplifiers to drive the actuators. The amplifiers use Apex PA12 power devices [10].

The experimental setup's system diagram is shown in Figure 4-25. We use a dSpace DS1103 controller board. The Sony BH20 encoder's output signals are buffered and interpolated by a Sony BH1100HC box to provide a resolution of 0.25nm per interpolated count. For every sample time, the encoder's dSapce driver requests a position measurement update right after the controller is sampled. In this way, the measurement is sampled at the exact same frequency as the control frequency, and aliasing due to non-integer multiple sampling rate mismatch is avoided. We measure the rate of change of the magnetic flux in the air gap linked by the sense coil ($d\lambda/dt$), the current passing through the actuator winding (I_s), and the force measured by the

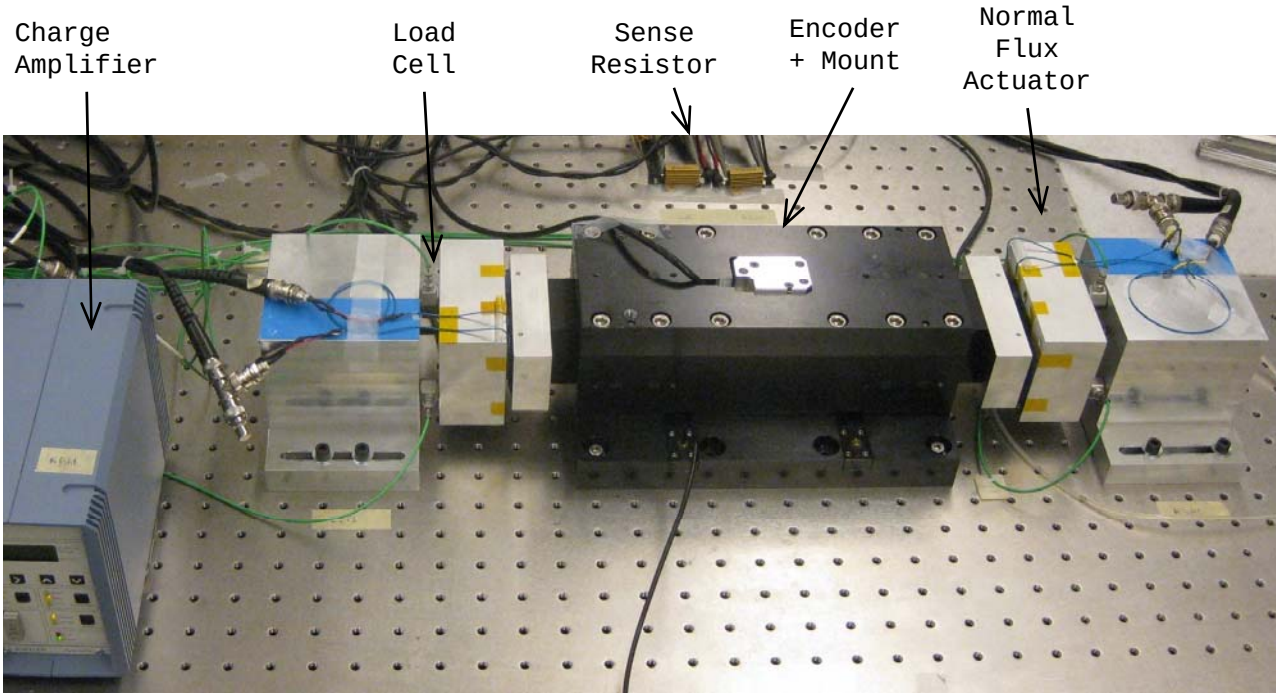

Figure 4-22: Assembled experimental setup used for researching soft-linearization of normal flux actuators through magnetic-flux control.

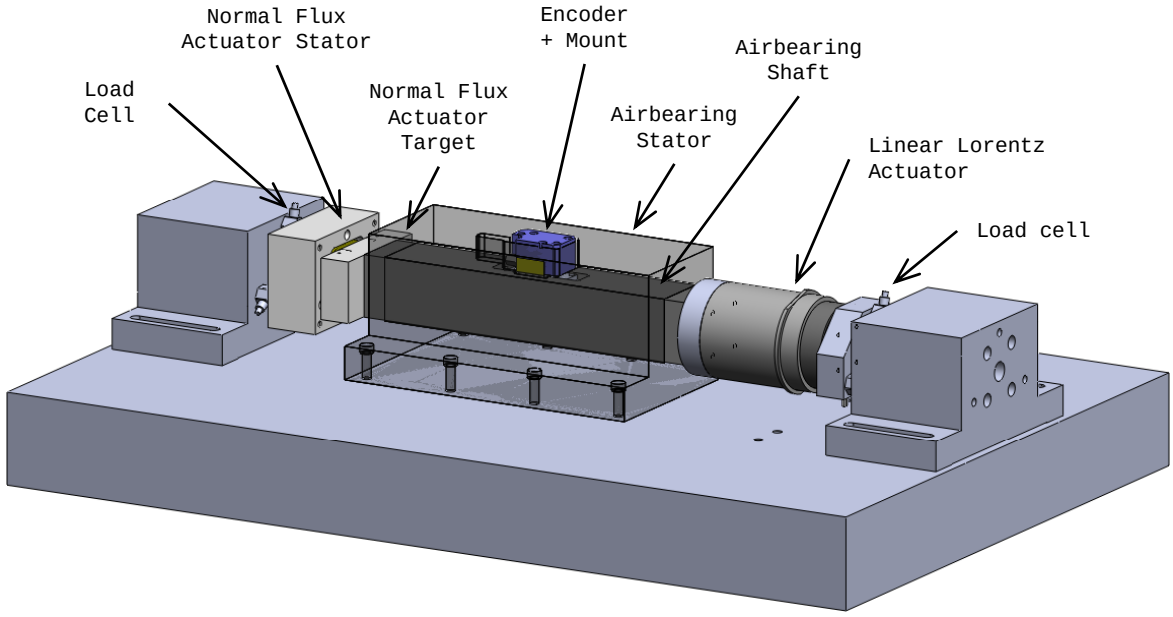

Figure 4-23: CAD model of the experimental setup used for researching soft-linearization of normal-flux reluctance actuators.

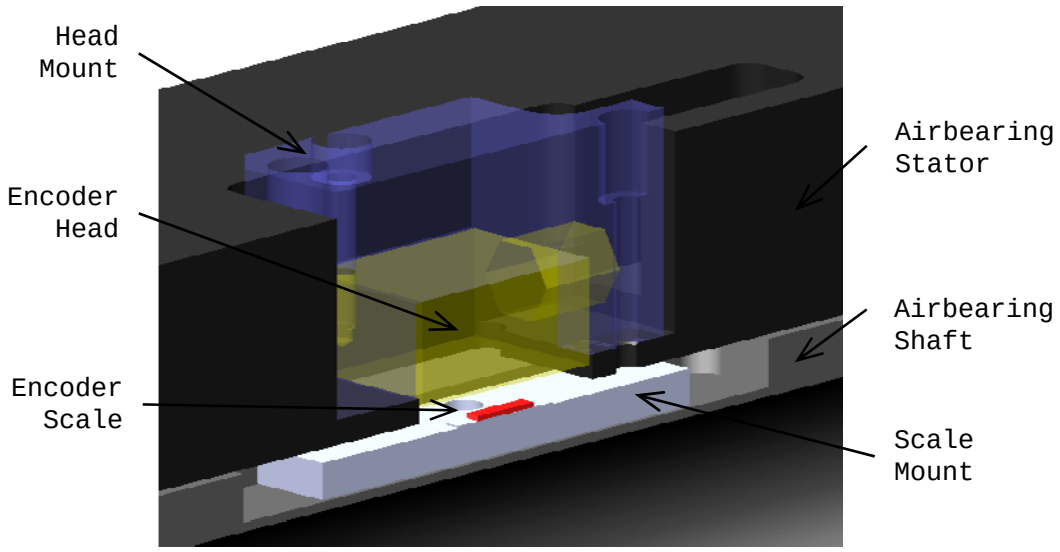

Figure 4-24: CAD Model showing a closer view of the encoder assembly

load cells (F). These signals are amplified and low-pass filtered by Tektronix AM502 differential amplifiers[81].

The magnetic actuator's design is shown in Figure 4-26. The actuator's stator consists of two adjacent U-cores with a 280-turn coil wrapped around their contacting legs. The actuator's mover consists of an I-core. The cores are SuperPerm49 with 0.1-mm thick lamination and 90% fill-factor [51].

4.7.2 Magnetic-Flux Sensing and Control

Normal-flux actuators' force output can be linearized by controlling magnetic flux. In this section, we describe how we sense and control the magnetic flux.

Sensing and Estimating Magnetic Flux

We use a sense coil wrapped on top of the actuator coil to sense the rate of change of the magnetic flux passing through the center legs. The actuator with the added sense coil is shown in Figure 4-27. The sense coil has 12 turns and is wound using a miniature coaxial cable. The voltage across the center conductor is measured as the rate of change of the magnetic flux linkage. The outer conductor is used for shielding. It is very important that the shield is connected to the ground only on the side where

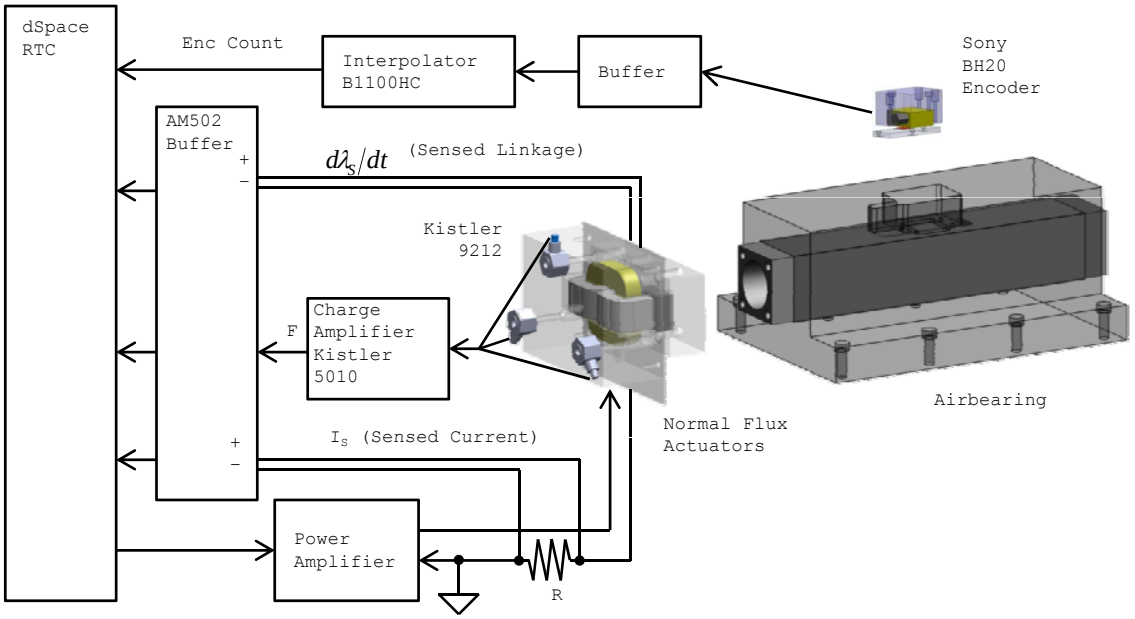

Figure 4-25: Experimental setup's system diagram.

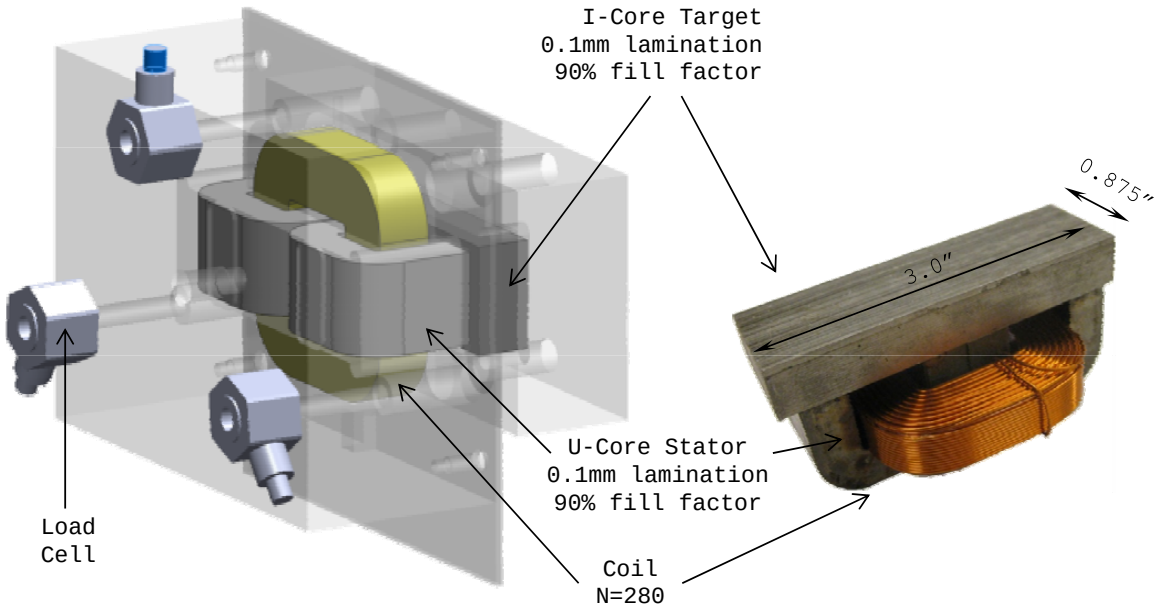

Figure 4-26: CAD model of the normal-force electromagnetic actuator (left) and the core structure of the actuator before assembly (right).

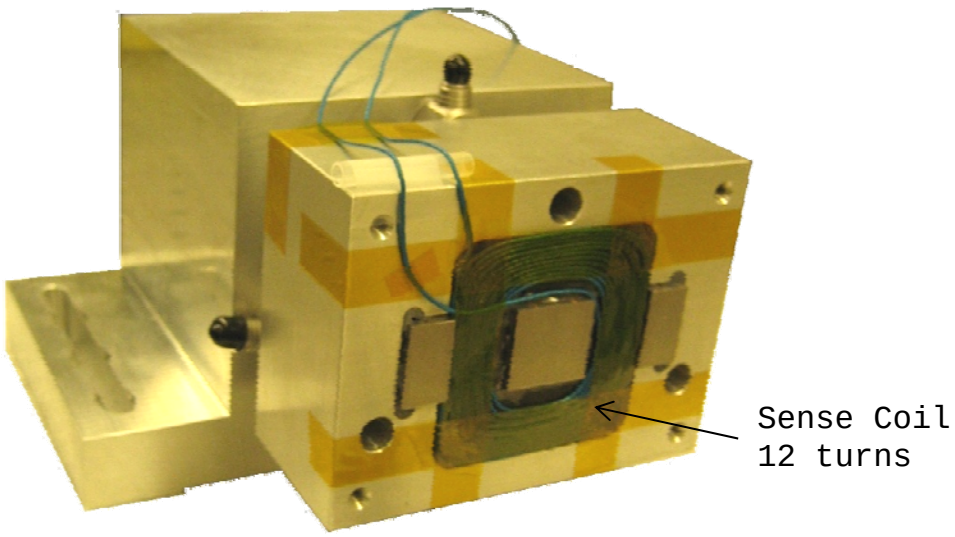

Figure 4-27: Electromagnetic normal-flux actuator with a flux sensing coil wrapped around the center pole piece using miniature coaxial shielded cable.

the center conductor is referenced to the ground. In this way, both the shield and the center conductor will have the same voltage distribution along their length; therefore, no parasitic capacitive coupling will exist between the two of them. If the shield is connected to the ground on both sides, the shield and the center conductor will have a voltage difference. Also, changing flux would induce current through the shield which will oppose the magnetic field. That is, we do not want to create a shorted transformer turn by grounding both ends.

For simplifying our analysis, we measure and control the magnetic flux linked by the sense coil, which is proportional to an average of the magnetic flux in the air gap (g). The block diagram of the flux estimation algorithm is shown in Figure 4-28. We estimate the flux by integrating the rate of change of flux ($d\lambda_S/dt$). To avoid integrator drift, we high-pass filter (HPF) the flux estimate from the sense coil. This will give us an estimate of flux at high frequencies (λ_{HF}). We estimate the flux at low frequencies (λ_{LF}) using the current passing through the actuator coil. The flux linkage can be estimated as the mutual inductance between the actuator coil and the sense coil (L_M) times the actuator coil current (I). We filter the low-frequency estimate (λ_{LF}) using a low-pass filter (LPF) complementary to the high-pass filter (HPF).

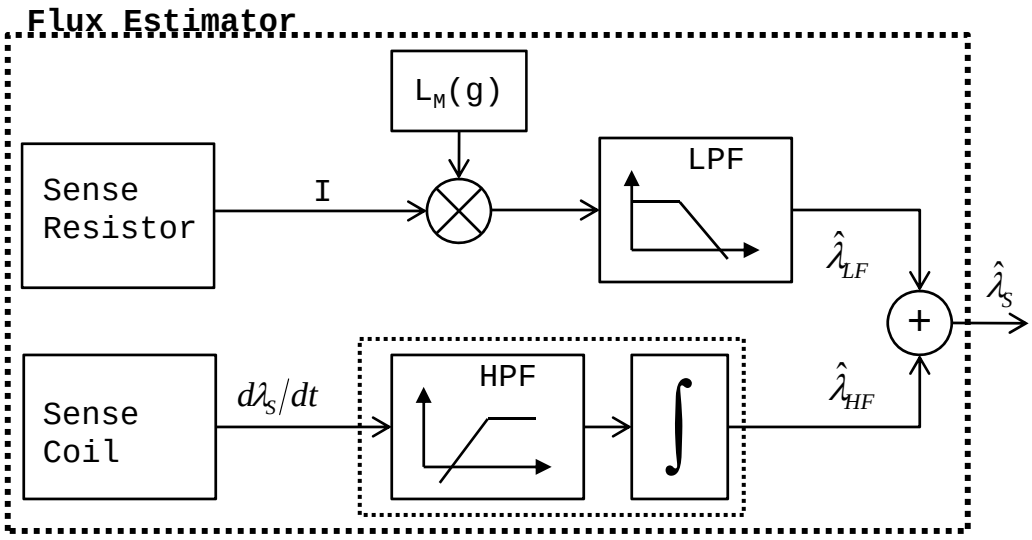

Figure 4-28: Block diagram of the flux estimation algorithm

The actuator's inductance changes with the air gap (g). We measure the inductance at different gap sizes and build a look-up-table (LUT) for estimating the inductance (L_m). At each gap size, we excite the coil using a sinusoidal current at a frequency high enough so that it can be detected by the sense coil. We estimate the mutual inductance as the slope of the line fitted to the plot of the magnetic flux linkage versus the current coil current. Figure 4-29 shows the experimentally measured mutual inductance of the actuator and the sense coil (L_m) measured at different air gap sizes for the actuators on the right and the left sides.

We combine the estimates of flux for high and low frequencies using a complementary filter pair (HPF and LPF). The complimentary filter pair is given as

$$LPF(s) = \frac{1}{(s/\omega_f p + 1)^2} \tag{4.16}$$

$$HPF(s) = 1 - LPF(s), \tag{4.17}$$

where $\omega_f p$ is the filter pair break frequency and is given as $\omega_f p = 2\pi$ rad/s. In this way, while the filters are used to assign each estimate to a certain frequency range, the two estimates complement each other to have an overall gain of one over all frequencies. In this work we use a second order complementary filter pair. In this way, the integrated flux-rate measurement offset does not propagate to the flux

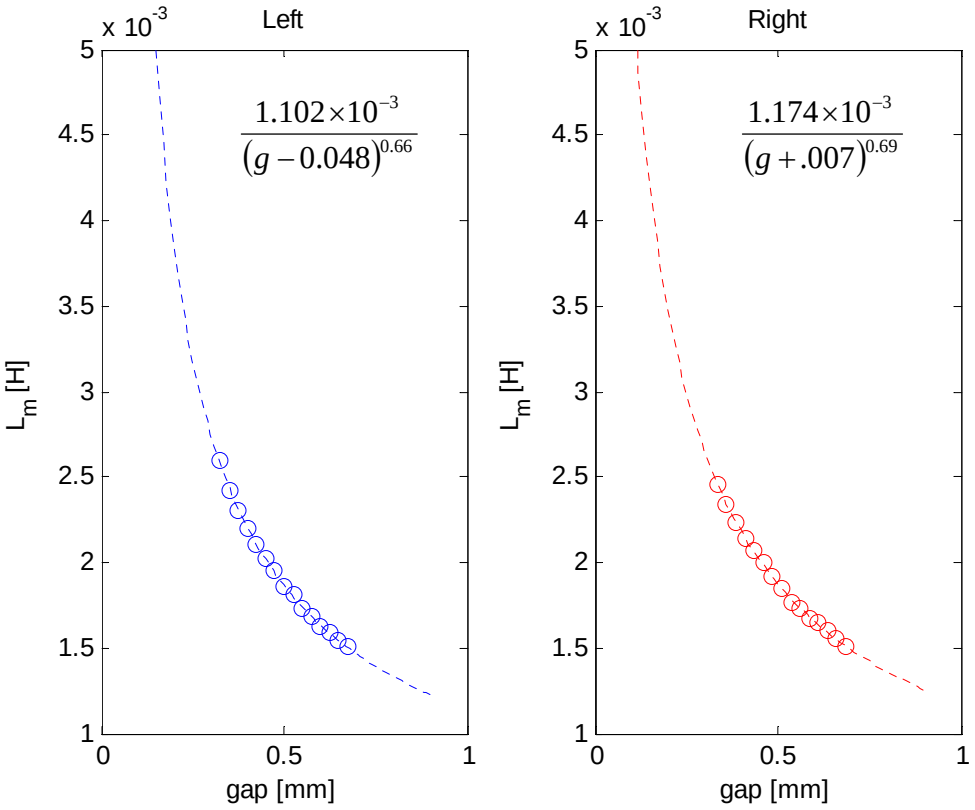

Figure 4-29: Experimentally measured mutual inductance of the actuator and sense coils (L_m) measured as a function of air gap for the actuators on the right and the left sides.

estimate ($\hat{\lambda}_s$).

Controlling Magnetic Flux

We use the magnetic flux estimator's feedback to control flux in closed-loop. The plant being controlled can be modeled as a resistor and an inductor, whose inductance changes with the size of the air gap (g). The magnetic linkage can be related to the electric voltage and current as

$$V = RI + d\lambda/dt,$$

where V, I, λ, and R are the stator coil's voltage, current, flux linkage, and resistance, respectively[55]. To include the effect of the actuator air gap, we define the magnetic flux linkage as

$$\lambda = L(g)I,$$

where L(g) is the inductance of the actuator as a function of the air gap. The inductance L(g) can be calculated as

$$L(g) = N_A^2 \frac{A\mu}{g}.$$

μ is the permeability of the magnetic core, g is the air gap, and A is the area of a single leg of the U-core. The variations in the gap and their effect on the magnetic flux are considered as a disturbance and are rejected by the flux controller. The sense coil acts as a transformer with a turn ratio of $N_S : N_A$; therefore, the sensed flux λ_S is scaled as $\lambda_S = \lambda \times N_s/N_A$, where N_A and N_S are the actuator and sense coil windings' number of turns respectively. A block diagram of the flux control system is shown in Figure 4-30. The flux estimator was described in Subsection 4.7.2 and is assumed to be a constant gain of one for control design purposes. The plant's transfer

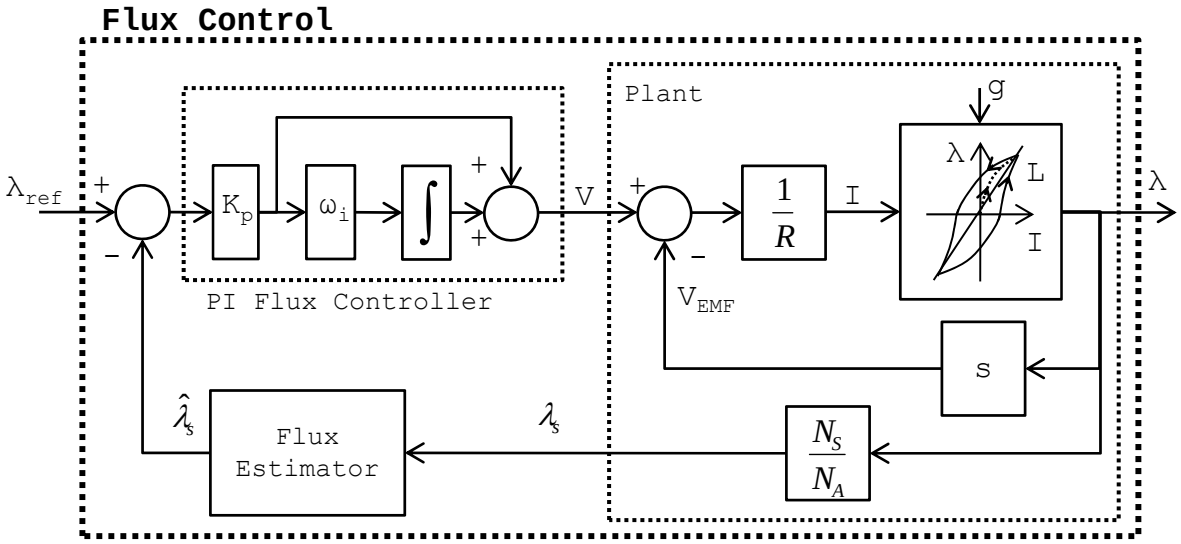

Figure 4-30: Block diagram of the flux control system

function can be derived from the block diagram as

$$\frac{\lambda_S(s)}{V(s)} = \frac{L(g)}{L(g)s + R}\frac{N_S}{N_A}. \tag{4.18}$$

The plant transfer function $\lambda_S(s)/V(s)$ given by (4.18) is changing with gap. The transfer function has a break frequency $\omega_b = R/L(g)$. Well above this frequency, the actuator's inductive impedance is much larger than its resistive impedance, and thus the resistance R in the denominator of the transfer function can be neglected. Well below the break frequency ω_b, the resistance is significantly larger than the inductive impedance, and thus the inductive impedance in the denominator can neglected. The transfer function can be approximated over each range as the following:

$$\frac{\lambda_S(s)}{V(s)} \simeq \begin{cases} \frac{L(g)}{R}\frac{N_S}{N_A} & \omega \ll \omega_b \quad \text{resistance dominant} \\ \frac{1}{s}\frac{N_S}{N_A} & \omega \gg \omega_b \quad \text{inductance dominant} \end{cases} \tag{4.19}$$

As can be seen, the plant transfer function is independent of the changes in the inductance for frequencies larger than ω_b. The experimental frequency responses of the plant ($\lambda_S(s)V(s)$) at different air gaps is shown in Figure 4-31 for the actuators on the right and the left sides. Our targeted crossover frequency is significantly larger than the possible values of ω_b. As a result, the frequency response at the crossover is

not affected by the changes in the inductance. Therefore, we can design the controller for a specific bandwidth and ensure stability independent of the variations of the inductance resulting from the changes in the air gap. We use a proportional-integral control law. The integral term is active up to the frequency (ω_i), which is chosen to be a tenth of the crossover frequency (ω_c). In this way, the integrator phase lag at the cross-over is negligible. The flux controller transfer function is given as

$$C_\lambda(s) = K_p \frac{\omega_i + s}{s},$$

where $1/K_p = |\lambda_S(s = j\omega_c)/V(s = j\omega_c)|$ and $\omega_i = \omega_c/10$.

The experimental frequency response of the compensated loop transmission ratio is shown in Figure 4-32 using the same controller at different air gaps for the actuators on the right and the left sides. As can be seen, a fixed control law can achieve a unity cross-over frequency of 1 kHz and 85 degrees of phase margin at the different air gaps. We used a low cross-over frequency of 1 kHz, so that the controller can be implemented on the dSpace controller. It is possible to achieve a much higher cross-over frequency if the controller is implemented using analog electronics or an FPGA device. If a faster controller is used, the achievable cross-over frequency would be limited by the Eddy-current losses of the magnetic core.

4.7.3 Force Control

The output force of the electromagnetic actuators can be calculated using the Maxwell stress tensor [85] as

$$F = \oint_{A_a} \frac{1}{2} HBdA, \tag{4.20}$$

where H and B are the magnetic field and flux density, respectively, and A_a is the surface enclosing the volume of the actuator components on which force is evaluated. The magnetic field is zero everywhere on the actuator mover surface, except on the

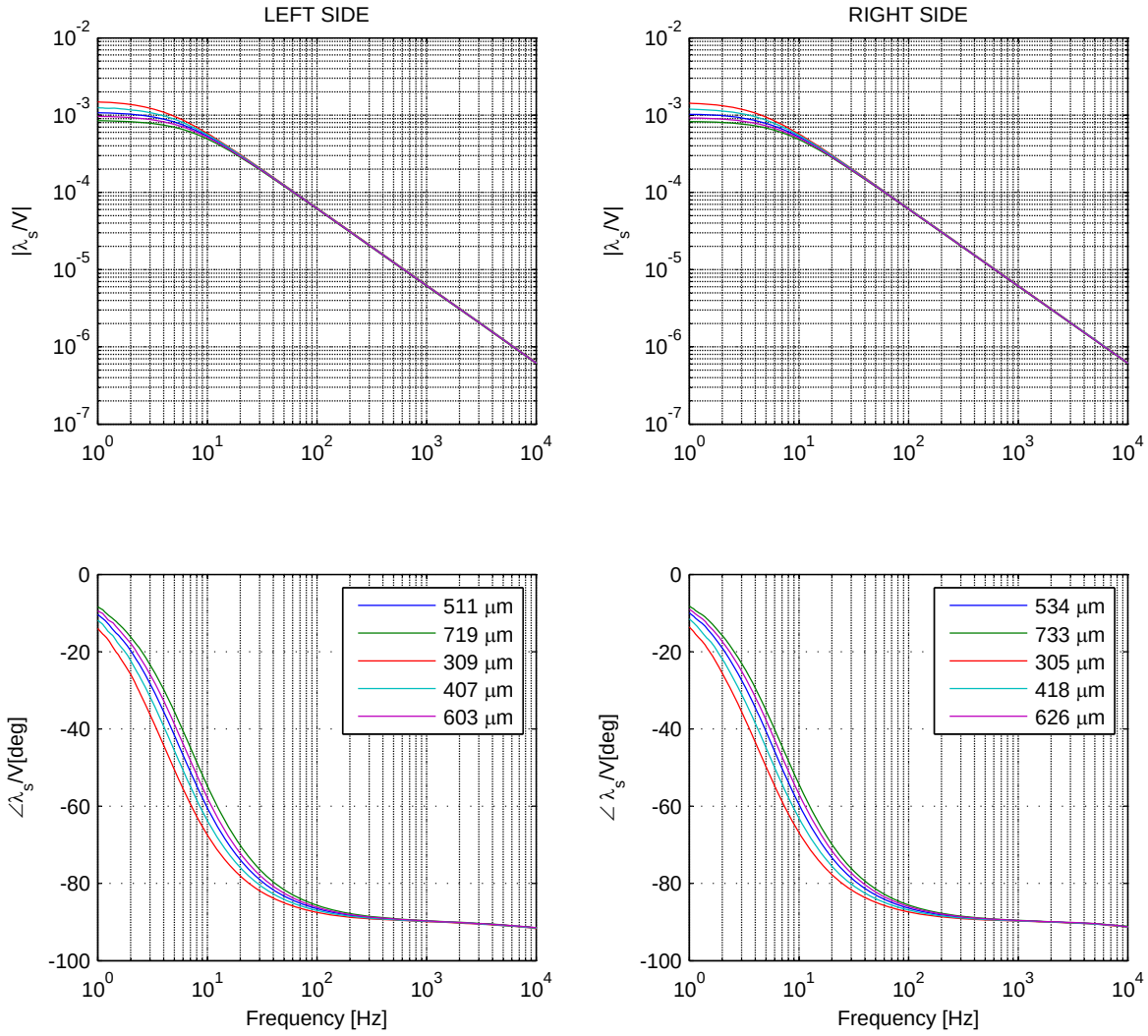

Figure 4-31: Experimental frequency responses of the flux-control plant from the applied voltage V to the sensed magnetic flux linkage λ_S is plotted at different air gaps for the actuators on the right (right) and the left (left) sides.

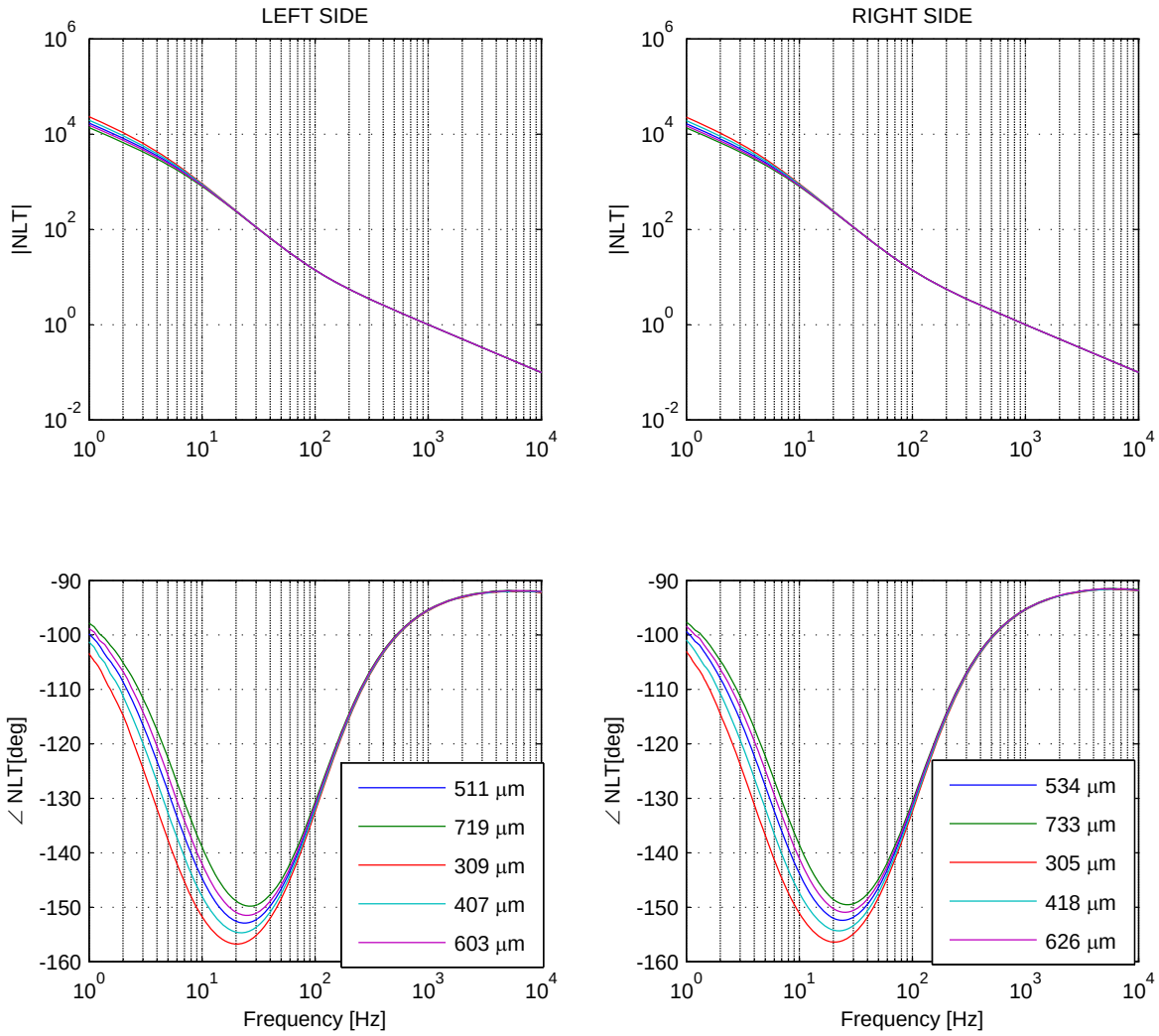

Figure 4-32: Experimental frequency responses of the compensated loop transmission for the flux linkage control system is plotted at different air gaps for the actuators on the right (right) and the left (left) sides.

face opposing the stator. Therefore, (4.20) can be simplified as

$$F = \int_{A_f} \frac{1}{2} HBdA, \tag{4.21}$$

where A_f is the area on the face of the mover opposing the stator. Air has a linear magnetic permeability very close to the magnetic permeability of vacuum (μ_o). The relationship between the magnetic field and flux in air is thus given by $B = \mu_0 H$. Equation 4.21 can be simplified by substituting for H using B:

$$F = \int_{A_f} \frac{1}{2\mu_0} B^2 dA \tag{4.22}$$

The actuator's force output is proportional to the average of the magnetic flux density squared over its face. The magnetic flux linked by the sense coil on other hand is given as

$$\lambda_S = N_S \int_{A_s} BdA, \tag{4.23}$$

where A_s is the sense coil area and is given as $A_s = A_f/2$. The flux linkage is thus proportional to the average of the magnetic flux density over the poles faces. If we assume that the magnetic flux distribution over the actuator's face is constant, the electromagnetic force would be proportional to the magnetic flux linkage squared.

However, the magnetic flux is not uniformly distributed in the air gap. Fringing fields are one main reason why the magnetic flux may have a non-constant spatial distribution. To make sure that our force control algorithm is not adversely affected by the constant-flux-distribution assumption, we construct and use a 2D look-up-table that relates the magnetic flux, force, and air gap. We calibrate the look-up-table experimentally. The calibrated force maps for the right and left actuators are shown in Figure 4-33. The same data is viewed in 2D with the use of colors in Figure 4-34. As can be seen, the force is proportional to the linkage squared for a fixed air gap. However, the proportionality constant changes slightly with the air gap. This could be due to the fringing fields growing with the air gap, which results in a wider spread

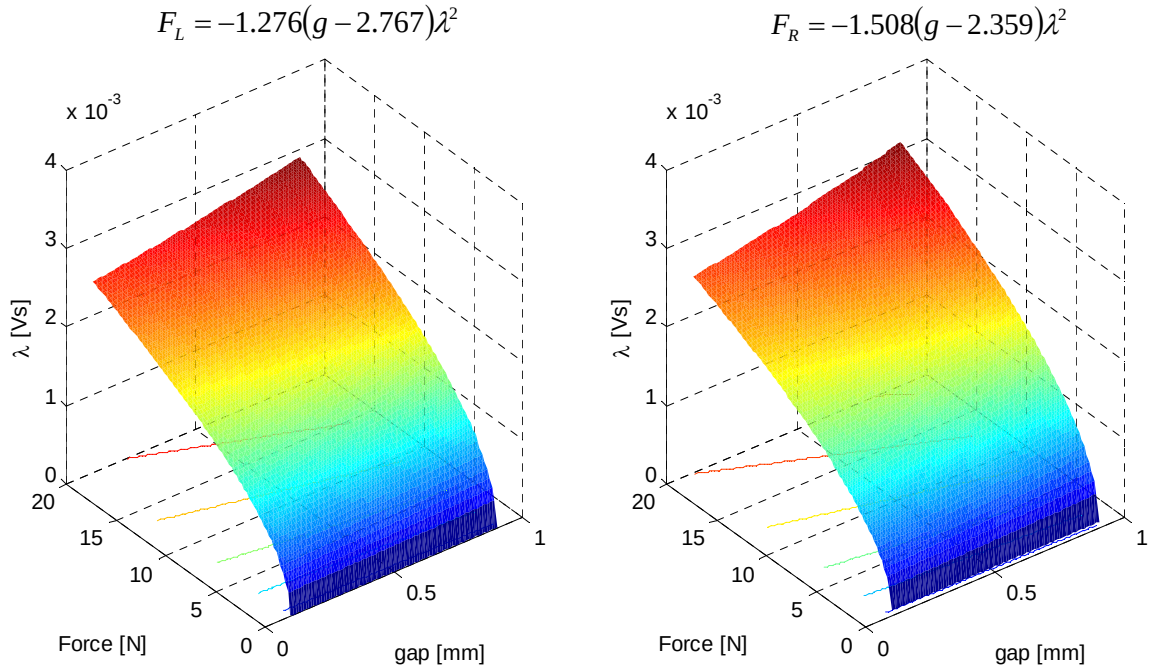

Figure 4-33: Experimentally calibrated force map of the right (right) and left (left) side actuators viewed in 3D. We use the map to find the the linkage required for generating a certain force at a given gap.

flux distribution and a lower linkage-squared to force constant relationship.

To take into account the changes resulting from the variation in the air gap, we can define the output force as $F = c(g)\lambda^2$, where $c(g)$ is a constant gain describing the variations in the flux-squared to force gain resulting from the changes in the air gap. A plot of the constant $c(g)$ versus the gap size (g) is shown in Figure 4-35. A good approximation of the correction constant c(g) can be obtained using a linear fit to the data. For our force control experiments, we calculate the required linkage as below:

$$\lambda_{ref} = \sqrt{F/c(g)} \tag{4.24}$$

where c(g) is given for each actuator by the following expressions:

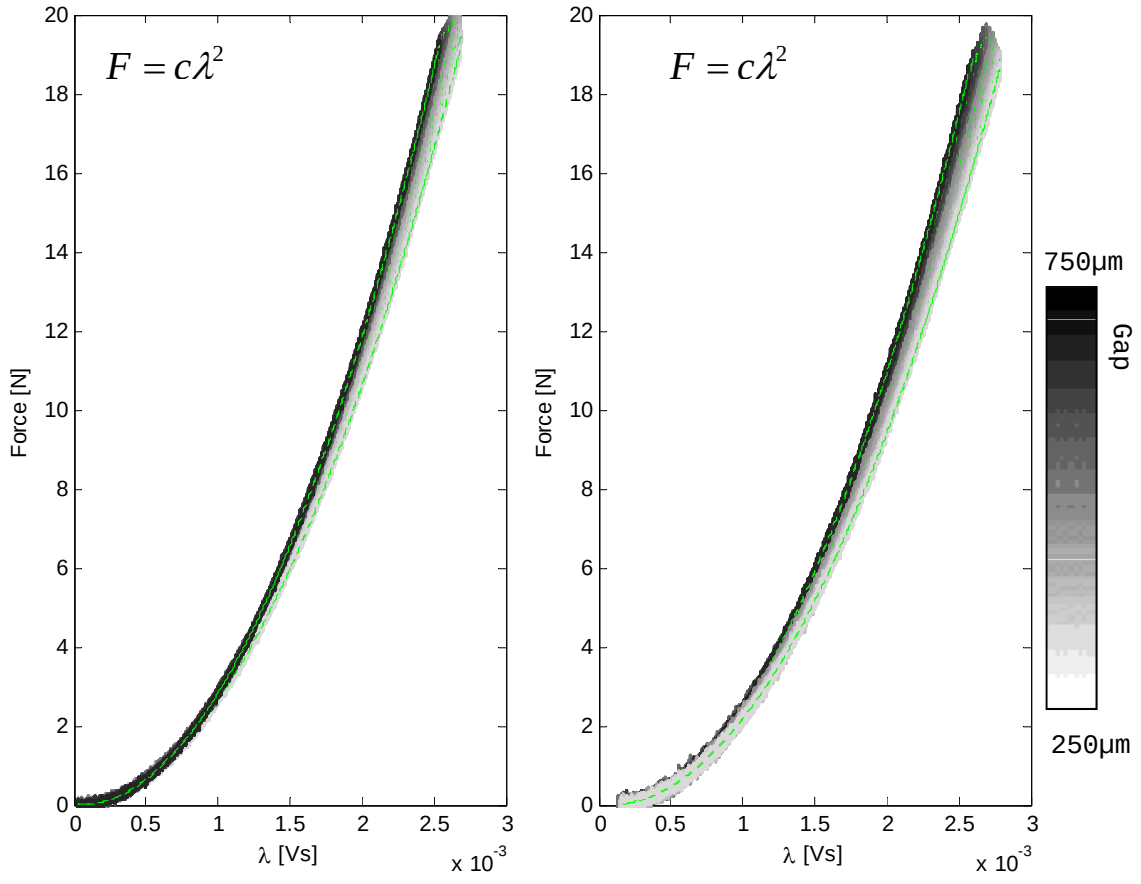

Figure 4-34: Experimentally captured plots of the force versus flux linkage at different gap sizes.

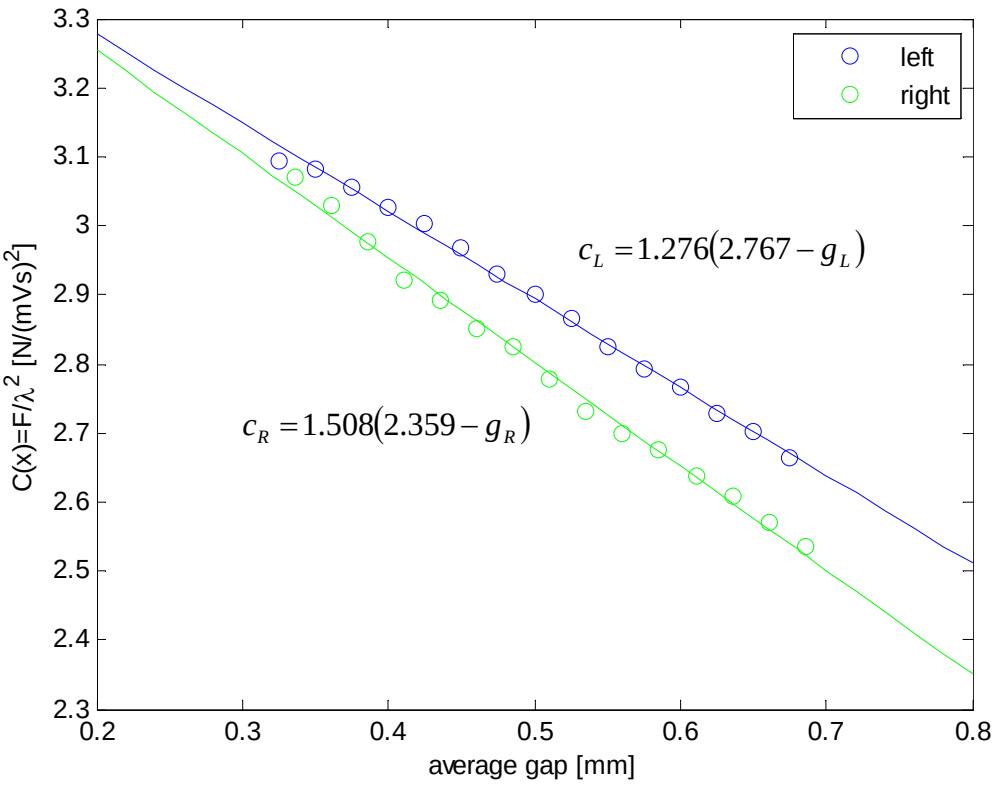

Figure 4-35: Plot of the correction constant c(g) versus the gap size (g) for the right and left actuators.

$$\begin{cases} c_L(g) = 1.276(2.767 - g_L) & \text{for left actuator} \\ c_R(g) = 1.508(2.359 - g_R) & \text{for right actuator} \end{cases} \tag{4.25}$$

The force output accuracy can be improved by using a look-up table for c(g) rather than a linear fit.

The normal-flux reluctance actuators, which we are using for this work can only exert a pulling force. We can generate bidirectional forces by using the two actuators together. The normal-flux actuators have a quadratic relationship from linkage to force. At zero force, they have a local sensitivity of zero to the changes in flux:

$$F \propto \lambda^2 \Rightarrow \frac{\partial F}{\partial \lambda}|_{F=0 \Rightarrow \lambda=0} = 0 \tag{4.26}$$

To prevent this from adversely affecting the performance of the control system,

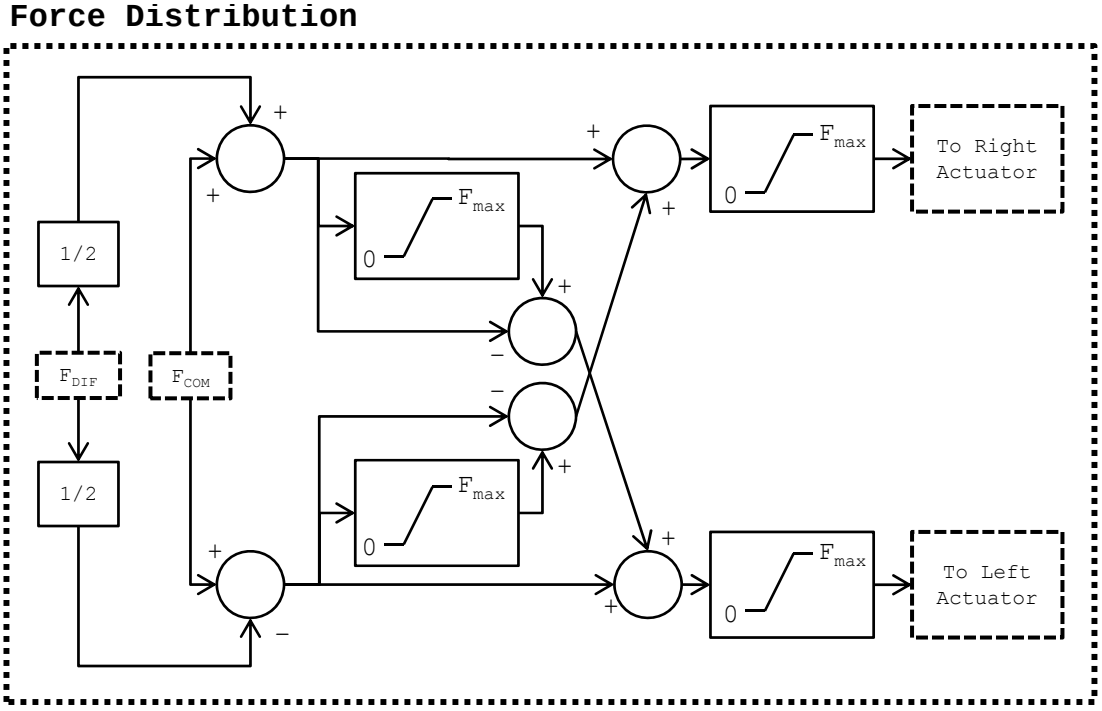

Figure 4-36: Block diagram of the force distribution subsystem. The subsystem generates a commanded bidirectional force by assigning force commands to the unidirectional actuators.

we operate the actuators around a common mode force setpoint. To create a net force around this common mode force, we add a differential force to one actuator and subtract the same differential force from the other actuator. The actuators have a maximum force output. The force distribution algorithm is shown in Figure 4-36. The algorithm generates a bidirectional force (F_{DIF}) by assigning a force commands to the unidirectional actuators. The algorithm also allows exertion of a common-mode force, with zero net force F_{COM}, on both sides of the moving assembly. The force distribution algorithm is designed, such that the assigned force of a saturated end can be carried by the other actuator. Such a situation could occur if a common mode force value other than the midpoint of the actuators force range is used.

We calibrate the actuator force maps by measuring their pulling force versus their flux linkage at different air gaps. To facilitate the experimental data collection, we use the actuators to actively control the position of the moving mass at a specific air gap. At each actively controlled air gap, we change the actuators' common mode force. At

the same time, the position controller uses the differential force to control the gap. In this way, the actuators go through a range of output forces while maintaining the air gap. We measure the output force of each actuator using its load cells and save the data along with the measured magnetic flux. For this method to work, we first need a stable position controller and a estimate of the force-map. Starting with an analytically derived approximation of the force map, we can iteratively improve its precision using this experimental method.

We use the open-loop force control algorithm to control the actuators output force. To experimentally test the effectiveness of our force control method, we use the actuators to follow a 0.2-Hz sinusoidal force profile at a gap of 0.5 mm on each side. The actuators output force is measured and is plotted against the reference force in Figure 4-37. The plotted result has a linearity of better than 0.5%. However, the accuracy is 1% for the right actuator and 5% for the left actuator. Accuracy can be improved by using an accurately calibrated look-up-table for the force correction constant c(g).

4.7.4 Position Control

We design a position controller to actively control the position of the moving mass using the encoder's position feedback. The controller commands a differential force based on the position error. A block diagram of the position control system is shown in Figure 4-38. The differential force is distributed by the force distribution algorithm between the left and the right actuators. The calibration data for the actuators is used to calculate the required flux value for generating the commanded forces. The flux controller algorithm for each actuator controls the flux to the reference flux.

The frequency responses of the position control system's plant, controller, and compensated loop transmission are shown on the Bode plot in Figure 4-39. The expected magnitude response when modeling just the airbearing mass is also plotted. The expected and experimental frequency responses of the plant match at high frequency. However, the experimental frequency response at low frequency resembles a stiffness element. We are using an airbearing which ideally should be free of static

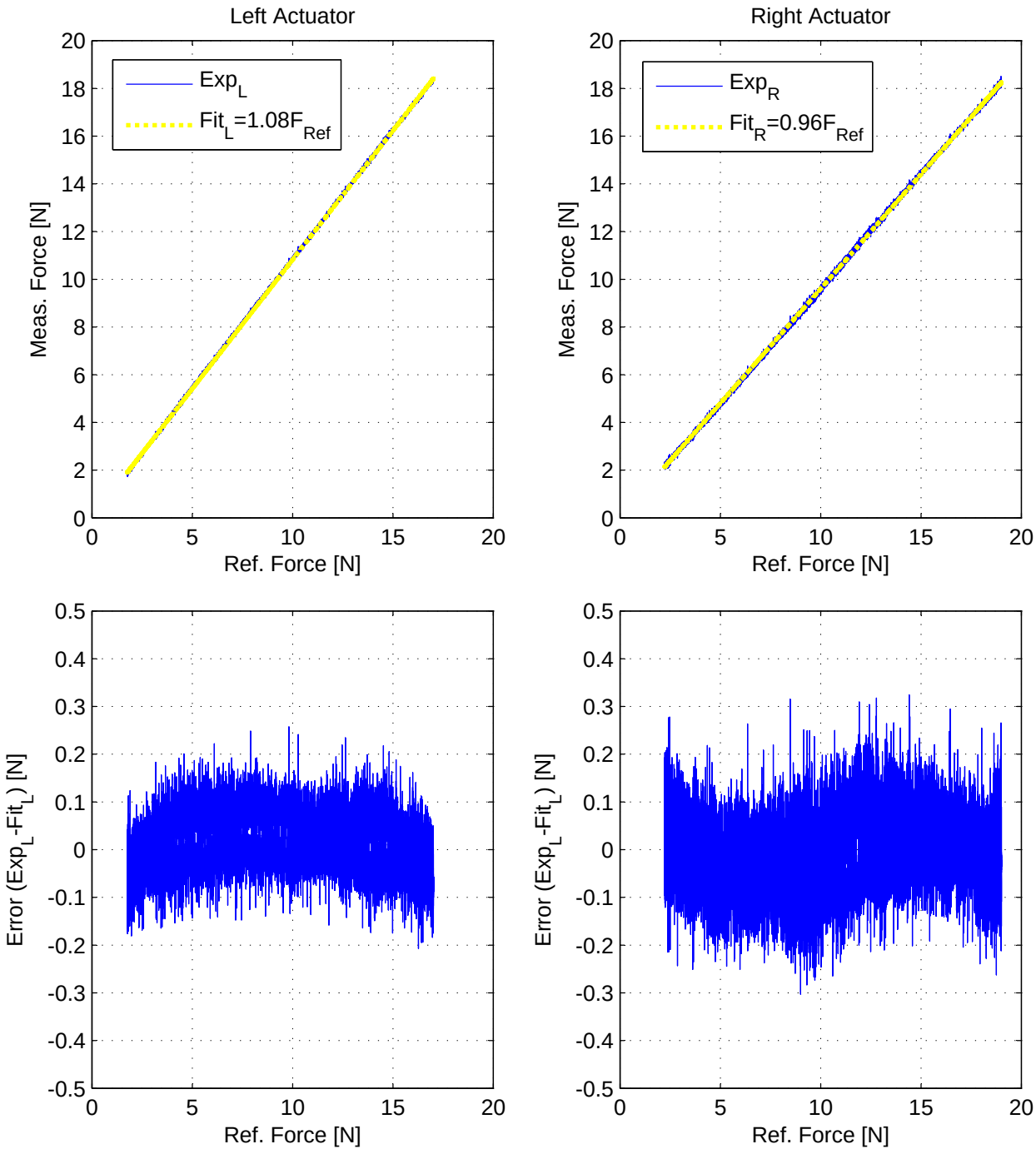

Figure 4-37: Measured output force plotted versus the reference force for the actuators on the left (top left) and right (top right) sides. The force nonlinearity plotted versus the reference force for the actuators on the left (bottom left) and right (bottom right).

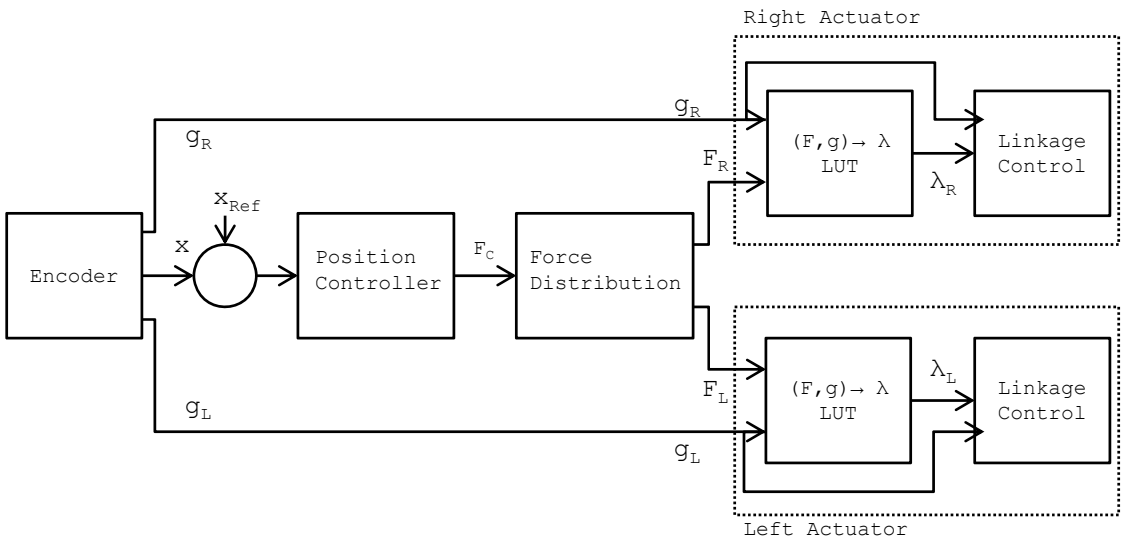

Figure 4-38: Block diagram of the position control system consisting of the position controller, force distribution, and flux linkage controller blocks.

friction and any stiffness. This may be due to small deformation in the airbearing shaft, which can create a preferred stable positions along the shaft. Particles in the airbearing pockets could also create static friction, which can act like a stiffness element within the presiding regime. Because this effect is at frequencies far below the cross-over frequency, it does not affect the controller design. The second roll-off at about 1-kHz is resulted from the limited bandwidth of the flux linkage controller.

The position control law consists of an integrator, a lead filter, and a roll-off filter. We use a first order lead filter to add phase at the cross-over and stabilize the system. We use an integrator to increase the loop gain and improve position tracking performance at low frequencies. We use the roll-off filter to attenuate the loop gain past the cross-over frequency and improve the noise performance. As shown in Figure 4-39, the position control system has a cross-over frequency of 200-Hz and phase margin of 40 degrees.

We have tested the control algorithm by stepping the reference position command from 50 μm away from the left actuator to 50 μm away from the right actuator. In this way, we can get the step response of the actuator at different air gaps. The test result is plotted in Figure 4-40. Positions of 0 mm and 1 mm correspond to the left and right actuator gaps being fully closed respectively. As can be seen, the

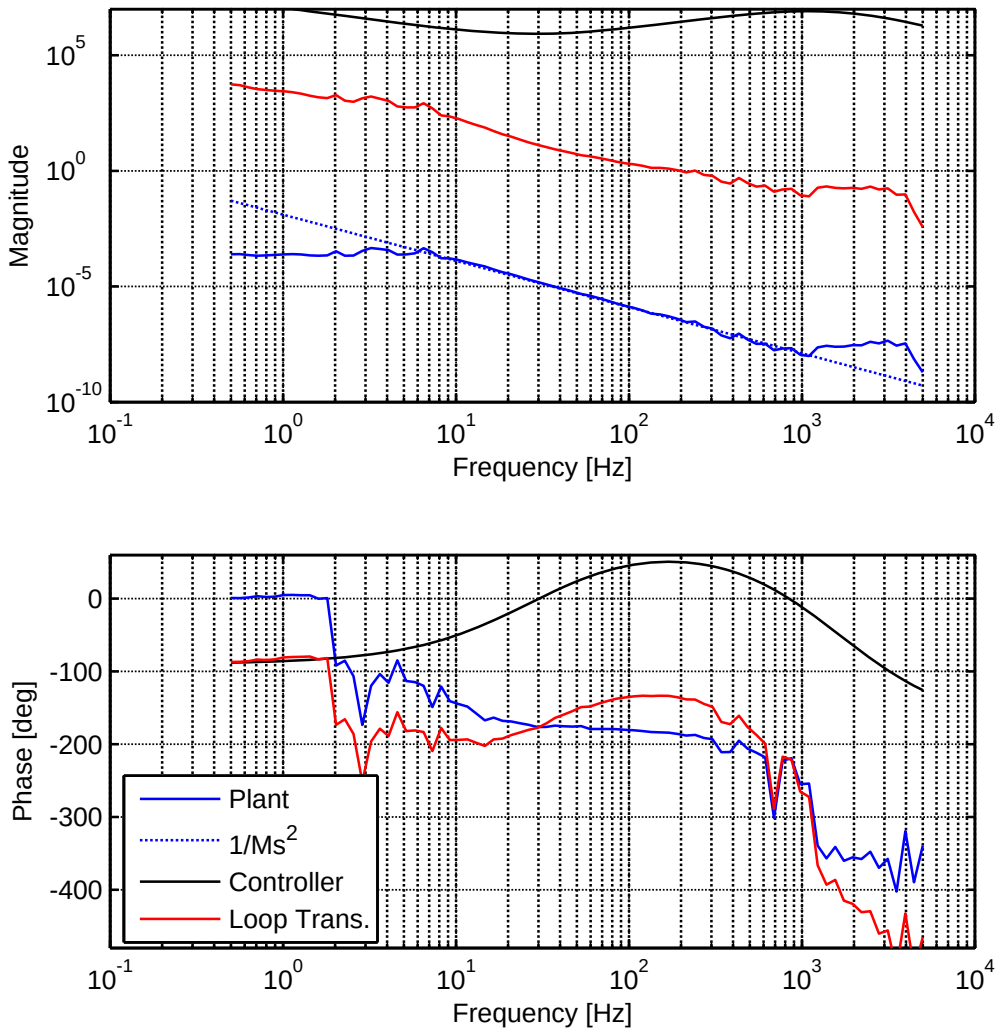

Figure 4-39: Bode plot showing the frequency responses of the position control system's plant, controller, and compensated loop transmission.

system stays stable within the whole range. The force calibration algorithm enables the two actuators to stay linear and work together to control the position even when one actuator has a 50-μm air gap and the other one has a 950-μm air gap. Due to time constraints, our force and inductance calibration data are from the 0.3mm to 0.7mm position range only. The calibration outside of this range is estimated by extrapolation. The position control performance degrades as we get farther outside of this range. A zoomed-in view of the step response is shown in Figure 4-41 for positions close to the center and within the calibration range and for positions outside of the calibration range and close to the right actuator. The controller does not perfectly track the reference at positions close to one actuator. This is due to the error in the calibration map. The integrator anti-windup limit is too low for the integrator to fully cancel this error. This problem can be directly addressed by calibrating the actuator over the whole motion range.

4.7.5 Finite Element Analysis

In this subsection, we present the finite element model of the electromagnetic actuator, which is developed using FEMM [2]. We use a 2D planar model of the actuator. The meshed model is shown in Figure 4-42. We model the core's lamination. We have defined MagX, MagY, and MagZ material types, which are SuperPerm49 with their lamination oriented in the direction normal to the X, Y, and Z axes respectively. It was not possible to model curved lamination in the corners of the U-cores, so we modeled the corners using a lamination normal to the Z axis. CoilIn and CoilOut model the coil currents flowing into and out of the page respectively. We use a Kelvin transformation for modeling the infinite boundary condition [53]. We model the saturation of the magnetic core. Figure 4-43 shows the B-H relation, which is modeled in FEMM. The BH characteristic for SuperPerm49 is taken from the data available on the manufacturer's website[3].

As an example, we have solved the model with a gap of 0.3 mm and a coil current

[2]Finite Element Method Magetics http://www.femm.info/wiki/HomePage
[3]Magnetic Metals: www.magmet.com

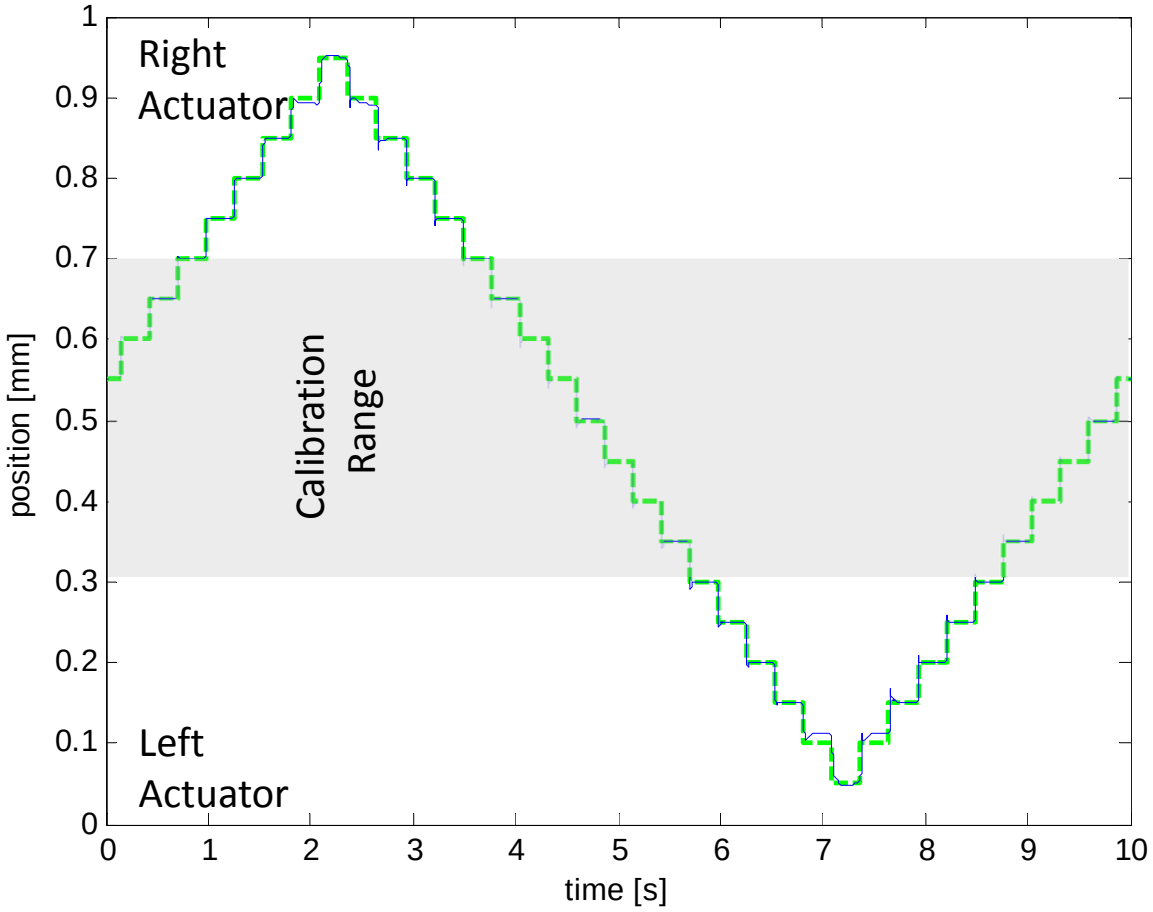

Figure 4-40: Experimentally captured step response of the position control system tested at different air gap sizes. Position 0.05 mm corresponds to 50μm away from the left actuator and position 0.95 mm corresponds to 50 μm away from the right actuator.

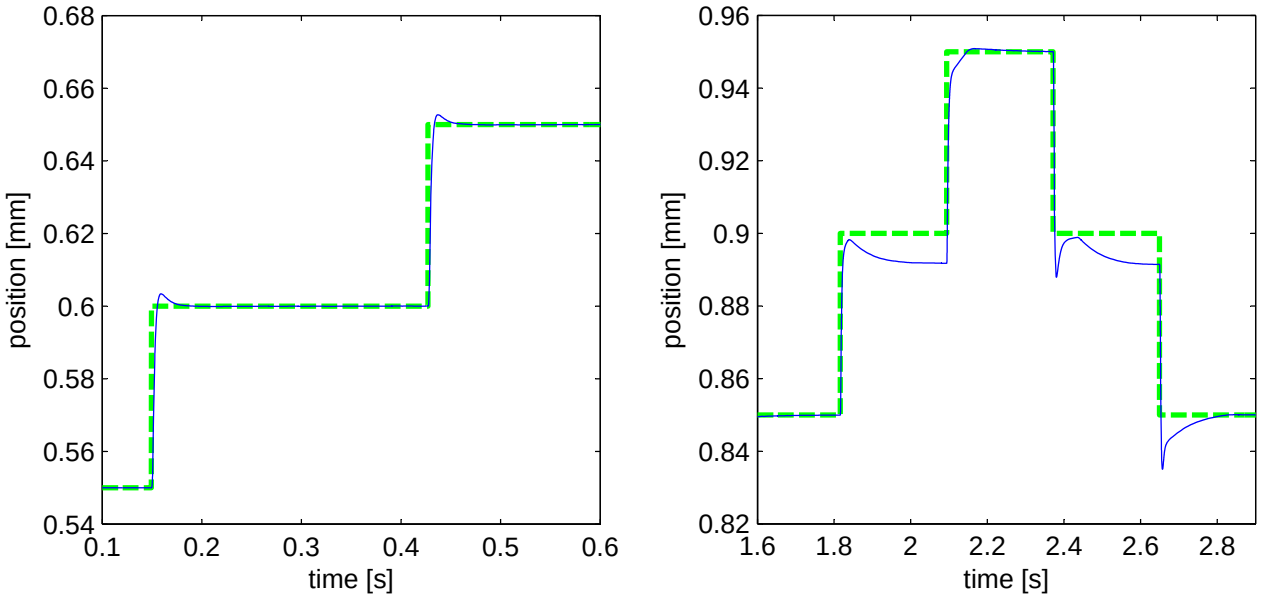

Figure 4-41: A zoomed in view of the position control system's step response close to the center and within the calibration range (left), and outside of the calibration range and close to the actuator face (right).

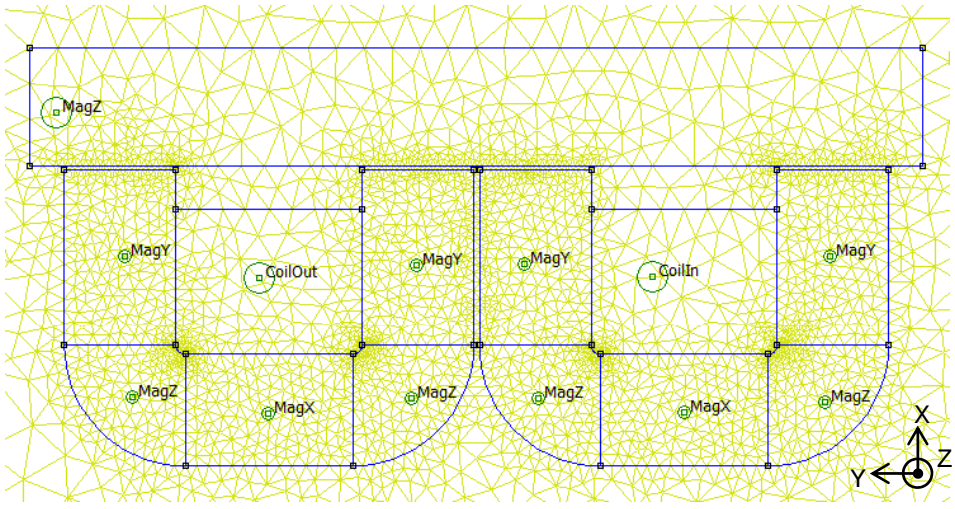

Figure 4-42: Meshed planar finite element model of the electromagnetic actuator.

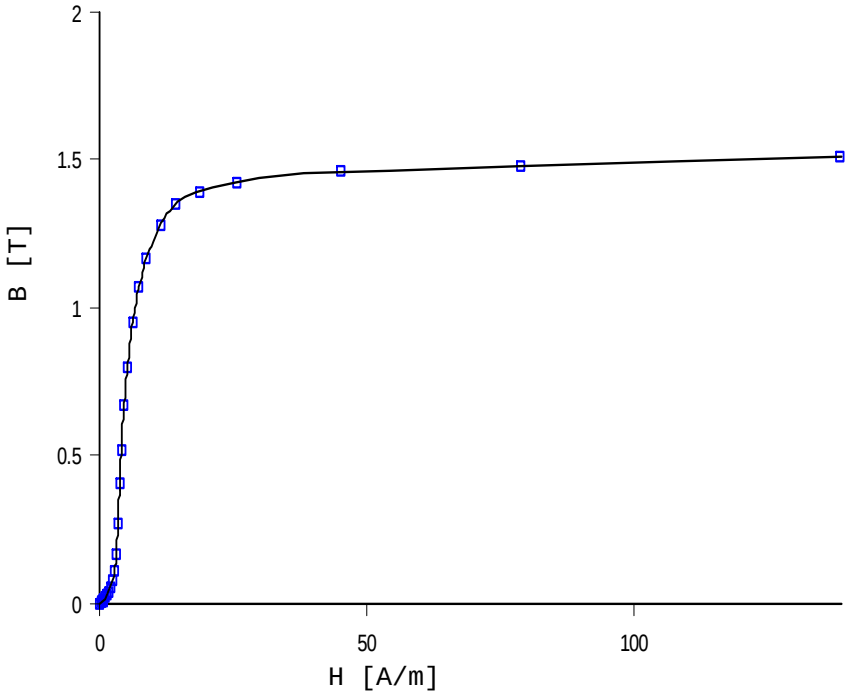

Figure 4-43: Non-Linear BH characteristic of the SuperPerm49 modeled in the FEA software. The cores are manufactured by Magnetic Metals. The data is obtained from the manufacturer's website

of 2 A. The magnetic flux density plot is shown in Figure 4-44. The line plot of the normal magnetic flux density over the face of the I-core is shown in Figure 4-44. Ignoring the reluctance of the magnetic core and the fringing fields, the expected magnetic flux density in the air gap can be estimated using the Ampere's law as the following:

$$NI = \oint_C H \cdot dl \simeq 2gH \tag{4.27}$$

$$\Rightarrow H = NI/2gB = \mu_0 H = \mu_0 NI/2g = 1.17\text{T} \tag{4.28}$$

The result from the finite element analysis is very close and shows 1.13 T on the outer pole faces and 1.21 T on the inner pole faces. As can be seen, the normal magnetic flux is not perfectly uniformly distributed over the pole faces.

We use the finite element model to simulate the actuator at different air gap values. At each air gap (g), we measure the actuator's mutual inductance (L_m) as well as

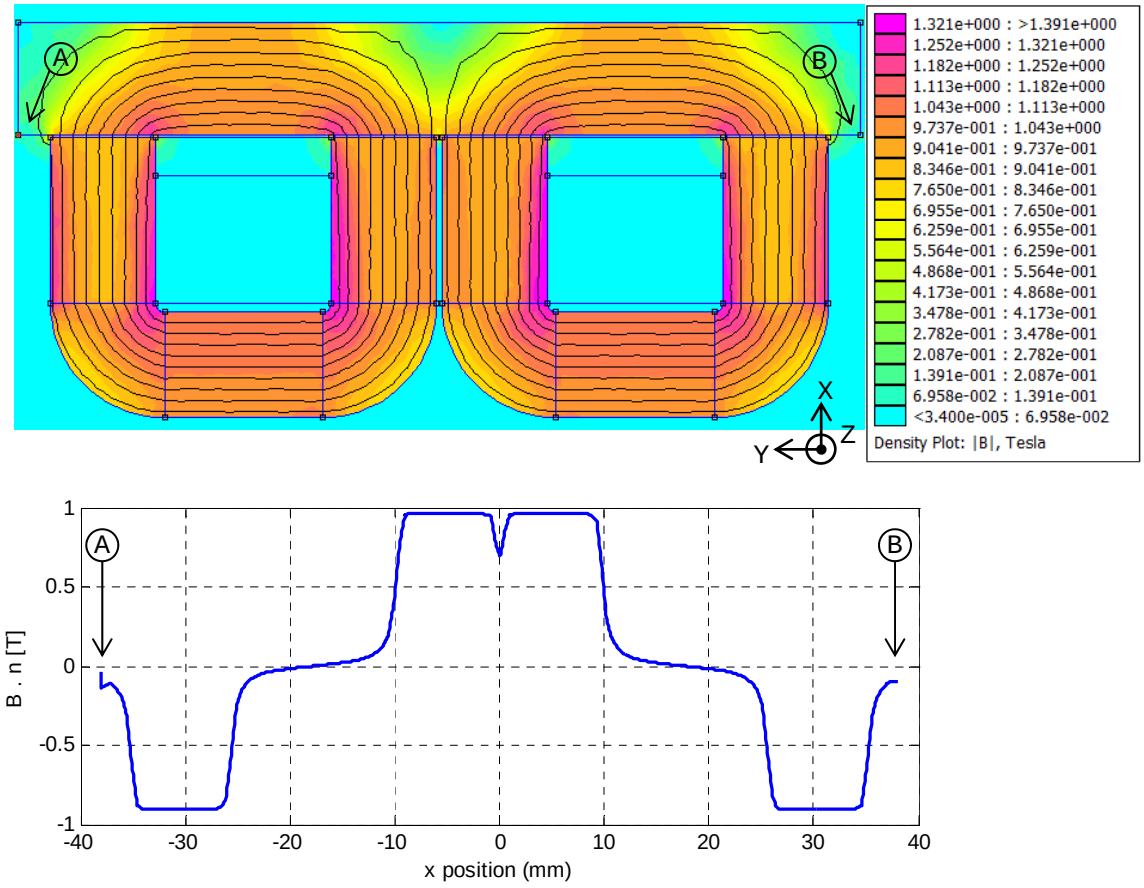

Figure 4-44: Simulation results using a coil current of 2A is shown as a magnetic flux density plot (top) and a line plot of the normal magnetic flux density over the face of the actuator's mover from point A to point B (bottom).

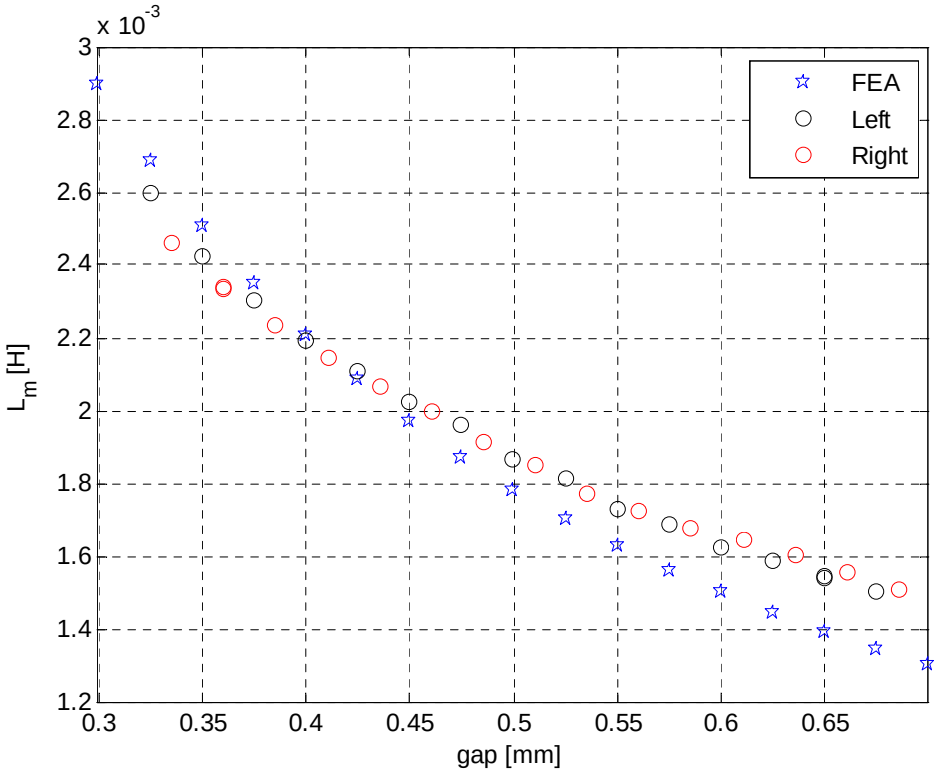

Figure 4-45: The mutual inductance (L_m) versus the air gap size is plotted based on the finite element model results and is compared to the experimental results for the right and left actuators.

its force correction constant (c). To automate this process, we have written a LUA script. The script opens the model, sets the air gap, sets the current, simulates the model, and takes the integrals required for calculating the sensed flux linkage (λ_S) and the output force (F). We use two nested loops for simulating the model at different coil current values and at different air gap sizes. In Figure 4-45 and Figure 4-46, the mutual inductance and the force correction constant, which have been calculated using the FEA model, are plotted versus the air gap size, and are compared to the experimental results from the right and left actuators.

The experimental and finite element results show the same trend. The mutual inductances match very closely; however, the force correction constants are slightly mismatched. The differences may be due to the following reasons:

- A planar model is used instead of an actual 2D model.

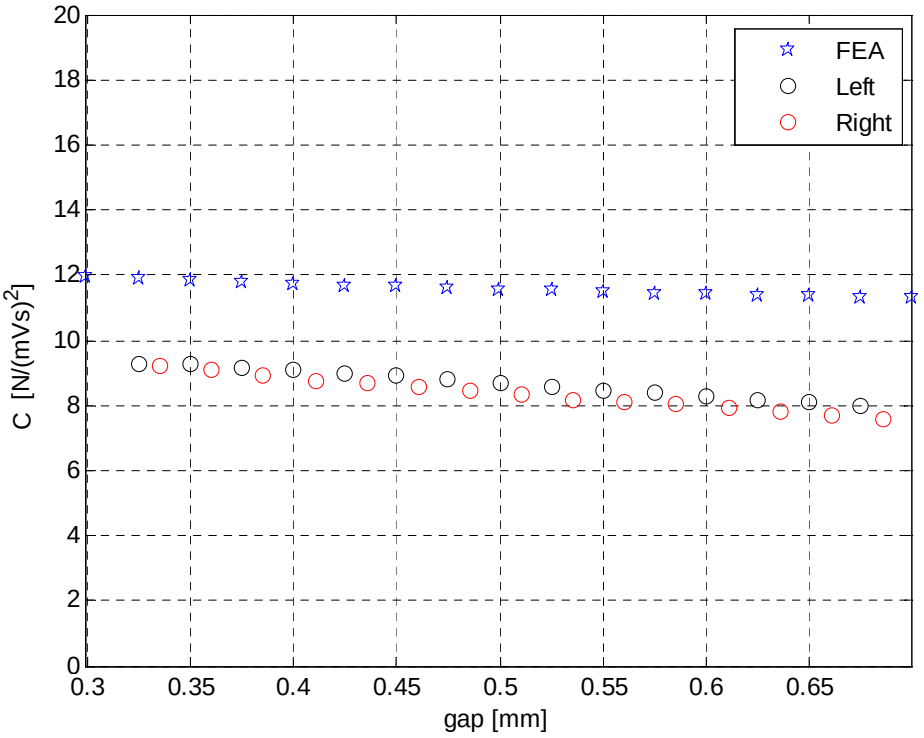

Figure 4-46: The force correction constant (c(g)) versus the air gap size is plotted based on the finite element model results and is compared to the experimental results for the right and left actuators.

- The manufactured actuator has deformed pole faces which differ from the assumed cuboid pole geometry. The pole faces are deformed by the large grinding forces exerted on the raised laminated pole faces. This could have been avoided by burring and supporting the pole faces using resin prior to grinding.

- The material properties and the sizes are not exactly matched between the model and the actuator.

4.8 Summary

We reviewed the prior art charge amplifiers. We analyzed a conventional charge amplifier and used it as a benchmark. We presented a VQV charge amplifier with a new feedback circuit design which is more robust to the addition of series load impedance. We also described a hybrid hysteresis method (HHC) which can be added to charge amplifiers to enable piezo hysteresis compensation at low frequencies. We use the improved VQV charge amplifier with HHC for controlling the extension of the piezoelectric actuator approximately linearly without the need for closed-loop control using the strain gauge feedback. In this chapter, we also present a magnetic flux control method which, in analogy to piezo linearization through charge control, can linearize normal flux electromagnetic actuators.

In the next chapter, we present a sensorless method for precisely detecting contact between the piezoelectric actuator and the reticle. The method is used by the control system to reference the piezo's extension relative to the reticle edge.

Chapter 5

Self-Sensing Contact Detection

Jones and Garcia [37] define self-sensing as measuring a signal from a smart-material actuator, such as piezoelectric or magnetostrictive actuators, without the need for any sensors or additional components. Self-sensing can improve a system's performance without incurring additional cost and space associated with using a separate sensor. Self-sensing is key to improving the precision of our reticle assist device by detecting contact between our actuator and the reticle. This method has been adapted from self-sensing of atomic force microscopy probes as in our high-accuracy atomic force microscope (HAFM) [83]. In this chapter, first, we present the prior art of self-sensing. Next, we provide an analytical derivation of our self-sensing method applied to piezoelectric and electromagnetic resonators. Then, we describe the application of our self-sensing contact-detection method to our reticle-assist device. Finally, we show the self-sensing contact detection method used with a piezoelectric atomic force microscope (AFM) and a macro-scale electromagnetic AFM.

5.1 Prior Art Self-Sensing

Self-sensing is referred to extracting a measurement signal without using any separate sensors or additional components. Typically, self-sensing uses a system's model to extract information about its states. An actuator's electro-mechanical model is used to relate the actuator's electric signals to for example its motion or force. This is

very similar to using an observer in a control system. For simple implementation of self-sensing, bridge circuits were initially used to extract such measurements from actuators. Later, observer-based self-sensing methods running on analog electronics or digital processors were utilized. Non-linearities of actuators, such as hysteresis and creep, are not included in the linear model of the actuators and can adversely affect the performance of the self-sensing algorithm. Observer based self-sensing methods have been proposed where a hysteresis model of the system is used to compensate for the actuator's nonlinearities. These approaches are described in more detail below.

According to reference Jones and Garcia [37], the first instance of self-sensing was implemented by De Boer in 1961. He used a bridge circuit to extract a measurement corresponding to the motion of a voice coil actuator and used it as feedback [13]. Dosch et al. applied self-sensing to piezoelectric actuators [18], where they used a bridge circuit to estimate the piezoelectric actuator's strain or strain-rate. They used the measurement for actively damping the vibration of a cantilever. Anderson and Hagood employed piezoelectric actuators for simultaneous sensing and actuation [6] and applied them in vibration damping of a strut. Jones and Garcia used self-sensing with a micro positioner [37]. The self-sensing methods, which are based on a linear model of the piezoelectric actuator, have errors in their measurement and control resulting from hysteresis non-linearities. Spangler integrated charge control and self-sensing to eliminate the phase delay resulting from the piezoelectric voltage-strain hysteresis [80]. Simmers et al. suggested that self-sensing can be improved by capacitor insertion [75]. Jones and Garcia applied hysteresis compensation to self-sensing [38]. They formulated an observer-based self-sensing algorithm which can estimate the actuator's force and strain from its voltage and charge. Their self-sensing algorithm models the piezoelectric actuator's capacitance using a generalized Maxwell slip (GMS) model. Self-sensing has also been applied to other smart materials. Pratt and Flatau applied self-sensing to a magnetostrictive actuator based on its linear model [68]. Kuhnen et al. [46] applied self-sensing with hysteresis compensation to a magnetostrictive actuator.

The self-sensing methods described above are for estimating motion or force. Their

estimation can be inaccurate due to the actuator hysteresis. If a hysteresis compensator is used, the accuracy limit is set by the compensator's accuracy. It is difficult to build a non-linear model of the actuator which is accurate over a broad range of frequencies. Furthermore, it is difficult to process such a model with good accuracy in real-time and achieve a fast estimation bandwidth. For our reticle assist device we are interested in repeatable force control at high bandwidth. In order to achieve this goal, we use a self-sensing method inspired by self-sensing AFM probes. We measure the shifts in the actuator's electrical admittance frequency response to detect contact between the actuator and the reticle with high sensitivity. Knowing the exact contact point, we can estimate and control the force by controlling the deformation of the mechanical force-loop stiffness relative to this contact point.

Gunther et al. used a quartz tuning fork resonator with a sharp vibrating tip for scanning near-field acoustic microscopy (SNAM), where they monitored the variations in the tuning fork electrical admittance near its resonance resulting from coupling between the resonator and the sample [32]. Karrai and Grober used a quartz tuning fork with an optical fiber for near-field optical microscopy (NSOM), where the variations in the tuning fork's electrical admittance near resonance were used as feedback for regulating the tip-sample distance [41]. Rychen et al. used a self-sensing quartz tuning fork with a sharp tip for low-temperature atomic force microscopy [71]. Self-sensing AFM probes eliminate the need for an optical lever mechanism, which typically consists of optics, a laser shining on the probe, and a multi-cell photodiode detector. Self-sensing AFM probes are suitable for NSOM because there is no interference from the optical-lever's laser light with the optical near-field scanning system. The tuning forks are also attractive for ultra-low-temperature applications because there is no heat added by a laser close to the measurement point. Tuning forks have a symmetric vibration mode, where inertial loads from the two prongs cancel. As a result, they are sensitive resonators with a high quality factor (Q-factor). [29]

Self-sensing AFM probes can be made by attaching a sharp tip to a tuning fork

from a watch quartz crystal. Bruker[1] and Nanosnesors[2] supply commercial self-sensing AFM probes. Nanosensors^{TM} carries the Akiyama probe, which consists of a cantilever symmetrically attached to the end of the tuning fork's prongs. Burker carries the DMASP self-sensing self-actuating probe, which consist of a piezoelectric cantilever with a sharp tip. We have used a self-sensing Akiyama probe in our HAFM [83]. We have also designed our own macro-scale self-sensing magnetic AFM. In the reticle assist device, we have applied self-sensing to a commercial piezoelectric stack actuator.

5.2 Self-Sensing Contact-Detection Principle

By monitoring the variations in an actuator's frequency response near resonance, we can detect contact between the actuator and an object with high sensitivity. To avoid sensors, we use the actuator's electrical impedance or admittance frequency response. The mechanical and electrical actuator models are coupled. Interactions in the mechanical domain, such as mechanical contact, reflect on the electrical domain dynamics. As a result contact can be detected by monitoring the electrical frequency response with highest sensitivity near resonance. In the following subsections, we model piezoelectric and electromagnetic resonators and show how their mechanical dynamics can be extracted from sensing of the electrical dynamics.

5.2.1 Piezoelectric Devices

A lumped parameter model of a piezoelectric resonator is shown in Figure 5-1. In the mechanical domain, the actuator is modeled as mass, stiffness, and damping with values corresponding to the actuator's first resonance mode. The surface, with intermitent contact, is modeled as a stiffness k_s. The piezoelectric effect is modeled as a force F_p exerted on the mass m. In the electrical domain, the resonator is modeled as a voltage source v_e driving a piezoelectric element and a parallel parasitic capacitance

[1]Burker AFM Probes: www.burkerafmprobes.com
[2]NanoSensors^{TM}: www.nanosensors.com

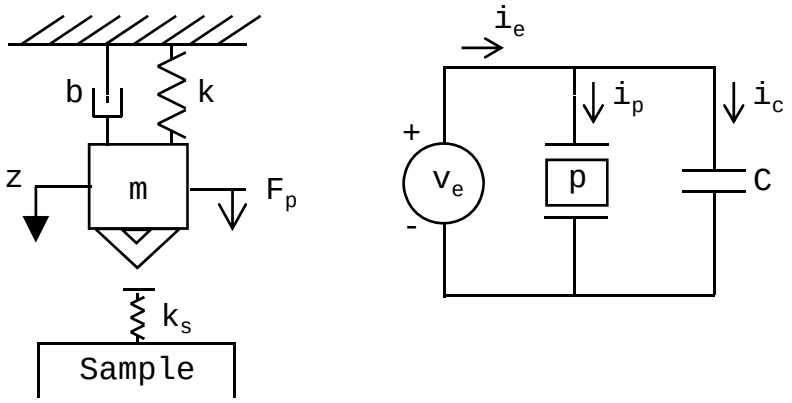

Figure 5-1: Lumped parameter model of a piezoelectric resonator modeling only the first resonance mode. The sample surface is modeled with a stiffness k_s.

C. The two domains are coupled by the piezoelectric element. The coupling equations are defined as

$$\begin{aligned} F_p &= pv_e \\ i_p &= p\dot{z} \end{aligned} \tag{5.1}$$

where the coefficient p is the piezoelectric constant with units of N/V.

We can write the equation of motion in the mechanical domain, use the coupling relation in (5.1) to substitute v_e for F_p, and thus derive a transfer function:

$$\begin{aligned} m\ddot{z} + b\dot{z} + kz = F_p & \\ \Rightarrow m\ddot{z} + b\dot{z} + kz &= pv_e \\ \Rightarrow \frac{\dot{Z}(s)}{V_e(s)} &= \frac{ps}{ms^2 + bs + k}. \end{aligned} \tag{5.2}$$

We can also write Kirchhoff's current law in the electrical domain, express i_p using the coupling relation in (5.1), and derive a transfer function by substituting for

$\dot{z}$ using the mechanical transfer function from (5.2):

$$
\begin{aligned}
i_e = C\dot{v}_e + i_p & \\
& \Rightarrow i_e = C\dot{v}_e + p\dot{z} \\
& \Rightarrow I_e(s) = CV_e(s)s + p\dot{Z}(s) \\
& \Rightarrow I_e(s) = CV_e(s)s + p\frac{\dot{Z}(s)}{V_e(s)}V_e(s) \\
& \Rightarrow \frac{I_e(s)}{V_e(s)} = Y_t(s) = Cs + \frac{p^2 s}{ms^2 + bs + k}. \qquad (5.3)
\end{aligned}
$$

According to (5.3), the electrical admittance transfer function seen by the excitation voltage source (v_e) consists of a passive capacitive admittance (Y_c) in parallel added to a piezoelectric admittance (Y_p):

$$
\begin{aligned}
Y_t(s) = Y_c(s) + Y_p(s) \qquad (5.4) \\
Y_c(s) = Cs \\
Y_p(s) = \frac{p^2 s}{ms^2 + bs + k}
\end{aligned}
$$

The mechanical transfer function given by (5.2) is proportional to the piezoelectric admittance (Y_p):

$$Y_p(s) = p^2 \frac{\dot{Z}(s)}{F(s)} \qquad (5.5)$$

As a result, the mechanical resonance can be sensed by measuring the load admittance and extracting the piezoelectric admittance from it. The piezoelectric current can be extracted from the source current by injecting a current opposite to the capacitive current at the measurement point. In this analysis we assumed that the actuator is not in contact with the sample surface. A simple model of contact is a spring-damper at the point of contact whose magnitude is proportional to the portion of the time that the actuator is in contact with the sample during one oscillation period. The added rigidity and constraint from the contact increases the natural resonance frequency of the resonator. We can detect contact as the shift in the frequency

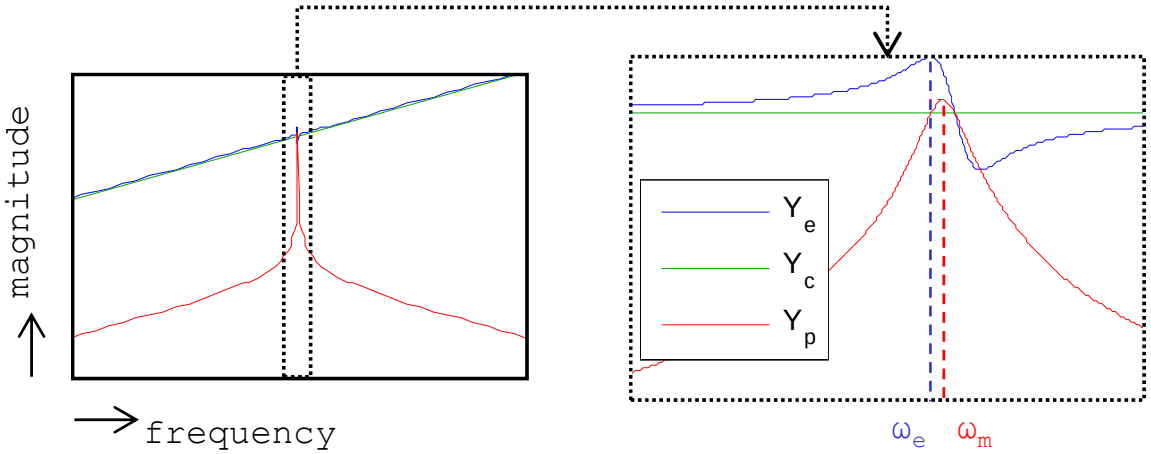

Figure 5-2: The shape of the magnitude response shape of the total, capacitive, and piezoelectric admittances are shown using arbitrary system parameter values. Note that the capacitive component hides the resonance.

response of the piezoelectric admittance near the resonance.

The shape of the magnitude frequency responses for the total, capacitive, and piezoelectric admittances are shown in Figure 5-2. The total admittance (Y_t) is the load admittance as seen by the excitation voltage source (v_e). The total admittance response does not have a sharp resonance. It has an asymmetric magnitude response consisting of a resonance followed by a notch. We refer to the resonance at frequency ω_e as the electrical resonance. This resonance peak does not however correspond to the mechanical resonance frequency. By compensating for the capacitive admittance (Y_c) via subtraction, we can extract the piezoelectric admittance (Y_p) which is proportional to the mechanical transfer function $\dot{Z}(s)/F(s)$. The resonance frequency of the piezoelectric admittance does correspond to the mechanical resonance frequency (ω_m), and is sharp and symmetric. We use the piezoelectric admittance for contact detection for two reasons. First, the system's dynamic stiffness is minimum at the mechanical resonance frequency (ω_m), and thus the probe is more sensitive to the addition of a stiffness disturbance from contact. Secondly, a sharp and symmetric resonance curve improves the robustness of the contact detection by reducing its sensitivity to other system dynamics.

The changes in the frequency response can be detected in several ways. For in-

stance, the resonator can be excited at its resonance frequency and the changes in the phase or amplitude response from the excitation voltage (v_e) to the current (i_p) can be calculated as a measure of the shift in the resonance of the piezoelectric admittance (Y_p). We used this method with the reticle-assist device. The methods, which use the open-loop amplitude or phase response are referred to as the amplitude- or phase-measuring methods. Alternatively, a feedback system can be designed to put the piezoelectric resonator in controlled-amplitude self-resonance at its natural resonance frequency. In this way, the shifts in the natural resonance frequency can be detected as the changes in the self-resonance frequency. Garcia and Perez provide a comprehensive review of the different detection methods used for atomic force microscopy, including the amplitude-, phase-, and frequency-measuring methods [26]. In Section 5.3, we describe how we apply self-sensing to the reticle-assist device's piezoelectric actuator. We present a high-accuracy atomic force microscope in Section 5.4, which uses a self-sensing Akiyama probe.

5.2.2 Electromagnetic Devices

The self-sensing contact detection method described previously is not specific to piezoelectric actuators and can be applied to other actuator types near their resonance frequency. In this section, we describe how an electromagnetically driven resonator can be used for self-sensing contact detection. A lumped parameter model of an electromagnetic resonator is shown in Figure 5-3. The resonator is modeled as a mass m supported by a spring k and a damper b, with the electromagnetic actuator force F_m acting on the mass m. In the electrical domain, a voltage source v_e is driving the coil, which is modeled as a resistance R, inductance L, and electromotive force (emf) voltage v_m in series. The contact with the sample is modeled as an intermittent stiffness k_s. The coupling between the electrical and mechanical domains is described by

$$\begin{aligned} F_m &= p i_e \\ v_m &= p \dot{z}. \end{aligned} \tag{5.6}$$

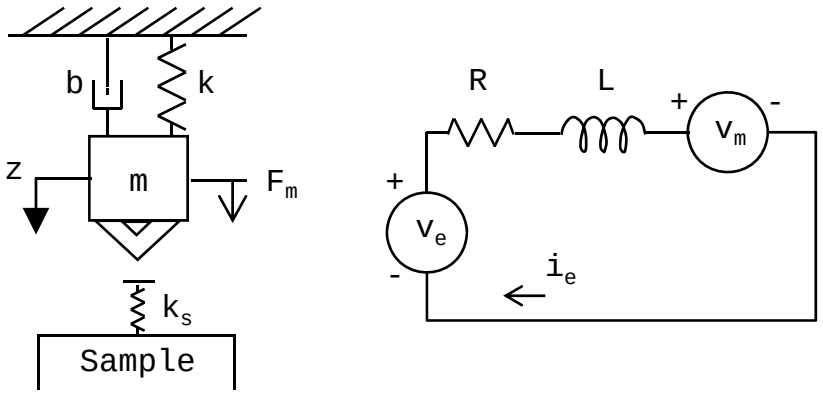

Figure 5-3: Lumped parameter electromechanical model of an electromagnetic resonator.

We can write the equation of motion in the mechanical domain, use the coupling relation in (5.6) to substitute i_e for F_m, and derive a transfer function:

$$
\begin{aligned}
m\ddot{z} + b\dot{z} + kz = F_m & \\
& \Rightarrow m\ddot{z} + b\dot{z} + kz = pi_e \\
& \Rightarrow \frac{\dot{Z}(s)}{I_e(s)} = \frac{ps}{ms^2 + bs + k}.
\end{aligned} \tag{5.7}
$$

We can also write Kirchhoff's voltage law for the electrical model, express v_m using the coupling relation in (5.6), and derive a transfer function by substituting for $\dot{z}$ using the mechanical transfer function from (5.7):

$$
\begin{aligned}
v_e = Ri_e + L\dot{i}_e + v_m & \\
& \Rightarrow v_e = Ri_e + L\dot{i}_e + p\dot{z} \\
& \Rightarrow V_e(s) = I_e(s)(R + Ls) + p\dot{Z}(s) \\
& \Rightarrow V_e(s) = I_e(s)(R + Ls) + p\frac{\dot{Z}(s)}{I_e(s)}I_e(s) \\
& \Rightarrow \frac{V_e(s)}{I_e(s)} = Z_t(s) = R + Ls + \frac{p^2 s}{ms^2 + bs + k}.
\end{aligned} \tag{5.8}
$$

The resulting impedance transfer function $Z_t(s)$ given by (5.8) can be divided into a passive electrical impedance (Z_{rl}) and an electromagnetic impedance (Z_m):

$$Z_t(s) = Z_{rl}(s) + Z_m(s) \tag{5.9}$$

$$Z_{rl}(s) = R + Ls$$

$$Z_m(s) = \frac{p^2 s}{ms^2 + bs + k}.$$

The electromagnetic impedance (Z_m) is proportional to the mechanical transfer function given by (5.7):

$$Z_m(s) = p^2 \frac{\dot{Z}(s)}{F(s)} \tag{5.10}$$

As a result, the electromagnetic impedance (Z_m) can be used for self-sensing contact-detection. We can extract the electromagnetic voltage (v_m) by subtracting an estimate of the resistive and inductive voltage (v_{rl}) from the voltage measured across the coil (v_e) as

$$v_m = v_e - v_{rl} = v_e - Ri_e + L\frac{di}{dt}. \tag{5.11}$$

The extracted electromagnetic voltage (v_m) and the excitation current (i_e) can be used for self-sensing contact detection. Contact creates a shift in the electromagnetic actuator's natural mechanical resonance frequency. This shift is visible in the electrical impedance frequency response and can be measured using amplitude-, phase-, and frequency-measuring methods, which were briefly described in the previous subsection. In Section 5.5, we will describe a macro-scale self-sensing electromagnetic profiler, which uses self-sensing contact detection.

5.3 Application to Piezoelectric Actuator

We apply self-sensing contact detection to the reticle assist device's piezoelectric actuator to detect contact between the actautor's pushing tip and the reticle. Precisely detecting contact is key to accurate force generation because we control the force by

controlling deformation of the mechanical force loop past the contact point. In the following sections, we describe the self-sensing method, show its implementation on an FPGA device, and present experimental results demonstrating successful contact-detection.

5.3.1 Self-Sensing Method

The piezoelectric actuator's frequency response shifts as a result of the constraint added by contact with the reticle. The shift can be detected with high sensitivity at the actuator's resonance, where its dynamic stiffness is minimum. The actuator's resonance frequency response from the applied voltage to the mechanical strain is shown in Figure 5-4. This was taken using the strain gauge built into the acutator; this gauge is not used in the self-sensing algorithm. The response is shown for the actuator free in air using different excitation amplitudes and in contact with different preload force values. The frequency response free in air is repeatable for the same excitation amplitude. As can be seen, the actuator's frequency response shifts to higher frequency with increasing the contact preload force. We have used pressure regulated air with a bellow to gradually increase the preload. The term ΔP used in the Figure's legend refers to an arbitrary positive change in pressure by turning the regulator knob.

As described in Section 5.2, the shift in the mechanical resonance is visible in the electrical admittance frequency response as well. The electrical admittance frequency is compared to the mechanical frequency response in Figure 5-5 for the actuator free in air. Near the mechanical natural resonance frequency, the two responses match very well. The added mass of the actuator's pushing tip has resulted in the piezoelectric current being significantly larger than the parasitic capacitive current at the resonance. As a result, the notch resulting from the capacitive current leakage path has little effect on the resonance peak and does not need to be compensated. We can detect contact by measuring the change in the total electrical admittance (Y_t) phase or amplitude response at the resonance frequency. We can apply phase- or amplitude-measuring contact detection to the reticle assist device because they are

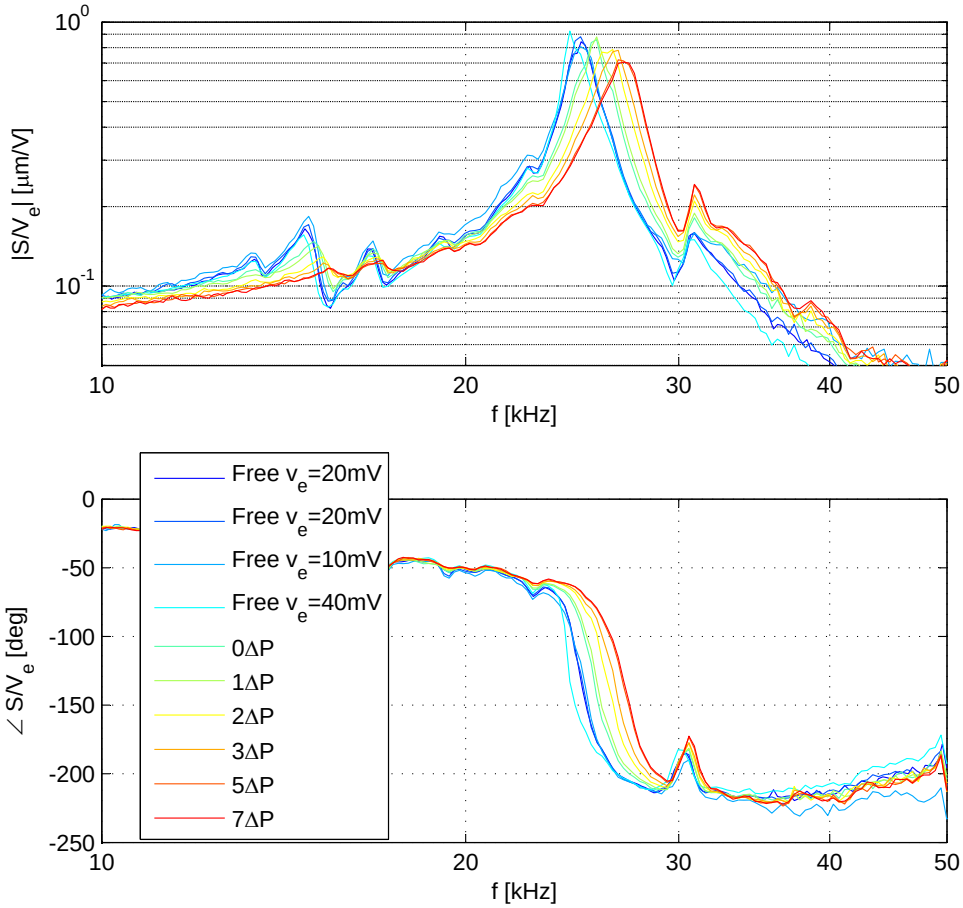

Figure 5-4: Piezoelectric actuator's frequency response from the applied voltage to the mechanical strain is plotted free in air at different excitation amplitudes, and in contact with the sample using an increasing range of preloading pressure values.

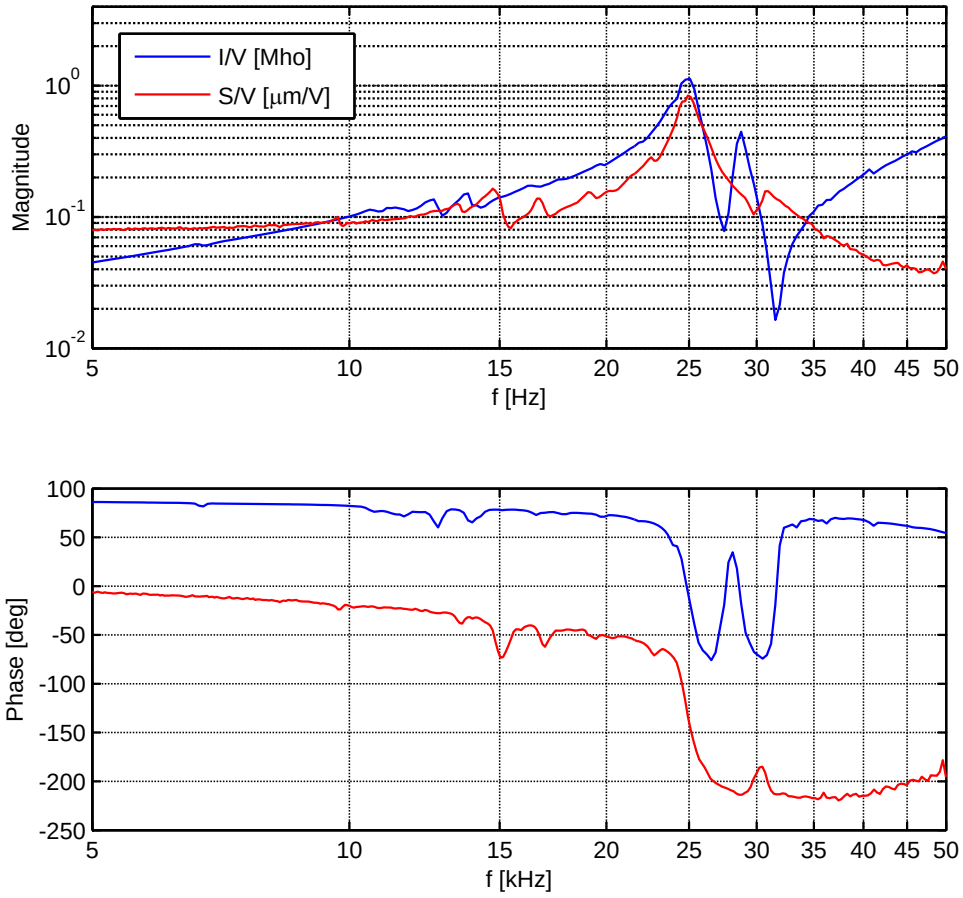

Figure 5-5: Comparing the piezoelectric actuator's electrical admittance and mechanical frequency response near resonance.

simpler to implement compared to the frequency-measuring AFM, and they provide a sufficient sensing bandwidth.

5.3.2 Implementation on an FPGA

To detect contact, we add a small sinusoidal excitation to the applied voltage and measure the amplitude ratio and phase difference between the current and the voltage signals. We implement the contact detection algorithm on a LabVIEW PXI-7854R FPGA card. The algorithm is sampled at 325 kHz. A block diagram of the contact detection system is shown in Figure 5-6. The power amplifier's reference voltage (v_r) is passed through the algorithm on the FPGA, where a sinusoidal excitation ($v_e \times sin(\omega_p t)$) is added to it. The sinusoidal excitation and contact detection can be

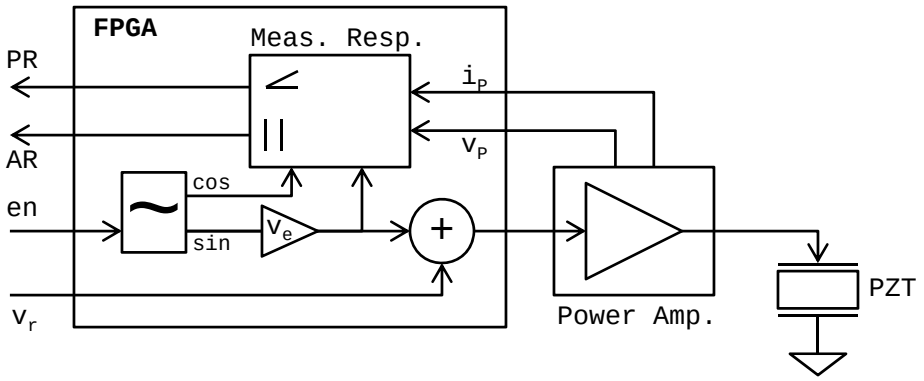

Figure 5-6: Block diagram of the contact detection algorithm implemented on an FPGA device.

enabled or disabled using the enable signal (en). The FPGA reads the piezo current and voltage measurements from the power amplifier. It uses these signals to calculate the phase and magnitude response from the actuator voltage to its current at the excitation frequency.

The response measurement algorithm is described below [25]. It first finds each signal's magnitude and phase relative to the excitation signal. The amplitude and phase responses are calculated as the phase difference and magnitude ratio of the two signals. To calculate the magnitude and phase at the excitation frequency we modulate signals using the sine excitation and its matched cosine signal:

$$i_{SM} = i_p \times sin(w_p t) \quad \text{sine modulated } i_p \tag{5.12}$$

$$i_{CM} = i_p \times cos(w_p t) \quad \text{cosine modulated } i_p \tag{5.13}$$

$$v_{SM} = v_p \times sin(w_p t) \quad \text{sine modulated } v_p \tag{5.14}$$

$$v_{CM} = v_p \times cos(w_p t) \quad \text{cosine modulated } v_p \tag{5.15}$$

The excitation frequency $\omega_p \simeq 25\ kHz$ is the actuator's resonance frequency. We low-pass filter the modulated signals to obtain its correlation sum with the sine excitation signal and its matched cosine signal. $lpf(t)$ is the impulse response of a

fourth order low-pass Butterworth filter with a cutoff frequency of 1 kHz:

$$i_{SC} = i_{SM} * lpf(t) \quad \text{sine-}i_p \text{ correlation} \tag{5.16}$$

$$i_{CC} = i_{CM} * lpf(t) \quad \text{cosine-}i_p \text{ correlation} \tag{5.17}$$

$$v_{SC} = v_{SM} * lpf(t) \quad \text{sine-}v_p \text{ correlation} \tag{5.18}$$

$$v_{CC} = v_{CM} * lpf(t) \quad \text{cosine-}v_p \text{ correlation} \tag{5.19}$$

The correlation sums can be considered as the Cartesian coordinates of each signal's complex frequency response at the modulation frequency. We convert the responses into the polar coordinates:

$$\angle i_p = \arctan(i_{SC}/i_{CC}) \quad \text{phase of } i_p \text{ relative to } v_e \tag{5.20}$$

$$|i_p| = \tfrac{1}{2}\sqrt{{i_{SC}}^2 + {i_{CC}}^2} \quad \text{amplitude of } i_p \tag{5.21}$$

$$\angle v_p = \arctan(v_{SC}/v_{CC}) \quad \text{phase of } v_p \text{ relative to } v_e \tag{5.22}$$

$$|v_p| = \tfrac{1}{2}\sqrt{{v_{SC}}^2 + {v_{CC}}^2} \quad \text{amplitude of } v_p \tag{5.23}$$

The phase and magnitude response from the applied voltage to the current can be calculated as the following:

$$\angle \tfrac{I_p(s)}{V_p(s)}_{s=w_p j} = \angle i_p - \angle v_p \quad \text{admittance phase @ } w_p \tag{5.24}$$

$$|\tfrac{I_p(s)}{V_p(s)}|_{s=w_p j} = |i_p| \div |v_p| \quad \text{admittance magnitude @ } w_p \tag{5.25}$$

5.3.3 Experimental Results

We have tested the self-sensing contact detection method. We extend the piezo actuator to make contact with reticle and increase the contact force from 0 N to approximately 70 N. The contact force is calculated as the deformation of the reticle membranes measured by the capacitive displacement gauges times the membranes stiffness in the force direction. The resulting phase and magnitude measurements are plotted versus the contact force in Figure 5-7. As it can be seen, the detection method

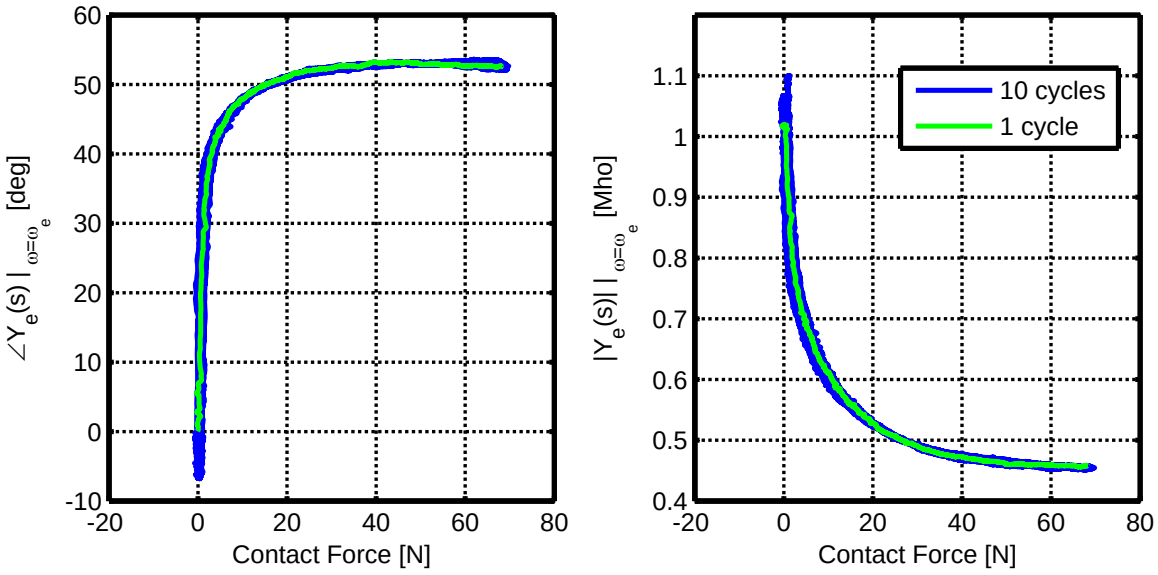

Figure 5-7: Self-sensing contact detection phase (left) and amplitude (right) response plotted versus the contact force. The probe is excited at the mechanical resonance $\omega_p \simeq$25 kHz with approximately 25-nm oscillation amplitude.

is very sensitive. A large change in phase and amplitude response is measured using a small contact force. The resonance frequency ω_p is stable, such that we have never needed to readjust the excitation frequency for our tests.

We use the contact detection method for finding the reticle's edge. The time plot for an experiment, where we use contact detection, is shown in Figure 5-8. As shown in the top subplot, the piezoelectric actuator approaches the reticle, and the contact detection system is activated at the same time. The contact detection system's phase measurement is shown in the bottom subplot. When activated, the phase measurement goes through a 1-ms transient. The phase measurement is a steady-state response, and thus it is valid after the transients have disappeared. After the 1-ms transient, contact is detected as the phase measurement raising above zero degrees. The resulting contact forces are shown in the middle subplot. Once the reticle edge is detected, the actuator retracts back. The detected edge location is shown in the top subplot.

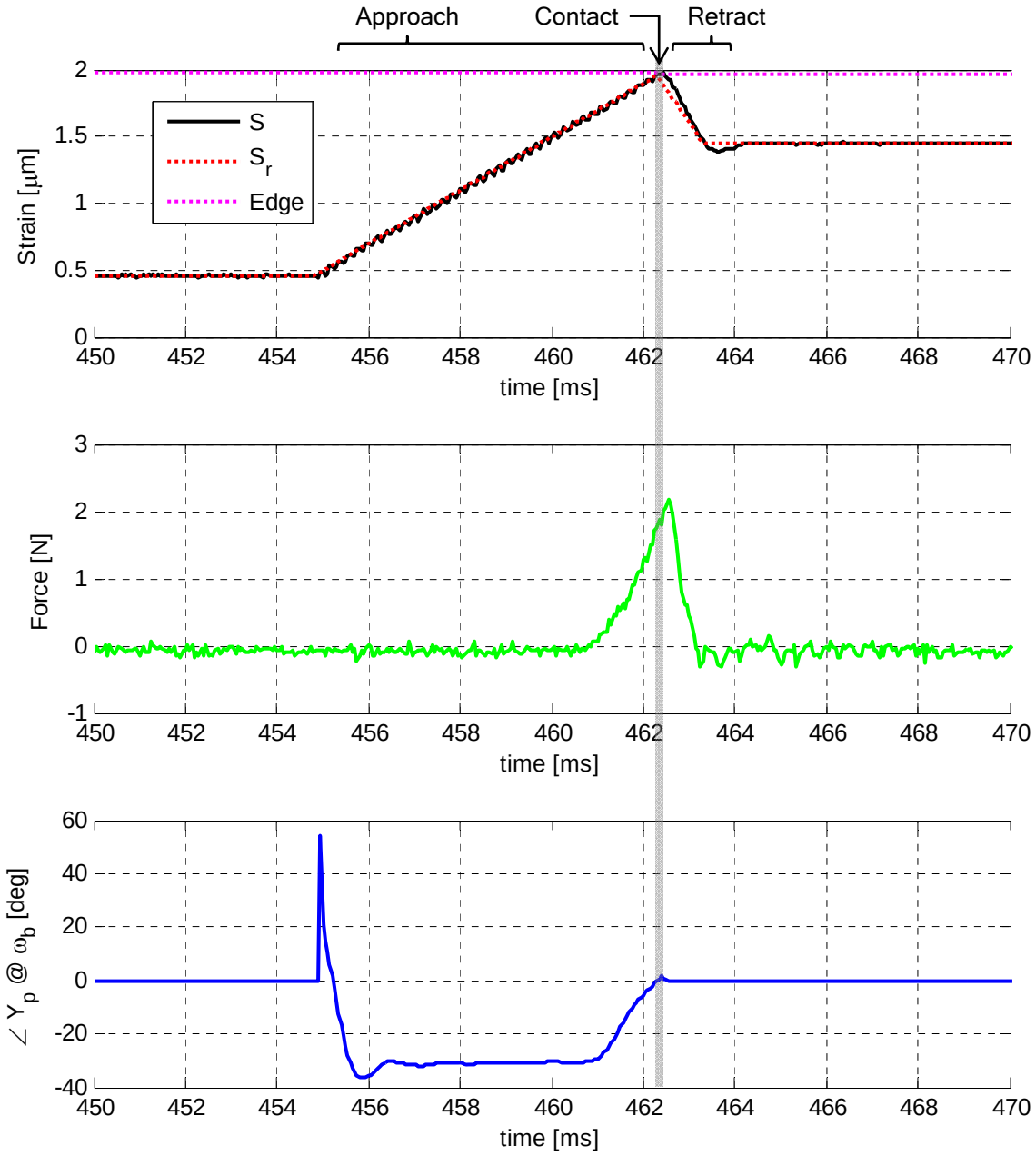

Figure 5-8: Self-sensing contact detection is used to detect the reticle's edge. The time plots of actuator's strain (top), contact force (middle), and phase response (bottom) are shown. In the top plot, the signals S_r, S, and *Edge* indicate the reference, the measured strain, and the registered edge location, respectively.

5.4 Application to Atomic Force Microscope

Application of the self-sensing contact detection method has been inspired by operation of self-sensing atomic force microscopes (AFM). In this section, we describe our high-accuracy atomic force microscope (HAFM), which uses a self-sensing probe [83]. We provide background information on the HAFM project, describe the HAFM design, instrumentation and control, and provide experimental results.

5.4.1 Background

The HAFM has been designed to be integrated with the sub-atomic measuring-machine (SAMM) positioning stage and be used for dimensional metrology with nanometer-scale accuracy. The project is a joint effort by researchers at MIT and UNC-Charlotte. The SAMM has been designed in the doctoral thesis of Holmes [33], and has more recently undergone extensive upgrades in measurement systems and control as described in [64]. HAFM's mechanical design was completed in the master thesis of Ljubicic [49]. The HAFM's electronics, instrumentation, and control were completed as a part of this thesis. The HAFM has been transferred and integrated with the SAMM stage at UNC-Charlotte. It is being used for dimensional metrology with nanometer accuracy over a measurement volume of 25 mm $\times$ 25 mm $\times$ 0.1 mm. Similar large-range AFMs have been designed for dimensional metrology by other institutes, such as Physikalisch-Technische Bundesanstalt (PTB) [17], National Institute of Standards and Technology (NIST) [45], National Metrology Institute of Japan (NMIJ) [57], and National Research Council of Canada (NRCC) [21].

A CAD model of the SAMM with the HAFM is shown in Figure 5-9. The sub-atomic measuring machine consists of two parts: an oil chamber and a metrology chamber. The platen is neutrally buoyant in fluorosilicone oil. The platen can be actuated in six degrees of freedom (DOF) by the four levitation linear motors. A sample holder, which carries the sample being measured, is in the metrology chamber and is fixed to the platen using support bars. The position of the sample holder is measured relative to the Zerodur metrology frame using laser interferometers for the in-plane

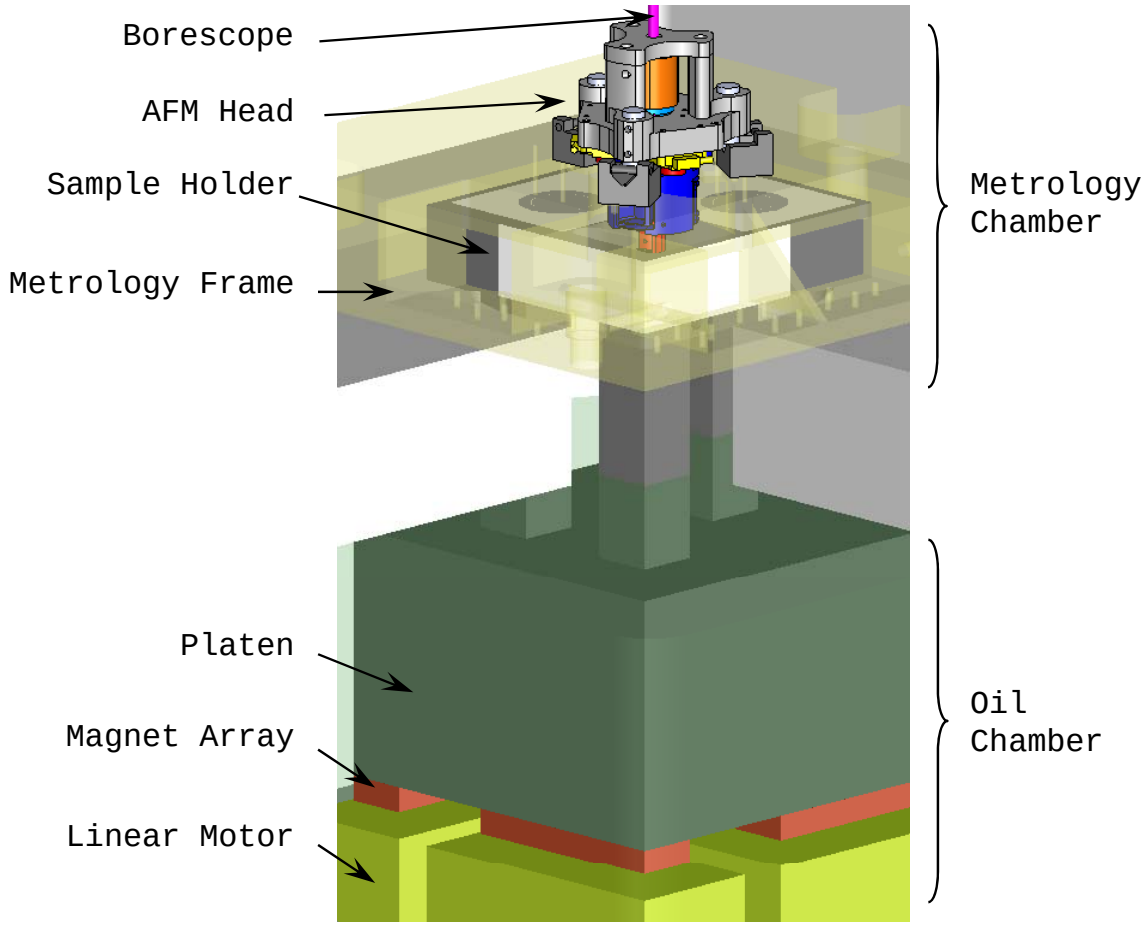

Figure 5-9: CAD drawing of the subatomic measuring machine (SAMM) with the high-accuracy atomic force microscope (HAFM) installed as its metrology probe.

DOFs (x, y, and θ_z) and using capacitive displacement sensors for the out-of-plane DOFs (z, θ_x, and θ_x). The HAFM is installed on the SAMM's metrology frame and measures and tracks the sample in the z-direction. A bore scope passes through the center of the HAFM and is used for visually locating features on the substrate to be measured.

5.4.2 High-Accuracy Atomic Force Microscope

The assembled HAFM and its cross-sectioned CAD model are shown in Figure 5-10. The AFM probe is fixed to the bottom of the moving stage. The moving stage is constrained by the guide flexure to motion in the Z-direction only. The moving stage is driven by a piezo stack actuator with a range of 20 μm. The actuator is

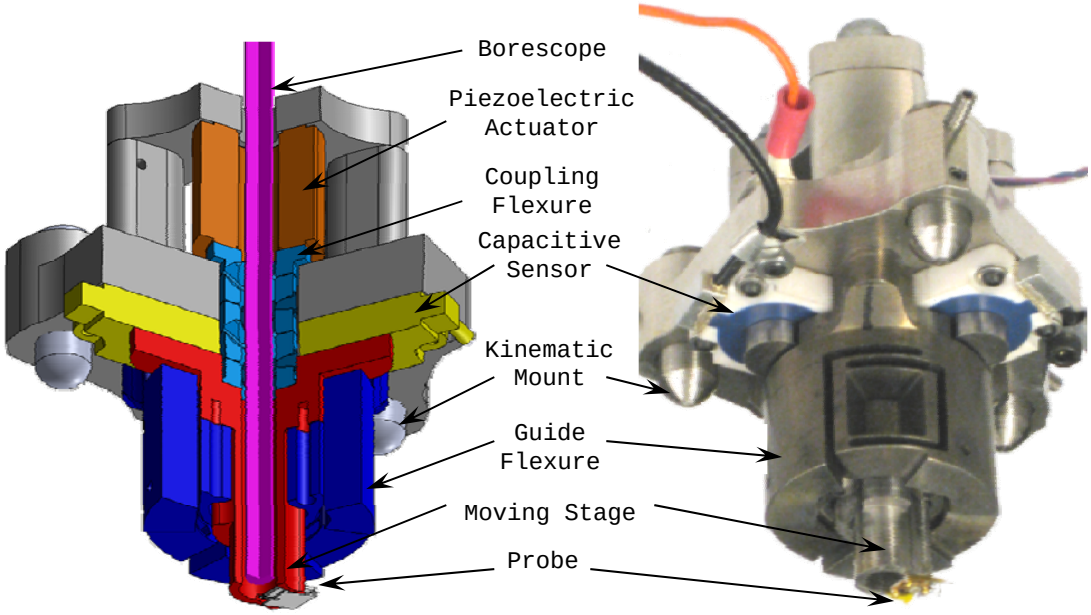

Figure 5-10: Photo of the assembled HAFM (right) and cross-sectioned CAD model of the HAFM (left).

connected to the moving stage using a coupling flexure. The coupling flexure is designed to be rigid only in the Z-direction in order to transfer only the Z-motion of the piezoelectric actuator, while attenuating its error motion. The position of the moving stage is measured using three capacitive displacement sensors symmetrically arranged around the moving stage. The center axis of the HAFM is left free for a borescope to pass through. More details on the HAFM's mechanical design can be found in the Master's thesis of Ljubicic [49].

A simplified block diagram of the HAFM control system is shown in Figure 5-11. Here, we use a self-sensing Akiyama probe. The preamplifier buffer and the self-resonance control electronics are used to amplify the probe's signals and set it in controlled-amplitude self-resonance. We use the probe in the period-measuring mode. The tracking controller uses the probe's self-resonance period as feedback and drives the piezoelectric actuator to track the sample surface. We implement the tracking controller using an FPGA device. The real-time computer is used for logging the image data and controlling the SAMM stage.

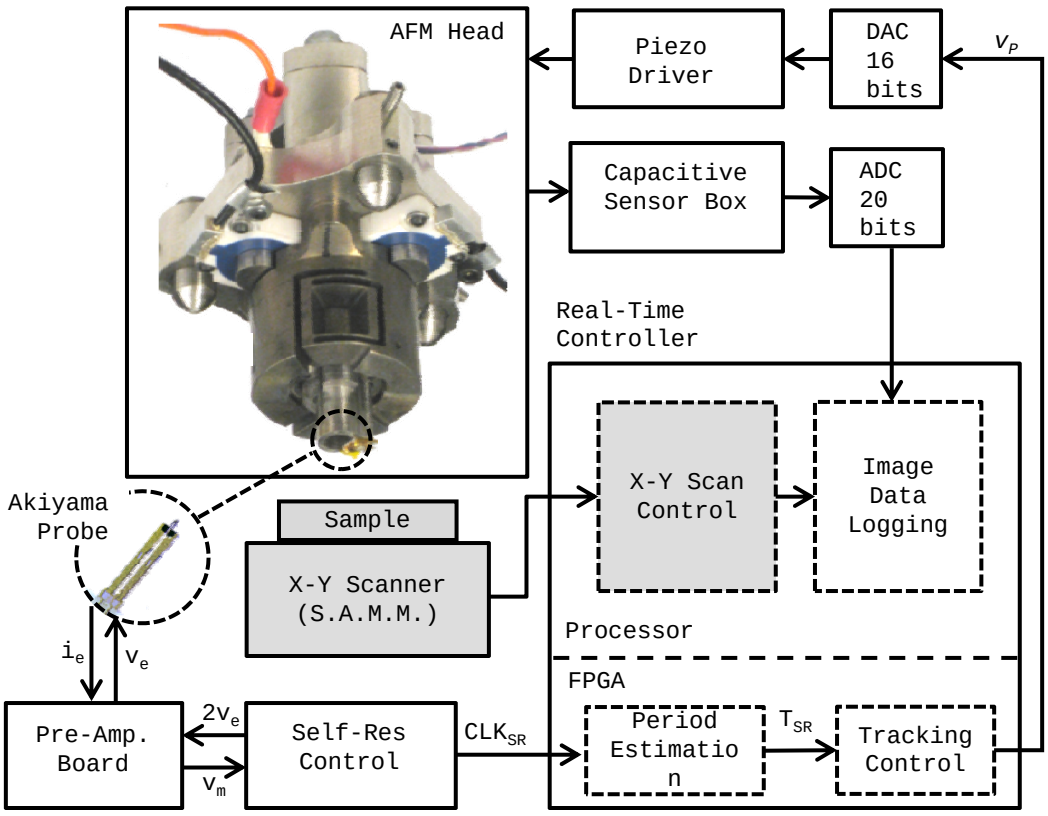

Figure 5-11: Simplified block diagram of the HAFM system.

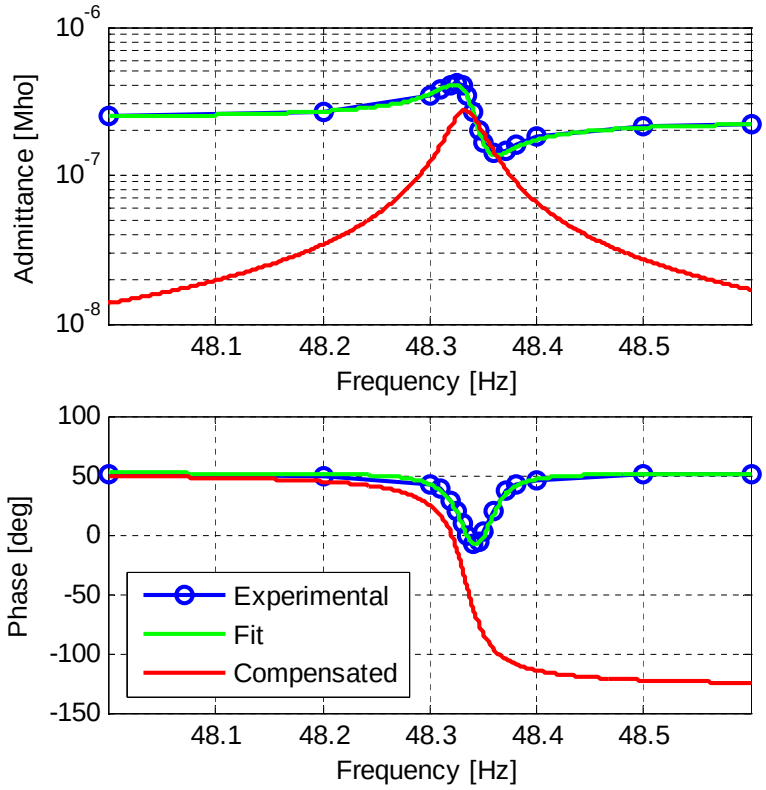

Figure 5-12: An Akiyama probe's admittance frequency response shown based on our experimental data (blue), the analytical fit(green), and the compensated analytical function (red).

5.4.3 Self-Sensing Probe

Conventional AFM systems use an optical-lever for sensing the probe's oscillation. To achieve a compact design, which can be more easily integrated with the SAMM, we use a self-sensing probe that eliminates the need for the optical-lever mechanism. We use a commercially available self-sensing Akiyama probe[3]. The Akiyama probe consists of a cantilever symmetrically attached to the ends of a tuning fork's prongs. Applying a voltage to the piezoelectric tuning fork creates an in-plane motion of the tuning fork prongs, which results in an out-of-plane tapping motion of the cantilever tip. The probe has been invented by Akiyama [2].

The Akiyama probe can be used for self-sensing contact detection as described in Section 5.2. The probe's admittance frequency response is shown in Figure 5-12 near

[3]The Akiyama probe is a product of NANOSENSORS^{TM}. Pictures of the Akiyama probe are a courtesy of NANOSENSORS, and are used with permission (http://www.nanosensors.com).

its first resonance frequency of about 48.3 kHz. The experimentally captured probe admittance consists of the parallel combination of a capacitive admittance (Y_c) and a piezoelectric admittance (Y_p). An analytical model is fitted to the frequency response using (5.4) with the added low-pass dynamics of the measurement buffer as

$$Y_t(s) = [\frac{p^2 s}{ms^2 + bs + k} + Cs]\frac{1}{\tau s + 1}, \tag{5.26}$$

where τ is the time-constant of the measurement buffer. The values for the fitted model are

$$\begin{aligned} m/p^2 &= 1.372 \times 10^4 \ \ [\mathrm{H}] \\ b/p^2 &= 2.867 \times 10^6 \ \ [\Omega] \\ k/p^2 &= 1.265 \times 10^1 5 \ \ [\mathrm{F}^{-1}] \\ C &= 0.99 \ \ [\mathrm{pF}] \\ \tau &= 2.59 \times 10^{-6} \ \ [\mathrm{s}]. \end{aligned}$$

The close agreement between the experimental data and the fitted model shown in Figure 5-12 confirms the validity of the model developed in Section 5.2.

To obtain the symmetric resonance corresponding to the mechanical resonance of the probe, we cancel the capacitive current as will be described in Section 5.4.5. The compensated piezoelectric admittance is shown in Figure 5-12 in red. As can be seen, the piezoelectric admittance peaks at a slightly higher frequency and is symmetric. For maximum sensitivity, we use the probe's compensated piezoelectric admittance frequency response at its resonance frequency.

5.4.4 Frequency Measuring AFM

Due to its tuning fork design, the Akiyama probe's first mechanical resonance has a high quality factor of approximately 1000 in air. A high quality factor means a sharper resonance peak with more sensitivity to contact. However, a high quality factor

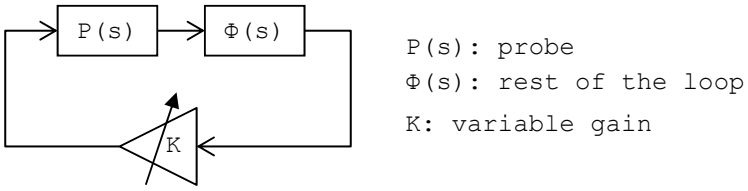

Figure 5-13: Simplified block diagram of the AFM self-resonance loop

resonator also dissipates less energy per cycle, which means any transient lasts longer before it disappears. This can reduce a probe's bandwidth if used in the amplitude or phase measuring mode, where it is excited at a fixed frequency and the changes in phase and amplitude are used as feedback for tracking the sample surface. Albrecht introduced the frequency-measuring AFM mode, which addresses this problem and eliminates the limit set on the detection bandwidth by the high quality factor [3]. Albercht uses constructive feedback, with an actively controlled feedback gain, to set the cantilever in controlled-amplitude self-resonance at its mechanical resonance frequency. In this configuration, the frequency of self-resonance shifts with the probe's mechanical resonance frequency, and thus can be used as feedback to track the sample. Atia uses this method with a near-field scanning optical microscope [11].

A simplified block diagram of a self-resonance loop, which consists of the probe $P(s)$, variable gain K, and the rest of the loop $\Phi(s)$, is shown in Figure 5-13. In order for this loop to self-resonate with a constant amplitude, it must have an imaginary pole pair on the imaginary axis, and hence, s=$j\omega_m$ must be a solution to the loop's characteristic equation:

$$\begin{aligned} & -P(s)\Phi(s)K+1|_{s=j\omega_m}=0 \\ & \Rightarrow P(s)\Phi(s)|_{s=j\omega_m}=1/K \\ & \Rightarrow \begin{cases} |P(s)\Phi(s)|_{s=j\omega_m}=1/K & \text{Amplitude Condition} \\ \angle P(s)|_{s=j\omega_m}=-\angle\Phi(s)|_{s=j\omega_m} & \text{Phase Condition} \end{cases}, \end{aligned} \tag{5.27}$$

For the loop to self-resonate at ω_m, the loop-transmission frequency response must satisfy the phase and amplitude conditions of (5.27). The phase response of the rest of the loop (Φ) is manually set, such that the phase condition is satisfied at

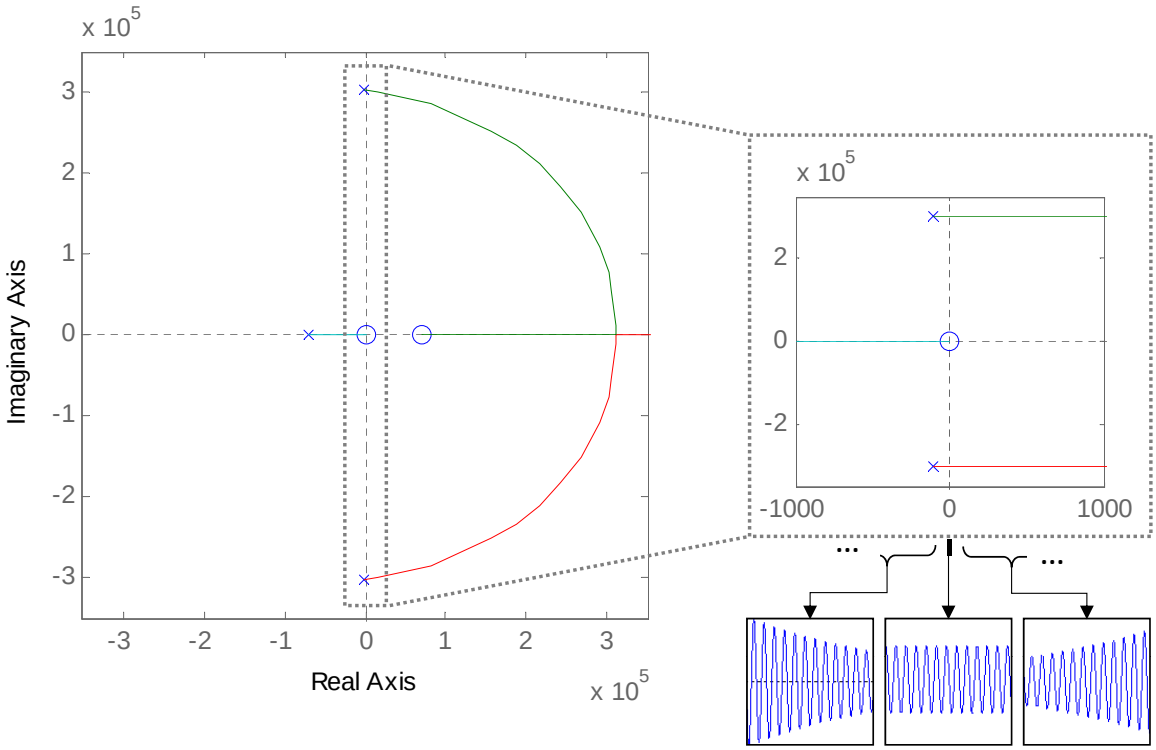

Figure 5-14: Root locus plot of the self-resonance loop

the probe's mechanical resonance frequency (ω_m). This ensures that self-resonance occurs at the probe's mechanical resonance frequency. The amplitude condition is satisfied by the amplitude controller, which actively varies the feedback gain K. The amplitude controller changes K to increase or decrease the loop gain to make the oscillation amplitude grow or decay respectively. The self-resonance control can also be analyzed using the root-locus plot shown in Figure 5-14. Increasing or decreasing the loop gain will shift the poles between the right- and left-half plane, resulting in the oscillation envelope to grow or decay respectively. Setting the phase for the rest of the loop (Φ) changes the departure angle of locus from the imaginary pole pair. We set the phase such that the locus for a positive feedback gain departs horizontally toward the imaginary axis. In this way, the probe will self-resonate at the same frequency as the mechanical resonance's imaginary pole pair. More information on modeling and controlling self-resonance can be found in [70, 83].

Setting the probe in self-resonance results in the probe oscillating at the frequency where it satisfies the phase condition in (5.27). As a result, Albercht's frequency-

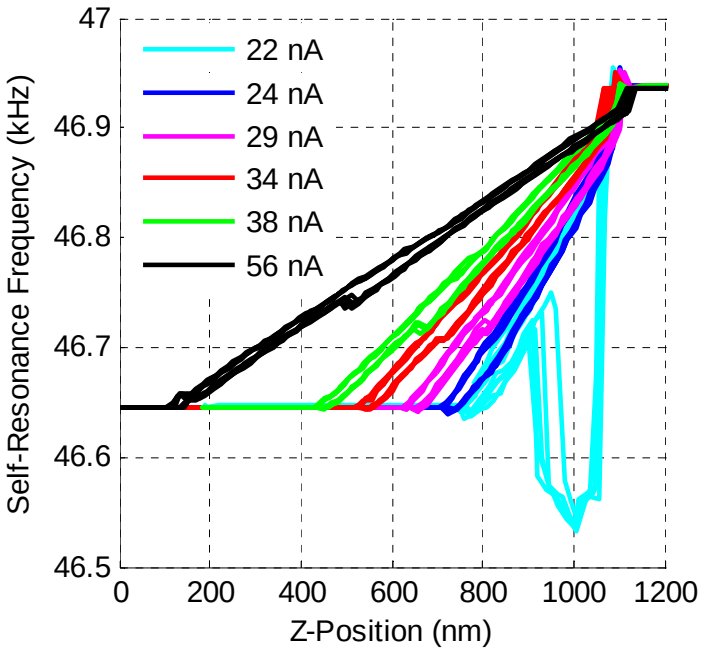

Figure 5-15: Experimentally obtained sense curves for an Akiyama probe under test at different oscillation amplitudes.

measuring method can also be implemented by measuring the probe's phase response at its mechanical resonance and changing its excitation frequency to control the measured phase response. Edwards [20] and Rychen [71] measure the probe's phase response and control it by changing the excitation frequency. They use the varying excitation frequency as feedback to track the sample surface. This implementation of frequency-measuring AFM requires a phase-locked-loop and a variable-frequency excitation source. However, it provides more flexibility and can potentially achieve a better resolution if used with a locked-in amplifier.

We use the frequency-measuring method for our AFM. Similar to Albercht's implementation, we set the probe in constant amplitude self-resonance and use the probe's self-resonance frequency as feedback to track the sample surface. More details on the implementation of the self-resonance controller is provided in Section 5.4.5. The sense curves for the Akiyama probe, which is set in self-resonance, are shown in Figure 5-15. As the probe approaches the sample, the self-resonance frequency increase from 46646 Hz, when free in air, to 46938 Hz when completely in contact with the sample. At a smaller oscillation amplitude, for a given approach distance, the probe spends

Table 5.1: Table of the probe sensitivity at different oscillation amplitudes

Electrical Amplitude (nA)	Estimated Mechanical Amplitude (nm)	Sensitivity (Hz/nm)
22	376	0.777
24	442	0.661
29	527	0.554
34	616	0.474
38	702	0.416
56	1074	0.272

a longer portion of its oscillation period in contact with the sample. As a result, the probe's sensitivity increases as the oscillation amplitude is decreased. A list of the probe's sensitivity at different oscillation amplitudes is provided in table 5.1. The mechanical oscillation amplitude is estimated as the length of Z-position range over which the frequency changes. As the probe approaches the sample, it takes a distance equal to the amplitude of oscillation to go from having no contact to having contact throughout the oscillation cycle. There is a minimum oscillation amplitude, below which stable oscillation cannot be sustained perhaps due to the small scale of the signals and pour signal-to-noise ratio. That minimum amplitude limit is found to be 22 nA, which is equivalent to approximately 376 nm tip oscillation amplitude.

5.4.5 Probe Electronics

Following the method introduced by Albercht [3], we set the probe in controlled-amplitude self-resonance using analog electronics. The electronics are adapted, with some modification, from the technical guide provided for the Akiyama probe [60]. We use a preamplifier board to amplify the small piezoelectric current close to the probe. A self-resonance control board is used to set the probe in controlled-amplitude self-resonance.

A schematic of the preamplifier board is shown in Figure 5-16. The preamplifier board has a transformer for interfacing the drive signal (V_E) from the self-resonance control board to the probe. Using a transformer prevents ground loops by providing

an AC coupled link, where the boards do not share a common ground. In this way, the ground nets of the preamplifier (CM_{PA}) and the self-resonance controller (CM_{SR}) boards are not connected in DC. A transformer with a center tap is used to obtain a signal opposite to the driving signal, which can be used for compensating the probe's capacitive current. The signal is used to drive a variable capacitor (VarC) and inject a current that cancels the probe's capacitive current. We tune the variable capacitor by minimizing the compensated probe current at a frequency well above the first resonance mode, for example at 100kHz, where the capacitive current is dominant. The circuit uses a transimpedance buffer for converting the piezoelectric current into a voltage measurement. The voltage signal is amplified again by another voltage buffer with a closed-loop gain of approximately five. The probe's current signal is very sensitive to noise. We use a miniaturized coaxial cable to shield the signal, as shown in the schematic. The circuit is designed, such that the shield and the current signal are at the same voltage. In this way, the shield's parasitic capacitance does not affect the current measurement, and the shield prevents stray electric field coupling. The transimpedance buffer's design keeps the connection to the probe at virtual ground. To ensure that the shield and signal voltages match, the shield is connected directly to the ground at the operational amplifier's non-inverting terminal.

A key part of the electronic design is the preamplifier's transimpedance buffer. It is important that the buffer has a high current to voltage gain, is stable, and has a high bandwidth. In order to achieve a relatively high crossover frequency, we use a de-compensated OP338, which is not unity-gain stable. Because the feedback resistor is large, the feedback at the cross-over is dominated by the capacitive voltage-divider formed by the feedback capacitor $C_1 = 1\ pF$ and the parasitic capacitance between the op-amp's inverting and non-inverting terminals. The parasitic capacitance consists of the op-amp's input capacitance as well as the shield and the circuit board's stray capacitance. With the parasitic capacitance being larger than the feedback capacitance, the capacitive voltage-divider's gain is significantly smaller than unity and can stabilize the de-compensated op-amp.

The schematic design of the self-resonance control board is shown in Figures 5-

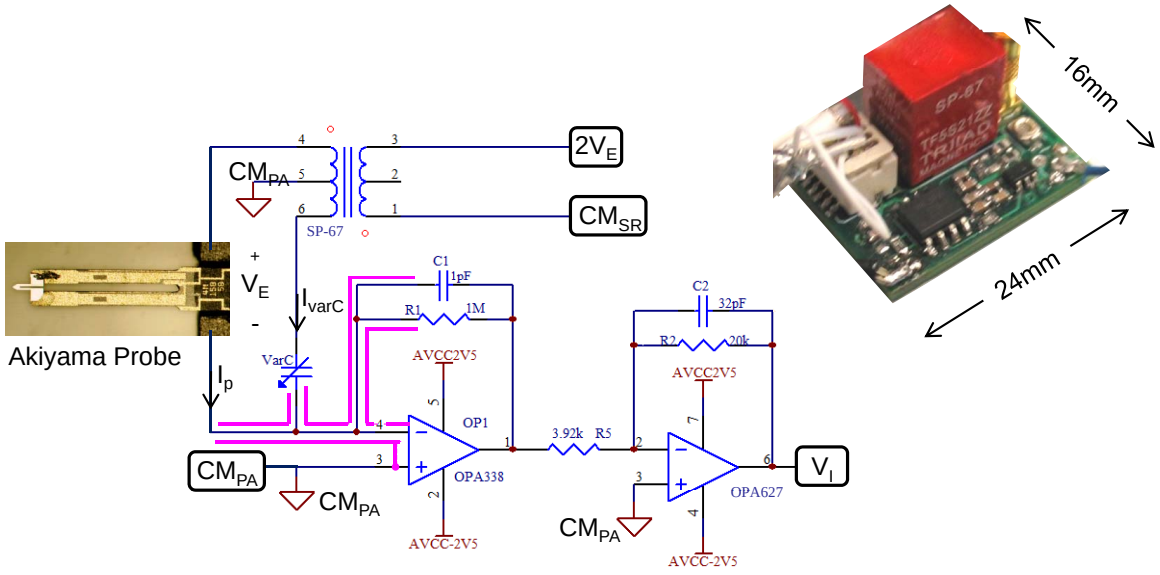

Figure 5-16: Schematic design of the preamplifier board. The picture of the Akiyama probe is courtesy of NANOSENSORS^{TM}. Shield connections are shown at input terminals of operational amplifier $OP1$.

17 and 5-18. As shown in Figure 5-17, we use a fully differential input buffer to measure and filter the amplified current measurement (V_I) from the preamplifier board. We convert the buffered differential signal (U_P and U_N) into a single ended signal (U_I) using an analog adder-subtractor buffer. We measure the period of the self-resonance using an FPGA device. An AD790 precision comparator is used to convert the differential current measurement signals (U_P and U_N) into a digital square-wave signal that can be read by the FPGA's digital input.

As shown in Figure 5-18, we use a precision rectifier and a low-pass filter to estimate the self-resonance signal's amplitude. We use an analog amplitude-controller consisting of an integrator and a lead-lag filter. The controller's proportional gain can be tuned using the POT2 potentiometer. The reference voltage can be adjusted using the POT3 potentiometer. The amplitude-control loop is nonlinear. We apply a resistor-capacitor (RC) low-pass filter (R_{30} and C_{18}) to the reference amplitude to ensure that rapid changes in the reference do not destabilize the nonlinear amplitude control system. The amplitude controller works by changing the feedback gain. We use an analog multiplier to apply the changing feedback gain to the current measurement. We use an all-pass filter to adjust the feedback phase and make sure that the

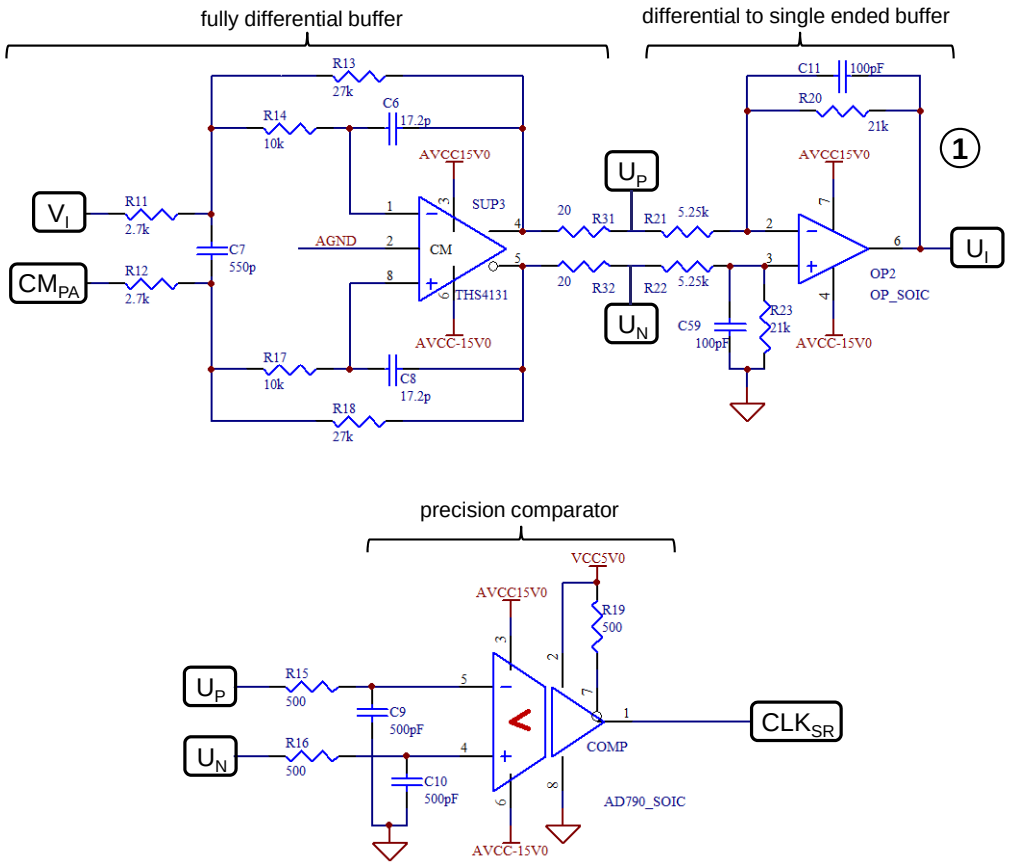

Figure 5-17: Schematic design of the self-resonance control board showing the fully-differential input buffer and precision comparator module used to digitize the self-resonance signal.

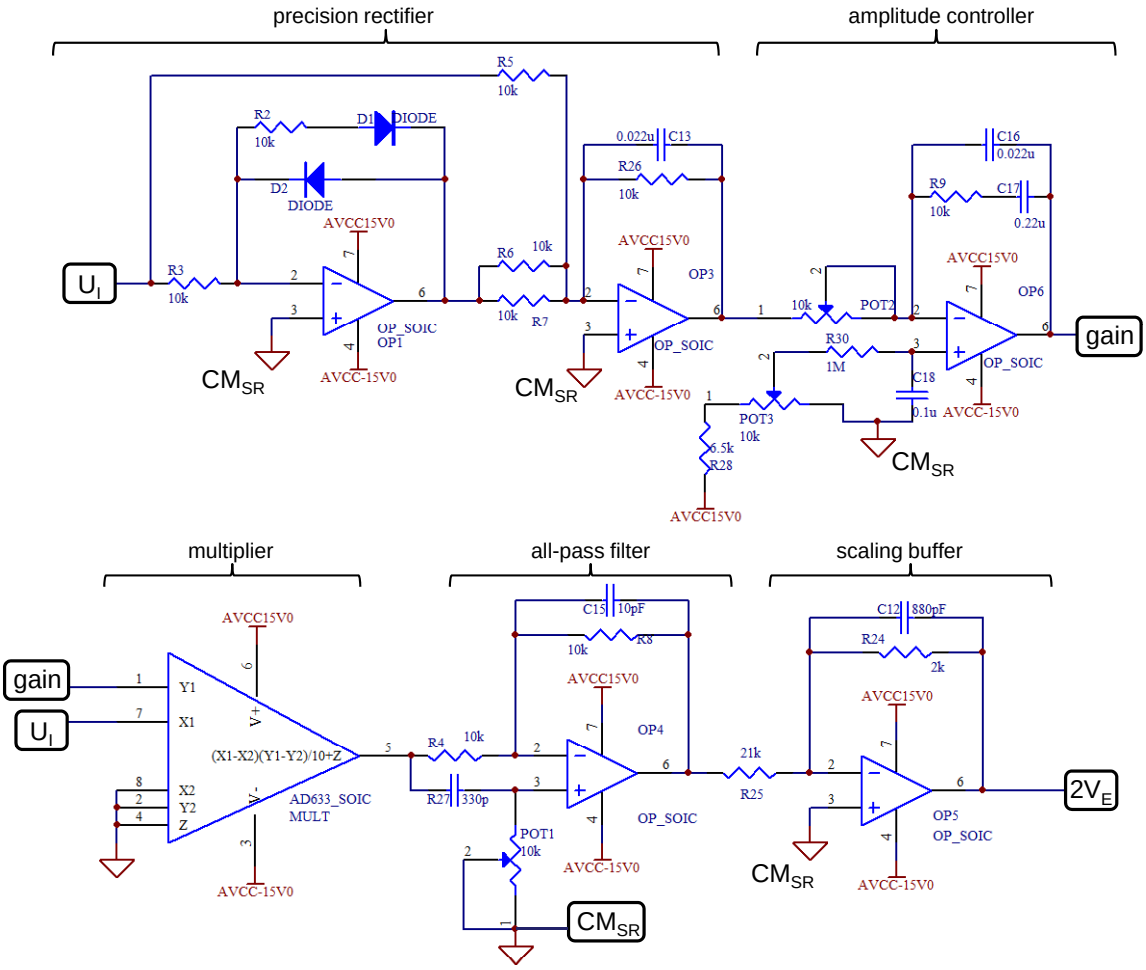

Figure 5-18: Schematic design of the self-resonance control board showing the control blocks consisting of amplitude measurement, loop gain control, and phase shifting.

phase-condition, given by (5.27), is satisfied at the mechanical resonance frequency. Finally, we use an additional analog buffer for scaling and low-pass filtering the feedback signal. The feedback signal must be low-pass filtered to avoid exciting the higher resonance modes of the probe.

5.4.6 Tracking Controller

We design a tracking controller, which uses the probe's self-resonance period as feedback to move the probe normal to the sample surface in order to track the surface. We have designed the tracking controller using loop-shaping. The frequency response of the tracking plant from the piezo amplifier's reference voltage to the change in the

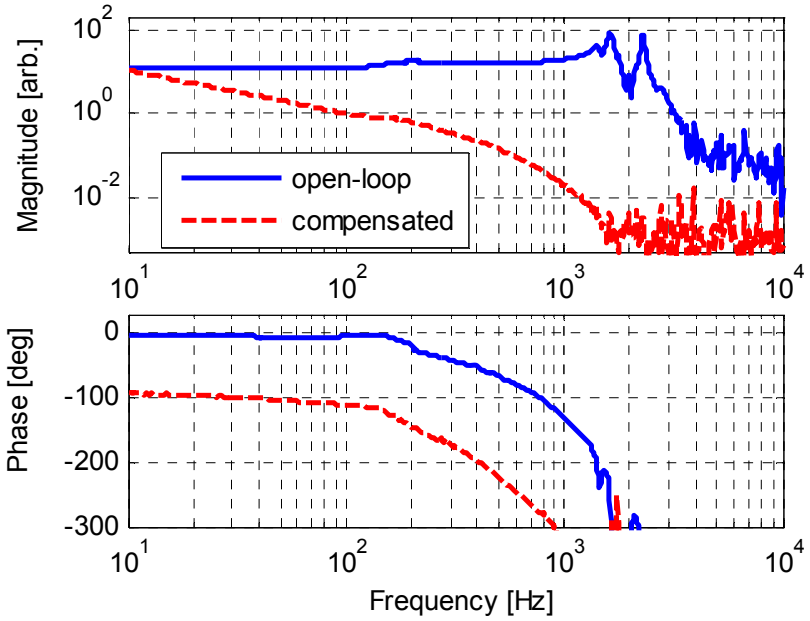

Figure 5-19: Bode plot of the tracking control system's open-loop and compensated-loop frequency responses.

self-resonance period is shown in Figure 5-19. The two resonance peaks are believed to be due to the AFM head's structural modes. The probe has nearly flat response up to the resonance peaks. The compensated loop-return-ratio is also shown in Figure 5-19. The compensated loop has a unity cross-over frequency of 100 Hz with 65° of phase margin. Relatively large phase margin is helpful for keeping this nonlinear loop stable through large-signal transitions.

The control law consists of an integrator, a low-pass filter, and two notch filters at 1.5 kHz and 2.3 kHz. The integrator provides loop gain below the cross-over frequency and a slope of -20dB/decade for achieving a robust cross-over point. We use a low-pass filter to attenuate the controller gain at frequencies higher than the loop cross-over frequency. We use two notch filters to mask the structural modes. A block diagram of the discrete control law is shown in Figure 5-20.

As shown in Figure 5-21, the period estimation and the tracking controller are implemented on a National Instrument's NI-PXI-7813R FPGA card. We detect the edges of the self-resonance signal using digital logic. We use a 200-MHz counter as the time reference. At every edge, we store the counter's value in a FIFO. The

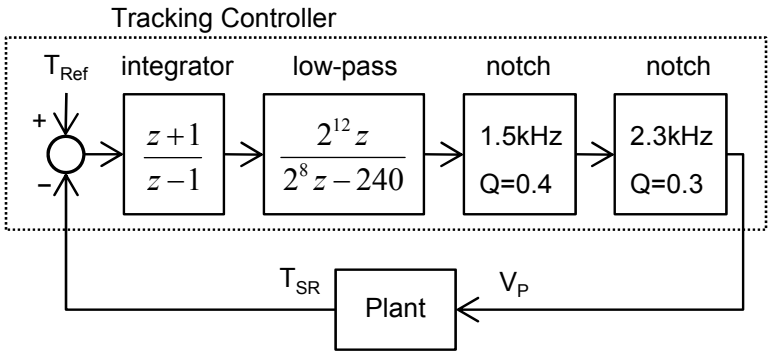

Figure 5-20: The tracking controller's discrete time control law. The controller will be sampled at two times the probe's resonance frequency; i.e. sampling is synchronous with the edges of the square wave CLK_{SR}, and thus sampling is at about $2 \times 46.8\ kHz = 93.6\ kHz$ where the exact value varies with the tip-sample engagement.

time-stamps are read from the FIFO within the slower running while-loop, where the change in the time stamp is calculated and is used as a measurement of the self-resonance period. The tracking controller uses this period measurement as feedback to follow the sample surface. The controller loop reads a new time-stamp as soon as a new value is written to the FIFO. Because there are two edges (falling and rising) per oscillation cycle, the controller samples at two times the self-resonance frequency. As will be explained in Section 5.4.7, sampling the controller synchronous to the tapping motion improves the tracking noise.

The tracking controller's step response is shown in Figure 5-22 at 100-Hz and 1-kHz measurement bandwidths. As can be seen with the 1-kHz measurement bandwidth, the HAFM's structural vibration modes are excited and are present in the tracking response. This is expected because the controller does not control the vibration modes. The notch filters only mask the modes, so that they are not visible to the controller and do not affect the system's stability. The step response with 100-Hz measurement bandwidth filters out the response due to the vibration modes and is much less noisy.

The HAFM's noise, when tracking a stationary sample, is measured using the capacitive displacement probes and is shown in Figure 5-23 at 100-Hz and 1-kHz measurement bandwidths. The loop bandwidth remains at 100 kHz for both of these

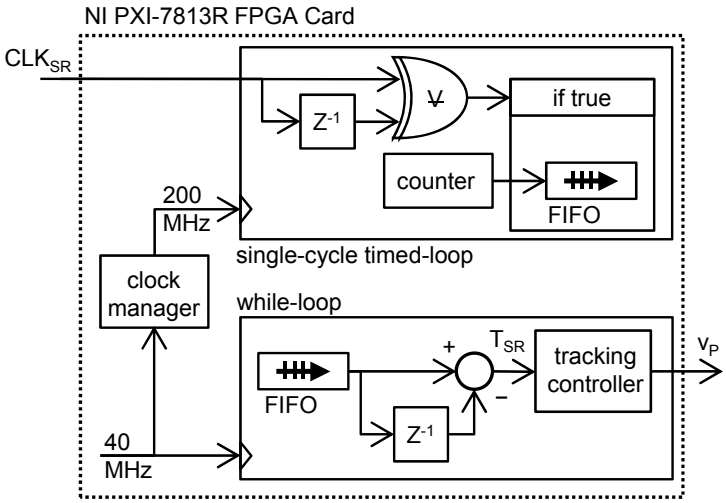

Figure 5-21: The implementation of period estimation and tracking controller on the FPGA device. The controller within the while-loop is updated at every rising or falling edge of CLK_{SR}, when a new value is written to the FIFO.

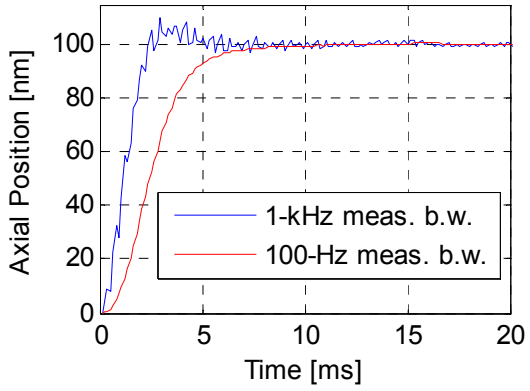

Figure 5-22: The step response of the HAFM's closed loop tracking system viewed at 100-Hz and 1-kHz measurement bandwidth.

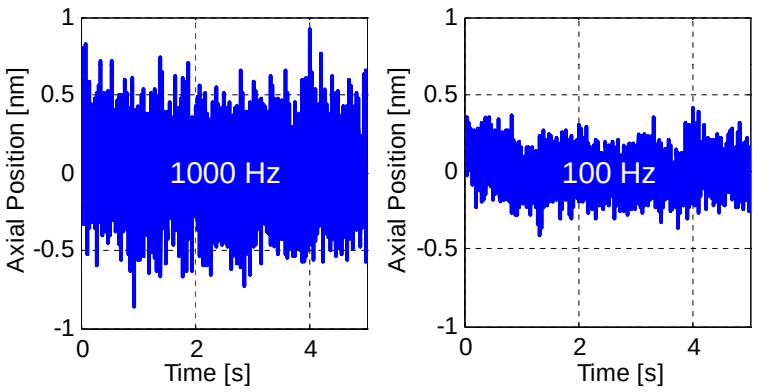

Figure 5-23: The HAFM's noise when tracking a stationary sample surface, viewed at 100-Hz and 1000-Hz measurement bandwidths.

measurements. The tracking noise is 0.12 nm and 0.24 nm RMS over five seconds at 100-Hz and 1000-Hz measurement bandwidths. The capacitive displacement sensors are the major contributors to the measured noise.

5.4.7 Tapping-Synchronous Controller Sampling

The probe's self-resonance period is used as feedback by the tracking controller. The period measurement updates at the zero-crossing edges of the self-resonance signal. There is a non-integer mismatch between the control and measurement update rates if the controller is sampled at a fixed rate in time. Such non-integer sampling mismatch within a control loop can introduce low-frequency aliased components, which will significantly degrade the controller's performance. We thus sample the controller synchronously with the zero-crossings of probe's self-resonance signal [5]. In this way, the measurement and control sampling rates will be identical and there will be no non-integer sampling rate mismatch.

Figure 5-24 shows the block diagram of the tracking control loop. The transfer function M(s) represents the HAFM actuation dynamics from the reference piezo voltage v_P to probe motion z. We model the probe as a constant gain p representing the probe's sensitivity in Hertz per nanometer. We use a probe sensitivity of 0.5 Hz/nm, which corresponds to the probe oscillating with a current amplitude of 34 nA. Measuring the period as the time between zero crossings of the signal is equivalent

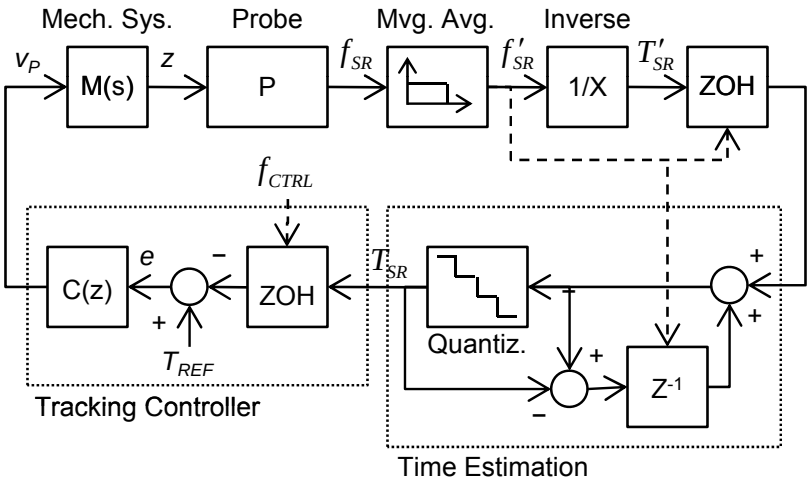

Figure 5-24: Block diagram of the HAFM's tracking control loop including the discrete-time measurement and control sampling. The dashed line indicates the frequency at which the blocks are updated.

to applying a moving average filter, with an averaging window width equal to half of a self-resonance period, to the probe's frequency and inverting the average frequency (f'_{SR}) to obtain the period estimate (T'_{SR}). The value of the period is sampled at the zero-crossings of the self-resonance signal. We use a 200-MHz clock incrementing a digital counter to estimate the self-resonance period, which provides a resolution of ± 2.5 ns. This is modeled using a quantization block (Quantiz.) with a step size of 5 ns. Any timing gain or loss from this quantization in one period measurement is added to the next period measurement. In other words, the accumulated timing error due to time discretization is limited to ± 2.5 ns and the average period is correctly measured. The tracking controller compares the self-resonance period to a reference period to calculate the error, which is passed to the tracking control law (C(s)). The diagram shows the controller being sampled at f_{CTRL}.

Within the control loop, sampling occurs at two points: probe oscillation period measurement at f_{SR} and tracking control at f_{CTRL}. Sampling a signal creates replicas of the frequency content shifted by integer multiples of the sampling frequency [63]. If the two sampling rates are integer multiples, the shifts will fold back on each other. However, if a non-integer mismatch exists, the frequency content can be mixed. This is particularly bad if high frequency measurement noise is mixed into the low-

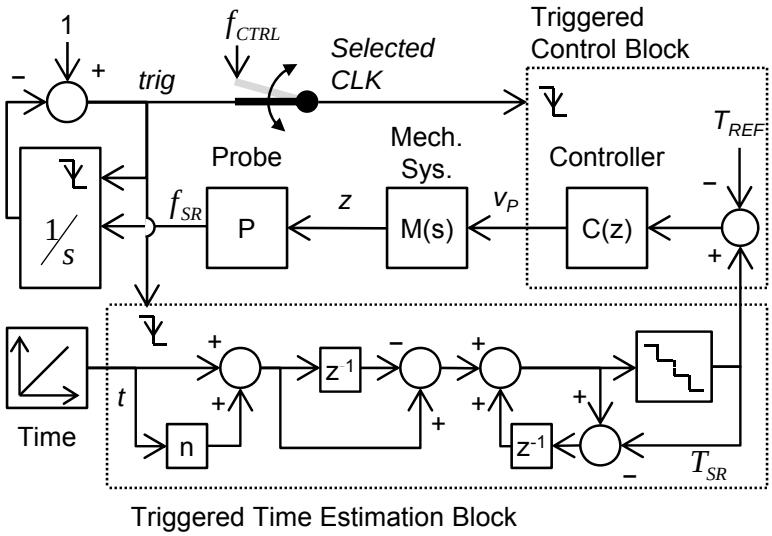

Figure 5-25: Diagram of the model used for simulating the tracking control loop in MATLAB Simulink.

frequency range, where the controller has enough bandwidth to respond and follow the noisy signal. Lu describes this issue in the case of using a digital quadrature optical encoder's feedback for position control. He addresses the problem by using a position estimator [50].

We test the significance of the non-integer sampling mismatch using a simulation model of the tracking controller in MATLAB Simulink. A block diagram of the model is shown in Figure 5-25.

As shown in Figure 5-25, the simulation uses Simulink's triggered blocks to model sampling. To efficiently generate the zero-crossings edges, we integrate in time the frequency of oscillation multiplied by two. Half of an oscillation period is completed and a new edge arrives when the integrator reaches the value one. We use this as a trigger for executing the triggered simulation blocks and for resetting the integrator. With this model, we can choose to sample the controller synchronous to the probe (f_{SR}) or at a fixed sampling rate (f_{CTRL}). The simulation also allows us to add noise (n) to the time measurement in order to model the effect of measurement noise, in addition to the time-discretization error. The noise sequence (n) is white noise, is randomly generated prior to simulation, and is loaded with time during simulation. The noise magnitude is equivalent to a signal-to-noise ratio of 100 for the self-resonance

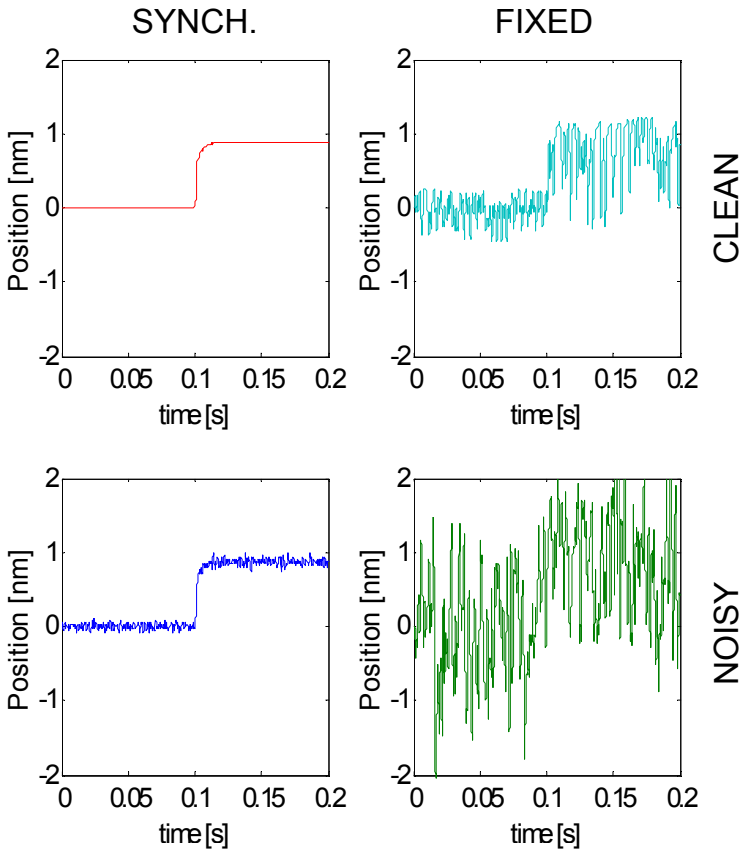

Figure 5-26: Simulated step responses for synchronous or fixed rate sampling with (noisy) or without (clean) measurement noise.

signal.

We use the simulation model to test and compare the HAFM's tracking noise for synchronous and fixed rate sampling with and without measurement noise (n). The HAFM's simulated 1-nm step response is shown in Figure 5-26. Note that the synchronously sampled controller's response is significantly less noisy than the fixed time sampling rate controller. With synchronous sampling, the measurement noise and the time discretization error remain at high frequency and are not mixed into the low frequency content, and thus they can be effectively filtered out by the tracking system's low-pass dynamics.

As another test, the root-mean-square (RMS) tracking noise of the HAFM is shown in Figure 5-27 versus the reference period for synchronous and fixed rate controller sampling and with or without added measurement noise. As can be seen,

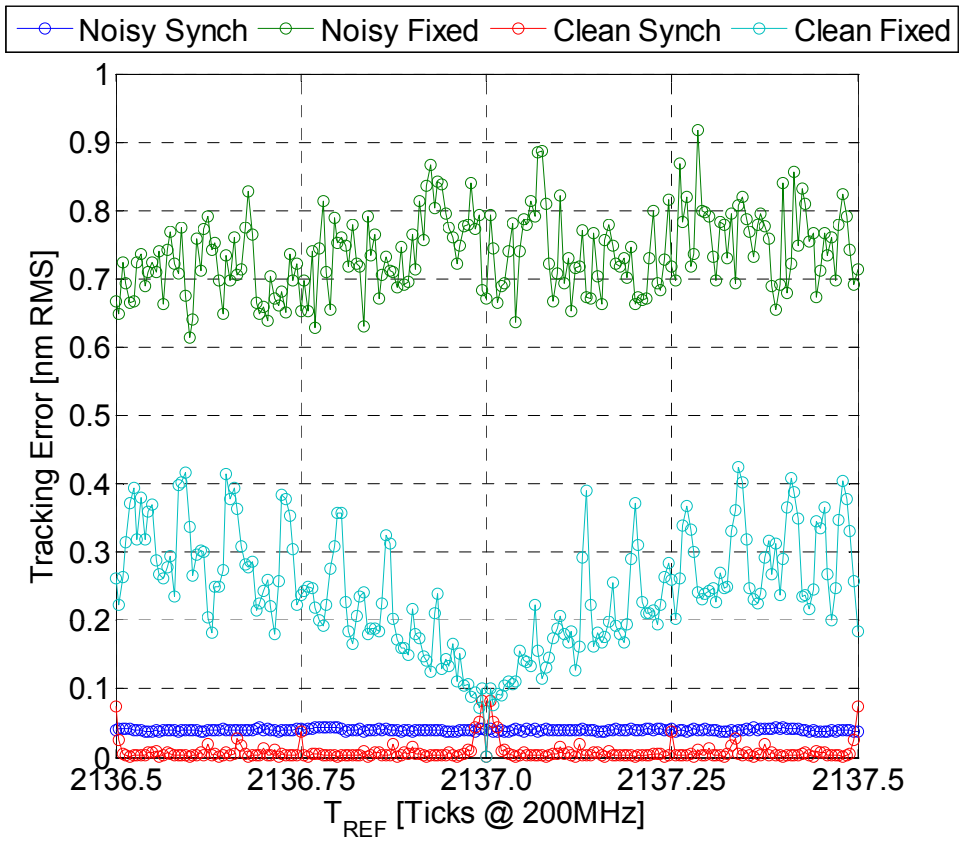

Figure 5-27: The HAFM's simulated RMS tracking noise for synchronous and fixed rate control with and without measurement noise.

synchronous sampling performs significantly better than fixed rate sampling. In the center, where $T_ref = 2137$ ticks, fixed-rate sampling performs well only if the signal is noise free because, in this special case, the fixed rate sampling is synchronous to the probe's oscillation. However, in presence of measurement noise, the RMS error is almost independent of the reference period and synchronous sampling performs significantly better than fixed rate sampling.

5.4.8 Experimental Results

Prior to transferring the HAFM to UNC-Charlotte, the HAFM was tested at MIT for imaging. We integrated the HAFM with a Veeco Multimode-E piezo-tube scanner which moved the sample to provide the XY raster scans. The HAFM provides the z-tracking. Resulting images of TGX01 and TGZ01 standard gratings manu-

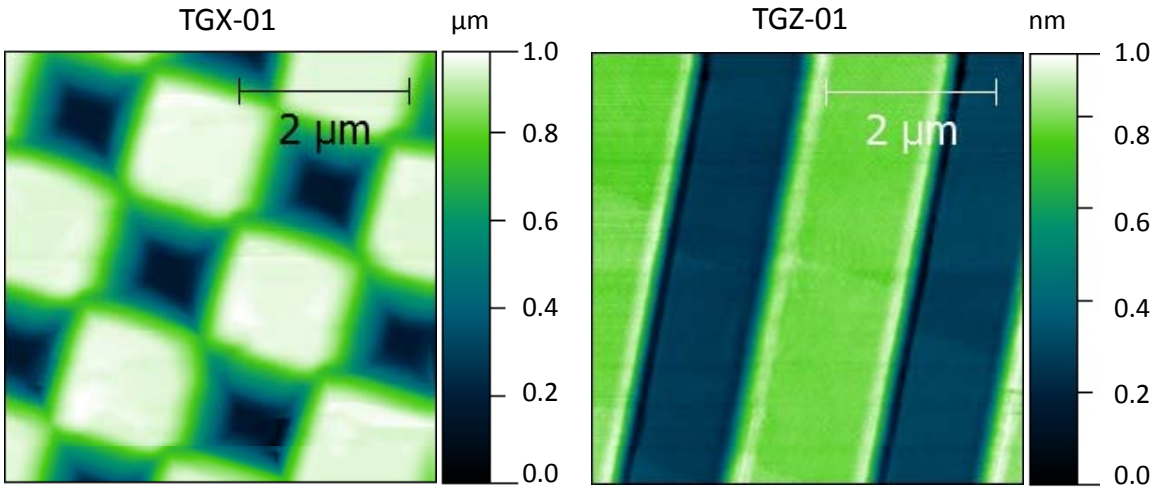

Figure 5-28: Images of the TGX01 (left) and the TGZ01 (right) standard gratings captured using the HAFM integrated with the Veeco Scanner at 10μm/s and 5μm/s scan speeds respectively.

factured by Mikromasch are shown in Figure 5-28. The TGX01 grating is a 1-μm high checkerboard grating. The grating has sharp edged flat tops, which can be used for extracting the geometry of the AFM tip. The TGZ01 grating has 25.5$\pm$0.1 nm peak-to-valley height. A histogram of the measured height across the TGZ01 grating is shown in Figure 5-29, which indicates an average to peak-valley height of 25.6 nm. Trace and retrace scans of the TGZ01 grating are shown in Figure 5-30 for different scan speeds. The line scan undershoots on the left side of the step. The undershoot is the same regardless of the scan direction. This makes us believe that the undershoot is a result of an actual tip-sample interaction, and it is not due to controller right half-plane zeros.

Once its performance was confirmed, the HAFM was transferred to UNC-Charlotte, where it was integrated with the SAMM and is now being used for metrology. Figure 5-31 shows the HAFM installed on the SAMM's metrology frame. Figure 5-32 shows an image of a triangular grating captured using the HAFM by Jerald Overcash at UNC-Charlotte. The grating has been manufactured using optical interference lithography using a tool created Mark Schattenburg at MIT, as described in [44]. The triangular grating has a pitch of 200 nm and a height of 30 nm. The image consists of 256 lines and is captured at a scan speed of 195 nm/s over 22 minutes and

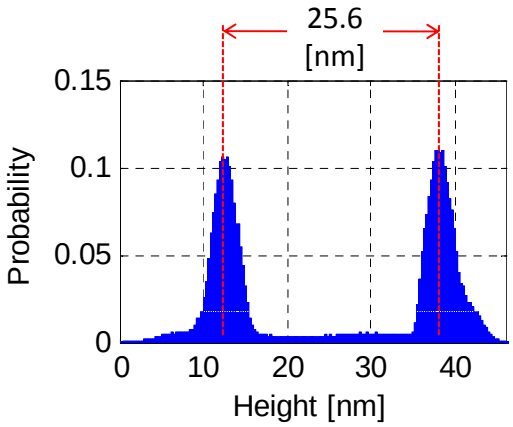

Figure 5-29: Histogram of height over the HAFM's image of TGZ01 grating.

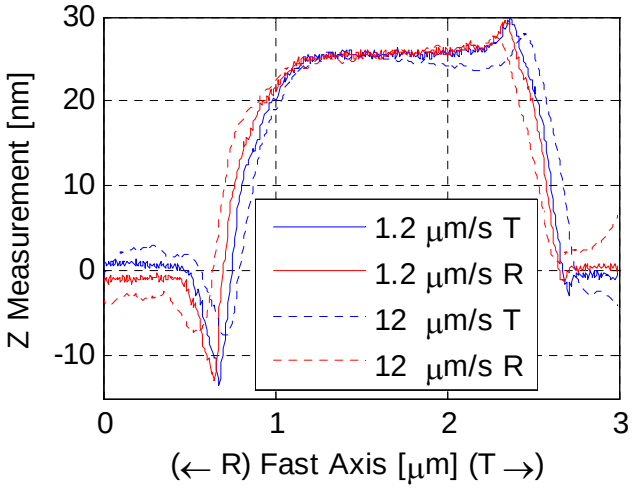

Figure 5-30: Trace and retrace line scans of the TGZ01 grating at different scan speeds.

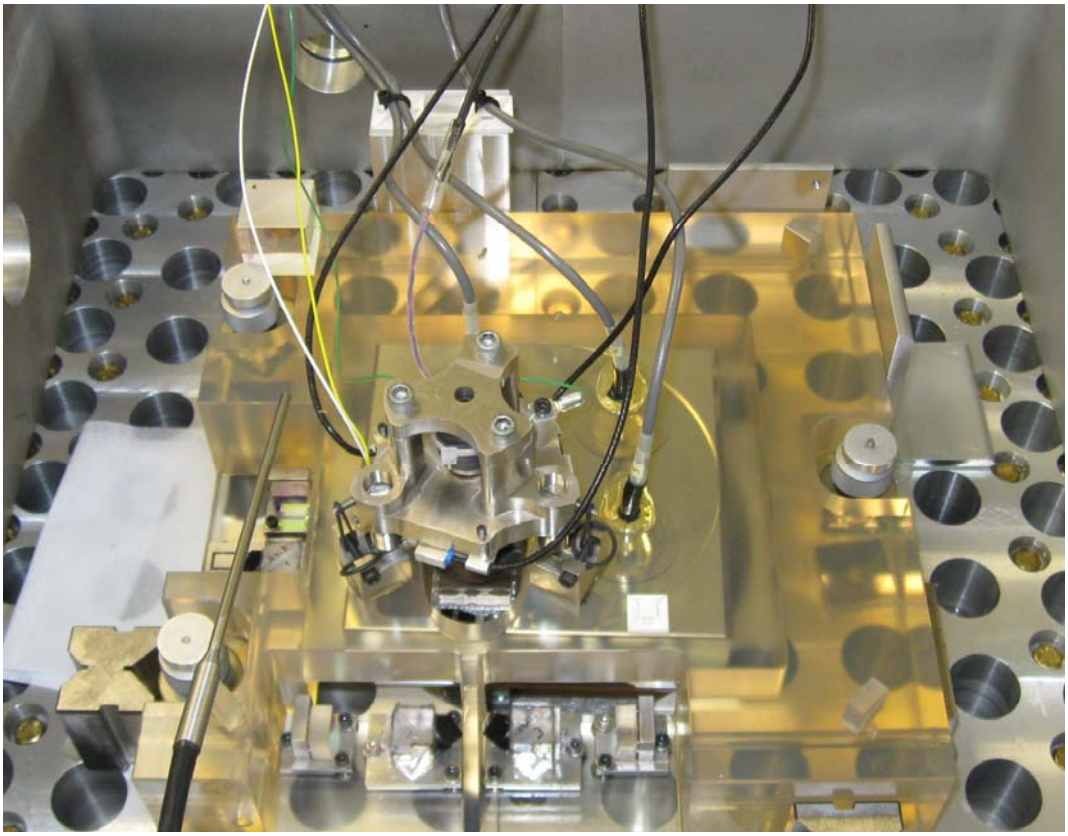

Figure 5-31: Image of the HAFM installed on the SAMM's metrology frame at UNC-Charlotte.

is plotted with no additional filtering or image correction.

5.5 Application to Magnetic Self-Sensing Imager

In this section, we present a magnetic macro-scale imager, which uses the self-sensing contact detection method. The imager uses a novel self-sensing and self-actuating electromagnetic probe. The design of the instrument has been inspired by the operation of AFMs. More details on the imager design, implementation, and control are provided in the following subsections.

5.5.1 Background

We have designed the macro-scale magnetic imager to be used in the teaching lab for Mechatronics (2.737), a graduate level course offered by the Mechanical Department

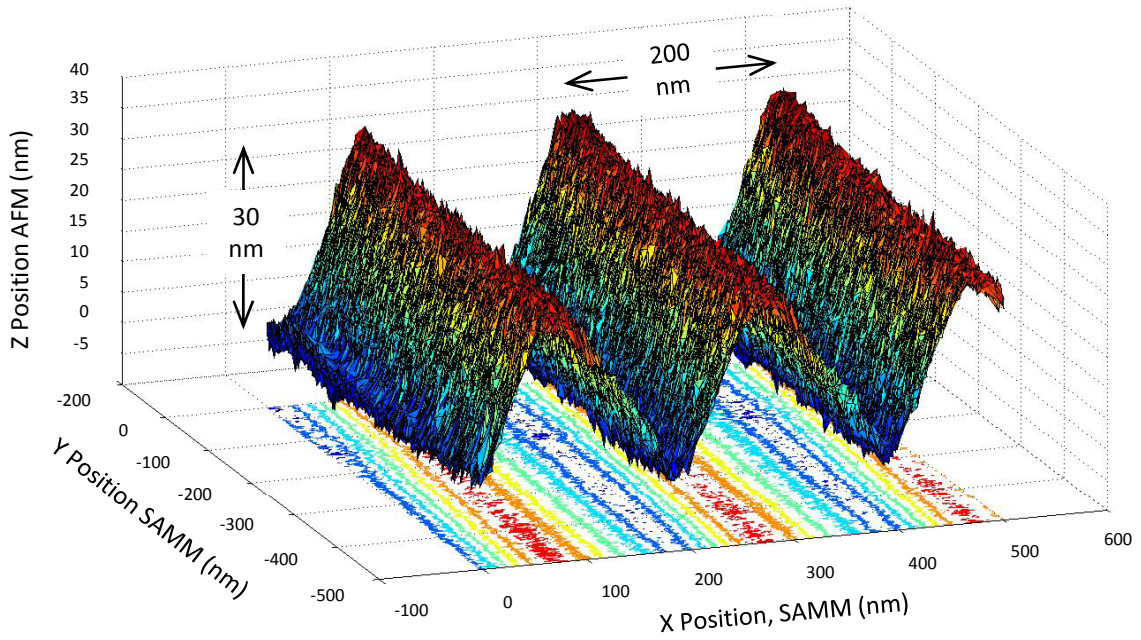

Figure 5-32: The HAFM's image of a saw tooth grating captured by Jerald Overcash using the HAFM and the SAMM at UNC-Charlotte.

at MIT. We have developed a set of eight new labs for this course based upon the imager hardware. The instrument is suitable for teaching because it is observable by the naked eye and can be touched and heard. It is rugged, easy to build, and very inexpensive. To the best of our knowledge the instrument is the first magnetic self-sensing self-actuating probe. It can also be scaled to a smaller size and be used as an inexpensive AFM.

5.5.2 Macro-Scale Magnetic AFM Probe

The self-sensing self-actuating probe consists of simply a metallic cantilever, a coil, and a permanent magnet. A CAD model of the probe is shown in Figure 5-33. The probe's support bracket is machined using a section of an L-shaped extruded aluminum bar. The cantilever is cut using water-jet out of a 0.008-inch thick sheet of Phosphorous Bronze Alloy 510. The cantilever is 1.5-inch long and 0.25-inch wide. The cantilever tip is created by bending down the sharp end of the cantilever. The cantilever is attached to the stator using a clamping piece bolted to the stator. The clamping piece has edges for a well defined and rigid contact. A solid clamp is nec-

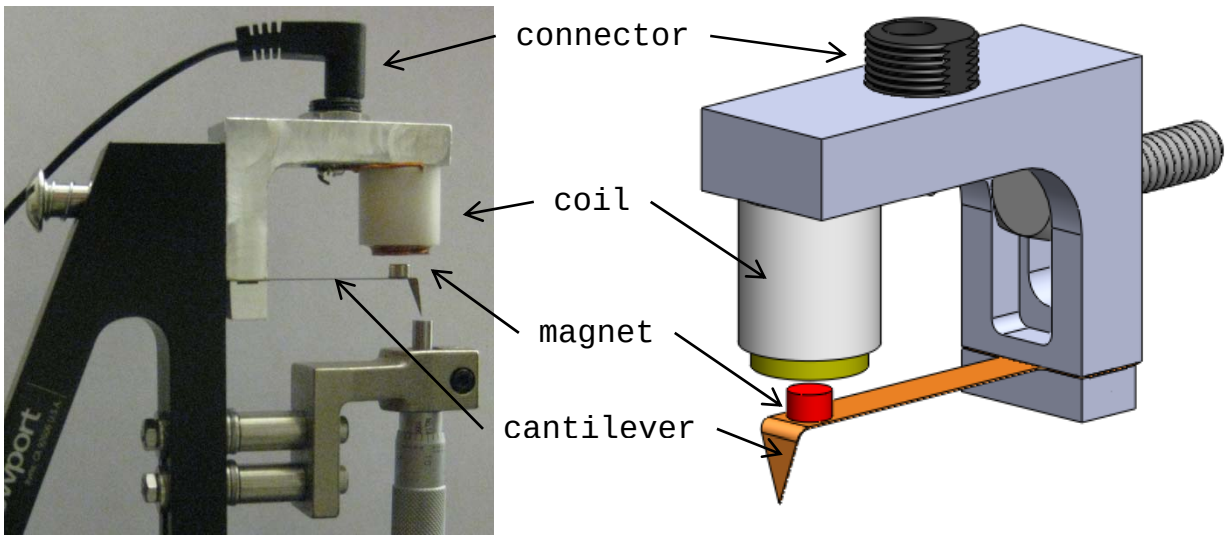

Figure 5-33: Assembled macro-scale self-sensing and self-actuating magnetic probe (top left), its CAD model (top right), and detailed side view showing the clamp design (bottom right).

essary for achieving a low-loss resonator. A magnet is attached to the end of the cantilever using a high-strength epoxy adhesive. The magnet is magnetized vertically. A coil, with 30 turns, is mounted onto the stator, and is positioned above the magnet. The coil is held by an adapter piece made out of Delrin and filled with epoxy. The adapter piece is bolted onto the stator. The coil's end wires connect to a barrel connector on the stator, which connects to the power amplifier. To exclude the connector's resistance from the coil voltage measurements, we use a four wire connection with the measurement buffer's input lines directly soldered to the coil.

The setup also includes a micrometer-head. We use the micrometer head for testing and calibrating the probe. The micrometer's anvil is used as a movable surface for interaction with the probe. By turning the micrometer, we can move the anvil up or down and thereby calibrate the probe. In this way, the probe can be tested without an actual scanner to move the sample under the probe.

5.5.3 Self-Actuation

Applying a current to the coil creates a Lorentz force acting between the coil and the magnet. We use this force to bend the cantilever up or down to follow the sample

surface. The actuation constant can be calibrated for each probe using the micrometer head. The probe under test is found to have an actuation constant of 0.5 mm/A. Considering our power amplifier's current limit of ±2 A, the probe thus has a tracking range of ±1 mm.

5.5.4 Self-Sensing

The magnetic probe is a mechanical resonator. The resonator's resonance frequency shifts to a slightly higher frequency as a result of contact. The resonator's mechanical dynamics reflect into the coil's electrical impedance response and can be measured. As a result, contact can be detected by monitoring the electrical signals of the coil. The probe can be modeled and used for self-sensing as described in Section 5.2.2. The probe's impedance frequency response is shown in Figure 5-34 based on experimental data as well as a fitted analytical model. When free in air, the probe's resonance peak is at 35.2 Hz. The probe's total impedance (Z_t) can be modeled using (5.8). The following parameters are obtained by fitting this model to the probe's frequency response:

$$\begin{aligned} m &= 0.6 \times 10^{-3} \quad [\text{kg}] \\ b &= 3.2 \times 10^{-4} \quad [\text{Ns/m}] \\ k &= 29.3 [\text{N/m}] \\ p &= 0.0118 \quad [\text{N/A}] \\ R &= 0.057 \quad [\Omega] \\ L &= 4 \quad [\mu\text{H}]. \end{aligned}$$

The magnetic impedance's (Z_m) resonance is visible within the total impedance (Z_t) frequency response and peaks out of the passive impedance (Z_{RL}). For imaging, it is desired to compensate for the passive impedance (Z_{RL}) and obtain the magnetic impedance (Z_M), which corresponds directly to the mechanical resonance. Unlike the total impedance (Z_t), the magnetic impedance's gain approaches zero away from

the resonance and its phase has a one-to-one relationship with frequency. Using the magnetic impedance makes the resonance controller more robust and also improves the noise performance of the probe. We obtain the probe's magnetic voltage (v_m) by estimating the voltage across the passive impedance (R and L in series) and subtracting that estimate from the measured probe voltage. In this way we can compensate the probe and obtain the magnetic impedance (Z_m) frequency response shown in red in Figure 5-34. Given the low frequency of resonance, we perform the compensation inside the real-time controller sampling at 5-kHz. Close to the resonance, the inductive voltage is negligible compared to the resistive voltage and can be ignored for compensation purposes, and thus only the resistance is compensated. We apply a low-pass filter to the compensated impedance response to filter the inductive voltage and the probe's other modes at higher frequencies.

5.5.5 Control System

To use the compensated probe for self-sensing contact detection, we set it in controlled-amplitude self-resonance at its natural mechanical resonance frequency. We use the changes in the self-resonance frequency as feedback to detect contact and follow the sample surface. A block diagram of the probe's control system is shown in Figure 5-35. The control system consists of compensation, self-resonance control, and tracking subsystems.

The voltage measured across the coil (v_e) is compensated by subtracting the estimate of the resistive and inductive voltages to obtain an estimate of the magnetic voltage ($\hat{v}_m$). The self-resonance control branch feeds back this voltage as a self-resonance current (i_{SR}) excitation to set the probe in self-resonance. The self-resonance controller changes the feedback gain r via the multiplier to control the amplitude of oscillation. We feed forward the gain r_0 which is the expected required gain for constant-amplitude self-resonance when oscillating freely in air. The amplitude of oscillation is measured by first band-pass filtering, then by taking the absolute value of the compensated voltage, and then by applying a moving average filter. We set the width of the moving average filter to five oscillation cycles of the probe. Using

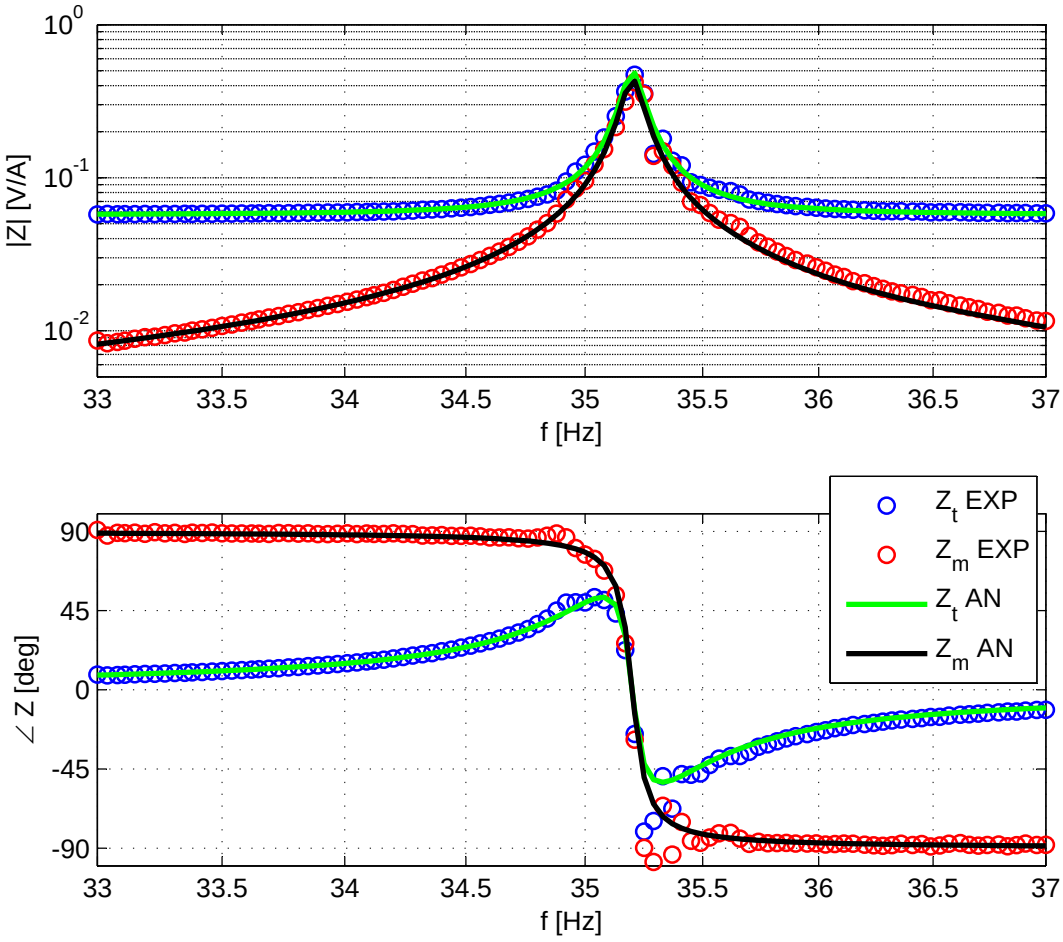

Figure 5-34: Experimental impedance frequency response of the magnetic probe shown before (Z_t EXP) and after (Z_m EXP) compensation for coil resistance as well as their corresponding analytical fits (Z_t AN & Z_m AN).

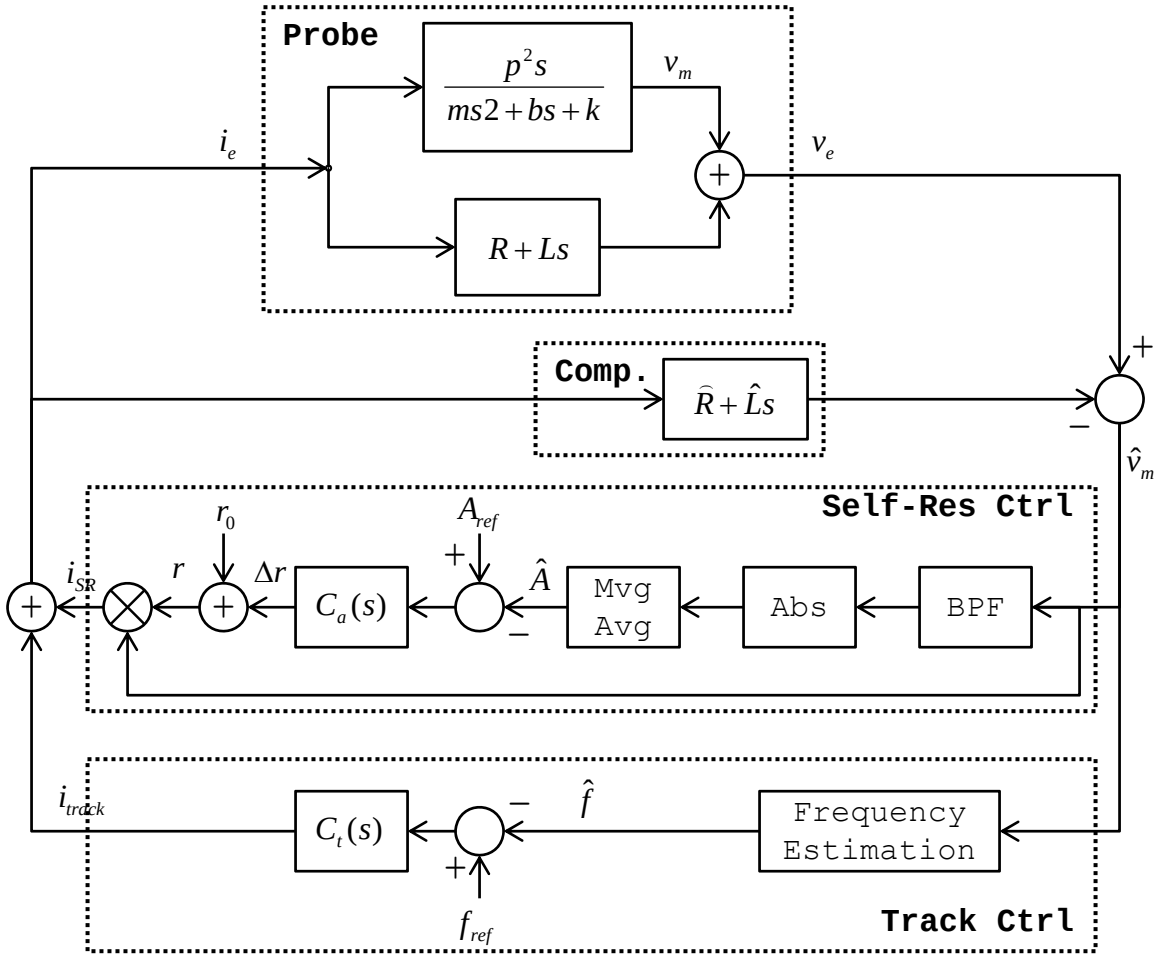

Figure 5-35: Block diagram of the probe's control system showing the compensation, self-resonance control, and tracking control subsystems. For the low resonance frequency, we let $\hat{L} = 0$

a width equal to an integer multiple of the oscillation period sets the discrete filter's notches at the fundamental oscillation frequency and its harmonics. This makes it more effective at filtering the amplitude measurement ripples. For imaging, we use a reference oscillation amplitude of $A_{ref} = 1.9$ mV peak-to-peak. We use a proportional integral amplitude controller with the following transfer function:

$$C_a(s) = K_p \frac{s + \omega_i}{s} = 200000 \frac{s + 1}{s} \tag{5.28}$$

The experimentaly measured and analytically fitted frequency responses of the amplitude control system's plant and its compensated-loop are shown in Figure 5-36. The experimental data is provided for the probe oscillating freely in air and locked to the sample using a reference frequency of 36 Hz. The analytical fit is based on the model of resonance amplitude control presented in [70] and a model of the discrete moving average filter. The compensated loop is shown based on the analytical fit and an amplitude controller given by (5.28). The loop is designed for a unity cross-over frequency of 1-Hz and a phase margin of 56°. Experiments show that a more conservative amplitude controller with $K_p = 50000$ and a lower cross-over frequency can result in less noisy images and a more robust control system. We have successfully imaged samples using amplitude control gains in range of 50000 to 200000.

The probe's self-resonance frequency shifts in response to tip-sample contact. The tracking controller $C_t(s)$ uses this as a feedback to follow the sample surface. We use a reference self-resonance frequency of 35.7 Hz, which is 0.5 Hz above the free air resonance frequency. This results in a light tapping contact between the sample and the probe. The self-resonance frequency is estimated by measuring the time between the zero crossings of the resonance signal. The tracking controller consists of an integrator term and a high-frequency roll-off filter:

$$C_t(s) = \frac{K_i}{s} \frac{\omega_r}{s + \omega_r} = \frac{2}{s} \frac{20\pi}{s + 20\pi} \tag{5.29}$$

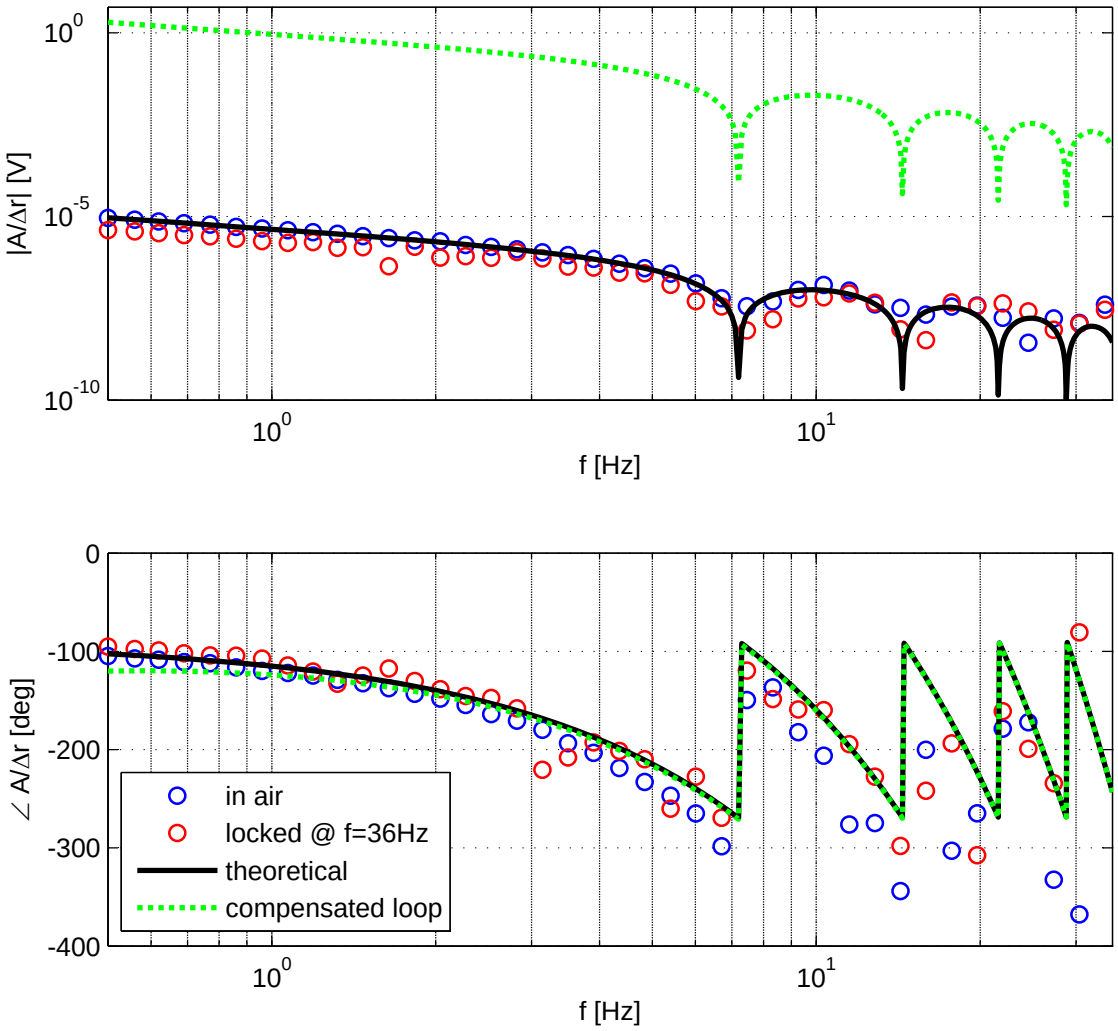

Figure 5-36: Experimental and analytically fitted frequency responses of the amplitude control system's plant and compensated-loop.

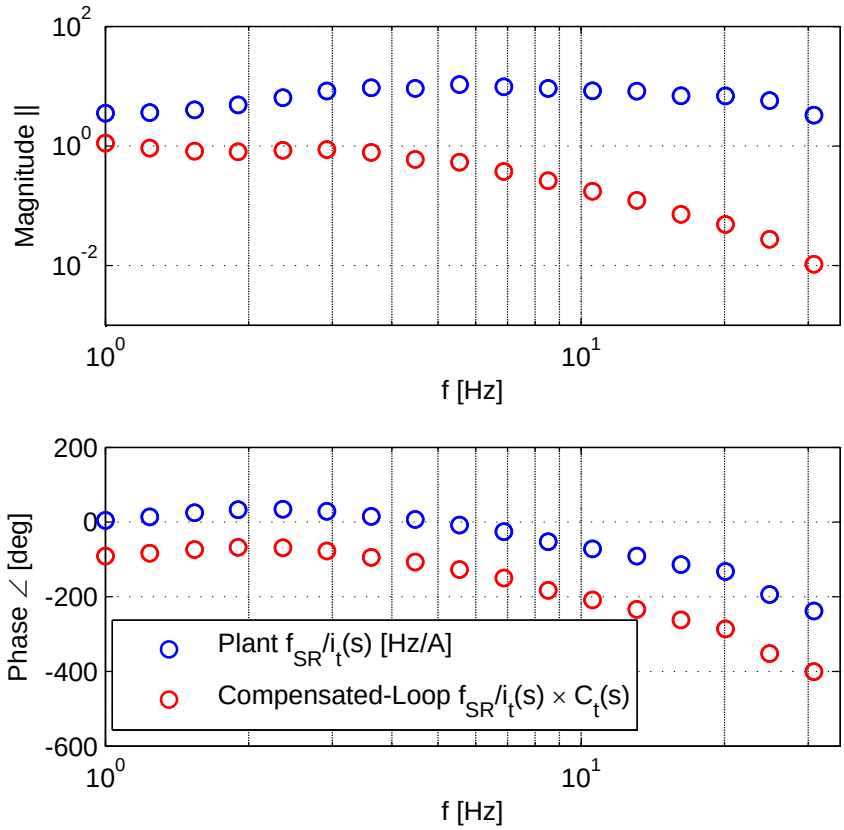

Figure 5-37: Experimentally obtained frequency responses of the plant and the compensated loop of the tracking control system.

The tracking control system's plant and compensated-loop frequency responses are shown in Figure 5-37. The tracking controller achieves a unity cross-over frequency of 1 Hz with 89° of phase margin. Given the non-linear nature of the probe, it is important to use a simple and robust controller which is not too sensitive to the changes in the plant frequency response. We have successfully imaged samples using an integral gain (K_i) of 0.5 to 2. Increasing the gain increases the probe's bandwidth but also increases its tracking noise.

5.5.6 Scanner Hardware

To image a sample, the imager needs a scanner to raster scan the sample under the probe. The scanner hardware for the imager is shown in Figure 5-37. The scanner consists of a voice coil position stage for the fast scan axis and a stepper positioning

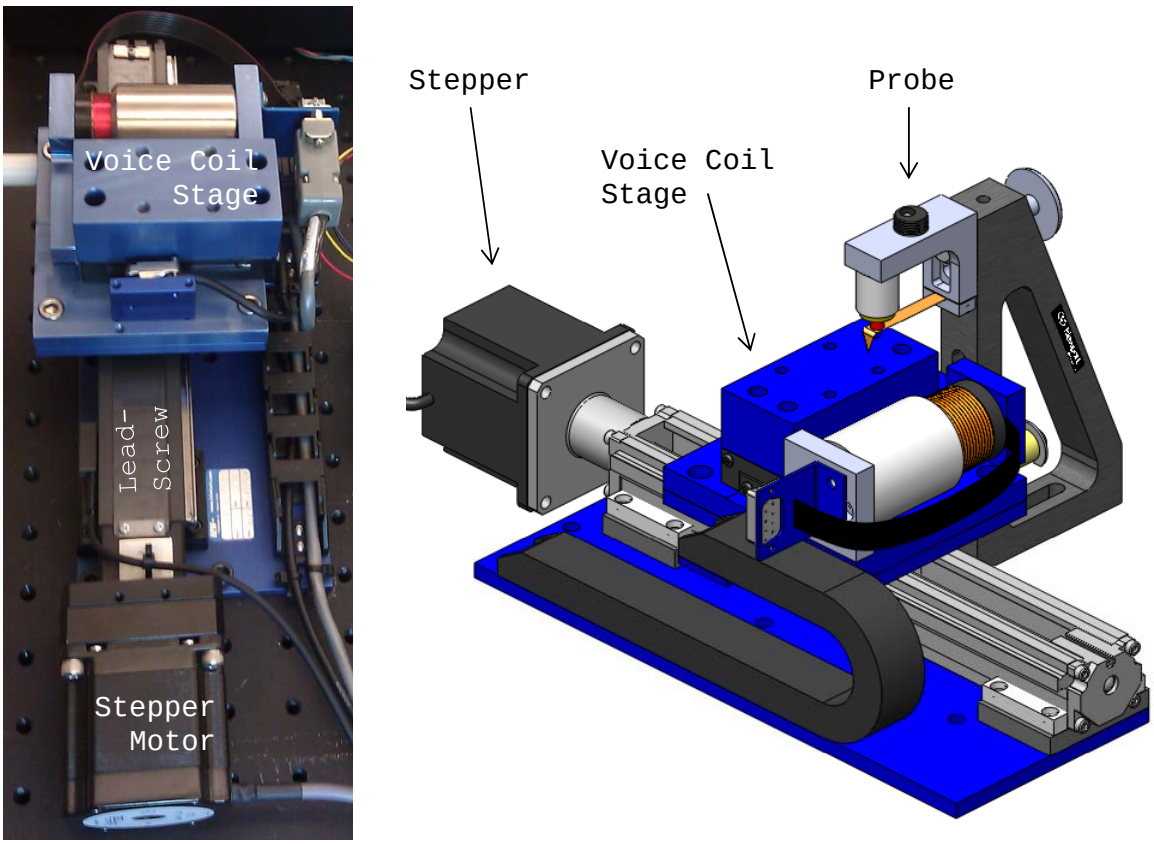

Figure 5-38: The imager's scanner hardware (left) and CAD design (right).

stage for the slow scan axis. We use the VCS14-020-BS-01SC-MCS voice coil stage and the SCS-05-08-1H stepper stage by H2W-Tech[4]. The position of the voice coil stage is measured using a MicroE Mercury 1000 sine-cosine encoder with a grating pitch of 20 μm. Interpolating this signal using the LabVIEW FPGA, we have achieved a stage position control resolution of better than 50 nm. The stepper stage realizes the slow scan axis by using a stepper with 200 full-steps per revolution and a lead-screw with 1-in pitch. By driving the stepper using 16 sub steps, we can achieve a positioning resolution of 1.6 μm.

The imager's hardware also includes a printed circuit board. The board has an instrumentation amplifier for amplifying the coil voltage by 50 times before measuring it using the controller's analog inputs. A sense resistor on the board is used for measuring the probe's current. The board also has buffers and comparators for am-

[4]H2W Technologies Inc.: www.h2wtech.com

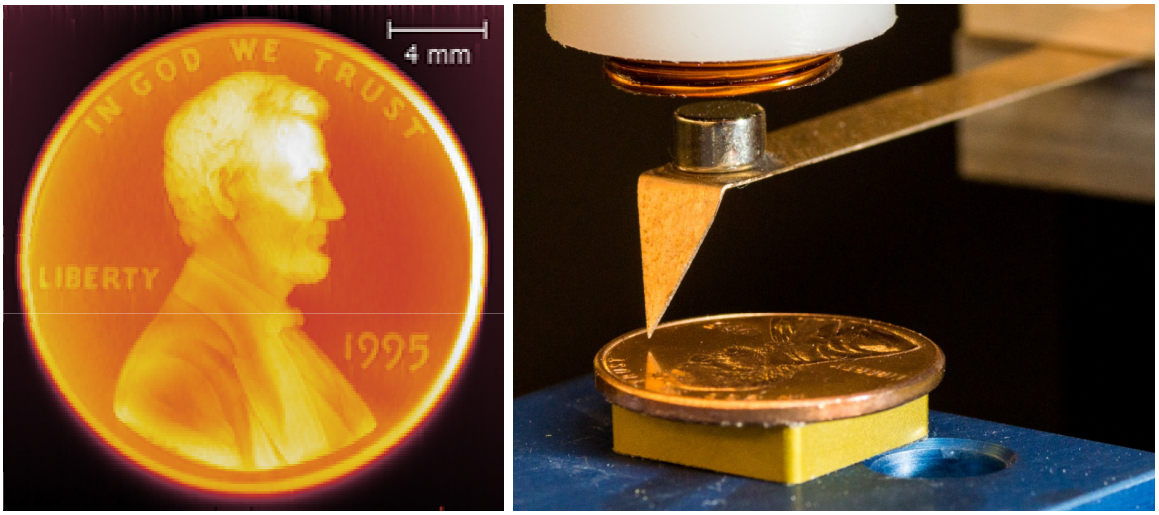

Figure 5-39: Macro AFM measuring a penny (right) and the captured image (left).

plifying and digitizing the encoder's analog sine and cosine signals, so that they can be measured by the controller's analog and digital inputs.

5.5.7 Experimental Results

We have used the imager to capture images of several different samples. Figure 5-39 shows the probe imaging a penny and the captured image. Figure 5-40 shows the probe imaging an MIT key chain. An image of a quarter captured using the probe is shown in Figure 5-41. The images have all been captured at a scan speed of 1mm/s.

5.6 Summary

We reviewed prior art self-sensing methods. We introduced a self-sensing contact detection method which can be used with actuated systems to precisely detect contact between the actuated system and a work piece. This method has been inspired by self-sensing atomic force microscopy. We presented the application of this method to the reticle assist device for detecting contact between the assist device and the reticle. By precisely detecting contact between the reticle and the assist device, we can control the piezo's extension in reference to the reticle edge. In this chapter, we also showed this method being used with two AFM systems: the HAFM which is

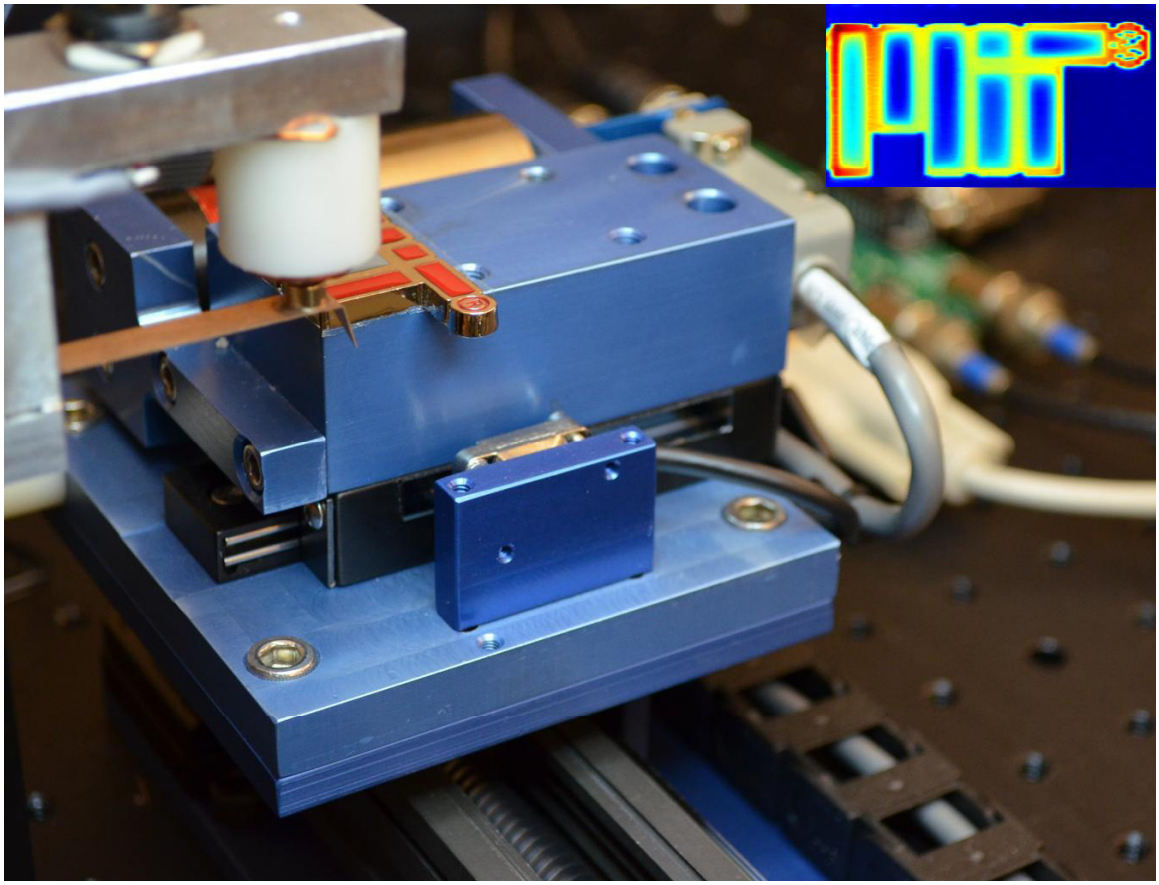

Figure 5-40: Macro AFM measuring an MIT key chain and the scanned image (top right).

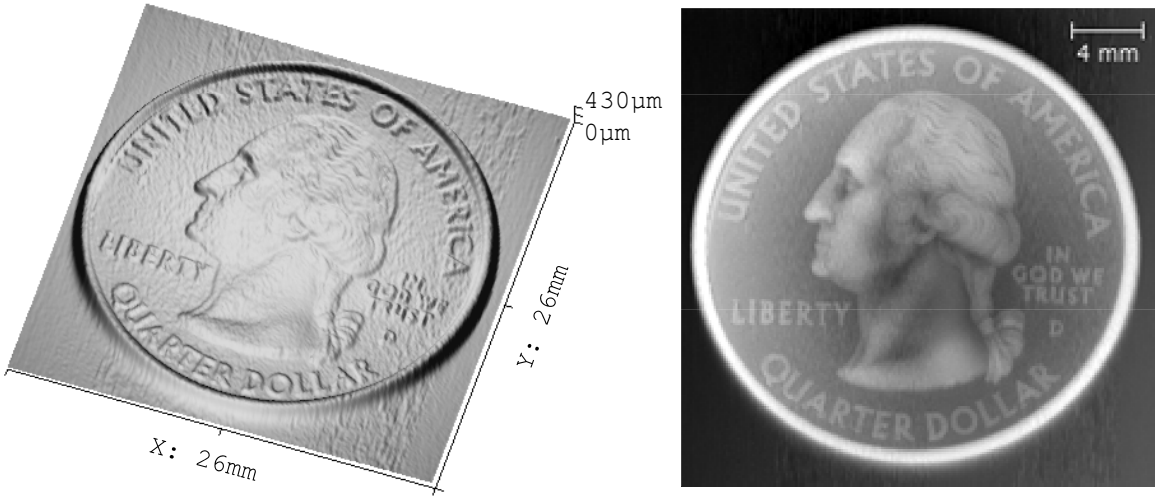

Figure 5-41: Images of a quarter captured using macro AFM visualized in 3D (left) and 2D (right).

designed for metrology, and the Macro AFM which is built as a lab instrument for teaching.

In the next chapter, we present the reticle assist device's control system design and the results of the reticle assist experiments. The control system utilizes the self-sensing contact detection method as well as the new VQV charge amplifier with HHC.

Chapter 6

Reticle-Assist Device Control and Experimental Results

6.1 Control System Design

Using the reticle assist device, we can compensate more than 95% of the simulated reticle inertial forces. In this chapter, we describe the reticle assist device's control system. We explain the operation of the assist device and how a state-machine design is used to automate the system. We describe two possible architectures for controlling the motion and the forces: using strain sensor's feedback and sensorless operation. We describe how we calibrate and control the reticle assist device's output force. We present the methods used for controlling the reticle assist device's motion. Finally, we briefly describe how we use self-sensing contact detection to detect the reticle's edge.

6.1.1 State-Machine Design

The reticle assist device's operation can be summarized as the following four steps:

1 **Coarse-Adjustment:** before a reticle exchange, a coarse-retract occurs. Once the new reticle is placed, a coarse-approach preloads the piezo actuator against the reticle. Once the piezo actuator is extended by the desired gap size, the

coarse-clamp is activated. In this way, we can position the piezo and approximately achieve the desired gap size.

2 **Fine-Actuation:** Fine-actuation is used to exert a pushing force on the reticle to cancel its inertial load. The fine-actuation consists of the following states:

2.1 **Approach:** prior to a simulated acceleration, the piezo approaches the reticle and finds its edge.

2.2 **Push:** the piezo stays at the reticle's edge and extends to push and cancel the simulated inertial loads.

2.3 **Retract:** the piezo retracts back to avoid contacting and disturbing the reticle during the sensitive exposure interval.

The coarse-adjustment occurs only once a new reticle is loaded. The fine-actuation occurs once per die exposure. We tested and confirmed the effectiveness of the coarse-adjustment method using a manual pressure regulator. We used a state-machine design to automate the fine-actuation process. A block diagram of the state-machine is shown in Figure 6-1. The different states as well as the coarse adjustment step are described in the following subsections.

Coarse-Adjustment

To test the coarse adjustment mechanism, we place the assist device such that the reticle's edge is within 0.5 mm of piezo actuator's tip. We extend the piezo actuator by 1 μm. Next, we manually adjust the pressure regulator's output from 0 to approximately 20 psi. The bellow extends and preloads the piezo actuator's tip against the reticle. Then we activate the coarse-clamp by applying vacuum to the pressure pocket. Finally, we retract the piezo back to its original length. In this way, we are able to create a gap of approximately 1 μm. The limited stiffness of the piezo-reticle contact causes the gap to be slightly less than 1μm. The created gap size also depends on the precision of the clamping mechanism and how much the clamp displaces the coarse stage as it is activated.

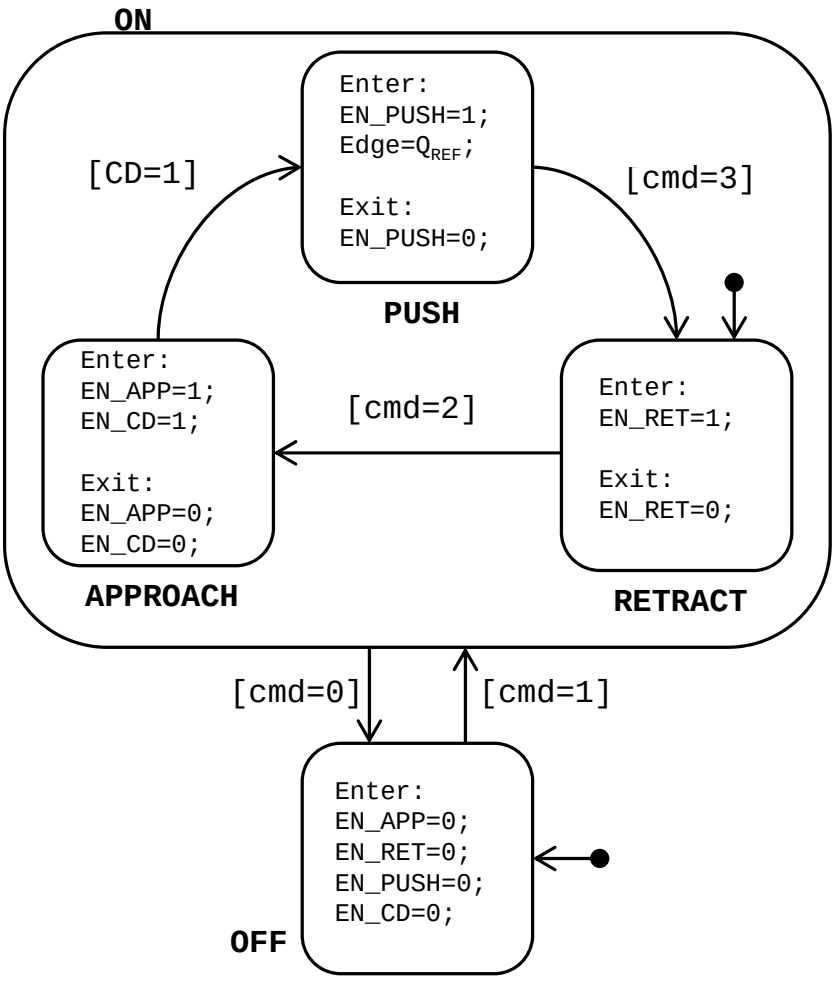

Figure 6-1: Reticle assist device's state-machine design used for automating the fine-actuation process.

Approach

While in the approach state, the piezo moves towards the reticle until it detects the reticle's edge. The state-machine enters the approach state when an input command of cmd = 2 is received. The command is issued 20 ms before the occurrence of the simulated inertial load. Once the machine enters the approach state, contact detection is enabled and the piezo starts to move towards the reticle at a speed of 150 nm/ms. Once the reticle's edge is detected, the contact detection method is disabled and the machine enters the push state. The contact detection subsystem excites the probe at its resonance. Because the excitation disturbs the reticle, we enable contact detection during the approach state only. In our implementation, the edge location is detected for every acceleration cycle. Although frequent edge detection is not necessary, it can be used as diagnostic tool for confirming the operation of the assist device.

Push

During the push state, the piezo is held at the reticle's edge and extends to push on the reticle to cancel the simulated inertial force. The pushing state can be entered from the approach state once contact is detected. Once the machine enters the push state, the reticle's edge location register is updated and the pushing method is enabled. To push on the reticle, the piezo is extended relative to the edge location. A calibrated look-up-table of the extension versus the pushing force is used to calculate the required extension based on the value of the simulated inertial force. The force calibration and control methods are described in Section 6.1.3. The pushing state is exited, when the acceleration cycle is finished and the pusher needs to retract back. We exit the pushing state and enter the retract state by issuing a command cmd = 3.

Retract

During the the retract state, the piezo moves back to 1.5 μm away from the reticle's edge. The retract state can be entered from the push state by issuing a command $cmd = 3$. Once the machine enters the retract state, it starts to move back at a

speed of 400 nm/ms and stops 1.5 μm away from the edge. When the assist device is enabled, it enters the retract state by default. The state machine can exit the retract state and enter the approach state if a command cmd=2 is given.

6.1.2 System Architecture Designs

In this section, we describe two system architectures for controlling the device's pushing force. The first design uses the strain sensor's feedback to control the piezo's motion. The second design does not use any sensors. Instead, it uses open-loop charge-control. The designs are described with more detail in the following subsections.

Strain-Controlled Operation

The design of the control system, when using the strain sensor's feedback, is shown in Figure 6-2. The design of the state machine was described in the previous section. A reference calculation block calculates the piezo's reference position based on the state of the device, edge location, and the required output force. In the retract and approach states, the block changes the reference signal to move the piezo away or toward the reticle at the specified retract or approach speeds respectively. During the push state, the block calculates the piezo extension relative to the reticle's edge required for creating the desired pushing force. The extension is calculated using a calibrated look-up-table of extension versus pushing force. Force control and calibration are described in Section 6.1.3. A strain controller is used for following the piezo reference (S_{REF}) position in closed-loop using the strain sensor's feedback (S). The strain controller is described in Section 6.1.4. The strain controller drives the piezo using the VQV charge amplifier which was presented in Chapter 4. Using charge control eliminates hysteresis and the phase lag resulting from it. Self-sensing contact detection is used to detect contact. In this configuration, contact is detected as the shift in the phase response from piezo voltage (V_M) to the piezo strain (S) when excited at the actuator's resonance frequency. Application of self-sensing to the reticle

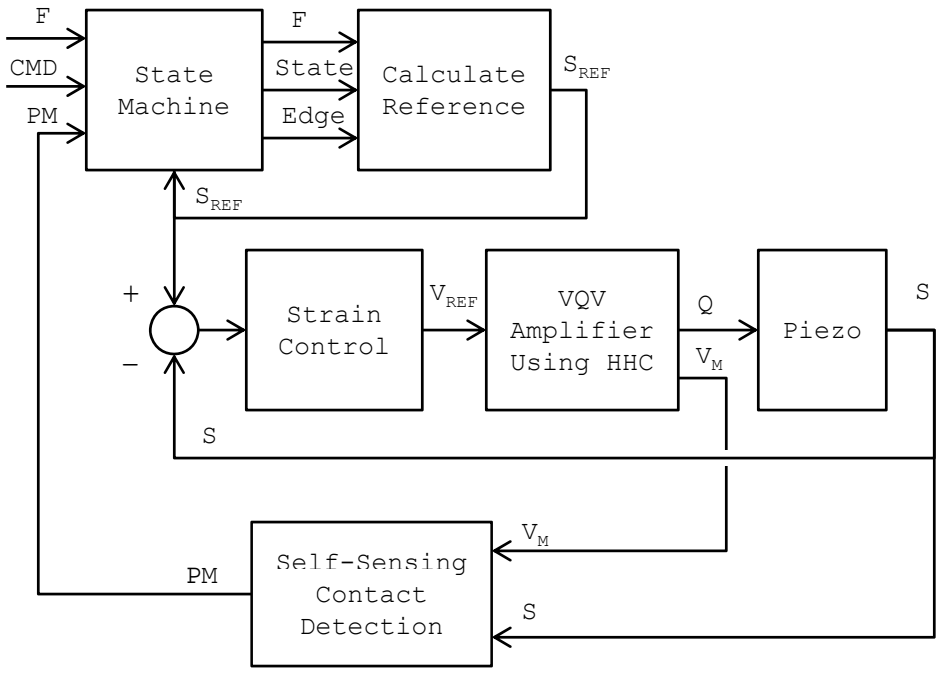

Figure 6-2: Simplified block diagram of the control system design using strain sensor's feedback for controlling the piezo's extension. Variable s is the strain gauge output; signal PM is the phase measurement from the Contact Detection block.

assist device was described in Chapter 5.

Sensorless Charge-Controlled Operation

The configuration described in the previous subsection required a strain sensor measurement. In this subsection, we describe a sensorless configuration, which does not require any sensor feedback. This architecture is based on charge control. Figure 6-3 shows a simplified block diagram of the charge-controlled architecture. In this configuration, the strain controller is replaced by charge control. In this configuration, the edge location and the required piezo extension are specified in terms of the charge amplifier's reference signal (V_{REF}). The Calculate Reference block uses a calibrated look-up-table of the pushing force versus the piezo extension. We drive the piezo using the VQV charge amplifier. We use hybrid hysteresis compensation, which eliminates the charge amplifier's transient and enables linear control of the piezo's extension even at low frequencies. Any remaining transient is compensated for by updating the edge location before every acceleration cycle. In this configuration, self-sensing

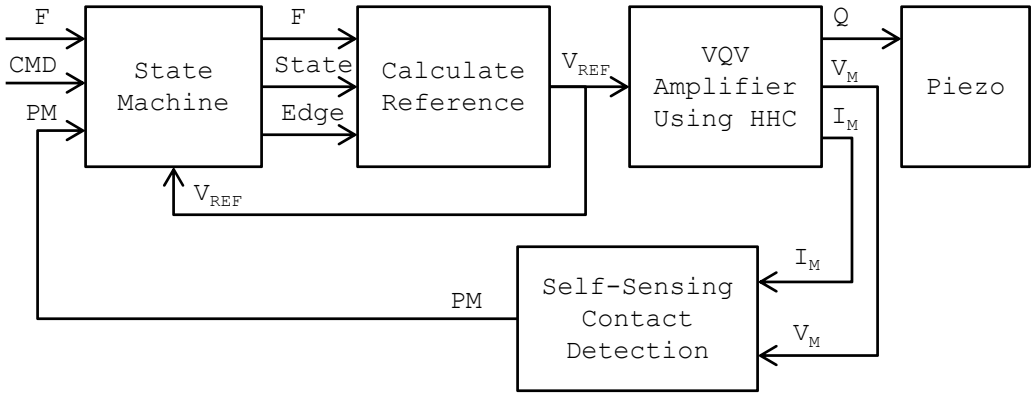

Figure 6-3: Simplified block diagram of the control system design using charge control for open-loop control of the piezo's extension.

contact detection is performed using the piezo's current (I_M) and voltage (V_M) measurements.

6.1.3 Force Calibration and Control

The reticle assist device controls its output force by controlling the deformation of its mechanical force-loop stiffness. The stiffness of the device's mechanical force loop is repeatable and can be used for open-loop force control. We use an experimentally calibrated look-up-table of the pushing force versus the piezo's extension to control the force. The contact force (F) versus the piezo strain (S) is shown in Figure 6-4 based on the experimental data and an analytical fitted model. The experimental measurement and calibration methods are presented in Section 6.2.2.

A model of the mechanical loop is shown in Figure 6-5. The mechanical force loop's stiffness consists of the reticle clamp (k_R), piezo to reticle contact (k_H), piezo stack (k_P), and the assist device clamp (k_C). All of the elements are modeled as a constant stiffness, except for the contact, which has a non-linear stiffness changing with the contact force F. We model the contact stiffness using the Hertz contact model [76]. Based on this model the contact force (F) and deformation (δ) are related as the following, where c is a constant whose value depends on the Young's modulus and

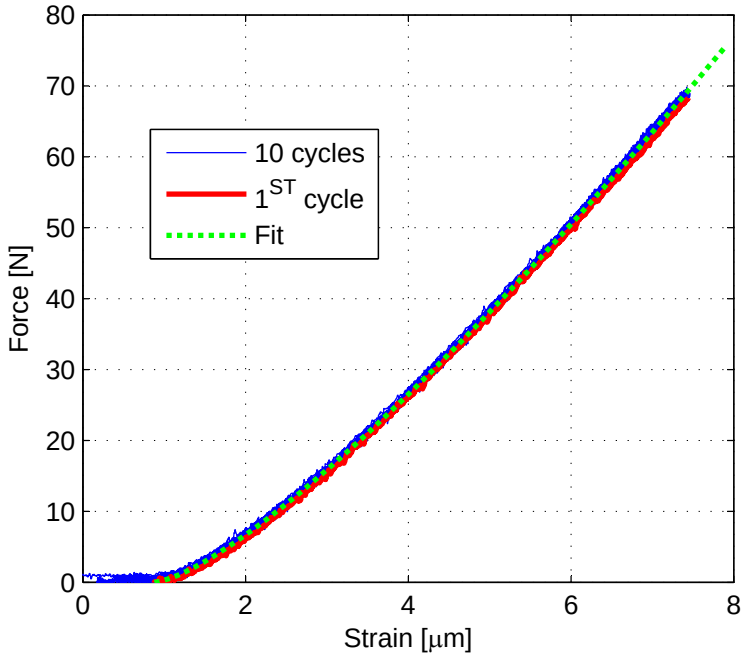

Figure 6-4: Experimental plot of the pushing force versus piezo strain with an overlaid least-squared fit based on the analytical model.

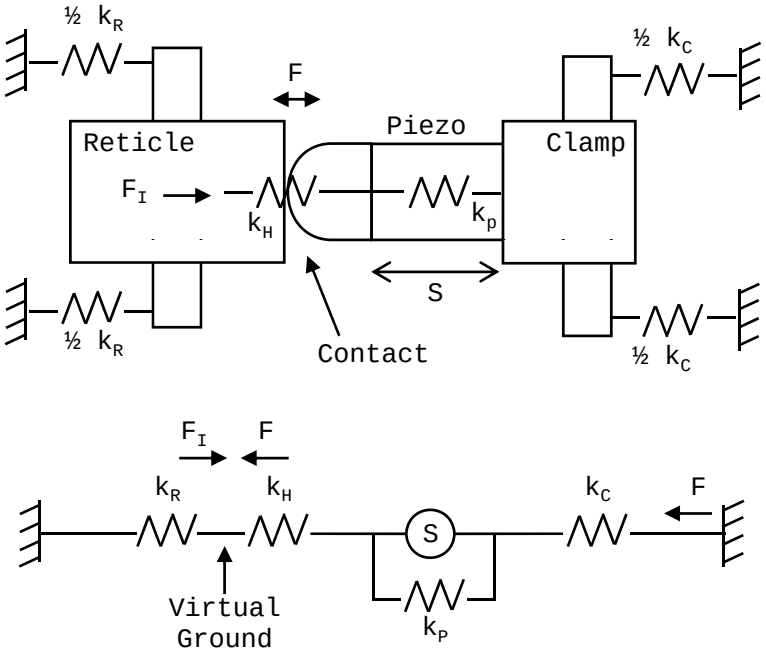

Figure 6-5: A simplified lumped stiffness model of the reticle assist device and the reticle.

curvature of the contacting parts:

$$\delta_H = cF^{\frac{2}{3}}. \tag{6.1}$$

The calibration map is the pushing force (F) versus the extension of the piezo (S) relative to the point of contact with the reticle edge. The calibration map is dependent on the reticle edge displacement. However, for successful operation of the assist device, the net force (inertial load minus the assist force) on the reticle is almost zero, and thus the reticle edge displacement is approximately zero as well. With the reticle being stationary, its clamp stiffness can be neglected when analyzing the mechanical force loop to create a model that can be fitted to the force calibration data. The piezo stiffness also does not affect the model because piezo's extension is measured across the piezo stack. Therefore, only the the contact and assist device clamp stiffness must be included in the model. The measured piezo strain is equal to the sum of the contact deformation (δ_H) and the assist device's clamp deformation (δ_C):

$$S = \delta_h + \delta_c = cF^{\frac{2}{3}} + \frac{F}{k_C} \tag{6.2}$$

where F is the force in Newtons, S is the piezo's extension in μm, k_C is the assist device clamp stiffness in N/μm, c is the constant used in (6.1) for defining the contact stiffness. The analytical model of (6.2) is fitted to the experimental data using a least-square fit method. The fitted parameters values are as the following:

$$c = 0.256 \quad \mu\text{m/N}^{2/3}$$
$$k_C = 31.0 \quad \text{N}/\mu\text{m}.$$

Please note that the value obtained for the stiffness of the clamp includes the stiffness of the assist device clamp structure in series with the stiffness of the surface plate holding the setup together. For a description of the mechanical design please refer to Chapter 3.

6.1.4 Motion Control

For the operation of the reticle assist device we require to control the position of the piezo's tip. In this section, we describe the two methods which we have used to control the piezo's motion: closed-loop extension control using the strain gauge feedback and open-loop extension control using charge-control.

Strain Feedback

The control system design shown in Figure 6-2 uses a closed-loop strain controller, which controls the piezo's extension based on the strain gauge feedback. We have designed a strain controller using the loop-shaping technique. The frequency response of the strain control system's plant, controller, and compensated loop transmission are shown in Figure 6-6. The plant frequency response is shown from amplifier reference voltage to the strain gauge measurement buffer output voltage. The plant frequency response is flat up to approximately 5 kHz, where a pole is intentionally added to the amplifier's reference input for protecting the piezo from being over excited at its resonance and also for low-pass filtering the input noise. The plant's frequency response also shows two resonances at 27 kHz and 31 kHz due to the mechanical vibration modes of the actuator. For our controller we use a double integrator, high-frequency roll-off filters, and two notch filters to attenuate the loop gain at the mechanical resonances. The resulting compensated loop frequency response shows a unity cross-over frequency of 2.5 kHz and a phase margin of 100 degrees.

We use double integrator to make sure that the strain controller can follow a ramp reference signal with zero steady-state error. The inertial loads typically increase as a ramp. As a result, the piezo reference signal is also approximately a ramp. Using a double integrator improves the piezo's ability to track the reference signals. To avoid large delays resulting from a slow sampling rate, we implement the controller using discrete-time transfer functions on a LabVIEW PXI-7854R FPGA card. The controller is sampled at 312.5 kHz. The controller transfer function in continuous

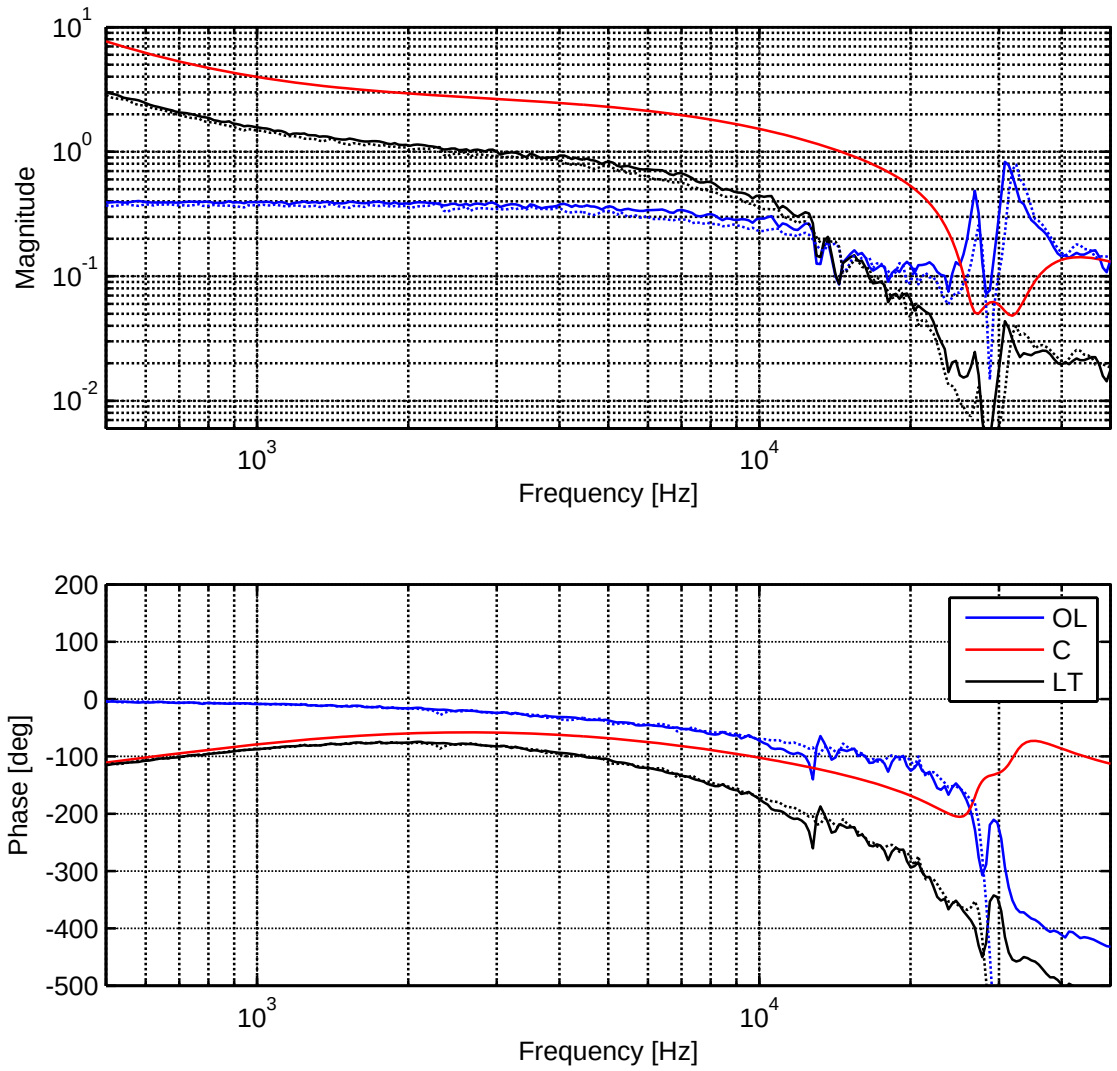

Figure 6-6: Frequency responses of the strain control system's plant (OL), controller (C), and compensated loop transmission (LT).

time is

$$C(s) = [\frac{\omega_c \alpha_1}{s + \omega_c \alpha_1} + \frac{\omega_c}{\alpha 1 s}] \times [\frac{\omega_c \alpha_2}{s + \omega_c \alpha_2} + \frac{\omega_c}{\alpha_2 s}] \times N_1(s) \times N_2(s) \times K_p. \tag{6.3}$$

The transfer functions N_1 and N_2 are notch filters at ω_1=27 kHz and ω_2=31 kHz respectively. By adding a low-pass filter and an integrator, we can obtain the integrator and the roll-off filters separated by a factor α^2 around the desired unity cross-over frequency (ω_c). The controller is discretized using the MATLAB $c2d$ function for implementation on the FPGA. The following are the controller parameter values:

$$\omega_c = 2500 \times 2\pi \quad \text{rad/s} \tag{6.4}$$

$$K_p = 2.3 \quad \text{V/V} \tag{6.5}$$

$$\alpha_1 = 3 \tag{6.6}$$

$$\alpha_2 = 6 \tag{6.7}$$

$$N1 = \frac{s^2 + 2 \times 0.2/5/\omega_1 s + \omega_1^2}{s^2 + 2 \times 0.2 \times 5/\omega_1 s + \omega_1^2} \tag{6.8}$$

$$N2 = \frac{s^2 + 2 \times 0.3/5/\omega_2 s + \omega_2^2}{s^2 + 2 \times 0.3 \times 5/\omega_2 s + \omega_2^2}. \tag{6.9}$$

Charge Control

For sensorless operation, we control the piezo's motion using charge-control. We use the VQV amplifier with hybrid hysteresis compensation (HHC). The amplifier design and the hysteresis compensation algorithm are described in Chapter 4. Using the HHC method enables linear and repeatable control of the piezo at low frequencies as well as the high frequencies. This is important because the piezo's reference signal includes a quasi-static component, which cannot be precisely followed in open-loop using a conventional charge amplifier without the HHC method.

6.1.5 Self-Sensing Contact Detection

The application of the self-sensing contact detection method to the reticle assist device is described in detail in Chapter 5. We use the shift in the phase response of the probe near its mechanical resonance to detect contact between the tip and the sample. Piezo's mechanical and electrical dynamics are coupled and both can be used for self-sensing. In the architecture shown in Figure 6-2, we use the probe's mechanical dynamics and perform self-sensing using the strain and voltage measurements. For the sensorless configuration shown in Figure 6-3, we use the probe's electrical dynamics and perform self-sensing contact detection using the probe's voltage and current measurements.

6.2 Experimental Results

In this section, we introduce the experiments used for testing the effectiveness of the reticle assist device. In the first section, we present the experimental hardware. Next, we present the experimental methods used for testing and measuring the performance of the assist device. Finally, we present the experimental results of the reticle-assist experiments. The results are presented for both the strain-controlled and sensorless operation of the assist device.

6.2.1 Experimental Setup

A picture of the experimental setup is shown in Figure 6-7. We use the setup for calibrating and testing the reticle assist device.

The mechanical hardware includes the reticle assist device, a reticle assembly, and displacement measurement sensors. The setup is mounted on a 1-in thick Aluminum plate. The design of the reticle assist device was described in Chapter 3. The reticle assembly includes a reticle, its mount, and a force actuator. The reticle's force actuator is used to simulate the inertial loads by exerting a force on the reticle. The reticle assembly has been provided to us by ASML. The experimental setup also includes

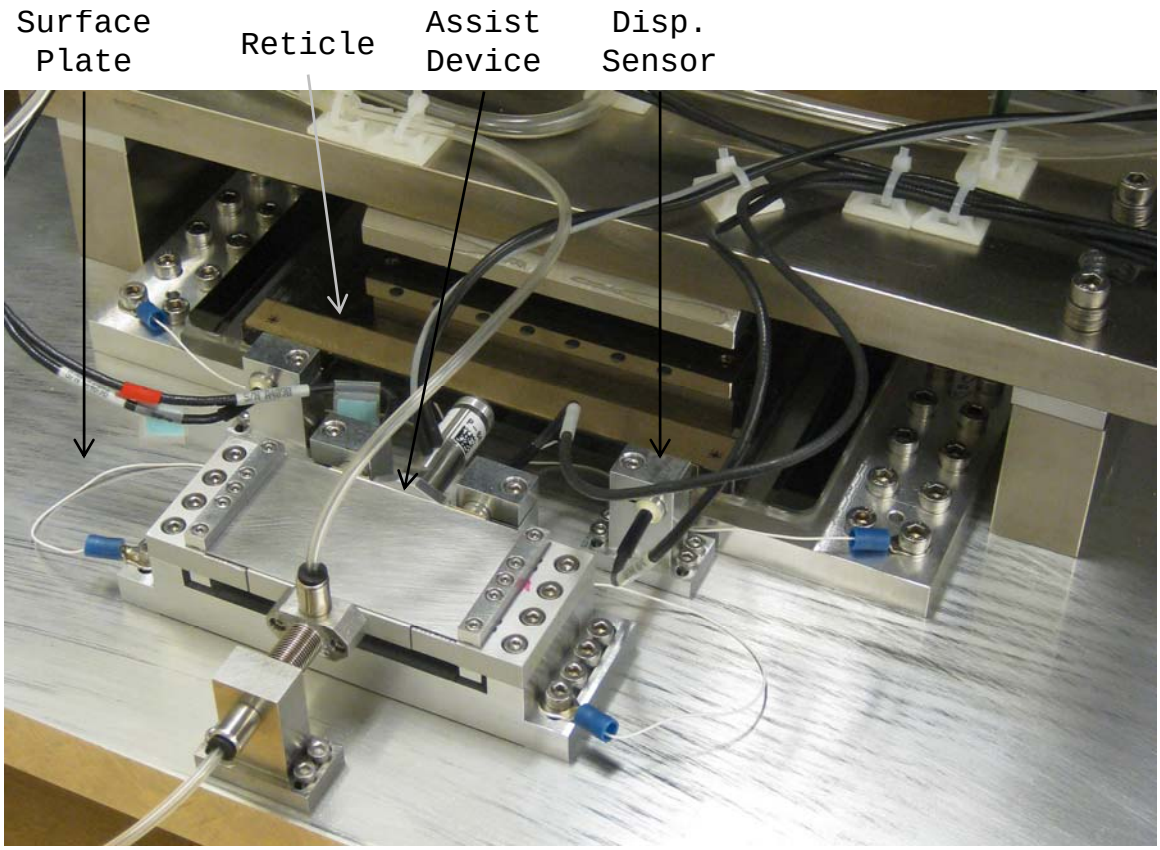

Figure 6-7: Experimental setup used for calibrating and testing the reticle-assist device.

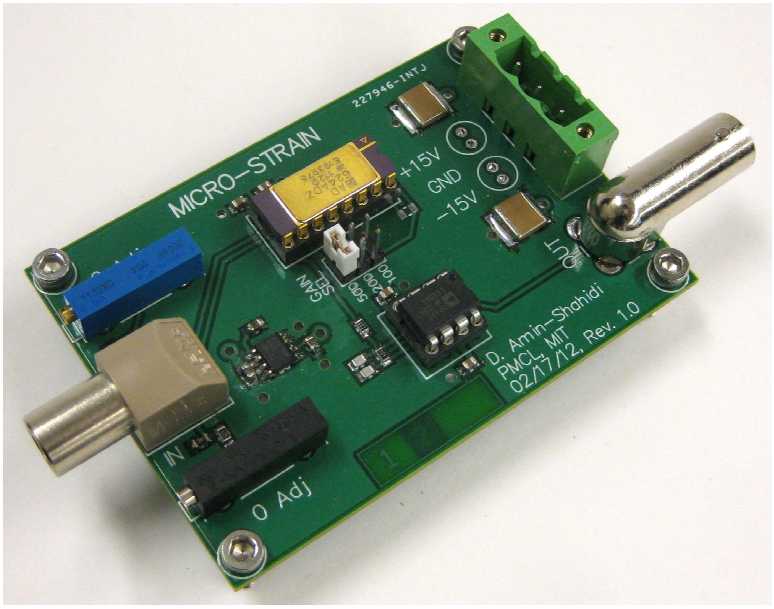

Figure 6-8: Picture of the strain gauge measurement circuit board.

capacitive displacement sensors for measuring the displacement of the assist device's vacuum clamp and the reticle relative to the surface plate.

For driving the assist device's piezoelectric actuator, the experimental setup uses the VQV charge amplifier, which was described in Chapter 4. We drive the reticle assembly's force actuator using a current-controlled power amplifier, which has been designed in our lab around a APEX PA-12 power device. Details on the power amplifier design can be found in [61]. We use our own Wheatstone bridge circuit to measure the changes in the strain gauge's resistance. A picture of the strain gauge measurement circuit is shown in Figure 6-8. The circuit uses an AD624 instrumentation amplifier and a REF5050 reference voltage regulator. Information on the design and measurement of piezo-resistive sensors can be found in [65].

The setup uses four capacitive displacement sensors. Two ADE 2805-S capacitive displacement probes measure the displacement of the assist device's clamp in the force direction. The ADE 2805-S probes have a range of ± 50 μm and are used with the ADE 3800 probe drivers. Two Microsense AD2823 capacitive displacement sensors are used to measure the displacement of reticle's edge in the force direction. The Microsense AD2823 probes have a range of ± 10 μm and are used with Microsense

8810 probe drivers.

The vacuum for the clamps is created using a Laybold Trivac D8B vacuum pump. We use two manual ball valves for switching the vacuum supplied to the reticle clamp and the assist device clamp. The pressure for actuating the bellow is provided using a manual pressure regulator operating on the 100-psi wall supply.

6.2.2 Experimental Methods

To test the effectiveness of the reticle assist device, we simulate the inertial loads on the reticle using the reticle assembly's force actuator. The force actuator applies a force equal to the expected inertial load. At the same time, the reticle assist device attempts to exert the exact opposite force onto the reticle's edge. In this way, the simulated inertial load is carried by the assist device. Depending on the assist device's force compensation accuracy, a net force remains, which is carried by the reticle clamp. The following are the main steps for testing the reticle-assist device:

1. Use the reticle assembly's force actuator to simulate an inertial load corresponding to a practical motion profile.

2. Use the pusher to create the exact opposite force on the reticle to cancel the simulated inertial force.

3. Use capacitive displacement sensors to sense the displacement of the reticle's edge as a measure of the remaining net force.

Reticle slip can be measured as the displacement of the reticle's edge relative to its original position after the forces are removed. The force compensation inaccuracy of the assist device is measured as the displacement of the reticle in response to the simulated force during the test. The following subsections provide more detail on how forces and displacements are estimated. We also explain how the assist device is calibrated.

Force Measurement

The reticle clamp deforms as a result of the remaining net force not compensated by the assist device. We measure this deformation using the capacitive displacement sensors. The reticle clamp has a constant stiffness with a linear force versus displacement behavior. Therefore, the reticle clamp's deformation can be used to estimate the residual force. With this setup, we can measure the displacement of the reticle's edge. Assuming that no slip occurs between the reticle and the clamp, the clamp's deformation can be measured as the displacement of the reticle's edge. We estimate the residual forces as the displacement of the reticle's edge times the stiffness of the reticle clamp. This measurement method is accurate below the first resonant mode of the reticle assembly, where the inertial force is negligible compared to the elastic forces. Given the first resonance frequency of the reticle assembly, this method provides us with sufficient measurement bandwidth. Knowing the residual force and the reticle actuator force, the assist device's output force can be estimated.

Displacement Measurement

Using the capacitive displacement sensors, we can measure the displacement of the reticle edge and the assist device's clamp relative to the surface plate. The strain gauge sensor measures the piezo's extension.

The displacement of the reticle's edge includes the deformation of the reticle clamp, slip at the reticle-clamp interface, and thermally-induced size variations of the reticle. Using the assist device, slip can be avoided. The thermally-induced changes are slow, and thus, over short periods, are negligible or can be separated from the measurement data. With no slip and negligible thermal variations, the reticle clamp deformation can be estimated as the displacement of the reticle edge. At the same time, slip can be detected as any displacement of the reticle edge, which is not recovered when the forces are removed. The force actuator, which is attached to the reticle, can heat up. The reticle has a very low coefficient of thermal expansion and does not expand significantly from the added heat. However, the reticle is deformed

by the expansion of the part of the force actuator attached to it.

All of the measurements are referenced to the surface plate. The surface plate is also a part of the mechanical force-loop. The pushing forces deform and excite the vibration modes of the surface plate. The excited vibration modes of the plate continue after the forces are removed. The plate vibration appears on our displacement measurements. This can be mitigated if the setup is designed such that the forces are on the support structure's neutral axis. Alternatively, the surface plate's stiffness can be increased if it is bolted to a thicker plate, such as the surface top of an optical table. We use a vibration damping pad underneath the surface plate to faster damp out its vibrations.

Force Calibration

We experimentally calibrate the reticle-assist device's output force versus the piezo extension. The extension can be expressed as the piezo's strain for the control architecture using the strain gauge feedback, and can be expressed in terms of the reference charge amplifier voltage for the sensorless control system design.

The forces can be estimated using the method described in Section 6.2.2. However, the method requires that the reticle does not slip. This can be achieved if an initial approximation of the force versus extension calibration map exists. For obtaining the first calibration map, we switch the role of the assist device and the force actuator. We extend the assist device to push on the reticle. At the same time, we drive the reticle's force actuator in closed-loop to keep the reticle's edge at a fixed position. In this way, the reticle does not slip, and the pushing force can measured as the force actuator's effort plus the stiffness of the clamp multiplied by any error in regulating the reticle's edge location. Using this method, we can accurately calibrate the assist device.

We only need to perform this once to obtain a calibration map. Once a good approximation of the calibration map exist, the assist device can operate effectively and can prevent reticle slip. Form this point on, the experimental test data can be used to update the force versus extension calibration map.

6.2.3 Strain-Controlled Reticle Assist Experiment

In this section, we present the results of the reticle assist experiment for the strain-controlled assist device. Time plots of the experimental results for 10 consecutive simulated acceleration cycles are shown in Figure 6-9. The same plots for the single acceleration cycle between the times 0.3 and 0.4 seconds are shown in Figure 6-10. The top plot shows the simulated inertial load, which is applied to the reticle using the reticle assembly's force actuator. For the experiments we use a simulated inertial load profile with a 60-N peak and a 6.4-N/ms maximum rate of change. The top-middle plot shows the displacement of the reticle's edge measured using the capacitive displacement sensors. The reticle's edge displacement is limited to 25 nm. With a reticle clamp stiffness of 100 N/μm this is equivalent to 2.5 N of residual force. This shows that the reticle assist device has compensated about 96% of the simulated inertial load. The bottom-middle plot shows the piezo actuator's reference extension, actual extension, and the extension corresponding to the reticle edge location. The bottom plot shows the contact detection method's phase response. Contact is defined as the point where the phase response at the resonance from voltage to strain rises above zero degrees. Contact detection is enabled during the approach state. When initially enabled, the contact detection methods goes through a transient where its output is not reliable. For this reason, the contact detection logic ignores the phase response for the first 2 ms.

Figure 6-11 shows the motion of the piezo actuator versus time with the state of the assist device marked on the plot. As can be seen, during the retract state, the piezo stands 1.5 μm away from the edge. The state switches from retract to approach 20 ms before the simulated inertial load is applied. The piezo extends toward the reticle edge at a speed of 1.5 μm/s until contact is detected. The state switches to push as soon as contact is detected. In the push state, the piezo changes its extension based on the force versus extension calibration map to follow the reference force input. As soon as the simulated inertial force is applied, the piezo extends and pushes on the reticle. At the end of the acceleration profile, the state switches from push to

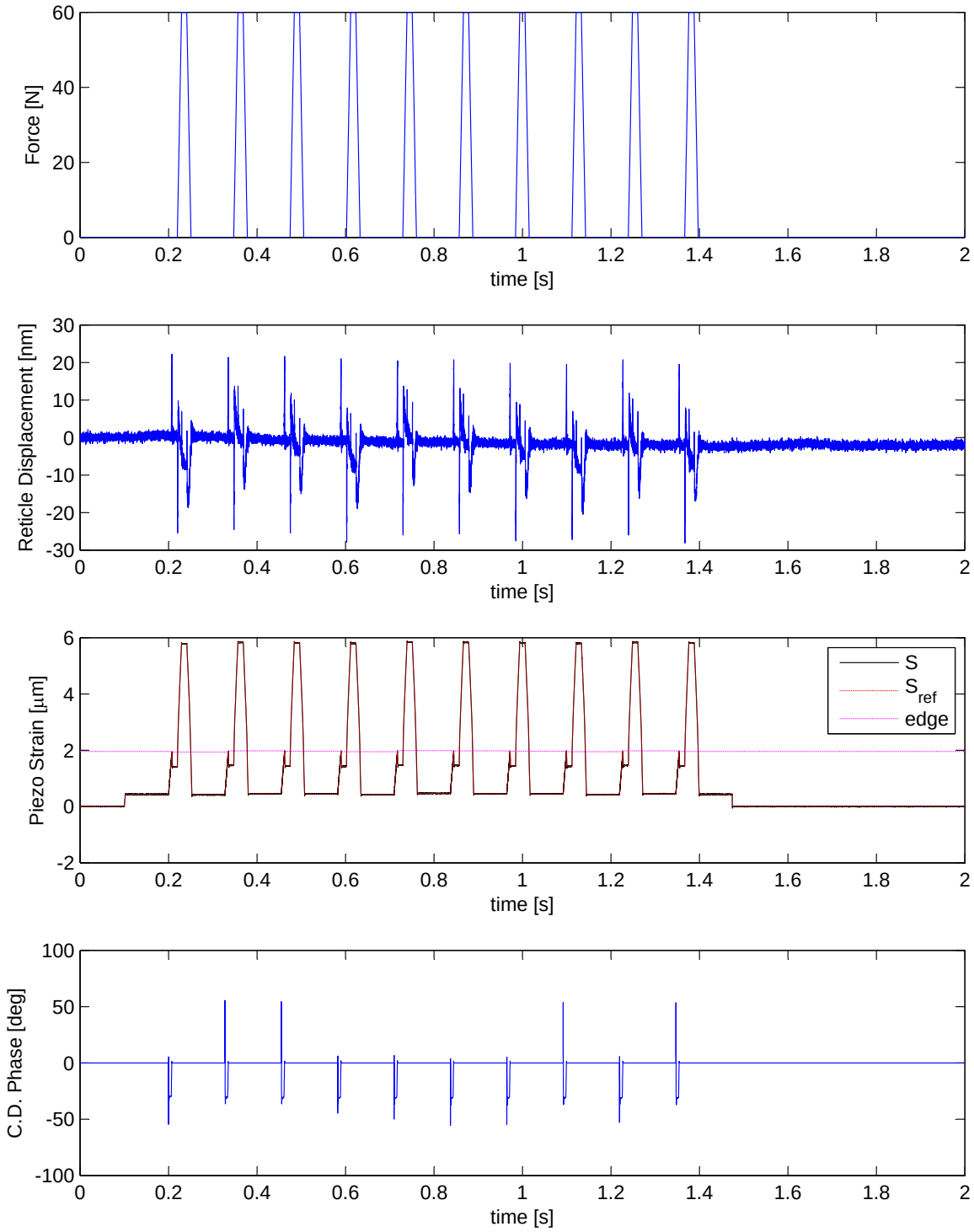

Figure 6-9: Time plot of the reticle-assist experiment for a strain-controlled reticle assist device showing 10 acceleration cycles with a corresponding peak inertial load of 60 N.

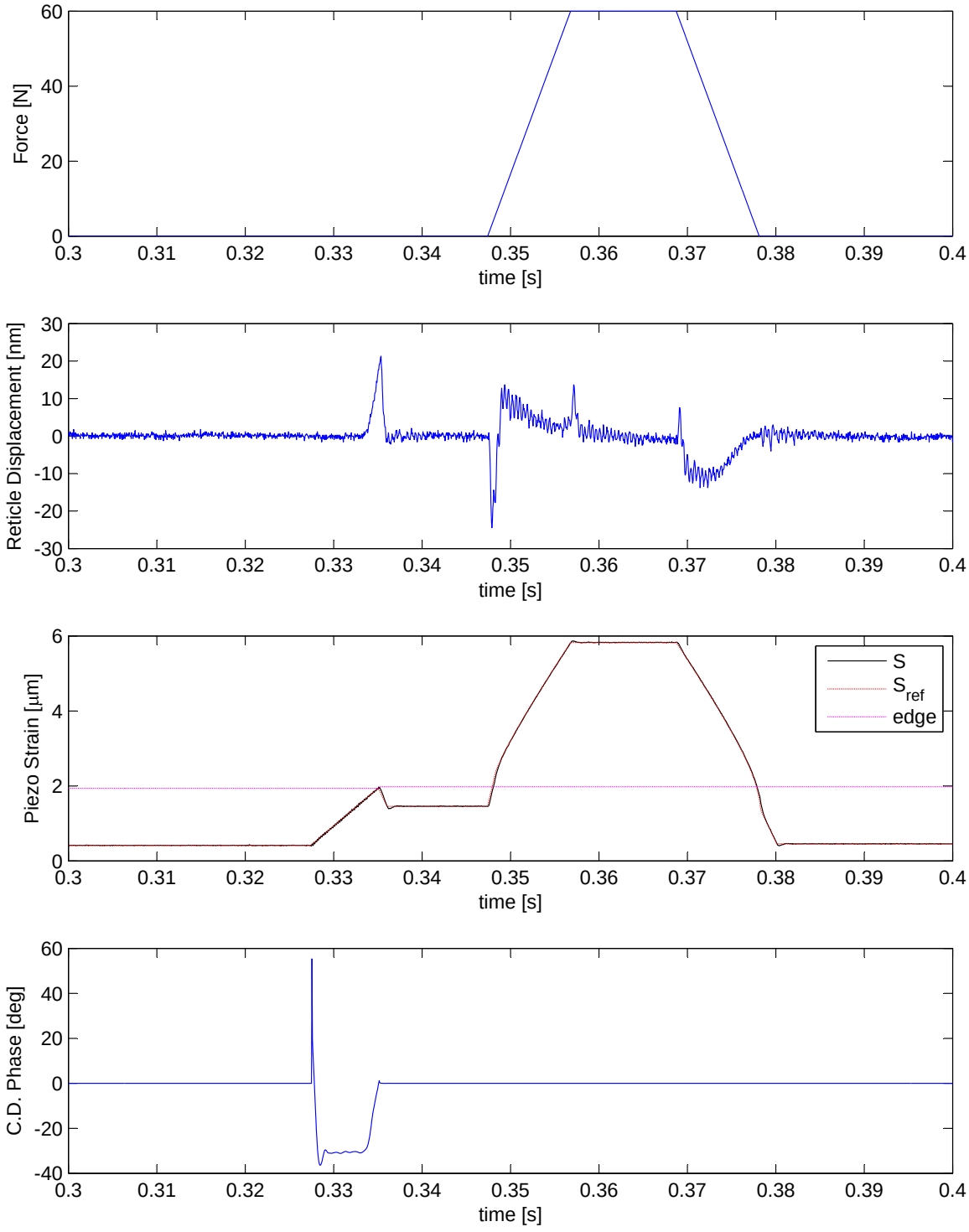

Figure 6-10: Time plot of the reticle-assist experiment for a strain-controlled reticle assist device showing a single acceleration cycles with a corresponding peak inertial load of 60 N.

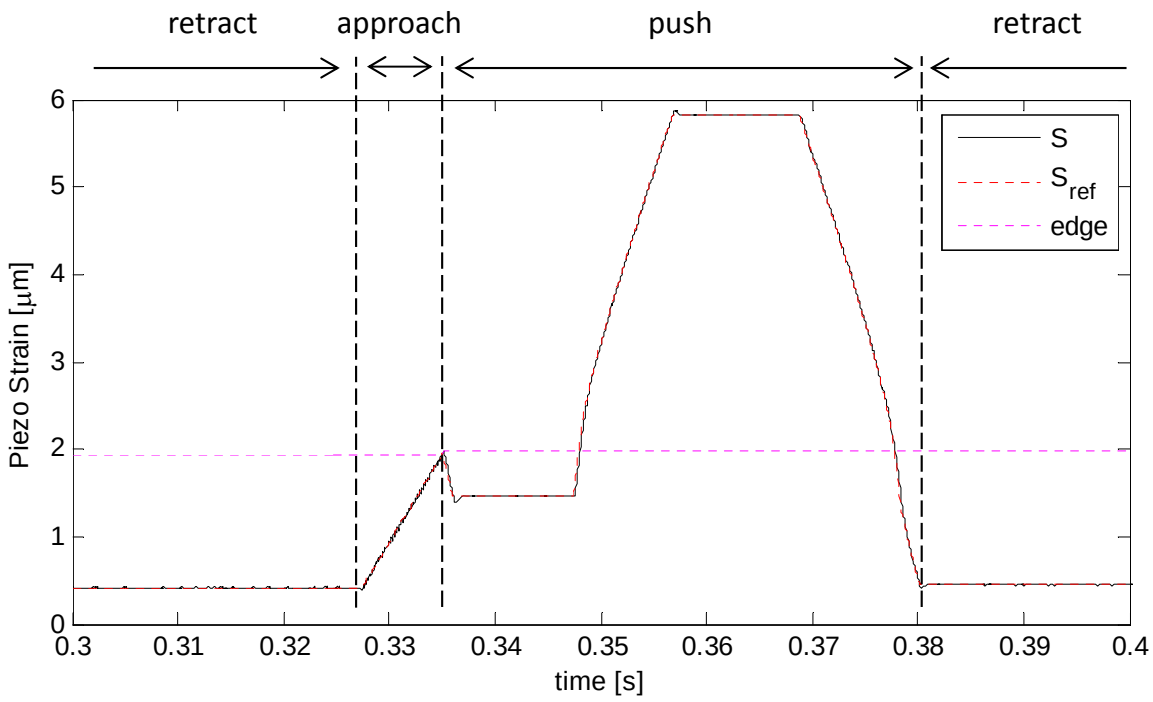

Figure 6-11: Time plot of the reticle assist device's piezo motion shown for one acceleration cycle with the state-machine's state marked on the plot.

retract, and the piezo moves back to a position 1.5 μm away from the reticle edge.

The plot of the reticle displacement in Figure 6-9 shows a slow drift in the reticle's position. This drift is due to forced expansion of the reticle resulting from the thermal expansion for the force actuator part attached to the reticle. Figure 6-12 shows the reticle edge displacement over a longer period of 10 seconds. As can be seen, the initial drift in the reticle position is recovered as the force actuator's temperature decreases with time.

6.2.4 Charge-Controlled Reticle Assist Experiment

Here, we present the results of the reticle assist experiment for the charge-controlled assist device. Time plots of the experimental results for 10 consecutive simulated acceleration cycles are shown in Figure 6-13. The same plots for the single acceleration cycle between the times 0.3 and 0.4 seconds are shown in Figure 6-14. The top plot shows the simulated inertial load, which is applied to the reticle using the reticle assembly's force actuator. For the experiments we use a simulated inertial load profile

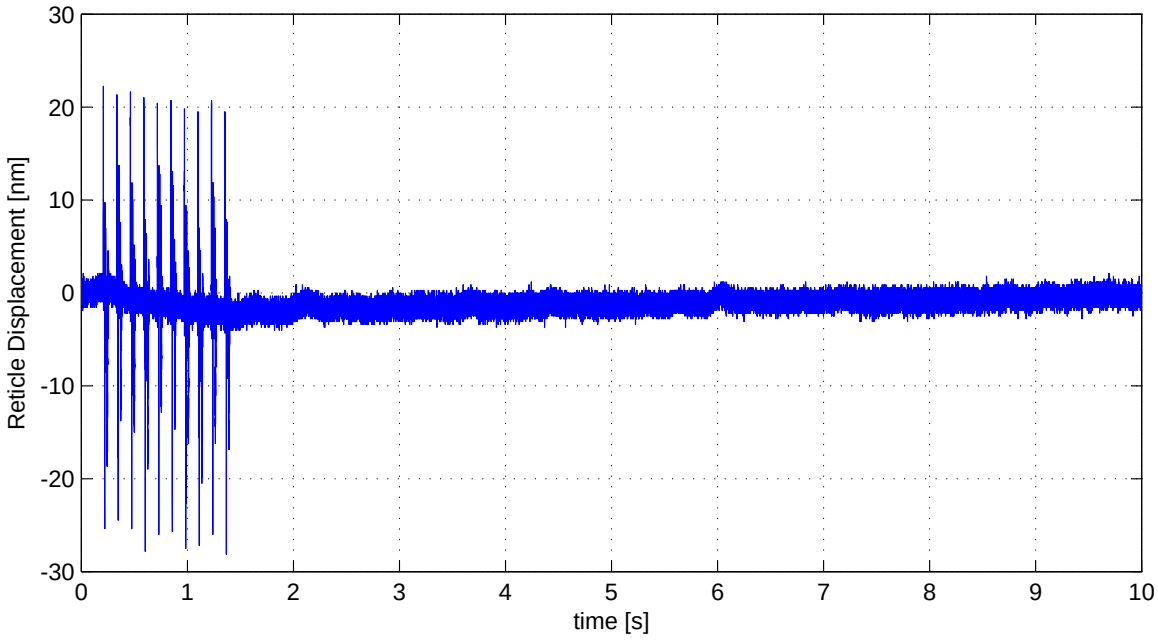

Figure 6-12: Time plot of the reticle edge displacement for the assist experiment shown over a longer period of 10 seconds.

with a 60-N peak force and a 6.4-N/ms maximum rate of change. The top-middle plot shows the displacement of the reticle's edge measured using the capacitive displacement sensors. The reticle's edge displacement is limited to 30 nm, which assuming a reticle clamp stiffness of 100 N/μm is equivalent to 3 N of residual force. This shows that the reticle assist device has compensated about 95% of the simulated inertial load. The bottom-middle plot shows the piezo actuator's charge reference extension, measured charge, HHC compensation charge, and the charge corresponding to the reticle edge location. The bottom plot shows the contact detection method's phase response. Contact is defined as the point where the phase response at the resonance from the peizo's voltage to its current rises above zero degrees. Contact detection is enabled during the approach state. When initially enabled, the contact detection methods goes through a transient where its output is not reliable. For this reason, the contact detection logic ignores the phase response for the first 2 ms.

As can be seen, the charge-controlled assist device is as effective as the strain-controlled assist device. We can successfully compensate 95% of the inertial load without using any sensors, by controlling piezo's charge and measuring its current and

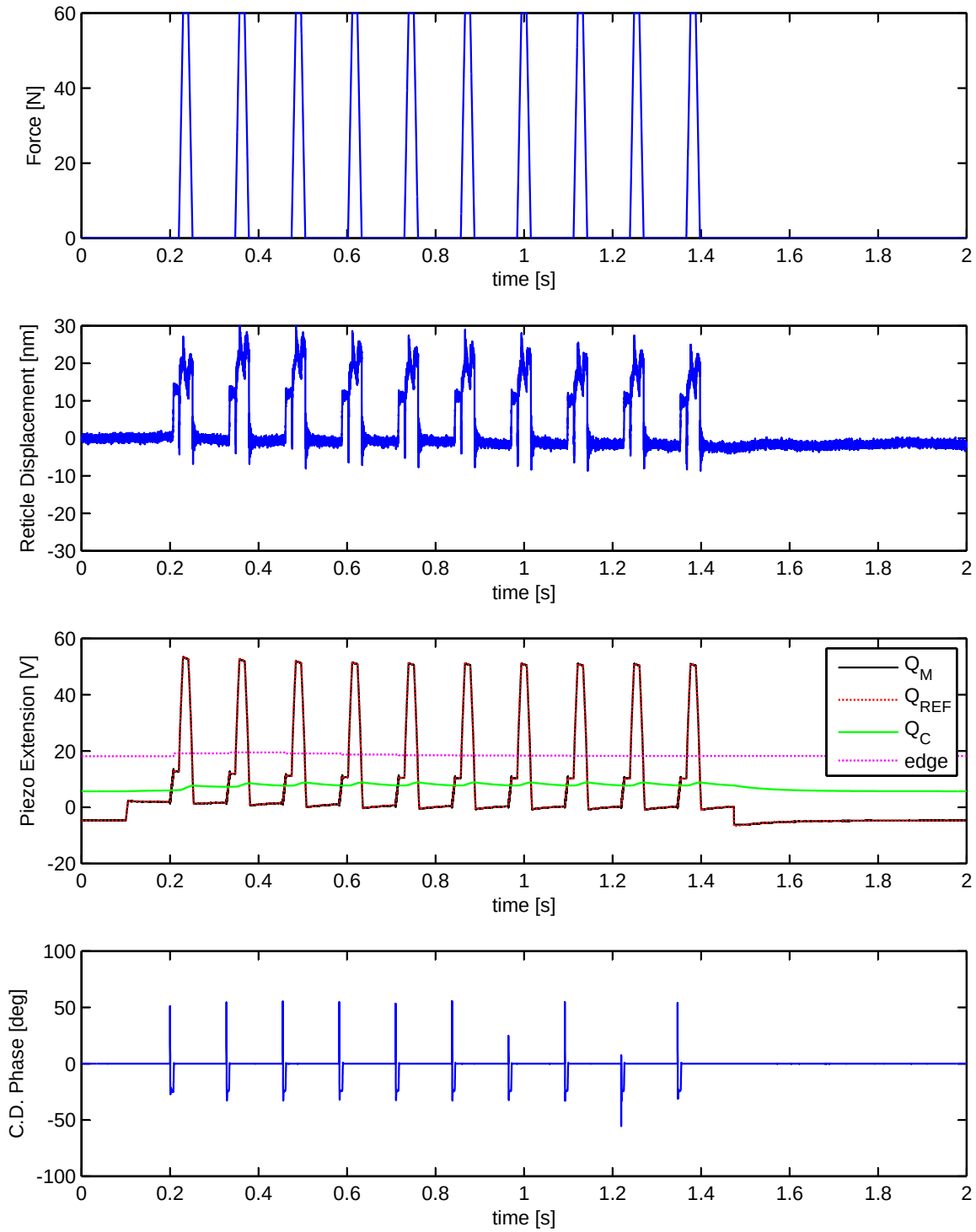

Figure 6-13: Time plot of the reticle-assist experiment for a charge-controlled reticle assist device showing 10 acceleration cycles with a corresponding peak inertial load of 60 N.

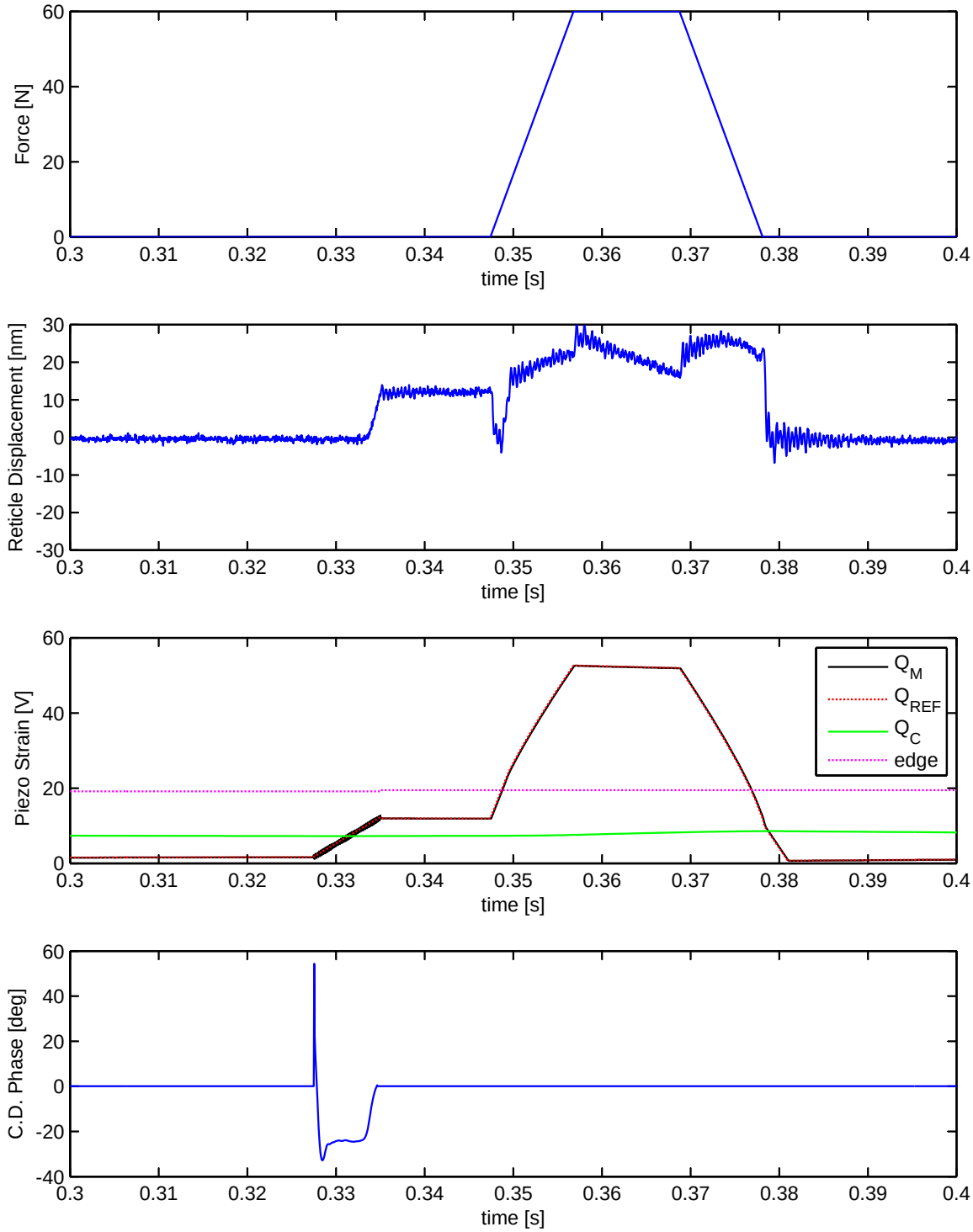

Figure 6-14: Time plot of the reticle-assist experiment for a charge-controlled reticle assist device showing a single acceleration cycles with a corresponding peak inertial load of 60 N.

voltage. As explained in the previous section, the slow drift in the reticle edge position is a result of thermally induced deformations in the reticle and will be recovered as the force actuator's temperature decreases with time. The charge-controlled assist device uses the same state-machine design as the strain-controlled device.

6.2.5 Additional Experimental Results

In this section, we present additional experimental data related to the operation of the assist device.

Force vs. Extension Calibration Map

Figure 6-15 shows the assist device's output force versus the piezo's charge and extension. The force versus charge plot is shown for the charge amplifier with and without the hybrid hysteresis compensation (HHC) method. As can be seen, the force versus charge plot without the HHC method is not repeatable and drifts as a result of the charge amplifier's transient. The drift reduces the assist device's force compensation accuracy. Using the HHC method, we can significantly attenuate the drift and obtain a repeatable force versus charge relationship, which can be accurately used as a calibration map for force compensation. The results presented in Section 6.2.4 are obtained using a charge-controlled device, which utilizes the HHC method and a force versus charge calibration map the same as the blue curve shown in Figure 6-15. The results provided in Section 6.2.3 are obtained using a strain-controlled device, which uses a force versus strain calibration map similar to the red curve in Figure 6-15.

Self-Sensing

Figure 6-16 shows the self-sensing method's phase response versus the contact force. The phase response is calculated at the piezo's first resonance frequency from the piezo's current to its voltage. We define contact as the point where the phase rises above zero degrees. Precise determination of the contact point is important to accurate force control. Detecting contact allows us to relate the piezo's extension to the

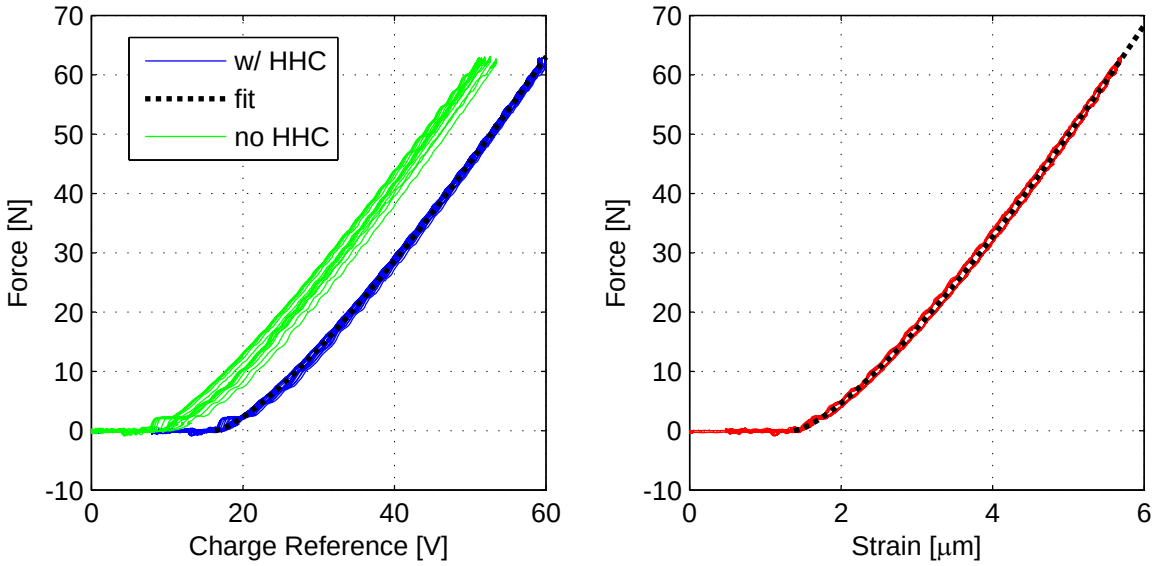

Figure 6-15: Assist device's output force plotted versus the piezo's charge (left) and extension (right). The piezo's force versus charge is shown for the charge amplifier with and without the hybrid hysteresis compensation (HHC) method.

deformation of the mechanical loop, which we use to control the pushing force.

Assist Device Clamp

The assist device uses a vacuum clamp. The clamp's force versus displacement behavior is shown in Figure 6-16. The clamp has hysteresis in the its pre-sliding regime. This is due to non-uniform distribution of compliance over the vacuum surface. Elements of the surface are linked to the load through mechanical links with different compliances. The clamp's pre-sliding behavior can be modeled using the Maxwell slip model. We fit a Maxwell slip mode to the clamp's virgin curve. The virgin curve is the clamp's behavior, when starting from a state where all surface asperities are relaxed. We can set the asperities to their relaxed state and obtain the virgin curve by turning the clamp off and then back on. The model follows the clamp's overall behavior. However, the experimental data shows a slow drift with time, which is not captured by the model. The drift may be due to mechanical creep or thermal drift.

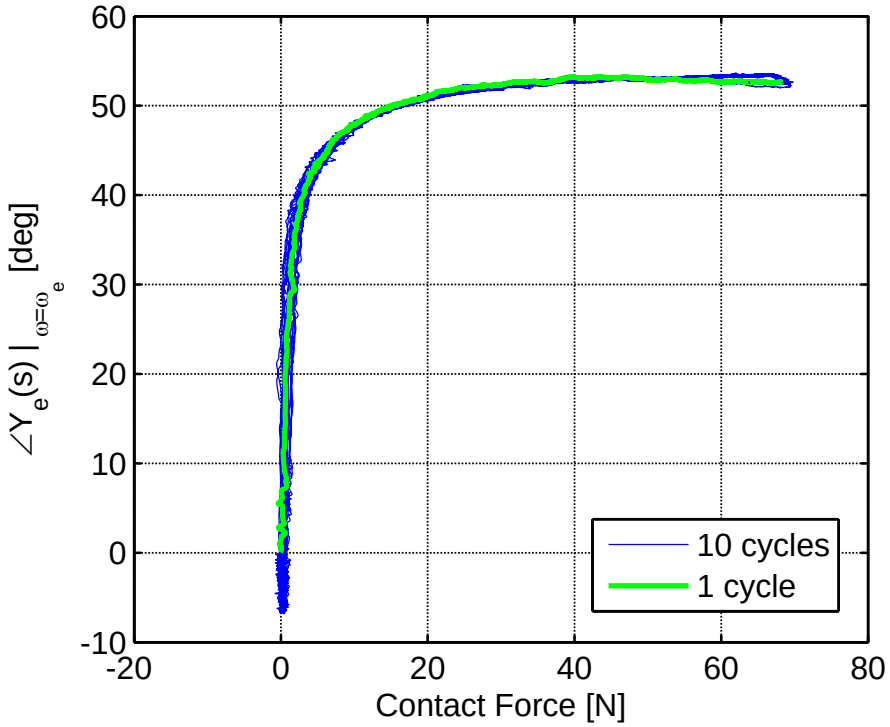

Figure 6-16: The self-sensing method's phase response versus the piezo extension. The phase response is calculated from piezo voltage to piezo current at the piezo's resonance frequency.

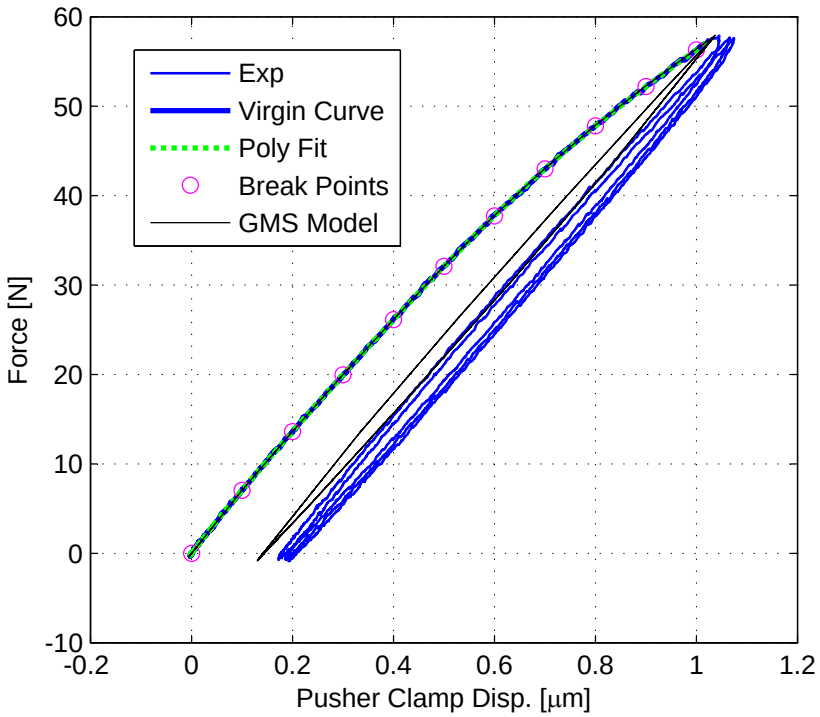

Figure 6-17: Assist device vacuum clamp's force versus displacement behavior within the pre-sliding regime. The plot shows the experimental data (blue), a fitted Maxwell slip model (circles), and the model's simulated output (black).

6.3 Summary

We presented the reticle assist device's control system design. We described the state-machine design which is used for automating the device's operation. We also showed two possible system architecture designs: a configuration that uses a strain gauge for closed-loop piezo position control and a sensorless configuration that uses the VQV charge amplifier with HHC for open-loop piezo position control. We introduced the pre-calibrated extension to force map, which is used by the device to control its output force. This map is based on the piezo extension past the reticle edge. We showed how the self-sensing contact detection method is used to register the piezo's extension in reference to the edge. We performed reticle assist experiments, where the assist device canceled better than 95% of the inertial loads and prevented reticle slip. The experimental setup, methods, and results were provided.

Chapter 7

Conclusions and Suggestions for Future Work

7.1 Conclusion

This thesis provides the design and the enabling control techniques for a high-force density sensorless reticle assist device. By completely eliminating the reticle slip problem in lithography scanners, the device allows a faster stage acceleration and can improve the manufacturing throughput. We designed and experimentally demonstrated successful operation of the reticle assist device. When tested with a simulated inertial force profile with 60-N peak force and 6400-N/s force rate, the device compensated better than 95% of the inertial forces and prevented reticle slip. The results of the reticle assist experiments are provided in Chapter 6, Section 6.2.

We designed and manufactured a piezoelectric solid-state assist device with a low mass, good dynamics, and a large force output. As an alternative, we also presented the detailed design of a novel thermally-balanced magnetostrictive assist device. The mechanical designs are described in Chapter 3. We developed a novel charge amplifier design with a more robust feedback circuit and a method for hysteresis compensation at low frequencies. We experimentally demonstrated the amplifier eliminating piezo's hysteresis at all frequencies. Analogous to the charge amplifier, we also designed a magnetic flux controller, which can be utilized for linearizing the force output of nor-

mal flux (reluctance type) electromagnetic actuators. We tested the magnetic flux amplifier by applying it to a electromagnetically actuated linear positioning stage. The charge amplifier and the magnetic flux controller are presented in Chapter 4. In Chapter 5, we presented a self-sensing contact detection method, which is inspired by atomic force microscopy. We applied this method to the assist device for contact detection and to two AFM systems (HAFM and Macro AFM) for imaging. Utilizing the novel charge amplifier and the self-sensing contact detection method, we implemented a control system which compensates better than 95% of the simulated inertial loads without using any sensors. The design of this control system is presented in Chapter 6.

The following list outlines the main contributions of this thesis:

1. Designed and implemented a high-force density reticle assist device consisting of a coarse approach mechanism and a fine actuation mechanism.

2. Designed a novel thermally balanced magnetostrictive actuator as an alternative actuation method for the assist device.

3. Invented a charge amplifier with better robustness and hysteresis compensation in DC.

   (a) Designed and implemented a charge-controlled amplifier with 100-W power, 140-V rail-to-rail voltage, and 100-kHz small signal bandwidth.

   (b) Introduced a new charge control feedback circuit, referred to as VQV-control, for improved amplifier controller robustness to added series load impedance.

   (c) Invented a method, referred to as hybrid hysteresis compensation (HHC), for compensating conventional charge amplifiers' hysteresis at low frequencies.

4. Applied a self-sensing contact detection method, which has been inspired by atomic force microscopy, to a piezoelectric stack actuator. Demonstrated precise contact detection using the piezo's current and voltage measurements.

5. Experimentally demonstrated the effectiveness of the reticle assist device at eliminating reticle slip. When tested with a simulated force profile with 60-N peak force and 6400-N/s force rate of change, the device compensated better than 95% of the inertial load.

6. As a part of this thesis, the self-sensing contact detection was applied to a piezoelectric self-sensing high-accuracy AFM and a macro-scale electromagnetic profiler:

   (a) Developed the electronics and control for a piezoelectric self-sensing high-accuracy AFM (HAFM). Helped with integration of the HAFM with the SAMM metrology stage at UNC-Charlotte. Confirmed the operation of the AFM by performing imaging tests at MIT.

   (b) Designed and built a novel macro-scale self-sensing magnetic profiler. Performed imaging tests to confirm the operation of the profiler.

7. Developed and tested techniques for electromagnetic reluctance actuator linearization, which were analogous to the methods used for linearization of piezos through charge control.

7.2 Suggestions for Future Work

The following sections outline suggested future work.

7.2.1 Design for Integration and Scan Testing

The reticle assist device was designed for experimental confirmation of the technology. The device was designed for easy manufacturing and operation. For integration with the lithography scanners, the reticle assist device can be re-packaged into a more compact design. In the current design, the bellow, the clamp, and the piezo actuator are stacked in series. The device can be made more compact if the piezo actuator and

the bellow are nested within the clamp. The clamp's size can be reduced by switching to a pressurized clamp. The re-packaged design can be tested on a scanner.

7.2.2 Charge Amplifier Automation

The hybrid hysteresis compensator (HHC) is tuned manually by the operator. The tuning process can be automated. The electronics required for automatic tuning and implementation of the HHC can be added in the form of a micro-controller to the charge amplifier. Additionally, the micro-controller can also be used for adjusting the amplifier's feedback circuit. In this way, the amplifier can be used with piezo actuators having different capacitance values.

7.2.3 Macro-Scale AFM

The Macro-scale AFM was described in Section 5.5. The following subsections discuss the potential to improve the macro AFM.

Low Cost Macro-Scale AFM

As described in Section 5.5, the macro-scale atomic force microscope uses our self-sensing electromagnetic probe design which can be produced at a low cost. However, the XY stage, which is used for raster scanning the sample, is purchased off-the-shelf and is expensive. The development of a low-cost XY stage can significantly reduce the cost of the macro-scale AFM and makes this instrument much more accessible.

Higher Resolution Macro-Scale AFM

The macro AFM has a resolution in the order of $1\mu m$. Future efforts can focus on improving the resolution of the macro AFM. The resolution can potentially be improved by reducing the probe size, which results in a more sensitive probe, by using a coil with more turns, which results in a larger coil voltage, and by using a higher resolution frequency estimation method, which reduces the feedback noise.

Longer Tracking Range Macro-Scale AFM

The macro-scale AFM uses self-actuates the probe for tracking the sample. The probe has a limited actuation range of ± 0.5 mm. The limited tracking range prevents imaging of samples with large features. The macro AFM's range can be improved if a separate actuator with a longer range is used for the tracking axis.

7.2.4 Thermally-Balanced Magnetostrictive Actuator

The design of a novel thermally balanced magnetostrictive actuator was presented in Section 3.4 as a potential alternative for building solid-state assist devices. The actuator was not selected for this application due its larger mass compared to the the piezoelectric stack actuators. However, such an actuator can have applications in other areas, such as fuel injectors. As future work, a thermally-balanced magnetostrictive actuator can be manufactured and experimentally tested.

Bibliography

[1] Introduction to charge drives. Technical report, PiezoDrive. http://www.piezodrive.com.

[2] T. Akiyama, U. Staufer, N. F. de Rooij, P. Frederix, and A. Engel. Symmetrically arranged quartz tuning fork with soft cantilever for intermittent contact mode atomic force microscopy. *Review of Scientific Instruments*, 74(1):112–117, 2003.

[3] T.R. Albrecht, D. Horne, and D. Rugar. Frequency modulation detection using high-q cantilevers for enhanced force microscope sensitivity. *J. Appl. Phys.*, 69:668–673, 1991.

[4] D. Amin-Shahidi. Patterning device support, October 26 2011. US Patent App. 13/281,718.

[5] D. Amin-Shahidi and D.L. Trumper. Oscillation-synchronous control of a frequency-measuring atomic force microscope. In *American Control Conference (ACC), 2012*, pages 2479–2484, 2012.

[6] E.H. Anderson and N.W. Hagood. Simultaneous piezoelectric sensing/actuation: Analysis and application to controlled structures. *Journal of Sound and Vibration*, 174(5):617 – 639, 1994.

[7] Apex Microtechnologies. *AN01 - General Operating Considerations*, 2012. http://apexanalog.com.

[8] Apex Microtechnologies. *EK59 - Evaluation Kit for MP38CL and MP39CL*, 2012. http://www.apexanalog.com.

[9] Apex Microtechnologies. *MP38 • MP38A Power Operation Amplifier*, 2012. http://www.apexanalog.com.

[10] Apex Microtechnologies. *PA12 • PA12A Power Operation Amplifier*, 2012. http://www.apexanalog.com.

[11] W. A. Atia and C. C. Davis. A phase-locked shear-force microscope for distance regulation in near-field optical microscopy. *Applied Physics Letters*, 70(4):405–407, 1997.

[12] M. K .M. Baggen, D.J. Bijvoet, S. N. L. Donders, J. F. Hoogkamp, A. J. M. Jansen, J. J. Kuit, P. Schaap, J. Janssen, H. B. Jasperse, and A. M. Van Der Wel. Stage apparatus, lithographic apparatus and device manufacturing method, December 2 2008. US Patent 7,459,701.

[13] E. De Boer. Theory of motional feedback. *Audio, IRE Transactions on*, AU-9(1):15–21, 1961.

[14] H. Butler. Position control in lithographic equipment [application of control]. *IEEE Control Systems Magazine*, 31(5):28–47, 2011.

[15] R. H. Comstock. Charge control of piezoelectric actuators to reduce hysteresis effects, April 21 1981. US Patent 4,263,527.

[16] D. Croft, G. Shed, and S. Devasia. Creep, hysteresis, and vibration compensation for piezoactuators: Atomic force microscopy application. *Journal of Dynamic Systems, Measurement, and Control*, 123(1):35–43, 2001.

[17] G. Dai, F. Pohlenz, H. Danzebrink, M. Xu, K. Hasche, and G. Wilkening. Metrological large range scanning probe microscope. *Rev. Sci. Instrum.*, 75:962–969, 2004.

[18] J. J. Dosch, D. J. Inman, and E. Garcia. A self-sensing piezoelectric actuator for collocated control. *Journal of Intelligent Material Systems and Structures*, 3(1):166–185, 1992.

[19] Edmund Optics. *LENS PCX 10mm DIA × 100mm FL UNCTD*, 2013. http://www.edmundoptics.com.

[20] H. Edwards, L. Taylor, W. Duncan, and A. J. Melmed. Fast, high-resolution atomic force microscopy using a quartz tuning fork as actuator and sensor. *Journal of Applied Physics*, 82(3):980–984, 1997.

[21] B. J. Eves. Design of a large measurement-volume metrological atomic force microscope (AFM). *Measurement Science and Technology*, 20(8):084003, 2009.

[22] A. J. Fleming and K. K. Leang. Charge drives for scanning probe microscope positioning stages. *Ultramicroscopy*, 108(12):1551–1557, 2008.

[23] A. J. Fleming and S. O. R. Moheimani. Precision current and charge amplifiers for driving highly capacitive piezoelectric loads. *Electronics Letters*, 39(3):282–284, 2003.

[24] A. J. Fleming and S. O. R. Moheimani. Sensorless vibration suppression and scan compensation for piezoelectric tube nanopositioners. *Control Systems Technology, IEEE Transactions on*, 14(1):33–44, 2006.

[25] G. F. Franklin, M. L. Workman, and D. Powell. *Digital control of dynamic systems*, chapter 12.2, pages 484–487. Addison-Wesley Longman Publishing Co., Inc., 1997.

[26] R. Garciaa and Ruben Perez. Dynamic atomic force microscopy methods. *Surface Science Reports*, 47(68):197 – 301, 2002.

[27] P. Ge and M. Jouaneh. Tracking control of a piezoceramic actuator. *Control Systems Technology, IEEE Transactions on*, 4(3):209–216, may 1996.

[28] H. M. S. Georgiou and R. B. Mrad. Electromechanical modeling of piezoceramic actuators for dynamic loading applications. *Journal of Dynamic Systems, Measurement, and Control*, 128(3):558–567, 2006.

[29] F. J. Giessibl. Advances in atomic force microscopy. *Rev. Mod. Phys.*, 75:949–983, Jul 2003.

[30] M. Goldfarb and N. Celanovic. A lumped parameter electromechanical model for describing the nonlinear behavior of piezoelectric actuators. *Journal of Dynamic Systems, Measurement, and Control*, 119:478–485, 1997.

[31] N. J. Groom. Permanent magnet flux-biased magnetic actuator with flux feedback, March 26 1991. US Patent 5,003,211.

[32] P. Günther, U.Ch. Fischer, and K. Dransfeld. Scanning near-field acoustic microscopy. *Applied Physics B*, 48:89–92, 1989.

[33] M. Holmes. *Long-Range Scanning Stage*. PhD dissertation, University of North Carolina at Charlotte, 1998.

[34] Huntsman. *Araldite® LY 5052 / Aradur® 5052*, 2010. http://www.huntsman.com/advanced_materials.

[35] K. Iwamoto. Stage apparatus, exposure apparatus and device manufacturing method, October 22 2002. US Patent 6,469,773.

[36] F. M. Jacobs, E. R. Loopstra, H. K. Van der Schoot, A. F. Bakker, A. M. Van der Wel, K. F. Bustraan, and M. K. M. Baggen. Lithographic apparatus and stage apparatus, February 23 2010. US Patent 7,667,822.

[37] L. Jones, E. Garcia, and H. Waites. Self-sensing control as applied to a pzt stack actuator used as a micropositioner. *Smart Materials and Structures*, 3(2):147, 1994.

[38] L. D. Jones and E. Garcia. Novel approach to self-sensing actuation. In *Proceedings of SPIE*, volume 3041, pages 305–314, 1997.

[39] S. B. Jung and S. W. Kim. Improvement of scanning accuracy of pzt piezoelectric actuators by feed-forward model-reference control. *Precision Engineering*, 16(1):49 – 55, 1994.

[40] H. Kaizuka and B. Siu. A simple way to reduce hysteresis and creep when using piezoelectric actuators. *Japanese journal of applied physics*, 27(5):773–776, 1988.

[41] K. Karrai and R. D. Grober. Piezoelectric tip-sample distance control for near field optical microscopes. *Applied Physics Letters*, 66(14):1842–1844, 1995.

[42] Kistler Instrument Corporation. *High Impedance Load Cells, Type 9212, 9222*, 2003. http://www.kistler.com.

[43] Kistler Instrument Corporation. *Charge amplifier – dual mode charge amplifier with Piezotron® Operating Mode, Type 5010B*, 2009. http://www.kistler.com.

[44] P. T. Konkola, C. G. Chen, R. K. Heilmann, C. Joo, J. C. Montoya, C. H. Chang, and M. L. Schattenburg. Nanometer-level repeatable metrology using the nanoruler. *Journal of Vacuum Science & Technology B: Microelectronics and Nanometer Structures*, 21(6):3097–3101, 2003.

[45] J. A. Kramar. Nanometre resolution metrology with the molecular measuring machine. *Measurement Science and Technology*, 16(11):2121, 2005.

[46] K. Kuhnen, M. Schommer, and H. Janocha. Integral feedback control of a self-sensing magnetostrictive actuator. *Smart Materials and Structures*, 16(4):1098, 2007.

[47] B. J. Lazan. *Damping of materials and members in structural mechanics*. Pergamon Press, 1968.

[48] S. H. Lee, T. J. Royston, and G. Friedman. Modeling and compensation of hysteresis in piezoceramic transducers for vibration control. *Journal of Intelligent Material Systems and Structures*, 11(10):781–790, 2000.

[49] D. L. Ljubicic. Flexural based high accuracy atomic force microscope. Master's thesis, Massachusetts Institute of Technology, 2008.

[50] X. Lu. *Electromagnetically-driven ultra-fast tool servos for diamond turning*. PhD dissertation, Massachusetts Institute of Technology, Department of Mechanical Engineering, 2005.

[51] Magnetic Metals Company. *SuperPerm 49 Laminations*, 1986. http://www.magmet.com.

[52] J. A. Main, E. Garcia, and D. V. Newton. Precision position-control of piezoelectric actuators using charge feedback. In *Smart Structures & Materials' 95*, pages 243–254. International Society for Optics and Photonics, 1995.

[53] D. Meeker. *Finite Element Method Magnetic*. Finite Element Method Magnetic, 2003. http://femm.neil.williamsleesmill.me.uk/femm-manual.pdf.

[54] D. C. Meeker. Optimal solutions to the inverse problem in quadratic magnetic actuators, 1996.

[55] H. Melcher. *Electromagnetic Fields and Energy*. Prentice Hall, 1989.

[56] J. Minase, T. F. Lu, B. Cazzolato, and S. Grainger. A review, supported by experimental results, of voltage, charge and capacitor insertion method for driving piezoelectric actuators. *Precision Engineering*, 34(4):692–700, 2010.

[57] I. Misumi, S. Gonda, Q. Huang, T. Keem, T. Kurosawa, A. Fujii, N. Hisata, T. Yamagishi, H. Fujimoto, K. Enjoji, S. Aya, and H. Sumitani. Sub-hundred nanometre pitch measurements using an AFM with differential laser interferometers for designing usable lateral scales. *Measurement Science and Technology*, 16(10):2080, 2005.

[58] B. Mokaberi and A. A. G. Requicha. Compensation of scanner creep and hysteresis for AFM nanomanipulation. *Automation Science and Engineering, IEEE Transactions on*, 5(2):197–206, april 2008.

[59] G. E. Moore. Cramming more components onto integrated circuits. *Electronics Magazine*, 38(8):33–35, 1965.

[60] NANOSENSORS. *Akiyama probe (A-probe) technical guide*, 2009. http://www.akiyamaprobe.com.

[61] Mohammad Imani Nejad. *Self-bearing motor control and design*. PhD dissertation, Massachusetts Institute of Technology, 2012.

[62] C. V. Newcomb and I. Flinn. Improving the linearity of piezoelectric ceramic actuators. *Electronics Letters*, 18(11):442–444, 1982.

[63] A. Oppenheim, A. Wilsky, and I. Young. *Signals and systems*. Prentice-Hall, 1983.

[64] J. L. Overcash, R. J. Hocken, and Jr C. G. Stroup. Noise reduction and disturbance rejection at the sub-nanometer level. In *Proceedings of ASPE Annual Meeting*, Monterey, CA, 2009.

[65] R. M. Panas, M. A. Cullinan, and M. L. Culpepper. Design of piezoresistive-based mems sensor systems for precision microsystems. *Precision Engineering*, 36(1):44 – 54, 2012.

[66] Physik Instrumente. *P-840 • P-841 Preloaded Piezo Actuators*, 2008. http://www.physikinstrumente.com/.

[67] PMG/Servometer. *Soft-Soldered Bellow Assemblies*. http://www.servometer.com/.

[68] J. Pratt and A. B. Flatau. Development and analysis of a self-sensing magnetostrictive actuator design. *Journal of Intelligent Material Systems and Structures*, 6(5):639–648, 1995.

[69] S. E. Del Puerto and E. Zordan. Reticle support that reduces reticle slippage, November 30 2009. US Patent App. 12/627,771.

[70] J. K. Roberge. *Operational amplifiers: theory and practice*. Wiley, 1975.

[71] J. Rychen, T. Ihn, P. Studerus, A. Herrmann, and K. Ensslin. A low-temperature dynamic mode scanning force microscope operating in high magnetic fields. *Review of Scientific Instruments*, 70(6):2765–2768, 1999.

[72] T. H. Sanders and J. T. Staley. Review of fatigue and fracture research on high-strength aluminum alloys. *Fatigue and Microstructure*, pages 467–522, 1979.

[73] Y. Shibazaki. Stage apparatus, fixation method, exposure apparatus, exposure method, and device-producing method, July 1 2008. US Patent 7,394,526.

[74] Y. Shibazaki. Stage apparatus, fixation method, exposure apparatus, exposure method, and device-producing method, August 28 2012. US Patent 8,253,929.

[75] G. E. Simmers, J. R. Hodgkins, D. D. Mascarenas, G. Park, and H. Sohn. Improved piezoelectric self-sensing actuation. *Journal of Intelligent Material Systems and Structures*, 15(12):941–953, 2004.

[76] A. Slocum. *Precision Machine Design*. Society of Manufacturing Engineers, 1992.

[77] Sony Manufacturing Systems Corporation. *Laserscale interpolator BD96-B1050HC/B1100HC/B1200HC*.

[78] Sony Manufacturing Systems Corporation. *Linear scale with reference mark BE10-111T54*.

[79] Sony Manufacturing Systems Corporation. *Positioning sensor BH20-* $\times \times \times$ *RED*, 2006.

[80] R. L. Spangler. *Broadband control of structural vibration using simultaneous sensing and actuation with nonlinear piezoelectric currents*. PhD dissertation, Massachusetts Institute of Technology, 1994.

[81] Tektronix, Inc. *AM 502 differential amplifier – instruction manual*, 1986.

[82] A. Tonoli, S. Oliva, S. Carabelli, and P. Civera. Charge-driven piezoelectric transducers in self-sensing configuration. In *SPIE's 8th Annual International Symposium on Smart Structures and Materials*, pages 743–752. International Society for Optics and Photonics, 2001.

[83] D. L. Trumper, R. J. Hocken, D. Amin-Shahidi, D. Ljubicic, and J. Overcash. *High-Accuracy Atomic Force Microscope*, volume 413 of *Lecture Notes in Control and Information Sciences*, pages 17–46. Springer Berlin Heidelberg, 2011.

[84] K. A. Yi and R. J. Veillette. A charge controller for linear operation of a piezoelectric stack actuator. *Control Systems Technology, IEEE Transactions on*, 13(4):517–526, 2005.

[85] M. Zahn. *Electromagnetic Field Theory: a problem solving approach.* Krieger, 1987.

[86] E. Zordan. Lithographic apparatus with support for an object and method for positioning same, February 7 2011. US Patent App. 13/022,247.

[87] E. Zordan. Reticle clamping system, June 24 2011. US Patent App. 13/168,109.